
Expedition 316 Site C0008¹

Expedition 316 Scientists²

Chapter contents

Background and objectives	1
Operations	1
Lithology	2
Structural geology	4
Biostratigraphy	5
Paleomagnetism	7
Inorganic geochemistry	8
Organic geochemistry	13
Microbiology and biogeochemistry	14
Physical properties	14
References	17
Figures	18
Tables	76

Background and objectives

Integrated Ocean Drilling Program (IODP) Site C0008 was proposed as contingency Site NT2-10 in an addendum to the IODP Expedition 316 *Scientific Prospectus* (Kimura et al., 2007). This site examined the slope basin seaward of the splay fault penetrated at IODP Site C0004. Site C0008 is ~1 km seaward of Site C0004 (Figs. F1, F2). This contingency site was selected during Expedition 316 because of its good fit with the available time window and the scientific objectives of Expedition 316. Recovered material from this basin will help assess the timing and relative age of past fault motions via identification of provenance and age of basin material. The age difference between newly deposited basin sediments and older uplifted fault blocks will constrain the deformation history. The permeability and geotechnical properties of the basin material will provide reference properties for the section overrun by the splay fault. Shipboard and shore-based study of these properties will constrain the fluid flow and consolidation response of the footwall to splay fault movement. In situ temperature data were also collected to assess the thermal gradient and heat flow in this area for comparison with the temperatures recorded at Site C0004.

Operations

Positioning on Site C0008

The D/V *Chikyu* relocated to Site C0008 (proposed Site NT2-10A) on 26 January 2008. The remotely operated vehicle (ROV) was launched in order to deploy seafloor transponders below the Kuroshio Current (running at 2.0–2.5 kt at the time), and the hydraulic piston coring system (HPCS)/extended shoe coring system (ESCS) bottom-hole assembly (BHA) was rigged up and readied while the vessel was calibrating for dynamic positioning system navigation and positioning over the site. The BHA was run to the seafloor, the ROV launched, position checked, and Hole C0008A (33°12.8229'N, 136°43.5997'E; water depth = 2751 m mud depth below sea level [MSL]) was tagged at 0130 h on 27 January.

Hole C0008A

The first core (316-C0008A-1H) was a successful mudline core that penetrated to 6.93 m core depth below seafloor (CSF) with 100% recovery. Cores 316-C0008A-2H through 28H, 29X through

¹Expedition 316 Scientists, 2009. Expedition 316 Site C0008. In Kinoshita, M., Tobin, H., Ashi, J., Kimura, G., Lallemand, S., Screaton, E.J., Curewitz, D., Masago, H., Moe, K.T., and the Expedition 314/315/316 Scientists, *Proc. IODP*, 314/315/316: Washington, DC (Integrated Ocean Drilling Program Management International, Inc.). doi:10.2204/iodp.proc.314315316.136.2009
²Expedition 314/315/316 Scientists' addresses.



42X, and 43H were collected with a total recovery of 271.2 m at a rate of 75.8% in interlayered mud, silt, and sand. Near the bottom of the hole, starting from Core 316-C0008A-34X, the drilling rate of penetration dramatically increased and recovery dropped to near 0%. After several repeated attempts to improve recovery by changing drilling and pumping parameters and a final attempt to successfully HPCS core the inferred unconsolidated sand at the bottom of Hole C0008A, the hole was abandoned. During this time, a request was made to the Center for Deep Earth Exploration (CDEX) and the Environmental Protection and Safety Panel (EPSP) to shift 215 m southeast and core Hole C0008B. This request was approved.

Pulling out and killing Hole C0008A took place between 0900 and 1815 h on 31 January 2008. The BHA was pulled out of the hole to 200 m above the seafloor and the rig was shifted to Hole C0008B between 1815 and 1930 h on 31 January. Table T1 shows the cores collected, meters recovered, and recovery percentage for Hole C0008A.

Holes C0008B and C0008C

The vessel was positioned above Hole C0008B (Hole C0008C is at the same location) at 2130 h on 31 January 2008 (33°12.7313'N, 136°43.6727'E; water depth = 2797 m MSL). The BHA was run in to the seafloor, and the seafloor was tagged at 2828 m drillers depth below rig floor (DRF). The first HPCS core (316-C0008B-1H) was shot at 2135 h but did not successfully capture the mudline. Hole C0008B was abandoned and Core 316-C0008C-1H (5.51 m of recovery, successful mudline) was shot in Hole C0008C at 0005 h on 1 February. Coring operations in Hole C0008C resulted in the collection of Cores 316-C0008C-1H through 21H, 22X, and 23X* through 25X* (0.0–176.2 m CSF) with total recovery of 189.7 m of core at a rate of 108% (Table T2).

During this operation, observations from previous Hole C0008A were used to adjust the determination of the advance of the piston core based on the drillers information and the observation of large amounts of exotic material sucked into the bottoms of HPCS cores deeper in the section (Cores 316-C0008C-7H through 21H). This phenomenon resulted in initial recovery rates that in some cases exceeded 200% (i.e., with an advance of 5 m and recovery of 10.2 m). However, X-ray computed tomography (CT) imagery and visual core description (VCD) have confirmed that the drillers advance data is a generally reliable measure of actual HPCS penetration. The intervals of each core occupied by exotic material pulled into the core bottom have been recorded, and use of the J-CORES depth processing and

“D-Tunes” functionality will allow postprocessing of the coring recovery and data registration with little difficulty.

After HPCS refusal was determined based on low penetration, severe core liner deformation, and severe core expansion problems in Cores 316-C0008C-17H through 21H, the ESCS coring system was employed. However, the first ESCS core (316-C0008C-22X) was not of sufficient quality to justify further coring (preservation of the unconsolidated portions of the lithologic section and gas hydrates were particularly poor). The scientific goals of this site were deemed to have been accomplished, total depth (TD) was declared, and the newly developed ESCS “punch” coring system was deployed for testing. Three cores (316-C0008C-23X* through 25X*) were collected using this system with excellent results. A postexpedition report of the results of this coring system test is available through the CDEX website.

Following collection of the final ESCS punch core at 2035 h on 2 February, Hole C0008C was abandoned, the hole killed with dense mud, and the BHA pulled out of the hole to the surface. The BHA was recovered at 0530 h on 3 February. The BHA was rigged down, excess drill pipe laid out, and the guidehorn rigged down. Transponders were recovered on the morning of 4 February and the *Chikyu* began transit to Shingu, Wakayama Prefecture, Japan. Expedition 316 ended with first line ashore at 0930 h on 5 February.

Lithology

Two lithologic units were recognized during examination of cores from Site C0008 (Fig. F3; Tables T3, T4). Two subunits are recognized in Unit I. Units and subunits are differentiated based on contrasts in grain size, mineralogy, composition, and presence (and thickness) of minor lithologies. In choosing unit boundaries, we also considered biostratigraphic information, paleomagnetic data, X-ray CT images, observations of structural style, and interpretations of seismic data.

Unit I (slope sediments)

Intervals: Sections 316-C0008A-1H-1, 0 cm, through 34X-1, 22 cm, and Sections 316-C0008C-1H-1, 0 cm, through 25X-7, 124 cm

Depths: Hole C0008A = 0.00–272.46 m CSF and Hole C0008C = 0.00–176.20 m CSF

Age: Pleistocene–Pliocene

Unit I has been divided into two subunits with a boundary between the two at 234.55 m CSF in Hole C0008A (Fig. F3; Tables T3, T4) and at 170.90 m CSF in Hole C0008C.

Subunit IA

Intervals: Sections 316-C0008A-1H-1, 0 cm, through 29X-CC and Sections 316-C0008C-1H-1, 0 cm, through 25X-7, 124 cm

Depths: Hole C0008A = 0.00–234.55 m CSF and Hole C0008C = 0.00–170.90 m CSF

Age: Pleistocene

The dominant lithology of Subunit IA is greenish gray silty clay with a substantial component of calcareous nannofossils, siliceous biogenic debris (sponge spicules, diatoms, silicoflagellates, and radiolarians), and volcanic ash. Calcite content is a distinctive feature of this subunit. Calcite determined by X-ray diffraction (XRD) ranges from 0% to 37% and averages ~7%. A consistent trend toward diminishing carbonate content with depth is observed (Fig. F4; Tables T5, T6). Faint green color banding is present throughout most of the unit, which is often disturbed by mottling or bioturbation.

Secondary lithologies include sand, sandy silt, silt, and volcanic ash, which vary significantly in thickness and frequency throughout the section. The section between 0.00 and 63.00 m CSF in Hole C0008A and 0.00 and 40.00 m CSF in Hole C0008C is dominated by mud with very thin (up to 5 cm) sand interbeds. The section between 63.00 and 116.55 m CSF in Hole C0008A and 40.00 and 65.00 m CSF in Hole C0008C consists of graded sand/silt to mud beds containing ~40% sand/silt and 60% mud. These beds are cyclic, typically with a sharp-based 2 cm dark gray sand, grading upward into 8 cm of burrowed clayey silt and 12 cm of silty clay that typically contains more pelagic debris (coccoliths and siliceous skeletal elements) (Fig. F5). Clusters of volcanoclastic debris and/or ash layers are common near the top of the clay-rich intervals, typically 1–3 cm beneath the base of the next sand bed (Fig. F5B). From 116.55 m CSF in Hole C0008A and 65.00 m CSF in Hole C0008C to the base of the subunit, these graded beds persist, but the sand and silt beds are thinner and less frequent. Some caution is required in interpretation, however, as many of the cores in this section suffered from extensive flow-in structures.

The silt and sand fraction is dominated by quartz and feldspar and metasedimentary lithic fragments and locally includes abundant clear volcanic glass and pumice fragments. Many of the sands are dark gray to nearly black, a coloration that arises from the high content of authigenic pyrite (Fig. F6) rather than from an abundant mafic volcanoclastic component. In the most pyrite-rich sands, pyrite takes the form of microcrystalline grain coatings that greatly hinder grain identification (Fig. F6A). In other sands, pyrite is in the form of disseminated framboids (Fig.

F6B) and also framboids that are localized on fragments of terrigenous organic matter (Fig. F6C).

Volcanic ash layers are distributed throughout Subunit IA (Fig. F7). A distinctive 5 m thick volcanoclastic sand bed is found at 185 m CSF in Hole C0008A with a very high volcanoclastic component (including basaltic fragments with brown glass) with abundant pumice and glass particularly concentrated near the top of the bed. The true thickness of this bed might be smaller as coring disturbance (flow-in structure) and/or gas expansion add uncertainty to the stratigraphic representation in the lower part of cores (see “Operations”). A thick ash layer encountered at 203 m CSF in Hole C0008A and 130 m CSF in Hole C0008B may serve as a regional stratigraphic marker (Fig. F7).

Locally the coarser lithologies (sand, silty sand, sandy silt, and ash) of Subunit IA contain subequant cavities 1–5 cm in diameter that are interpreted as voids left by the decomposition of methane hydrates (see “Organic geochemistry”).

The lower part of Subunit IA is a coarsening-upward sequence. We recognize a substantial decrease in sand and silt content in the upper 63 m CSF of Hole C0008A and above 40 m CSF in Hole C0008C. Subunit IA is interpreted as a slope succession. Reduced sand and silt input affected the upper part, possibly reflecting a change upslope that modified the supply of coarser sediment.

Subunit IB

Intervals: Sections 316-C0008A-29X-CC, 35 through 34X-1, 22 cm, and Sections 316-C0008C-25X-7, 124 cm, through 25X-CC, 21 cm

Depths: Hole C0008A = 234.55–272.46 m CSF and Hole C0008C = 170.90–176.20 m CSF

Age: early Pleistocene–late Pliocene

Subunit IB consists of a series of interbedded mud-clast gravels and silty clay beds. The upper boundary of Subunit IIB is based on the first appearance of gravel-size mudclasts in the core and, compared to Subunit IA, displays lesser calcite content (average = 1%) and greater plagioclase content (average = 32%) in the mud as shown in XRD analysis (Table T6). Gravel beds range from 2 to 80 cm thick and are composed of greenish gray to dark greenish gray slightly indurated silty clay clasts and pumice pebbles, which range in size from <1 mm to 5 cm, in an olive to greenish gray silty clay or silt matrix (Fig. F8). The gravel is mostly unconsolidated, but where more highly consolidated sections do exist, they show a variation in clast-matrix fabric from matrix-supported to clast-supported. The great majority of

clasts are rounded to subrounded, with rare subangular pieces (Fig. F8). In smear slides, an abundance of possible sand-size clay clasts is observed (Fig. F8C). The degree of clast induration and rounding is markedly greater than that observed in the sedimentary breccias at Site C0004. Another contrast with the sedimentary breccias at Site C0004 (Subunit IIA) is the lack of a pronounced unconformity capping the coarse units. As at Site C0004, no shipboard observations address the proximate source of these gravels.

Subunit IB is interpreted as a mass-transport complex that accumulated in the lower slope environment, possibly during an early stage of postaccretion sedimentation.

Unit II (sand-rich turbidites)

Interval: Sections 316-C0008A-34X-1, 22 cm, through 40X-CC, 11 cm

Depth: Hole C0008A = 272.46–329.36 m CSF

Age: Pliocene

The dominant lithology is dark gray fine- to coarse-grained and locally pebbly sandstone with minor silty clay interbeds. The three mud samples analyzed by XRD contain amounts of calcite near the detection limit for the XRD method (0.5% in one sample). Sands are polymictic, and smear slide observations reveal abundant quartz, feldspar, and heavy minerals (mostly pyroxene) with common brown to black semi-opaque grains, which could be mafic-intermediate volcanic rock fragments, clay clasts, or glauconite. Pebbles include rounded fragments of basalt, plutonic rocks, schist, vein quartz, chert, sandstone, and mudstone. This detrital grain assemblage is similar to that observed in the sands and associated gravels encountered in Unit II at Site C0007. As at Site C0007, the sands correspond to a zone of high drilling penetration rate and limited core recovery.

The coarse-grained nature of this unit is consistent with the more axial portion of a trench wedge deposit.

X-ray CT number

X-ray CT images were used extensively by the science party for evaluation of sedimentological and structural features. Figure F9 shows the depth trends for CT number (averaged pixel intensity for a 1 mm² area) determined for coherent rock pieces and tectonic conglomerate clasts of silt clay. CT number reflects the average sample density at the scale of the CT observation, a value that is affected by sample composition (mineral composition and density) and porosity (bulk density), although in these porous samples it is largely dominated by the porosity. Across Units I and II CT number increases with depth.

Structural geology

The two holes drilled at Site C0008 sampled the same nondeformed to weakly deformed sediments as found in the footwall of the major splay faults imaged by seismic reflection and sampled at Site C0004. Structural data measured on cores are given as a supplementary material (see C0008_STRUCT_DATA.XLS in folder 316_STRUCTURE in “[Supplementary material](#)”). Where possible, planar structures were corrected to true geographic coordinates using paleomagnetic data (see “[Structural geology](#)” in the “Expedition 316 methods” chapter). The distribution of planar structures and lithologic divisions with depth are shown in Figure F10.

The main structural features encountered in Holes C0008A and C0008C are subhorizontal bedding and normal faults. Deformation bands and sediment-filled veins were not observed at Site C0008.

Bedding and fissility

At Site C0008, bedding surfaces seldom dip >30° (Fig. F10). Figure F11 shows the distribution of poles to bedding surfaces after correction based on paleomagnetic data. The dip directions do not show any preferred orientation.

Fissility is poorly developed at Site C0008. It can be observed in Hole C0008A at depths >263 m CSF and is not observed in Hole C0008C. Given the small number of measurements, fissility data are not included in the data for Figure F11.

Faults

Cores from Site C0008 are moderately faulted. The distribution and dip of faults with depth are given on Figure F10. In Hole C0008A, they are distributed throughout, whereas in Hole C0008C, they are found between 35 and 175 m CSF. Where determinable, the sense of slip is always normal (Fig. F12). In most cases, the amount of slip does not exceed 5 cm.

At the shallowest levels, normal faults do not consist of sharp slip surfaces but rather of shear zones that range from <1 mm to ~2 cm thick. Where the shear zone is thick enough to allow internal observation, ductile deformation structures such as heterogeneous stretching of layers testify to the unconsolidated state of the sediments at the time of faulting. Striations are usually weakly developed.

At deeper levels where sediments are more consolidated, faults appear as dark seams that do not exceed 1 mm in thickness. Such structures, which were also observed at Site C0007 (see “[Structural geology](#)” in the “Expedition 316 Site C0007” chapter), are called healed faults. Like faults in unconsolidated sedi-

ments, most healed faults dip $\sim 60^\circ$ or steeper (Fig. F13A) and commonly show normal offsets of 5 cm or less. Some healed faults are horizontal or nearly horizontal and parallel to bedding (Fig. F13B). In such cases, the sense and amount of slip cannot be determined. After correction based on shipboard paleomagnetic data, fault surfaces from either hole of Site C0008 do not reveal any preferred orientation (Fig. F14).

A high concentration of normal faults is found in Hole C0008C between 35 and 80 m CSF. It is interesting to note that this concentration of normal faults is located near a discontinuity in bedding dip apparent in seismic reflection profile Inline 2675 (see Fig. F3 in the “Expedition 316 summary” chapter). X-ray CT scan image analysis suggests the existence of a 5 cm thick gently dipping shear zone in Section 316-C0008C-5H-6, 93 cm, which could correspond to this discontinuity.

Discussion and summary

After reorientation based on shipboard paleomagnetic measurements, normal faults from Site C0008 do not indicate any clear direction of extension. They rather show scattered directions suggesting vertical compaction of the sedimentary pile.

The location of Hole C0008C was chosen in order to crosscut a seismic imaged discontinuity between two packages of sediments having slightly different bedding orientation. The discontinuity could represent a low angle normal fault or the basal detachment fault of a landslide. No major shear zone could be observed in cores at the corresponding depth.

Biostratigraphy

Three holes were drilled at Site C0008 (Holes C0008A, C0008B, and C0008C). The biostratigraphy determined for Site C0008 was mainly based on examination of calcareous nannofossils and radiolarians from Holes C0008A and C0008C.

Calcareous nannofossils

All core catcher samples plus additional samples from some critical intervals in the vicinity of zonal boundaries were examined for calcareous nannofossils at Site C0008. Calcareous nannofossils are generally abundant and moderately preserved above 100 m CSF in Holes C0008A and C0008C; they are in low abundance and moderately to mostly poorly preserved below that depth in both holes (Tables T7, T8).

In Hole C0008A, 16 nannofossil biostratigraphic events are recognized (Table T9). The uppermost Sample 316-C0008A-1H-CC contains few *Emiliania*

huxleyi and abundant *Gephyrocapsa* spp. ($>3.5 \mu\text{m}$), indicating the transition (X) of *Gephyrocapsa* spp. ($>3.5 \mu\text{m}$) to *E. huxleyi* (<0.063 Ma) within Zone NN21. Samples from 316-C0008A-2H-CC through 31X-CC are assigned to Zone NN19, based on the presence of *Pseudoemiliania lacunosa* and absence of reliable occurrence of *Discoaster brouweri* (marker of Zone NN18). The top of Zone NN19 is not marked by the last occurrence (LO) of *P. lacunosa*, as Sample 316-C0008A-2H-CC contains *Reticulofenestra asanoi* but lacks *Gephyrocapsa* spp. ($\geq 4 \mu\text{m}$), indicating an age interval of Zone NN19, between 1.04 Ma (reentrance [RE] of *Gephyrocapsa* spp. [$\geq 4 \mu\text{m}$]) and 1.078 Ma (first consistent occurrence [FCO] of *R. asanoi*). There should be low sedimentation rates or a discontinuity between these two samples. The subdivision of Zone NN19 is somewhat difficult as the event sequence of the LO of *Gephyrocapsa* spp. ($>5.5 \mu\text{m}$), LO of *Helicosphaera sellii*, FCO of *Gephyrocapsa* spp. ($>5.5 \mu\text{m}$), and LO of *Calcidiscus macintyreii* ($\geq 11 \mu\text{m}$) repeats (Table T9; Fig. F15). The age reversal occurs above and below Sample 316-C0008A-9H-CC. The radiolarian record in Hole C0008A suggests the age reversal occurs below Sample 316-C0008A-9H-CC in agreement with the nannofossil record. As seismic results showed a continuous normal sequence in this hole, it is hard to explain the record at the present time. Considering the location of Hole C0008A on the unstable slope, slumping might be one possible cause for the sequence disturbance. On the other hand, the possibility exists that determinations of microfossil events were affected by reworked fossils. The latter possibility will be examined in postcruise study. The lowest event of Zone NN19 is the first occurrence (FO) of *Gephyrocapsa* spp. ($>3.5 \mu\text{m}$) at 238.91 m CSF. Pliocene Zones NN18, NN17, and NN16 are recognized in the lower sequence from 254.10 to 282.35 m CSF in Hole C0008A (Table T9; Fig. F15). The occurrence of *Sphenolithus* spp. at 282.35 m CSF is taken as its LO event for the lowest possible event in Zone NN16. No reliable data were obtained below 282.35 m CSF because of poor recovery. The lowermost sample from 329.36 m CSF contains abundant *Reticulofenestra pseudoumbilicus* ($>7 \mu\text{m}$), dominant *Sphenolithus* spp., and a few *Discoaster quinqueramus* (marker of Zone NN11), indicating an age of Miocene Zone NN11. This sample may be a mudclast (lithoclast) fallen from one of the mudstone gravels encountered higher in the borehole. No other samples of Miocene age were identified during shipboard study, however. Postcruise study will clarify the association of this lowermost sample.

A total of six Pleistocene nannofossil events were determined for Hole C0008C (Table T10). Sample 316-C0008C-1H-CC contains dominant *E. huxleyi*,

indicating the sample is younger than the transition of *Gephyrocapsa* spp. (>3.5 μm) to *E. huxleyi*, and is assigned to Zone NN21 (<0.063 Ma). Sample 316-C0008C-2H-CC contains *Gephyrocapsa* spp. (>5.5 μm) and abundant *Gephyrocapsa lumina* (an earlier Pleistocene species) in the *Gephyrocapsa* medium II group, and the occurrence of the *Gephyrocapsa* spp. (>5.5 μm) is determined as its LO event. As a result, Sample 316-C0008C-2H-CC is assigned to Zone NN19. A ~1 m.y. difference between Samples 316-C0008C-1H-CC and 2H-CC implies low sedimentation rate or discontinuity between these two samples (Fig. F16). Zone NN19 sediments in Hole C0008C are divided by the following events: the LO of *H. sellii*, FCO of *Gephyrocapsa* spp. (>5.5 μm), LO of *C. macintyrei* (≥ 11 μm), and FO of *Gephyrocapsa* spp. (>3.5 μm). These events are comparable to the same events below Sample 316-C0008A-9H-CC in Hole C0008A. The sporadic occurrence of the Pliocene Zone NN18 marker *D. brouweri* in the Pleistocene sequence is clearly due to reworking. Therefore, the entire sequence recovered in Hole C0008C is assigned to the Pleistocene.

In addition, the nannofossil record at Site C0008 is notable. Sample 316-C0008A-19H-CC in Hole C0008A and Samples 316-C0008C-15H-CC and 16H-CC in Hole C0008C contain a number of small forms (~2.5–3 μm) that are morphologically very similar to *E. huxleyi* (marker of Zone NN21), and their occurrence in these samples is marked with a “?” (Tables T7, T8). These samples are assigned to Zone NN19 according to the presence of *Gephyrocapsa* spp. large (>5.5 μm) and abundant *G. lumina* (an earlier Pleistocene species) at the present time. A detailed study on this small form is necessary to refine biostratigraphy of Site C0008 during postcruise study, including examination of more samples and study with a scanning electron microscope (SEM).

Other microfossil groups

Radiolarians, diatoms, and foraminifers are common to abundant and moderately to poorly preserved throughout the upper part of Holes C0008A, C0008B, and C0008C. Sediments retrieved below Core 316-C0008A-30X are barren of radiolarians but contain a few silty horizons with abundant foraminifers, mainly benthic. All core catchers from both holes and a few additional discrete samples (Hole C0008A only) have been processed for radiolarian content. When foraminifers were abundant, samples were also checked for marker species.

Radiolarians are common to abundant and moderately to poorly preserved in the upper part of the sequence in Hole C0008A (until Section 316-C0008A-5H-CC). Preservation and abundance de-

creases but radiolarians still occur sparsely to Core 316-C0008A-30X. Two zones are identified. Sample 316-C0008A-1H-CC and possibly 2H-CC are included in the *Botryostrobus aquilonaris* Zone (Fig. F17). In Sample 316-C0008A-3H-CC, the occurrence of *Eucyrtidium matuyamai* and *Stylatractus universus* assigns that sample to the *Eucyrtidium matuyamai* Zone, implying an age gap within the *S. universus* interval. This gap correlates with low sedimentation rates or a discontinuity between Cores 316-C0008A-1H-CC and 2H-CC, clearly shown by the calcareous nannofossil age determination. The interval to Sample 316-C0008A-30X-CC was also attributed to the *E. matuyamai* Zone, although the marker species only occurs to Core 316-C0008A-25X-CC, but species occurring only in the Pleistocene were found to Core 316-C0008A-30X (e.g., *Spongaster tetras*).

Between Cores 316-C0008A-27X and 30X, layers with abundant foraminifers are observed. Most of these foraminifers are benthic with very few small planktonic taxa. In Cores 316-C0008A-31X through 316-C0008A-40X, no radiolarians are found.

In Hole C0008C (including Section 316-C0008B-1H-CC), radiolarians are common to abundant and moderately to poorly preserved in the upper part of the sequence (until Section 316-C0008C-15H-CC). Preservation and abundance decreases downhole, but radiolarians still occur sparsely to Core 316-C0008C-24X. The *Botryostrobus aquilonaris* Zone is identified to Sample 316-C0008A-2H-CC. The occurrence of *E. matuyamai* in the interval from Sample 316-C0008C-3H-CC through Sample 316-C0008C-24H-CC indicates an age range between 1.05 and 1.98 Ma for this interval (25.37–166.90 m CSF) and implies an age gap spanning at least the entire *S. universus* Zone between 15.48 and 25.37 m CSF.

Summary

Two microfossil groups (from core catcher samples), calcareous nannofossils and radiolarians, were analyzed for biostratigraphy at Site C0008. Moderately preserved and abundant calcareous nannofossils and radiolarians were seen in samples from the upper part of the sequences in Holes C0008A and C0008C, whereas they are relatively poorly preserved in the lower part of the sequences in both holes.

In Hole C0008A, calcareous nannofossil zones from Pleistocene Zone NN21 through Pliocene Zone NN16 were recognized and Pleistocene radiolarians *B. aquilonaris* and *E. matuyamai* zones were determined. Records from both of these microfossil groups suggest a discontinuity between Samples 316-C0008A-1H-CC and 3H-CC and a possible age reversal or disturbance between Samples 9H-CC and 10H-CC.

In Hole C0008C, calcareous nannofossil zones from Pleistocene Zones NN21 through NN19 were recognized and Pleistocene radiolarians *B. aquilonaris* and *E. matuyamai* zones were determined. Records from both of these microfossil groups suggest a discontinuity between Samples 316-C0008A-1H-CC and 3H-CC.

Paleomagnetism

By the end of Expedition 316, coring penetrated to ~329 m CSF in Hole C0008A and ~176 m CSF in Hole C0008C and recovered various sediments and rocks (see “**Lithology**”). At Site C0008, we continued to perform measurements of archive half core sections and progressive demagnetization measurements of discrete samples. Pass-through magnetometer measurements on split-core archive sections were made at 5 cm intervals. Archive-half cores were demagnetized to 40 mT using alternating-field (AF) demagnetization. A number of core sections that have distinctive flow-in structures were not measured or sampled. Before the measurement data were uploaded to the J-CORES database, we excluded data from voids and from the top and bottom ~15 cm to avoid end-core edge effects. In order to test accuracy of the half-core data and provide additional insight into remanence magnetization direction and carriers, we demagnetized a total of 80 discrete samples using AF (77) and thermal (3) demagnetization techniques. Because of the time limit at the end of the expedition, pass-through measurements were carried out with only two demagnetization steps of natural remanent magnetization (NRM) and 40 mT for the cores from Hole C0008C and their data were processed postcruise. For this reason, discrete sample measurements were only performed with samples from Hole C0008A.

Natural remanent magnetization and magnetic susceptibility

Downhole variations of paleomagnetic data obtained from Holes C0008A and C0008C are shown in Figures **F18** and **F19**, respectively. In Hole C0008A, sedimentary cores recovered from 0 to 45 m CSF continue to be nannofossil-rich mud and sand layers and volcanic ashes. These sediments have low NRM intensity (mean = ~10 mA/m) and low magnetic susceptibility (mean = ~12 × 10⁻³ SI units). Sediments between ~40 and 150 m CSF have a higher NRM intensity (mean = ~39 mA/m) and magnetic susceptibility (mean = ~21 × 10⁻³ SI units). Cores between 160 and 270 m CSF have the strongest NRM intensity (mean = ~207 mA/m) and magnetic susceptibility (mean = ~119 × 10⁻³ SI units). As shown in Figure **F18**, magnetic susceptibility (Fig. **F18A**) and NRM intensity variations (Fig. **F18B**, green) through

sedimentary units are closely correlated. Two significant increases in magnetic susceptibility are present at ~45 and 165 m CSF. Interestingly, the stable inclinations (Fig. **F18C**, red crosses) also switch polarity from normal to reversed at ~165 m CSF, suggesting that characteristic susceptibility and NRM intensity response might be useful for identifying geomagnetic event boundaries. High and low susceptibility peaks throughout Hole C0008A range from 824 × 10⁻³ to 5 × 10⁻³ SI units. These variations in susceptibility are probably caused by variations in the magnetic mineral type or variations in the content of magnetic minerals in the observed volcanic ashes and silty clay with depth. Below 270 m CSF, poor recovery of the sand layers in lithologic Unit II limits magnetic characterization of this unit. A few pass-through whole-core magnetic susceptibility measurements give an indication of relatively higher susceptibility values (>350 × 10⁻³ SI units) (Fig. **F18A**).

Two significant magnetic susceptibility increases can also be found in Hole C0008C at ~48 and 108 m CSF (Fig. **F19A**). Mean values are 13 × 10⁻³ SI units (0–48 m CSF), 27 × 10⁻³ SI units (48–108 m CSF), and 84 × 10⁻³ SI units (108–176 m CSF), which are consistent with those values at corresponding depths in Hole C0008A. NRM intensity varies from 14 mA/m (0–48 m CSF) to 150 mA/m (48–108 m CSF) and 156 mA/m (108–176 m CSF) in Hole C0008C, which shows that the middle part does not agree with values in Hole C0008A. Although the second magnetic susceptibility increase in Hole C0008C appeared 40 m shallower than that in Hole C0008A, there are ~10 m thick characteristically low susceptibility zones (~10 × 10⁻³ SI units) just above the increase. A gradual downward increase of inclination values starts from ~108 m CSF in harmony with the second increase of magnetic susceptibility and NRM intensity in Hole C0008A. This resemblance suggests that the boundary at 150 m CSF in Hole C0008A can correspond to the one at 108 m CSF in Hole C0008C.

Discrete samples and core orientation

Remanent magnetization of discrete samples was investigated using stepwise AF or thermal demagnetization (Figs. **F20**, **F21**). The steep downward component of magnetization imparted by the coring process can be removed by both demagnetization techniques, but AF demagnetization appears to be more effective in removing this drilling-induced component (Fig. **F20**). Thus, AF demagnetization was preferred over the thermal technique for sediments and rocks in Hole C0008A. We also noted that several samples from 100 m CSF display a higher stability of remanent magnetization (Fig. **F20C**), suggesting that the magnetization of these samples are

carried by grains with high coercive force. The characteristic inclinations from 80 discrete samples are mostly concentrated at 52°, suggesting these samples maintain an inclination close to the expected dipole inclination for the latitude of this site (52°) and indicating they may represent the primary magnetization when the sediments were deposited.

At Site C0008, we also obtained representative paleomagnetic directions from several intervals for structural analysis and core orientation. The preliminary results suggest that overall paleomagnetic data are reasonably robust to provide information about the geographic north and serve as reference directions for structural studies (see “[Structural geology](#)”).

Magnetostratigraphy

We used stable inclinations from both pass-through and discrete measurements to define magnetic polarity sequences for Holes C0008A and C0008C (Fig. [F22](#), [F23](#)). For Hole C0008A, both calcareous nannofossils and radiolarians allowed us to tentatively correlate certain parts of the magnetic polarity interval recorded in the sediments with the geomagnetic reversal timescale. Biostratigraphic samples at a mean depth of 17.0 m CSF have been assigned ages between 1.04 and 1.08 Ma; hence, the observed positive inclinations at this depth range (Fig. [F22](#)) suggest that these sediments were likely deposited within the Jaramillo Subchron (0.99–1.07 Ma; see Gradstein et al., 2004) instead of the Brunhes Chron. The polarity shift from normal to reversed at 24.8 m CSF (in Section 316-C0008A-3H-10) may thus represent the beginning of the Jaramillo normal polarity subchron. The Emperor event (0.42 Ma), a short reversal within the upper part of the Brunhes normal chron, appears not to have been recorded by the recovered cores in Hole C0008A, although two discrete samples at 5–8 m CSF revealed negative inclinations (Fig. [F22](#)).

Below 220 m CSF, a dominantly normal polarity sequence appears to correspond to the Olduvai normal subchron, as the available coeval biostratigraphic indicators are also placed in this depth interval. Shipboard biostratigraphic data suggest that sediments below 186 m CSF are older than 1.6 Ma and nannofossil biostratigraphic Zone NN18 (~2.06 Ma) is placed at 259 m CSF (see “[Biostratigraphy](#)”). This information suggests that the dominantly normal polarity sequence between 220 and 270 m CSF may represent part of the Olduvai Subchron (1.77–1.95 Ma).

For Hole C0008C, the polarity shift from normal to reversed occurred at 30.5 m CSF, which might correspond to the beginning of the Jaramillo Subchron (Fig. [F23](#)). A short spike of polarity change at 7.3 m CSF within biostratigraphic Zone NN20 appears to be related to the Emperor event (0.42 Ma).

The polarity changes to normal at 160 m CSF, which is located between biostratigraphic data of 1.67 Ma at ~143 m CSF and younger than 1.98 Ma at ~167 m CSF. This normal polarity is considered to be the end of Olduvai Subchron (1.77 Ma) and appears 60 m shallower than in Hole C0008A. The shallowing of corresponding depth between Holes C0008A and C0008C was found in two independent data sets such as magnetic susceptibility and inclination.

In summary, preliminary shipboard paleomagnetic studies revealed some important magnetostratigraphic signatures at Site C0008 that await verification by shore-based studies.

Inorganic geochemistry

The main objectives of the geochemical program at Site C0008 are to

- Characterize in situ biogeochemical reactions;
- Constrain in situ inorganic diagenetic reactions with depth;
- Identify potential deep-sourced fluids within fault zones and other permeable horizons, as well as fluid-sediment reactions at the source; and
- Constrain the subsurface hydrology, including fluid flow pathways and possible transport mechanisms.

A total of 67 whole-round samples were collected for interstitial water analyses at Site C0008 (35 from Hole C0008A, 1 from Hole C0008B, and 31 from Hole C0008C). Whole-round lengths ranged from 6.5 to 42.5 cm with larger subsamples collected from cores recovered deeper within the hole where the sediments were more consolidated.

Samples were collected at a higher spatial resolution in the uppermost 30 m of Holes C0008A and C0008C to define the sulfate-methane transition (SMT) in order to constrain the relative importance of anaerobic oxidation of methane (AOM) versus ordinary organic matter oxidation in producing the observed profile at this site, as well as for future geochemical and microbiological studies. Below Cores 316-C0008A-3H and 316-C0008C-3H, one sample was taken per core. The main geochemical objectives below the SMT were to identify the main in situ diagenetic reactions in the sediment section and any exotic/deeper-sourced fluids along permeable horizons and zones of deformation. This was done through analysis of dissolved elements that reflect inorganic fluid-rock reactions or microbially mediated reactions. Pore fluid chemical compositions and $\delta^{18}\text{O}$ isotopic ratios are reported in Tables [T11](#) and [T12](#) and plotted as a function of depth in Figures [F24](#), [F25](#), [F26](#), [F27](#), [F28](#), [F29](#), and [F30](#). Samples from Sections 316-C0008C-11H-2 and 14H-6 are not in-

cluded in the figures. These cores recovered more sediment than was penetrated and had clear flow structures associated with suction during HPCS coring; thus, the curated depths are not accurate (see “Operations”). Furthermore, some of the ESCS cores were extremely difficult to clean prior to processing, especially within more coarse-grained lithologies. All of the contaminated samples were collected below the SMT, where in situ SO_4 concentration is expected to be zero. Thus, these few samples that were slightly contaminated by drilling fluid exhibit slightly elevated SO_4 values below the SMT. Because Site C0008 was cored at the end of the expedition, there was insufficient time to correct the chemical data for drill water contamination. Thus, only uncorrected concentrations are presented in Tables T11, T12, and T13.

Because of the paucity of argon at the time of drilling Site C0008, which is used as a carrier gas for both inductively coupled plasma-atomic emission spectroscopy (ICP-AES) and inductively coupled plasma-mass spectrometry (ICP-MS) analyses, the ICP-MS measurement program was halted for the remainder of Expedition 316. This stoppage ensured that there was enough argon available to measure the major and minor element concentrations via ICP-AES. Trace element analyses were performed onshore via ICP-MS for Hole C0008C. In addition, $\delta^{18}\text{O}$ in Holes C0008A and C0008C was analyzed via isotope ratio mass spectrometry. Trace metal and $\delta^{18}\text{O}$ data are tabulated in Table T13.

Salinity, chloride, and sodium

Pore fluid salinity rapidly decreases in the upper 15.5 m of Hole C0008A (Fig. F24A). From 15.0 to 87.0 m CSF, salinity slightly increases but starts decreasing again below 87.0 m CSF, accompanied by two negative excursions at 120.3 and 136.3 m CSF. These excursions coincide with similar excursions in Cl and Br (Figs. F24C, F26C). Below this depth, pore fluid salinity remains relatively constant to the Subunit IA/IB boundary. At 202.4 m CSF, salinity increases slightly to 33.28 at 267.0 m CSF. The decrease in salinity in the upper ~30 m of the sediment section reflects active sulfate reduction and the subsequent precipitation of authigenic carbonates consuming pore fluid SO_4 , Ca, alkalinity, and Mg within this interval (Fig. F27).

Pore fluid salinity in Hole C0008C decreases from seawater value at 1.5 m CSF to 32.33 at 56.0 m CSF. Below this depth, salinity is scattered with pronounced negative excursions at 86, 95, 96, 102, 135, 150, 161 and 167 m CSF (Fig. F24E). At the bottom of Hole C0008C, salinity is depleted by ~9% relative to modern seawater value. The negative excursions

in the salinity profile are the result of gas hydrate dissociation during the core recovery process.

Chloride increases rapidly in the upper ~30 m of Hole C0008A and then remains relatively constant between 30 and 94 m CSF with a maximum of 585 mM (~5% higher than modern seawater value). Cl decreases from ~80 to 140 m CSF. At 120.3 and 136.3 m CSF, two negative Cl excursions (552 and 536 mM) are detected. During core recovery, gas hydrates dissociate, releasing freshwater into the pore spaces, thus diluting pore fluid Cl. The two negative excursions in the Cl profile clearly indicate gas hydrate dissociation during core recovery, with Cl values within these horizons being ~1% and 4% lower than modern seawater value, respectively. The steady increase in Cl in the upper part of Hole C0008A and below 150 m CSF may reflect either active gas hydrate formation or in situ ash alteration, both of which consume water and increase pore fluid Cl concentration.

Chloride in Hole C0008C increases rapidly in the upper 7 m of the sediment section from 553 mM to 563 mM (Fig. F24F). Cl continues to increase with depth below 7 m CSF to a lesser extent. At 38.1 m CSF, a Cl maximum of 569.7 mM was observed, below which Cl decreases and becomes highly variable between 71 and 172 m CSF. Pronounced negative Cl excursions are observed at 73, 86, 95, 96, 102, 135, 144, 150, 161, and 167 m CSF, with a minimum recorded Cl value of 293 mM (48% of modern seawater value). These negative Cl excursions likely reflect pore fluid freshening because of the dissociation of gas hydrates. This is further substantiated by the coincidence of Cl minima with minima in Br, Na, K, Ca, Mg, NH_4 , Li, B, Sr, Ba, and H_4SiO_4 (Figs. F24, F25, F26, F27, F28) and maxima in $\delta^{18}\text{O}$ (Fig. F30). The core was scanned with an infrared (IR) camera in the core cutting area, and particularly cold intervals were sampled as potential gas hydrate-bearing samples. Some of the observed concentration minima correlate well with methane maxima (see “Organic geochemistry”). The gas hydrate-bearing horizons are mainly associated with ash and, to a lesser extent, coarse sand layers (see “Lithology”).

Dissolved sodium increases in the upper ~40 m of the sediment section of Hole C0008A. At 58.7 m CSF, a Na maximum is detected (523 mM) and remains elevated to 114.0 m CSF. This broad zone of elevated Na mimics the broad Cl maximum. Below 114.0 m CSF are two negative Na excursions at 120.3 and 136.3 m CSF. These negative anomalies coincide with a minimum in pore fluid salinity and Cl, Br, and Sr and likely reflect the localized occurrence of gas hydrate. Below the two gas hydrate occurrences, Na increases to 525 mM at TD. Dissolved sodium in

Hole C0008C increases above seawater value in the upper 70 m of the sediment section (Fig. F24G). Between 71 and 172 m CSF, Na shows seven discrete negative anomalies associated with gas hydrate-bearing horizons. At the bottom of Hole C0008C, Na is 512 mM (~7% enriched relative to modern seawater value).

Pore fluid constituents controlled by microbially mediated reactions

Sulfate and alkalinity

In Hole C0008A, sulfate decreases monotonically from 23.86 mM at 1.7 m CSF to 2.27 mM at 8.5 m CSF (Fig. F25B). At 15.5 m CSF, sulfate is below detection limit. Headspace methane starts to increase at ~5–6 m CSF (see “Organic geochemistry”), suggesting that the SMT is somewhere between 5 and 10 m CSF. Below the SMT, sulfate remains depleted with excursions up to 5 mM (Table T11). These samples were collected using the ESCS, and the elevated sulfate reflects minor contamination by seawater circulating in the borehole during drilling. Pore fluid data were not corrected for drill water contamination at this site.

The sulfate profile in Hole C0008C is similar to that of Hole C0008A, but the decrease in the upper part of the sediment section is more rapid. Sulfate decreases rapidly from 24.7 mM at 1.5 m CSF to 4.6 mM at 4.4 m CSF. At 6.9 m CSF, sulfate is totally depleted, suggesting an SMT depth of 4.4–6.9 m CSF (Fig. F25F). Sulfate remains depleted below the SMT with excursions as high as 3.9 mM because of minor contamination of ESCS cores by drilling fluid. The SMT in Holes C0008A and C0008C was penetrated at much shallower depths than in the other holes drilled during Expedition 316. Methane concentration at this site was also elevated with respect to previous sites (see “Organic geochemistry”). Overall, the shallow SMT at this site indicates that the upward methane flux is higher and the rates of AOM are greater in this region of the margin. It is very likely that this high methane flux is the main reason for the shallow occurrence of appreciable gas hydrate concentration at this site.

Pore fluid alkalinity increases rapidly in the upper part of Hole C0008A and reaches a maximum of 22.33 mM at 8.5 m CSF, just above the SMT (Fig. F25C). Below the SMT, alkalinity decreases steadily and reaches 5.24 mM at the bottom of the hole. In Hole C0008C, pore fluid alkalinity increases sharply from 6.2 mM at 1.5 m CSF to 22.8 mM at 6.9 m CSF, coinciding with the depth of sulfate depletion (Fig. F25G). Below the SMT, alkalinity displays an overall decreasing trend with negative excursions coinciding with gas hydrate-bearing horizons. The elevated

alkalinity in the upper 10 m in Holes C0008A and C0008C reflects rapid alkalinity production in the region of intense sulfate reduction likely occurring through both organic matter oxidation and AOM. The relative extent of AOM will be constrained by shore-based $\delta^{13}\text{C}$ -DIC analyses.

Ammonium, phosphate, and bromide

Dissolved ammonium increases monotonically in Hole C0008A from 1.7 to 58.7 m CSF. The dissolved ammonium profile then exhibits a broad maximum of ~4700 μM between 60.0 and 105.1 m CSF (Fig. F26A), below which ammonium decreases. In Hole C0008C, dissolved ammonium increases steadily from 232 μM at 1.5 m CSF to 3902 μM at 70.8 m CSF (Fig. F26D). Dissolved ammonium is scattered below this depth and the overall trend is decreasing. Local ammonium minima coincide with ash and coarse sand layers where gas hydrates occur. The initial rapid increase in ammonium in both holes is the result of microbially mediated decomposition of organic matter. The decline with depth likely reflects decreasing metabolic rates, thus declining ammonium production, as well as NH_4 sorption on clay minerals.

Phosphate in Hole C0008A increases sharply in the upper part of the sediment section, peaking at 38.8 m CSF. Below this maximum, PO_4 decreases (Fig. F26B). Below 150.0 m CSF, PO_4 varies slightly and remains close to the detection limit. At 120.3 and 136.3 m CSF, two local minima are observed; these coincide with minima in salinity, Cl, Br, and Sr (Figs. F24A, F24B, F28C). Phosphate in Hole C0008C is generally lower than in Hole C0008A. Phosphate increases rapidly from 11 μM at 1.5 m CSF to 38 μM at 4.4 m CSF and then suddenly decreases before starting to increase again, reaching a maximum of 44 μM at 38.1 m CSF (Fig. F26E). Below this maximum, phosphate generally decreases to 5 μM at the bottom of the hole. The initial rapid increase in phosphate in Holes C0008A and C0008C reflects active organic matter decomposition, which occurs in the zone of most active sulfate reduction. This zone extends deeper in Hole C0008A than in Hole C0008C. The decreasing and low phosphate in both holes below the depths of maximum concentration is likely controlled by the solubility of apatite, which is a major sink for phosphate.

Bromide in marine interstitial waters is sensitive to organic matter diagenesis with elevated concentrations reflecting marine organic matter decomposition. Dissolved bromide in Hole C0008A (Fig. F26C) increases in the upper 100 m of the sediment section, below which dissolved Br remains relatively constant with local minima reflecting gas hydrate

dissociation during core recovery. In Hole C0008C, Br increases in the upper 70 m of the sediment section, below which Br is highly variable with negative concentration excursions coinciding with the gas hydrate-bearing intervals. The overall elevated background Br indicates that Br production is mainly the result of decomposition of marine organic matter and, unlike the other sites drilled during Expedition 316, a much lower amount of terrestrial organic matter degradation. This is consistent with the sediment carbon/nitrogen ratio within the depth interval spanning Holes C0008A and C0008C, which indicates that organic matter in the sediment section is primarily marine in origin (see “**Organic geochemistry**”).

Major cations (Ca, Mg, and K)

Calcium in Hole C0008A decreases monotonically from 1.7 to 8.5 m CSF, below which the profile reverses and Ca starts to increase (Fig. F27A). The initial decreasing trend reflects Ca consumption during authigenic carbonate formation in the zone of most intense sulfate reduction. The increase in Ca with depth is consistent with progressive ash alteration and carbonate diagenesis downhole. The calcium profile for Hole C0008C resembles the Hole C0008A profile, with a rapid decrease followed by an overall increasing trend with depth (Fig. F27E). However, superimposed on this increasing trend are pronounced Ca minima coinciding with gas hydrate occurrences.

Magnesium decreases throughout Hole C0008A (Fig. F27B). The decrease is more rapid in the upper ~10 m of the sediment section. This zone of rapid Mg depletion coincides with the SO₄ reduction zone and the SMT, indicating some precipitation of Mg with authigenic carbonates within this depth interval, as well as uptake in clay minerals. The general decrease in Mg indicates Mg uptake in hydrous silicate minerals (mainly clays) formed during volcanic ash alteration. Magnesium in Hole C0008A decreases rapidly from near-seawater values to 23.58 mM at 22.1 m CSF, below which Mg decreases more slowly (Fig. F27F). Between 71 and 172 m CSF, Mg varies with negative excursions similar to those seen in many of the other dissolved elements.

The potassium profile for Hole C0008A varies yet decreases with depth (Fig. F27C). Potassium in Hole C0008C is similar to that in Hole C0008A, but the scatter with depth is more pronounced in Hole C0008C and coincides with gas hydrate-bearing horizons (Fig. F27G). The higher than seawater concentration in the upper ~20 m of Holes C0008A and C0008C is likely a sampling artifact resulting from pressure changes during core recovery and ion exchange with NH₄ on clay surfaces. The overall

decline in K likely reflects the uptake of dissolved potassium in authigenic zeolites formed during the alteration of volcanic ash and feldspars.

Minor elements

(B, Li, H₄SiO₄, Sr, Ba, Mn, and Fe)

Boron in Hole C0008A decreases from 515 μM at 1.7 m CSF to 330 μM at 49.4 m CSF (Fig. F28B). Between 50 and 140 m CSF, B varies and is lower than modern seawater value. From 143.2 m CSF, B increases with depth (Fig. F28B) to ~30% higher than modern seawater value at 215 m CSF. In Hole C0008C, boron does not decrease as rapidly as in Hole C0008A (Fig. F28E), but there is an overall decreasing trend from 504 μM at 1.5 m CSF to 350 μM at 73.1 m CSF. Below this depth, the trend reverts and increases overall. Superimposed on this increasing trend are several negative B excursions, corresponding to gas hydrate-bearing layers. The increase in B at the base of Holes C0008A and C0008C to values as high as 859 μM was not observed at the other sites drilled during Expedition 316 and will be the focus of postcruise research at this site.

Dissolved lithium in Hole C0008A decreases relatively rapidly from seawater value at 1.7 m CSF to 13.8 μM at 38.8 m CSF. Below this depth, Li gradually increases to seawater value (Fig. F28A). Between 120.3 and 143.2 m CSF, Li is higher than modern seawater value. Below this local maximum, Li remains relatively constant and then increases slightly from the Subunit IA/IB boundary to 31.1 μM at TD. Lithium in Hole C0008C is generally lower than in Hole C0008A and below seawater value throughout the hole (Fig. F28D). Li decreases rapidly from 22.9 μM at 1.5 m CSF to 16.3 μM at 6.9 m CSF. Minimum concentration between 71 and 172 m CSF is observed where gas hydrates are inferred.

Dissolved silica is higher than modern seawater value throughout Hole C0008A and displays an overall scattered profile with pronounced minima at 49, 77, and 202 m CSF and local maxima at 23, 87, 155, and 193 m CSF. In Hole C0008C, Si is relatively constant in the upper 50 m of the sediment section. However, between 60 and 172 m CSF, dissolved silica is scattered (Fig. F27H). The general trend in both holes is likely caused by opal diagenesis, and variations in the Si profile likely reflect other varying dominant silicate diagenetic reactions, as well as gas hydrate dissociation during core recovery.

Strontium in Hole C0008A rapidly decreases in the uppermost few meters of the sediment section before starting to increase, reaching a maximum of 96 μM at 49.4 m CSF (Fig. F28C). Below this depth, Sr decreases and then increases slightly below 200 m CSF. Superimposed on this decreasing trend are two nega-

tive excursions, coinciding with similar minima in Cl, Na, PO₄, and salinity and maxima in δ¹⁸O. Strontium is lower than modern seawater value throughout Hole C0008C (Fig. F28F) and remains relatively constant in the upper 70 m of the sediment section. Below this depth, seven Sr minima are associated with gas hydrate occurrences.

Dissolved barium in Hole C0008A is close to modern seawater value in the upper 10 m of the sediment section, below which Ba increases, reaching a broad maximum of 58 μM between 77 and 94 m CSF. At ~100 m CSF, the profile reverses and Ba decreases (Fig. F25D). A local minimum at 120.3 m CSF coincides with minima in Cl, Na, Sr, PO₄, and salinity and maxima in δ¹⁸O, indicating intervals of gas hydrate occurrence. The increase in Ba below the SMT is likely the result of barite dissolution, and the variability in the dissolved Ba profile is likely controlled by the abundance of barite in the sediment. Dissolved Ba rapidly increases from near-seawater value at 1.5 m CSF to 113 μM at 6.9 m CSF in Hole C0008C (Fig. F25H). Below this maximum, Ba decreases rapidly to 63 μM at 22.1 m CSF. Thereafter, the decrease rate is slower, and at the bottom of the hole, Ba reaches 20 μM. The rapid increase from 4.4 to 6.9 m CSF coincides with the inferred SMT depth. Below the SMT, barite becomes unstable and thus a significant amount of Ba²⁺ is released to the pore fluids. The more extensive increase in Hole C0008C is probably due to a greater amount of barite dissolution at this interval.

Dissolved manganese rapidly decreases in Hole C0008A from 6.44 μM at 1.7 m CSF to 0.63 μM at 5.5 m CSF (Fig. F29A). Below this rapid decline, Mn remains relatively constant until 29.3 m CSF, where Mn starts increasing rapidly, reaching a local maximum at 49.4 m CSF (4.67 μM). Mn displays an overall increase between 50 and 175 m CSF and reaches a second local maximum at 173.8 m CSF. Toward the bottom of Hole C0008A Mn is scattered. The elevated concentration in the upper ~6 m at this site reflects MnO₂ reduction within a depth interval where MnO₂ is a favorable and important electron acceptor for microbially mediated organic matter decomposition. A remarkably similar manganese profile is observed in Hole C0008C (Fig. F29E), but the scattered behavior is more pronounced in Hole C0008C than in Hole C0008A, and toward the bottom of Hole C0008C, the Mn profile is characterized by an overall decreasing trend.

Dissolved iron in Hole C0008A is close to the detection limit in the upper 40 m of the sediment section. Fe increases in some horizons with depth and approaches the detection limit toward the bottom of Hole C0008A. In Hole C0008C, Fe rapidly decreases

in the upper part of the sediment section. Considerable mobility is displayed at various horizons throughout Hole C0008C (Fig. F29F).

Trace elements (Rb, Cs, V, Cu, Zn, Mo, Pb, U, and Y)

Because of the paucity of argon (which is used as a carrier gas for ICP-MS analyses) toward the end of the expedition, the trace metal program was halted before coring at Site C0008. Trace element concentrations were subsequently analyzed shore based via ICP-MS; however, there was only time to analyze the samples from Hole C0008C before publication of the Expedition Report.

Rb concentration decreases from above seawater values to 0.83 nM at 38.1 m CSF. Below this depth, Rb remains relatively constant to TD, except for concentration minima at 73.0, 86.0, 96.0, 150.0, and 161.4 m CSF (Fig. F27I). These Rb excursions are the result of gas hydrate dissociation during core recovery. Cs generally decreases with depth from 2.2 nM at 1.5 m CSF to 1.81 nM at 47.9 m CSF (Fig. F27J), with a concentration maxima of 2.8 nM at 12.3 m CSF. Below ~50 m CSF, Cs concentration generally increases to 3.4 nM at TD. Superimposed on this increasing trend are concentration minima at 86.0, 96.0, 150.0, and 161.0 m CSF that are associated with gas hydrate-bearing intervals (see “[Summary](#)”). Molybdenum is relatively low and variable from 1.5 to 83.4 m CSF, ranging from 7.7 to 172 μM (Fig. F29C). Below this depth, concentrations are generally higher and more variable to TD, ranging from 33 to 435 μM.

Copper is generally low and relatively constant with depth, except for six peaks at 12.3, 38.1, 82.9, 96.0, 150.0, and 167.0 m CSF. Some of these peaks correspond with gas hydrate occurrences, and they likely reflect contamination of the pore fluid sample with drilling fluid that invaded voids left by the dissociating hydrate, as observed in the sulfate profile (Figs. F29I, F25). Zinc concentration is variable and ranges from 0.37 to 6465 nM (Fig. F29J). Vanadium initially increases from 28 nM at 1.5 m CSF to 40 nM at 4.4 m CSF (Fig. F29K). Below this depth, concentrations generally remain below 20 nM with concentration maxima at 83, 96, and 161 m CSF associated with intervals of gas hydrate occurrence.

Uranium generally decreases from 6.1 nM at 1.5 m CSF to 0.4 nM at 56.0 m CSF. Below this depth, background concentration is slightly higher, ~1 μM, to the base of the hole with concentration maxima up to 6.3 nM at 88.0, 103.0, and 161.2 m CSF (Fig. F29G). Lead concentration is relatively low in Hole C0008C. Background concentration ranges from 0.3 to 6 nM (Fig. F29D). Superimposed on the low background concentration are three peaks at 22.1, 47.9,

and 83.4 m CSF. Yttrium generally decreases with depth from 2.8 pM at 4.4 m CSF to 1.2 pM at TD (Fig. F29H). There are two concentration maxima of 4.2 pM at 88.2 m CSF and 3.1 pM at 102.8 m CSF.

$\delta^{18}\text{O}$

Pore fluid $\delta^{18}\text{O}$ ratios in Holes C0008A and C0008C were measured on shore. In Hole C0008A, $\delta^{18}\text{O}$ decreases relatively rapidly from -0.08‰ at 1.5 m CSF to -3.12‰ at 68.5 m CSF (Fig. F30). Below this depth, $\delta^{18}\text{O}$ continues to decrease, but the change in $\delta^{18}\text{O}$ with depth decreases reaching -4.25‰ at 164.3 m CSF. From this depth, $\delta^{18}\text{O}$ increases to -3.61‰ at TD. There are no variations in the $\delta^{18}\text{O}$ profile where there are anomalies in the Cl concentration profile at 120 and 136.3 m CSF. When gas hydrates form, H_2^{18}O is preferentially incorporated in the hydrate structure and the pore fluids become depleted in $\delta^{18}\text{O}$. When gas hydrates dissociate, H_2^{18}O is released back to the pore fluids and they become enriched in $\delta^{18}\text{O}$. It is possible that gas hydrate concentrations were too low, as indicated by the Cl, Br, and Na profiles, to impact the $\delta^{18}\text{O}$ profile upon dissociation at these depths.

In Hole C0008C, $\delta^{18}\text{O}$ decreases with depth from -0.27‰ at 1.5 m CSF to -3.77‰ at 70.8 m CSF. Below this depth, background $\delta^{18}\text{O}$ remains relatively constant. Superimposed on the background $\delta^{18}\text{O}$ profile from ~ 71 m CSF to TD are five positive excursions at 83, 86, 96, 150, and 161 m CSF that coincide with Cl concentration minima (Fig. F30). The positive excursions in the $\delta^{18}\text{O}$ profile at Hole C0008C confirm the presence of gas hydrate within these depth intervals.

Summary

The primary features of the pore fluid geochemical profiles collected in Hole C0008 are (1) the relatively shallow SMT, (2) evidence of disseminated gas hydrate and two occurrences of gas hydrates at low concentration in Hole C0008A, and (3) disseminated gas hydrates with seven localized occurrences of elevated pore space gas hydrate concentration in Hole C0008C.

Sulfate reduction is relatively rapid in the upper 9 m of the sediment section in Hole C0008A and in the upper 4 m in Hole C0008C, likely indicating a much higher upward methane flux at Site C0008 in comparison with other sites drilled during Expedition 316. This elevated methane flux is likely one of the main factors contributing to the elevated occurrence of gas hydrate at this site. There is evidence of localized occurrences of gas hydrate in Holes C0008A and

C0008C. The localized gas hydrate occurrences in Hole C0008A are manifested by two sharp and local Cl minima detected at ~ 120 and 136 m CSF with Cl values being $\sim 1.5\%$ and 4% less than modern seawater value, respectively. These Cl minima coincide with minima in Na, PO_4 , Sr, and salinity at the same depths. In Hole C0008C, the occurrences of gas hydrate-bearing horizons were even greater than in Hole C0008A, and these horizons contain higher gas hydrate concentration. Between 70 and 172 m CSF in Hole C0008C, most of the dissolved elements display scattered behavior with discrete excursions to fresher values with respect to modern seawater, which clearly indicates the existence of gas hydrate-bearing intervals. The sampled gas hydrate-bearing horizons are associated with ash and coarse-grained sand layers.

Organic geochemistry

Hydrocarbon gas composition

Headspace gas composition was rapidly analyzed for safety monitoring (Table T14) and by using a more time consuming extracting procedure for scientific interpretation (Table T15; Fig. F31). The SMT is located at ~ 4 – 8 m CSF in Holes C0008A and C0008C. Methane concentration increases sharply at the SMT to a peak of 9.1 mM at 19.90 m CSF in Hole C0008A and 17.5 mM at 12.17 m CSF in Hole C0008C. Below this depth, methane concentration decreases to ~ 2 mM at 60 m CSF and remains at this value to the base of the sediment column (except for a localized enrichment that reaches 15 mM at ~ 140 m CSF in Hole C0008A). This indicates the occurrence of gas hydrates, which also correlates with anomalously low chloride concentration in this interval (see “**Inorganic geochemistry**”). The ethane concentration profile from Hole C0008A follows the methane profile to ~ 70 m CSF. Below that depth, ethane concentration increases. This increase is also reflected in the methane/ethane (C_1/C_2) ratio. The C_1/C_2 ratio increases in the uppermost 15 m CSF and then declines to 372 at ~ 160 m CSF. Below this depth, the ratio slightly increases again. The ethane concentration profile in Hole C0008C shows the same trend with slightly higher concentration at ~ 168 m CSF. Because no propane or butane was detected, the lower ratio values are probably not due to thermogenic ethane formation or migration.

Sediment carbon, nitrogen, and sulfur composition

Calcium carbon (CaCO_3) content is relatively high in the upper 50 m of Unit I with concentration up to

23.4 wt%. In the lower portion of the unit, concentration decreases (Table T16; Fig. F32). The lowest concentration is at the Unit I/II boundary. Total organic carbon (TOC) and total nitrogen (TN) concentrations remain low throughout the cores and show a strong positive correlation. Similar to CaCO₃ content, the TOC and TN concentrations are lowest at the bottom portion of Unit I. The TOC to TN (C/N) ratio remains generally low throughout the site, indicating marine origin of the organic matter, although some values exceed 10. The total sulfur (TS) content is rather high in the upper 50 m and in the lower ~60 m of the sediment column, correlating with the presence of iron sulfides (see “Lithology”). At ~180 m CSF, TS concentration increases and is highest throughout the lowest portion of Unit I (Subunit IB), related to pyrite occurrence at this interval (see “Lithology”).

Microbiology and biogeochemistry

Sample processing

To study microbiological and biogeochemical characteristics in sediments at Site C0008, samples were obtained from 142 and 143 different depth locations in Holes C0008A and C0008B–C0008C, respectively (Tables T17, T18). The presence of methane hydrates was monitored by IR camera immediately after core recovery on deck. Hydrate-bearing sediments were sampled on deck and immediately stored anaerobically in a refrigerator and/or liquid nitrogen tank. For high-resolution enumeration of cell abundance, 3 cm³ of sediment was collected from core section ends on deck. All whole-round core sample processing was carried out after X-ray CT scanning, except for the hydrate samples, and was completed within 1 h after core recovery on deck.

Cell abundance

Cell abundance in sediments at Site C0008 was enumerated by microscopic direct count of SYBR Green I-stained cells. Most observed cells were small irregular coccoids, and some short rods and aggregate structures were also observed as minor components. The vertical profile of cell abundances in sediment in Holes C0008A and C0008C showed that 10⁸–10⁹ cells/cm³ was consistently observed throughout the cores and the populations in Hole C0008C were approximately double those in Hole C0008A (Fig. F33). The average cell abundances in Holes C0008A and C0008C were $2.01 \times 10^8 \pm 1.25 \times 10^8$ cells/cm³ ($N = 16$) and $4.71 \times 10^8 \pm 1.79 \times 10^8$ cells/cm³ ($N = 12$), respectively. In Hole C0008A, gas hydrate was observed at

~120 and 136 m CSF (Section C0008A-15H-1), whereas ~10 occurrences of gas hydrate were observed in volcanic ash and sand layers by IR camera and in the pore fluid chloride profiles in Hole C0008C (see “Inorganic chemistry”). The reason for the differences in population size and activity of seafloor microbial life will be a focus of postcruise research.

Physical properties

At Site C0008, physical property measurements were made to provide basic information characterizing lithologic units, states of consolidation, deformation, and strain and to correlate coring results with downhole logging data. After capturing X-ray CT images and letting the core reach thermal equilibrium with ambient temperature at ~20°C, gamma ray attenuation (GRA) density, magnetic susceptibility, natural gamma radiation, *P*-wave velocity, and non-contact electrical resistivity were measured using a multisensor core logger (MSCL) system on whole-round core sections (MSCL-W). Thermal conductivity was measured using either a full-space needle probe method or half-space line source method on split working halves. The half-space method was used on lithified sediments deeper in the hole that were impenetrable with the needle probe. Cores were split in two longitudinally, one half for archiving and one half for sampling and analysis. A photo image capture logger (MSCL-I) and a color spectrophotometer (MSCL-C) were used to collect images of the split surfaces of the archive halves. Moisture and density (MAD) were measured on discrete subsamples collected from the working halves as well as from “clusters” adjacent to whole-round samples removed before splitting. Vane shear and penetration experiments were performed on the working halves. Additional discrete subsamples from working halves were used to perform electrical conductivity measurements, *P*-wave velocity measurements, and anisotropy calculations.

Density and porosity

Values of bulk density at Site C0008 were determined from both MSCL GRA measurements on whole cores and MAD measurements on discrete samples from the working halves of split cores (see “Physical properties” in the “Expedition 316 methods” chapter). A total of 186 discrete samples were analyzed for MAD (172 from Hole C0008A and 14 from Hole C0008C).

MAD wet bulk density increases continuously with depth from ~1.60 g/cm³ just below the seafloor to 1.95 g/cm³ at ~272 m CSF (Fig. F34A). Maximum MSCL bulk density values also show similar trends.

GRA bulk density is generally lower than MAD bulk density and reveals a larger degree of scatter compared to MAD bulk densities. The scatter in MAD bulk density is likely due to lithologic variations among the silty clay sediments at this site. Grain density values were also determined via MAD measurements on discrete samples and are consistent throughout the hole (Fig. F34B).

Porosity values were estimated from whole-round core MSCL scan data and calculated from MAD measurements on discrete samples. MAD porosity (see “Physical properties” in the “Expedition 316 methods” chapter) generally decreases with depth (Fig. F34C) and varies inversely with MAD bulk density. Minimum MSCL porosity corresponds well with MAD porosity (Fig. F34C).

As shown in Figure F34C, porosity decreases monotonically with depth from ~63% just below the seafloor to ~47% at 270 m. No significant deviations from the porosity versus depth trend are observed.

***P*-wave velocity and electrical conductivity in discrete samples**

At Site C0008, *P*-wave velocity and electrical conductivity data in discrete samples were acquired from 225 to 265 m CSF (Subunit IB, cf. lithology) in Hole C0008A. The small amount of data acquired does not allow any description in terms of variation with depth. *P*-wave velocity values (Fig. F35A) average 1750 m/s, which is significantly lower than average values obtained at Sites C0006 and C0007. Electrical conductivity data (Fig. F35C) show high values, which could reflect relatively high porosity compared to that at other sites. Transverse electrical conductivity anisotropy (Fig. F35D) shows high values at ~250 m CSF with a very high conductivity parallel to the bedding surface.

Thermal conductivity

Thermal conductivity measurements were conducted on whole-round HPCS and ESCS cores. Thermal conductivity values associated with Hole C0008A vary between 0.7 and 1.2 W/(m·K) (Table T19; Fig. F36A) and modestly increase with depth but also show a great deal of scatter. Thermal conductivity values associated with Hole C0008C vary between 0.7 and 1.2 W/(m·K) (Table T20; Fig. F37A), decrease with depth, and also show significant scatter. Increased gas hydrate concentration was found in Hole C0008C, which may explain both the decrease in thermal conductivity with depth and the increased scatter because gas expansion cracks were prevalent throughout most of the core. Significant negative spikes at 140 m CSF in Hole C0008A and 90

m CSF in Hole C0008C may be associated with the occurrence of hydrates.

In situ temperature

In situ temperature was measured using the advanced piston coring temperature tool (APCT3) in Holes C0008A and C0008C. In Hole C0008A, APCT3 measurements were supplemented with the sediment temperature (SET) tool. All measurements were made in calm to moderate seas and were successful (Tables T21, T22). Temperature-time series for each temperature measurement in Holes C0008A and C0008C are shown in Figures F38 and F39. The temperature tool was stopped at the mudline for up to 10 min prior to each penetration. The average apparent bottom water temperature is 2.0° and 1.8°C in Holes C0008A and C0008C, respectively (Tables T21, T22). Determinations of bottom water temperature were much more consistent in Hole C0008C than in Hole C0008A. The variability in measured bottom water temperature is likely due to uncertainty in the core winch depth meter. Significant frictional heating occurred on all penetrations with the temperature versus time records exhibiting the characteristic probe penetration heating pulse and subsequent decay (Figs. F38, F39). Equilibrium temperature estimates are based on a 1/time approximation from the temperature-time series while the tool is in the bottom. The effective origin time of the thermal pulse associated with tool penetration was estimated by varying the assumed origin time until the thermal pulse decay followed the theoretical curve. A delay of 55–94 s from the initial penetration heating time gives a best fitting linear 1/time plot for both holes. In Hole C0008A, the temperature measurement at 119.0 m CSF shows multiple temperature spikes near the beginning of the penetration, and the tool may have double penetrated. This would put excess heat into the formation relative to theory and may explain the slightly high temperature relative to the best-fit gradient (Fig. F36B). Additionally, this equilibrium temperature is based on a shorter time series than the other measurements, further degrading the measurement. In Hole C0008A, the one SET tool measurement at 243.8 m CSF is consistent with APCT3 measurements. The best-fit thermal gradients are 51° and 57°C/km in Holes C0008A and C0008C, respectively (Figs. F36C, F37C).

Heat flow

If heat transfer is by conduction and heat flow is constant, the thermal gradient will be inversely proportional to thermal conductivity according to Fourier’s law. This relationship can be linearized by plotting temperature as a function of summed ther-

mal resistance (Bullard, 1939) (see the “[Expedition 316 methods](#)” chapter). For Holes C0008A and C0008C, the least-squares fit to the temperature and thermal resistance data indicates a heat flow of 52 and 46 mW/m², respectively (Figs. [F36C](#), [F37C](#)). In Hole C0008A, the estimated bottom water temperature is the same as the average of the mudline temperatures, whereas in Hole C0008C the estimated bottom water temperature is 0.2°C greater than the average of the mudline temperatures (Tables [T21](#), [T22](#)). A constant conductive heat flow appears to describe the overall thermal structure for both holes quite well.

Shear strength

Shear strength measurements were conducted using a semiautomated miniature vane shear device and a pocket penetrometer. Measurements were made at discrete locations on the working halves of split cores at a frequency of approximately three measurements per core (generally in sections 2, 5, and 7). Tests were conducted on relatively intact and homogeneous regions of these sections, generally somewhere between 50 and 100 cm below the top of the section. To minimize error induced by disturbance of the core by the measurement technique, vane shear tests were conducted first, followed by penetrometer tests 1–2 cm from the site of the vane shear penetration. No vane shear measurements were conducted on whole cores. Both instruments were inserted orthogonally to the surface of the working halves. The rotation rate of the semiautomated vane shear apparatus on board the *Chikyu* is 71°/min. At Site C0008, shear strength was measured to 220 m CSF in Hole C0008A and 137 m CSF in Hole C0008C (Fig. [F40](#)).

Shear strength increases linearly overall in both holes along a trend of 0.45 kPa/m. In Hole C0008A, measured shear strength decreases past 180 m CSF, but this is inferred to be an effect of tensile cracking in the split cores rather than a real strength decrease at depth. In Hole C0008C, a gap in the core record below 60 m CSF precedes a zone of decreasing shear strength from 70 to 90 m CSF. Beyond this zone, shear strength increases at ~0.45 kPa/m to the bottom of the hole at 137 m CSF.

Color spectrometry

Results from the measurement of color reflectance are presented in Figures [F41](#) and [F42](#). Trends between Holes C0008A and C0008C are similar with the L* and b* values decreasing slightly with depth. The L* values range from ~20 to 50. The a* values range from -2 to 2, and the b* values range from 0 to 4. There are no significant anomalies.

Magnetic susceptibility

Volumetric magnetic susceptibilities were measured using the whole-round core MSCL in all recovered cores from Site C0008 (Fig. [F43](#)). Uncorrected magnetic susceptibility values are presented in this chapter. Magnetic susceptibility varies between ~0 and 600 × 10⁻³ SI with a mean of ~137 × 10⁻³ SI. Magnetic susceptibility values are low from the seafloor to ~150 m CSF where there is a positive excursion centered at ~175 m CSF. Values between 200 and 260 m CSF appear cyclic and may reflect interbedded conglomerates and silty clay.

Natural gamma ray

Natural gamma ray (NGR) results are reported in counts per second (cps). The background scatter, produced by Compton scattering, photoelectric absorption, and pair production, was measured at the beginning and subtracted from measured gamma ray values. In general, NGR decreases from the seafloor to ~235 m CSF at the Subunit IA/IB boundary (Fig. [F44](#)). At this boundary, NGR values are offset toward lower values and then rise relatively quickly to ~272 m CSF.

Integration with seismic data

There are no logging-while-drilling (LWD) data at this site and core-seismic integration between these holes is mainly based on prestack depth-migrated seismic profiles. The distance between Holes C0008B, C0008C, and C0008A is 215 m (Fig. [F1](#)). Seismic profile Inline 2675 from the CDEX 3-D seismic survey (Fig. [F2](#)) passes through Holes C0004B, C0008B, and C0008C and lies 10–30 m from Holes C0004C, C0004D, and C0008A, which are projected onto the seismic profile.

Generally, core recovery is good at Site C0008 and provides continuous NGR logs for correlations between holes. NGR data from core logs are superimposed on the seismic data (Fig. [F45](#)) The seismic data highlight some key reflections that match well with core data and image key sedimentary facies and faults.

In Hole C0008A between ~50 and 150 m CSF, interbedded mud and turbidite sand create high amplitude reflections that are continuous to Hole C0008C. The NGR logs show cyclic variations through this interval. Between 150 and 234 m CSF, continuous seismic reflections caused by thick sands and volcanic ashes provide references for correlation between these two holes. NGR logs show characteristics that can also be well correlated between these holes. However, depth shifts between the seismic reflections and NGR peaks are up to 15 m.

References

- Bullard, E.C., 1939. Heat flow in South Africa. *Proc. R. Soc. London, Ser. A*, 173:474–502.
- Gradstein, F.M., Ogg, J.G., and Smith, A. (Eds.), 2004. *A Geologic Time Scale 2004*: Cambridge (Cambridge Univ. Press). <http://www.stratigraphy.org/>
- Kimura, G., Sreaton, E.J., and Curewitz, D., 2007. NanTroSEIZE Stage 1: NanTroSEIZE shallow megasplay and frontal thrusts. *IODP Sci. Prosp.*, 316. doi:10.2204/iodp.sp.316.2007
- Moore, G.F., Bangs, N.L., Taira, A., Kuramoto, S., Pangborn, E., and Tobin, H.J., 2007. Three-dimensional splay fault geometry and implications for tsunami generation. *Science*, 318(5853):1128–1131. doi:10.1126/science.1147195

Publication: 11 March 2009
MS 314315316-136



Figure F1. Locations of Sites C0008 and C0004. Solid lines = seismic profile coverage.

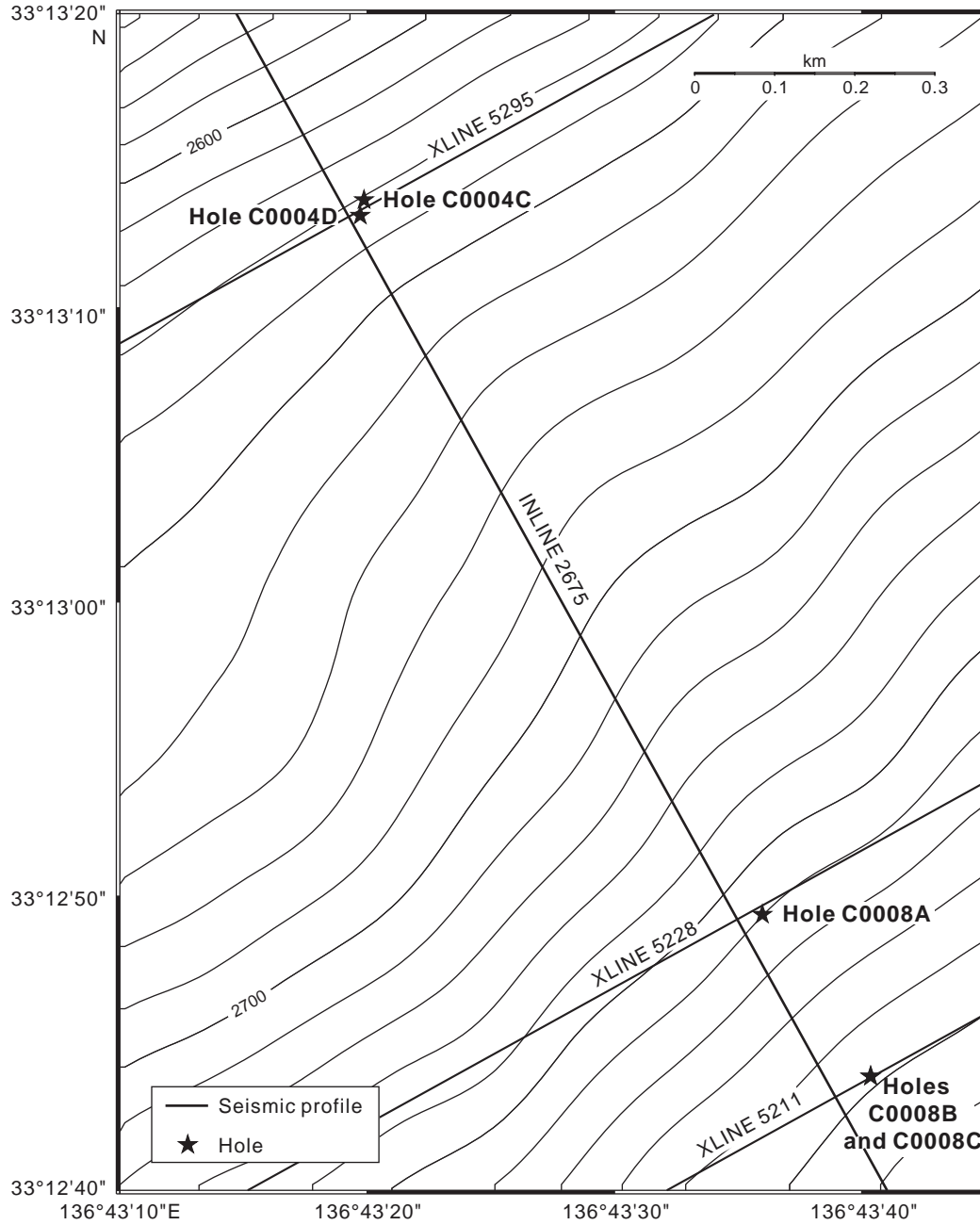




Figure F2. 3-D seismic profile through Site C0008 and nearby Site C0004 (Moore et al., 2007; see [Moore et al.](#)). A. Inline 2675. VE = vertical exaggeration. (Continued on next two pages.)

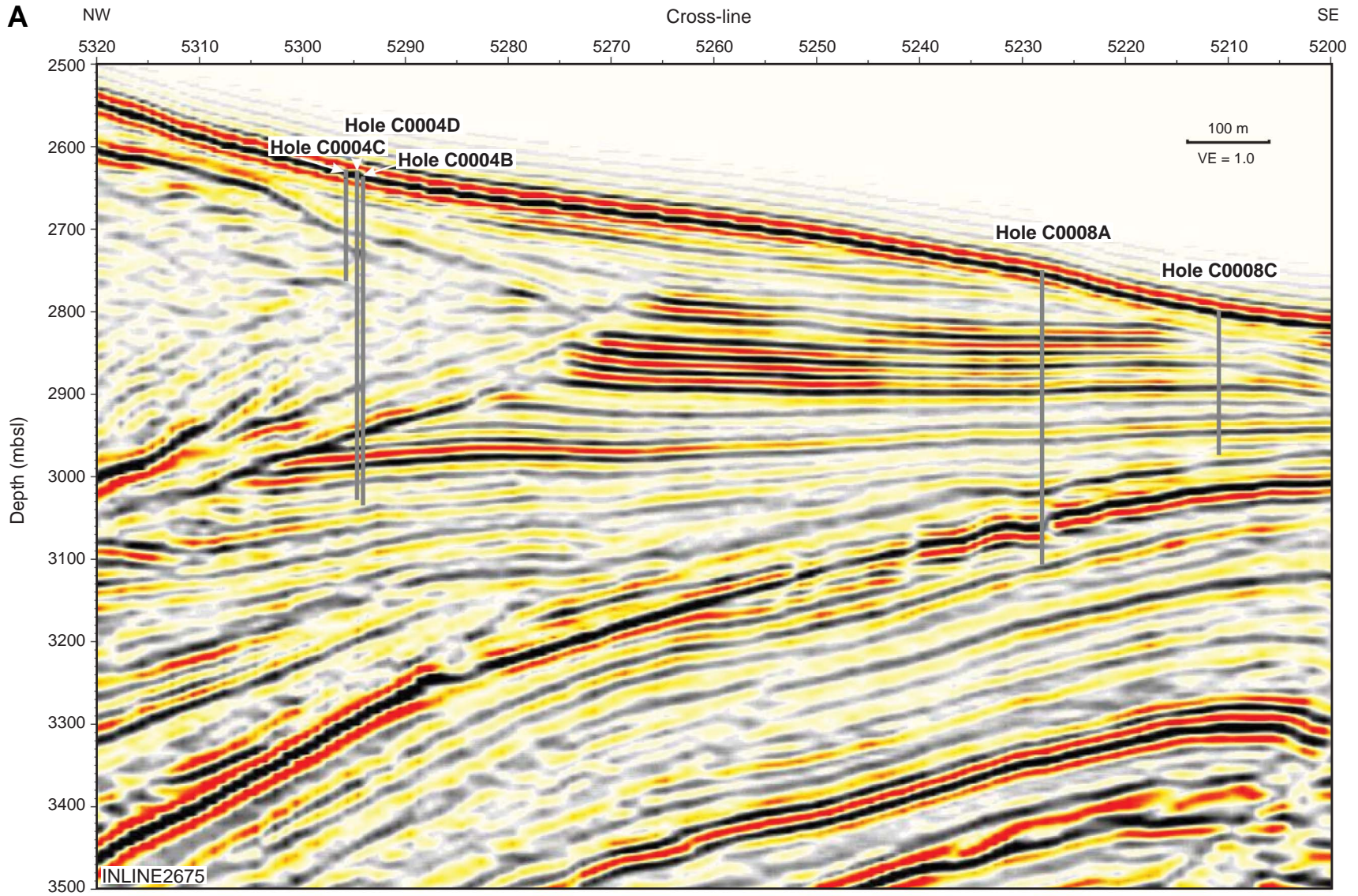




Figure F2 (continued). C. Cross-line 5211, Hole C0008C.

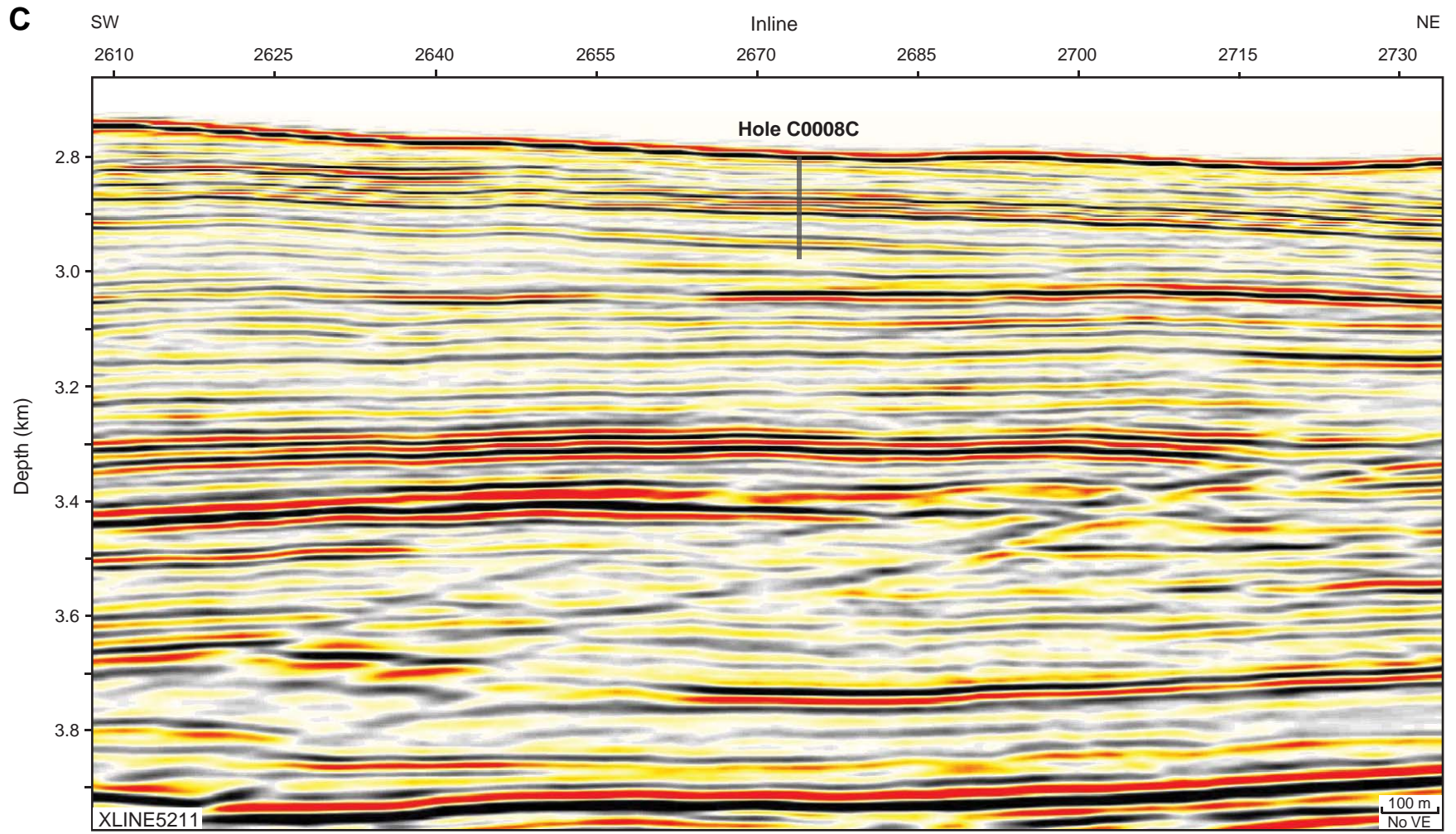


Figure F3. Core recovery and sand and silt distribution, Site C0008. **A.** Core recovery and lithologic units, Hole C0008A. CSF = core depth below seafloor. (**Continued on next three pages.**)

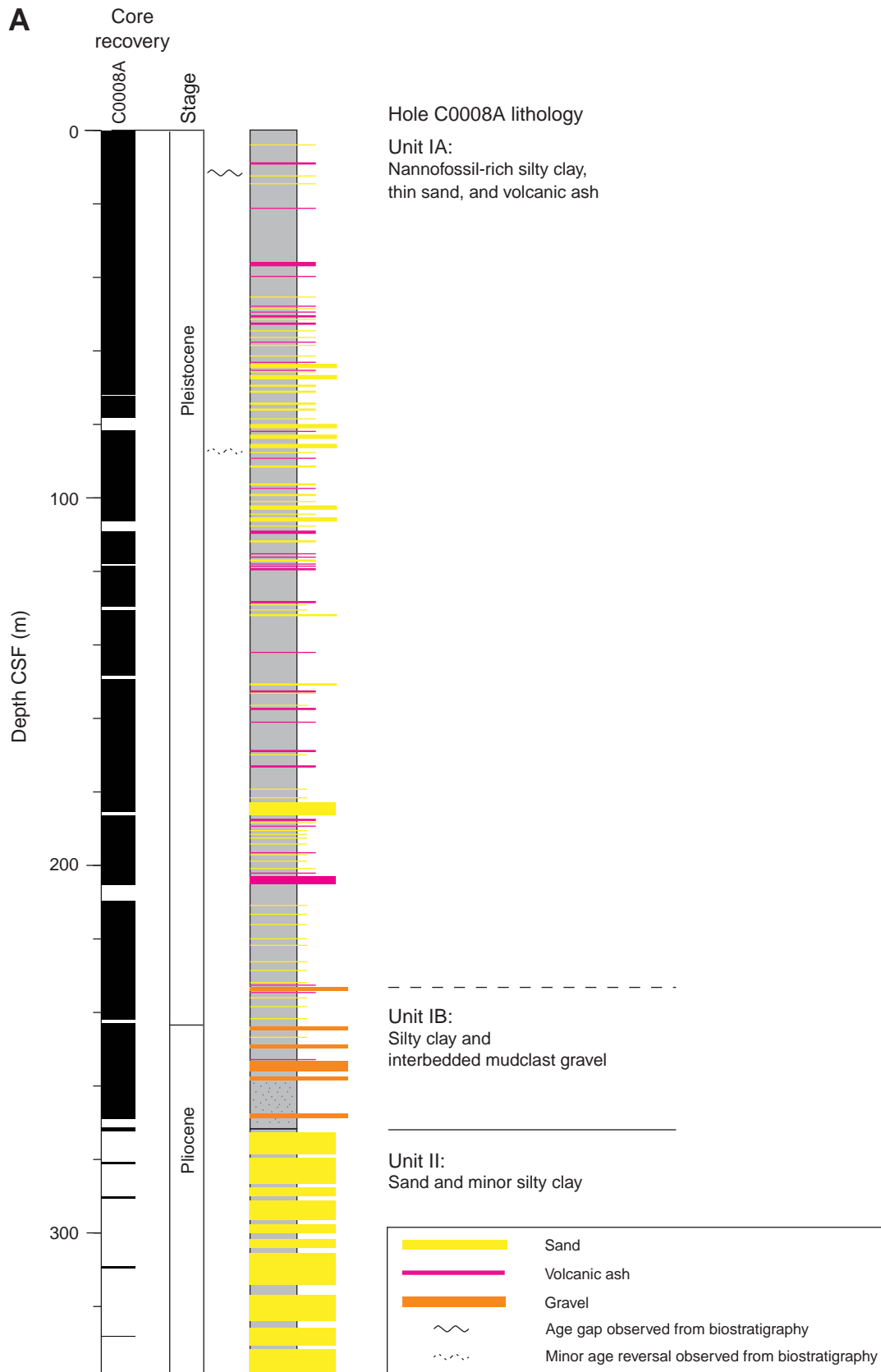


Figure F3 (continued). B. Distribution of sand and silt layers, Hole C0008A. (Continued on next page.)

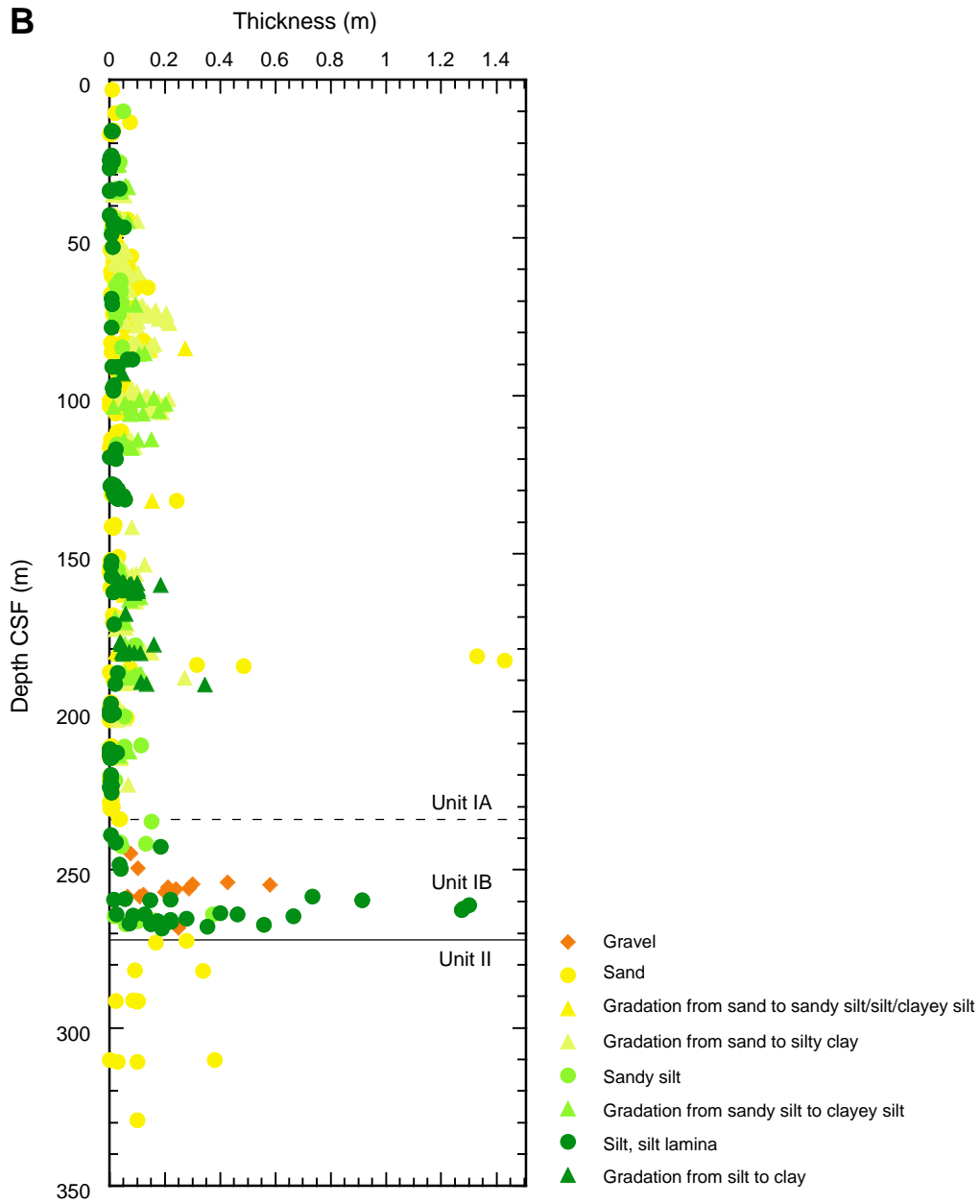


Figure F3 (continued). C. Core recovery and lithologic units, Holes C0008B and C0008C. (Continued on next page.)

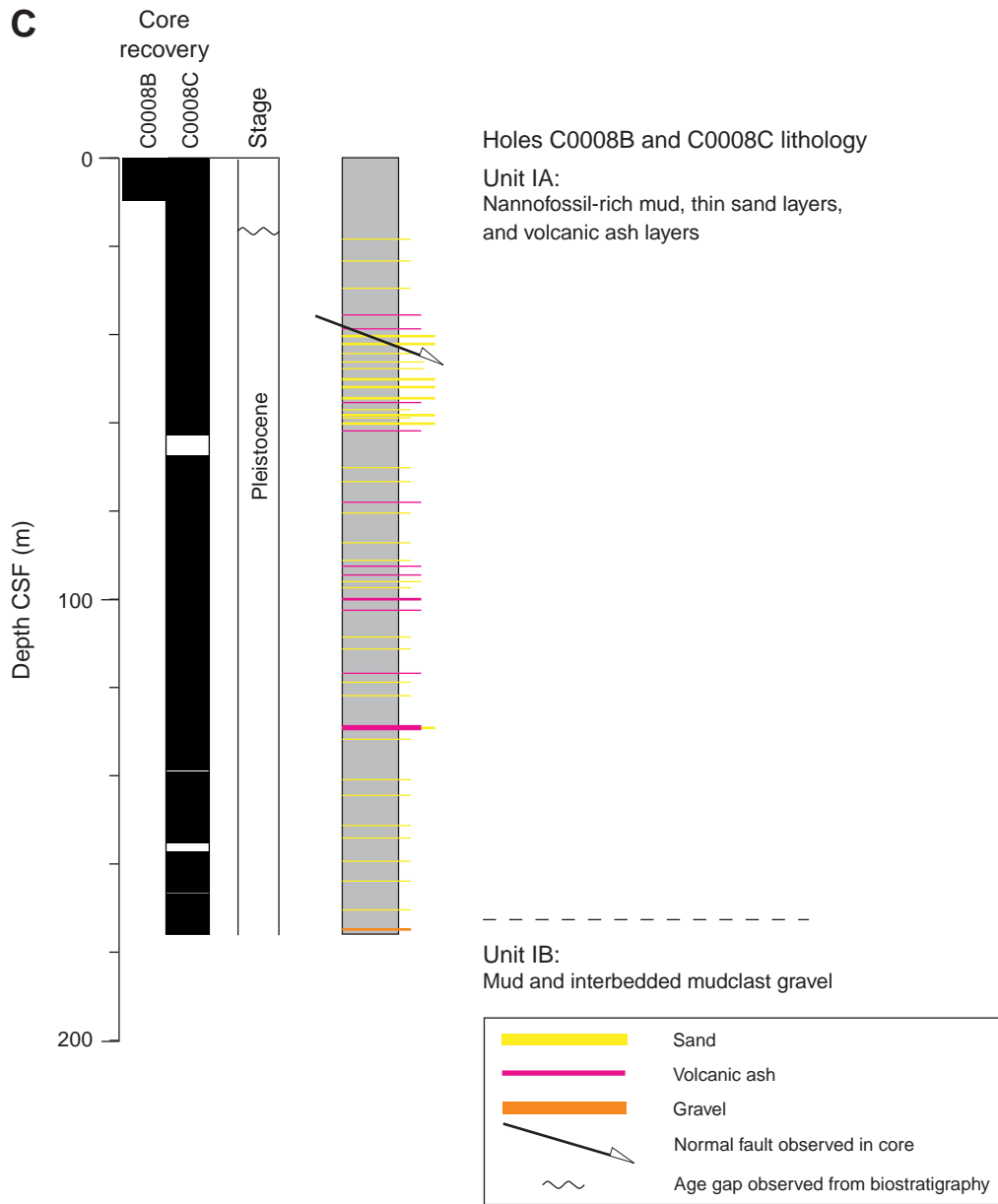


Figure F3 (continued). D. Distribution of sand and silt layers, Holes C0008B and C0008C.

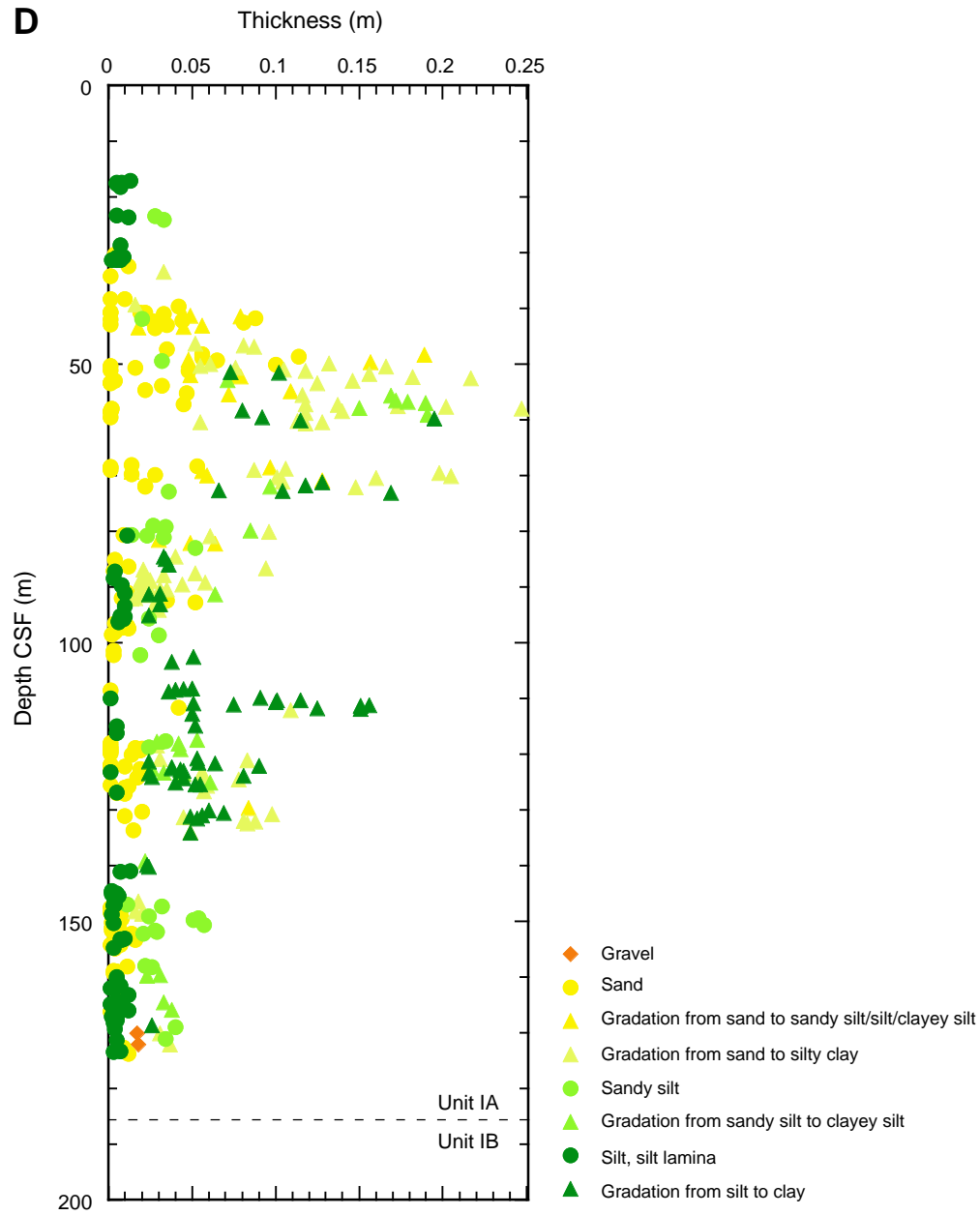


Figure F4. XRD data. A. Hole C0008A. B. Hole C0008C. CSF = core depth below seafloor.

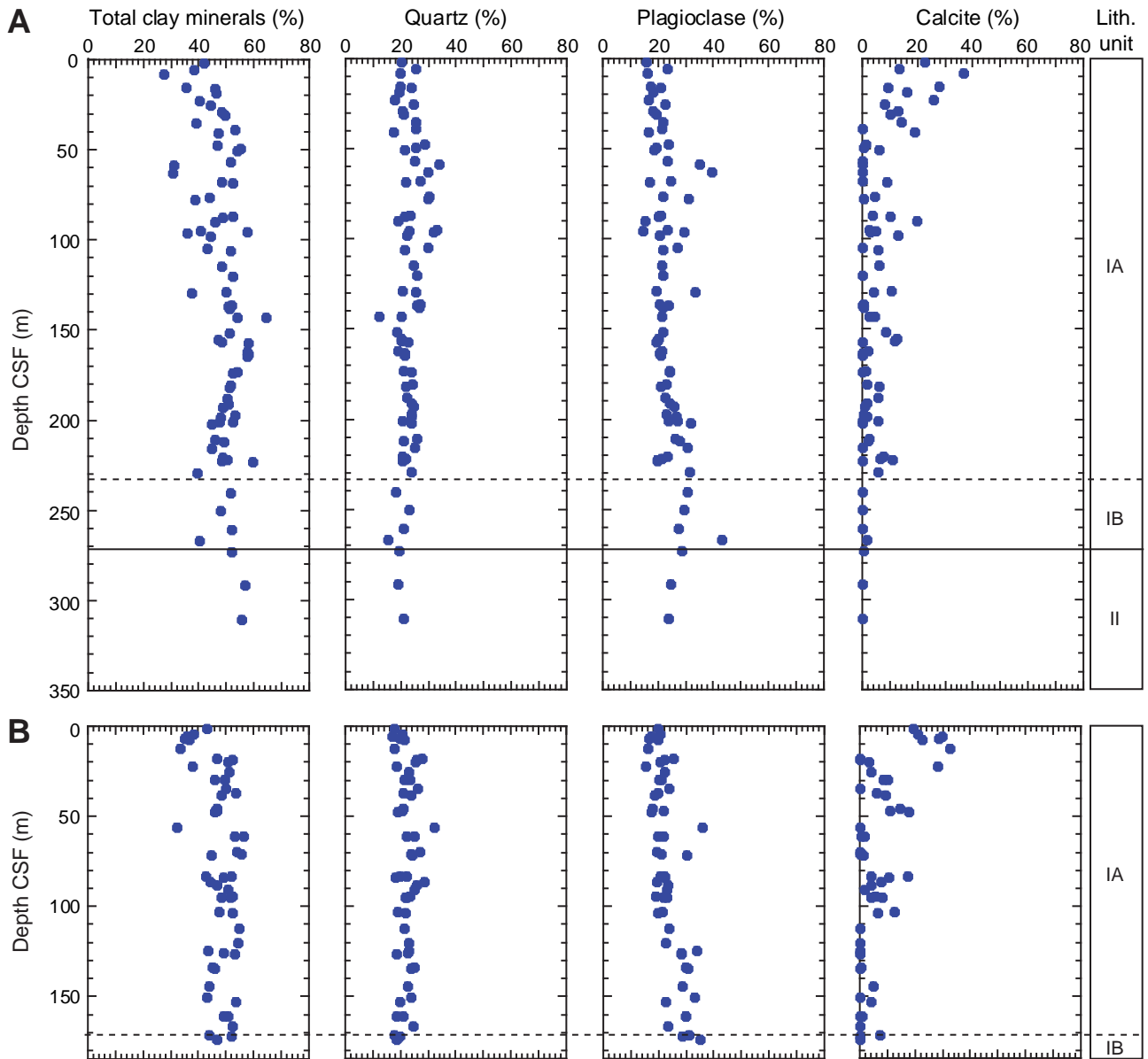


Figure F5. Core photograph examples, Unit I. **A.** Normal fault in mud-dominated succession in Subunit IA (interval 316-C0008C-5C-7, 26–80 cm). **B.** Cyclic graded sand-clay sequences in Subunit IA, Hole C0008C. Clusters of volcanic ash aggregates occur near the tops of the clay-rich portions of the sequences.

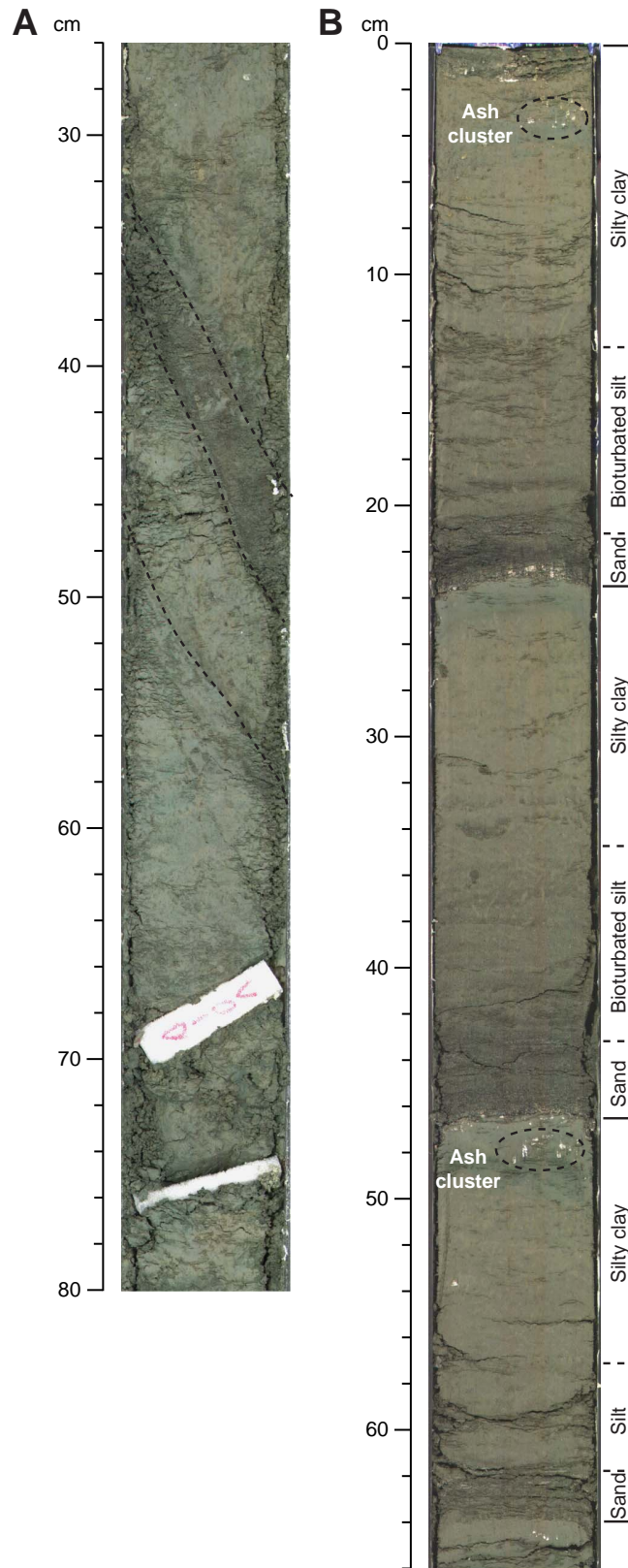


Figure F6. Photomicrographs of pyrite in sand, Subunit IA. **A.** Microcrystalline pyrite grain coatings (Sample 316-C0008C-7H-6, 115 cm). **B.** Disseminated pyrite framboids (Section 316-C0008C-10H-5, 6 cm). **C.** Pyrite framboids localized on woody debris (Sample 316-C0008C-4H-4, 34 cm).

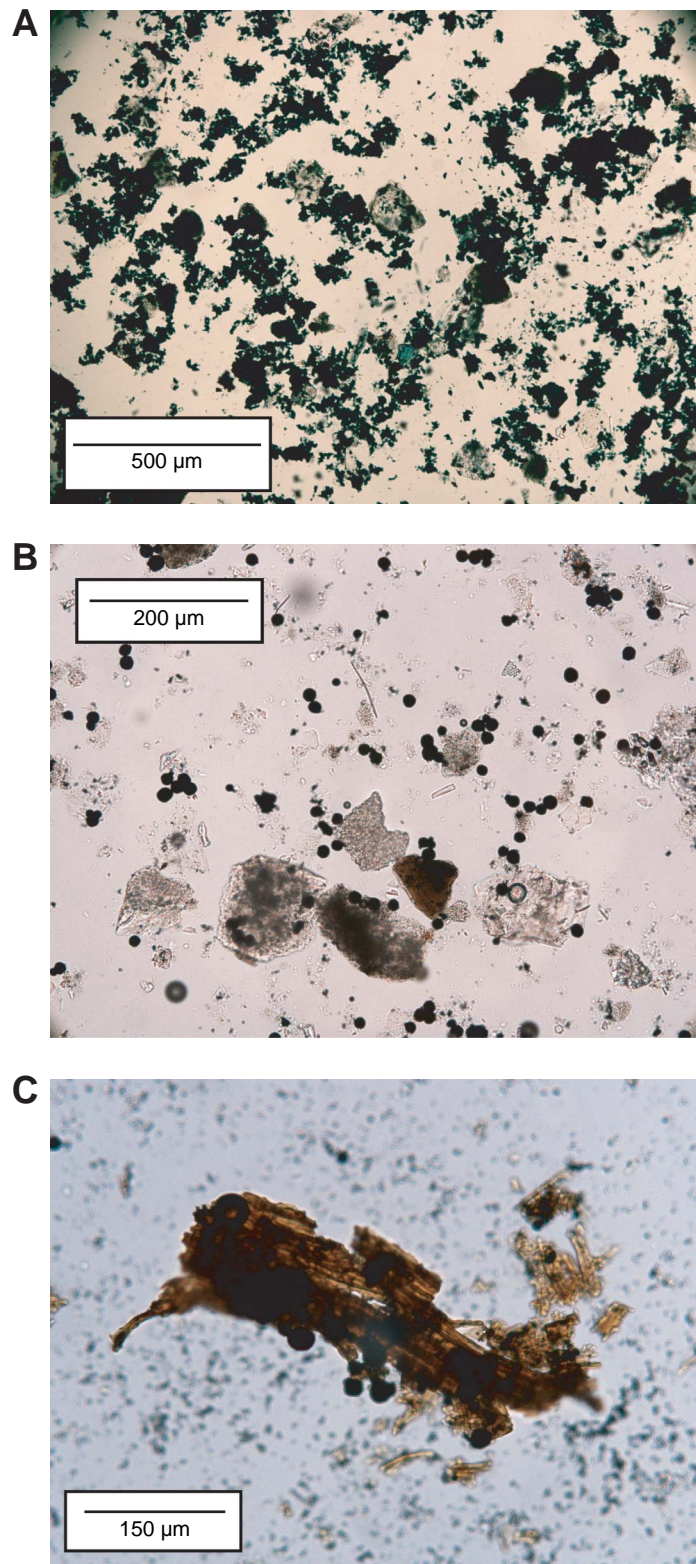


Figure F7. Ash layers and volcanic clasts, Site C0008. **A.** Hole C0008A. **B.** Hole C0008C. **C.** Thick ash layer (Sample 316-C0008A-26H-4, 30 cm). **D.** Photograph of typical ash layer (interval 316-C0008A-6H-4, 74–99 cm). CSF = core depth below seafloor.

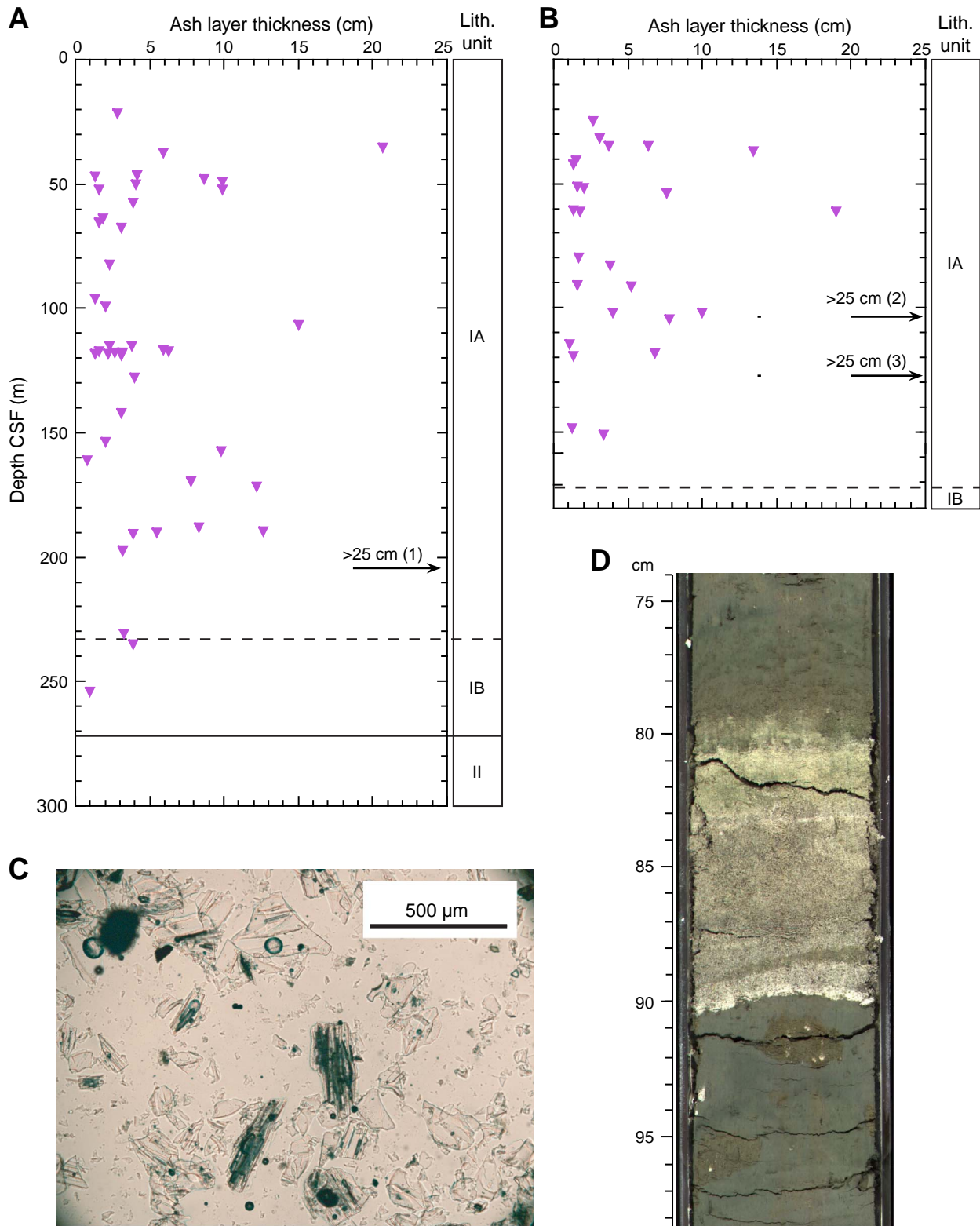


Figure F8. Photographs of gravel and sand, Subunit IB. **A.** Gravel (interval 316-C0008A-32X-2, 10–70 cm). **B.** Rounded mudstone pebbles in gravel (interval 316-C0008A-32X-1, 100–110 cm). **C.** Mudstone clasts (Sample 316-C0008A-25X-8, 85 cm).

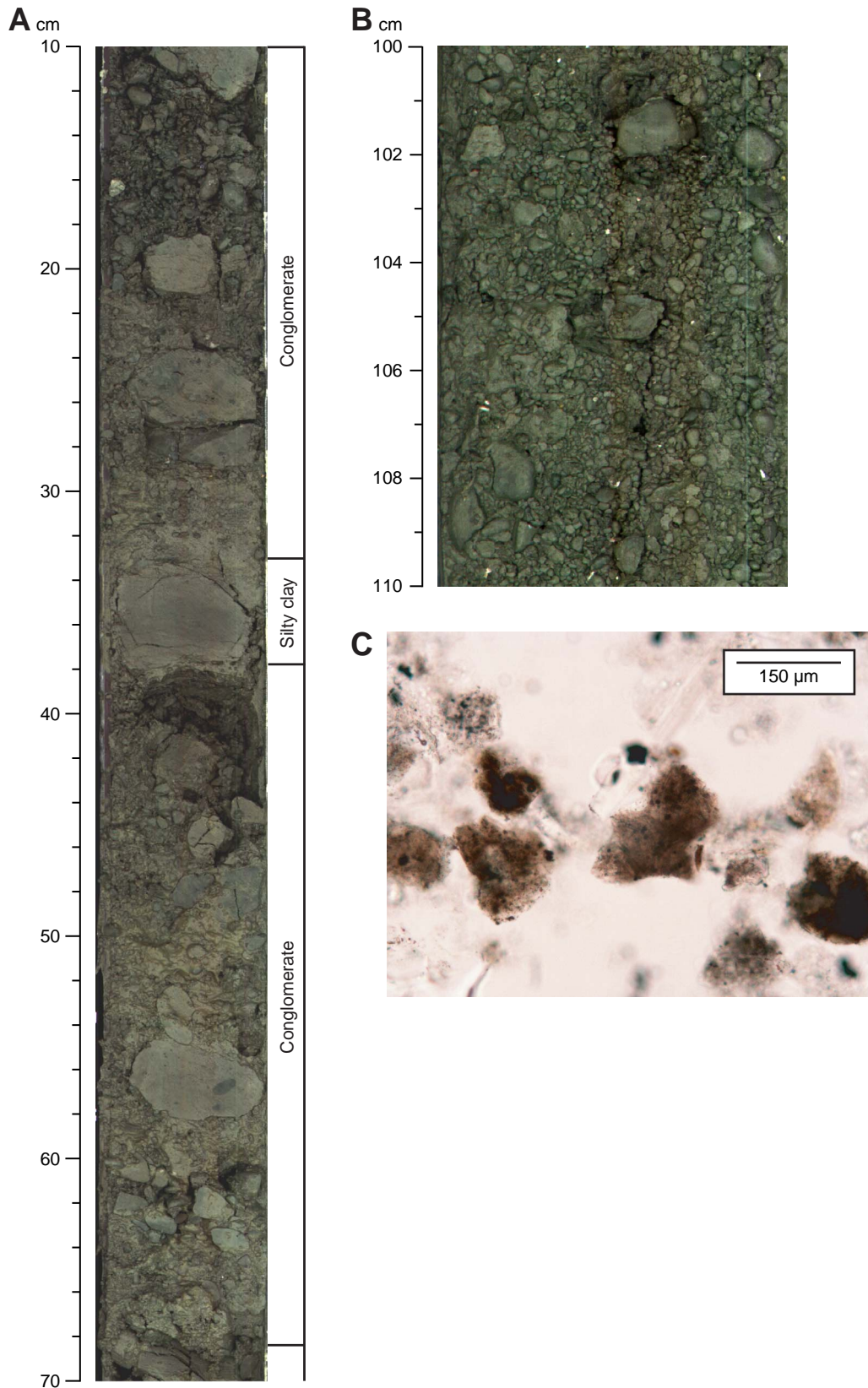


Figure F9. Depth trend in computed tomography (CT) number, Holes C0008C and C0008D. Average value for each core obtained from ~70 measurements with a 4–10 cm interval. CSF = core depth below seafloor.

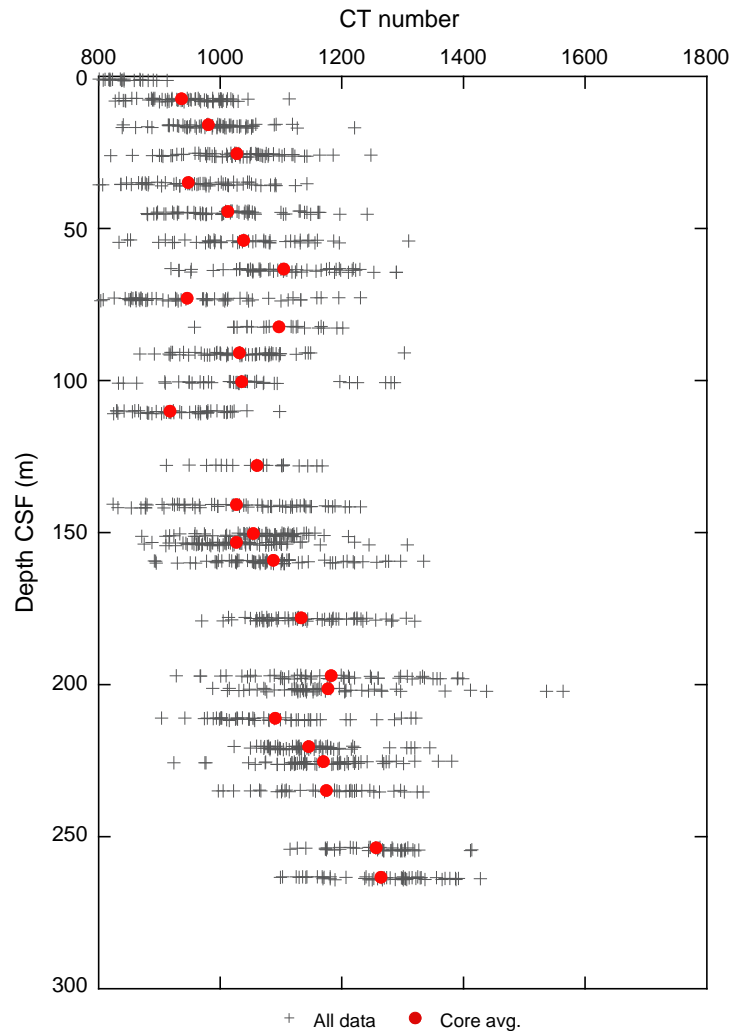


Figure F10. Distribution of planar structures with depth. Data deduced from core observation and CT scan image analyses. A. Hole C0008A. CSF = core depth below seafloor. (Continued on next page.)

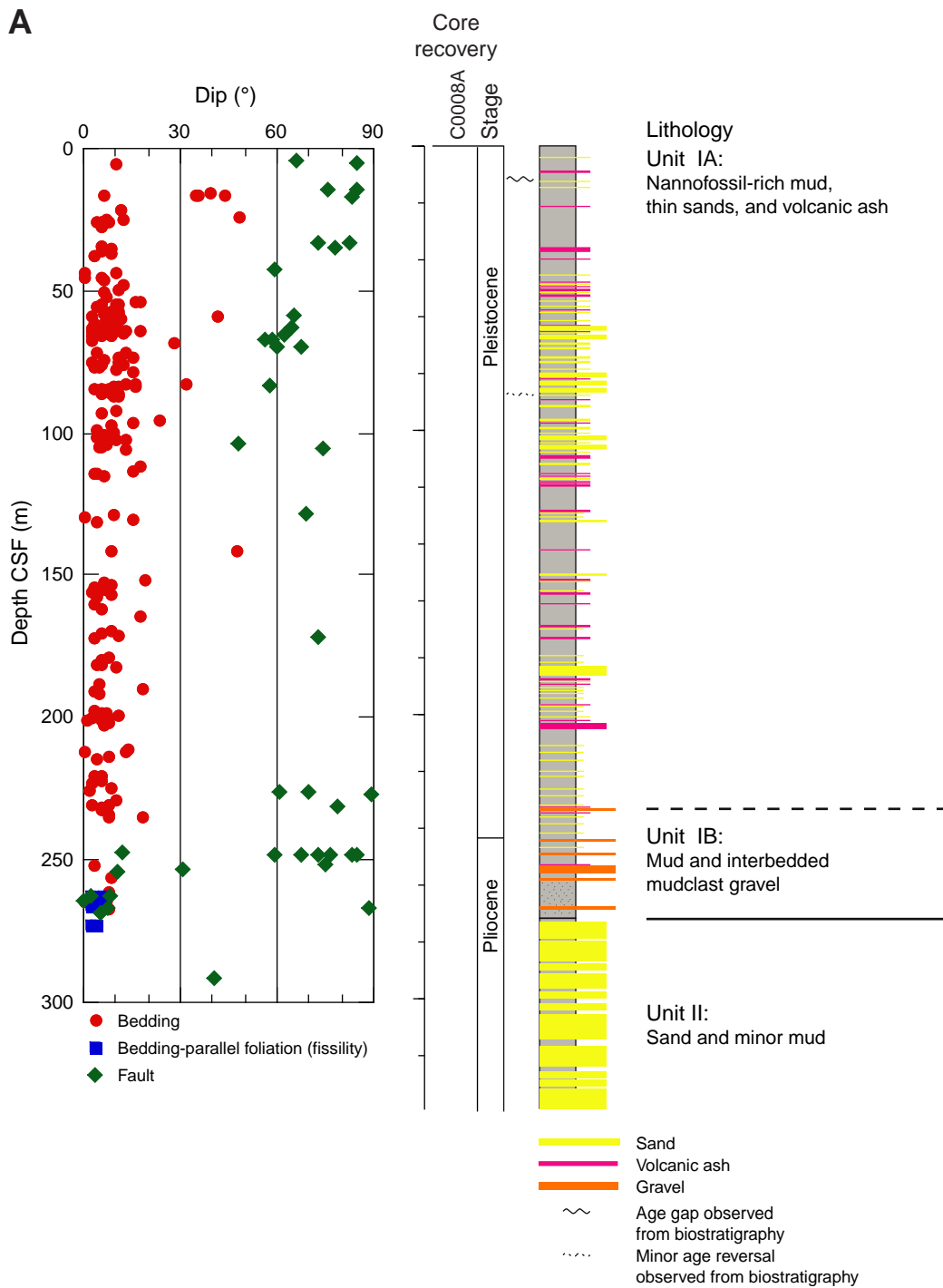


Figure F10 (continued). B. Holes C0008B and C0008C.

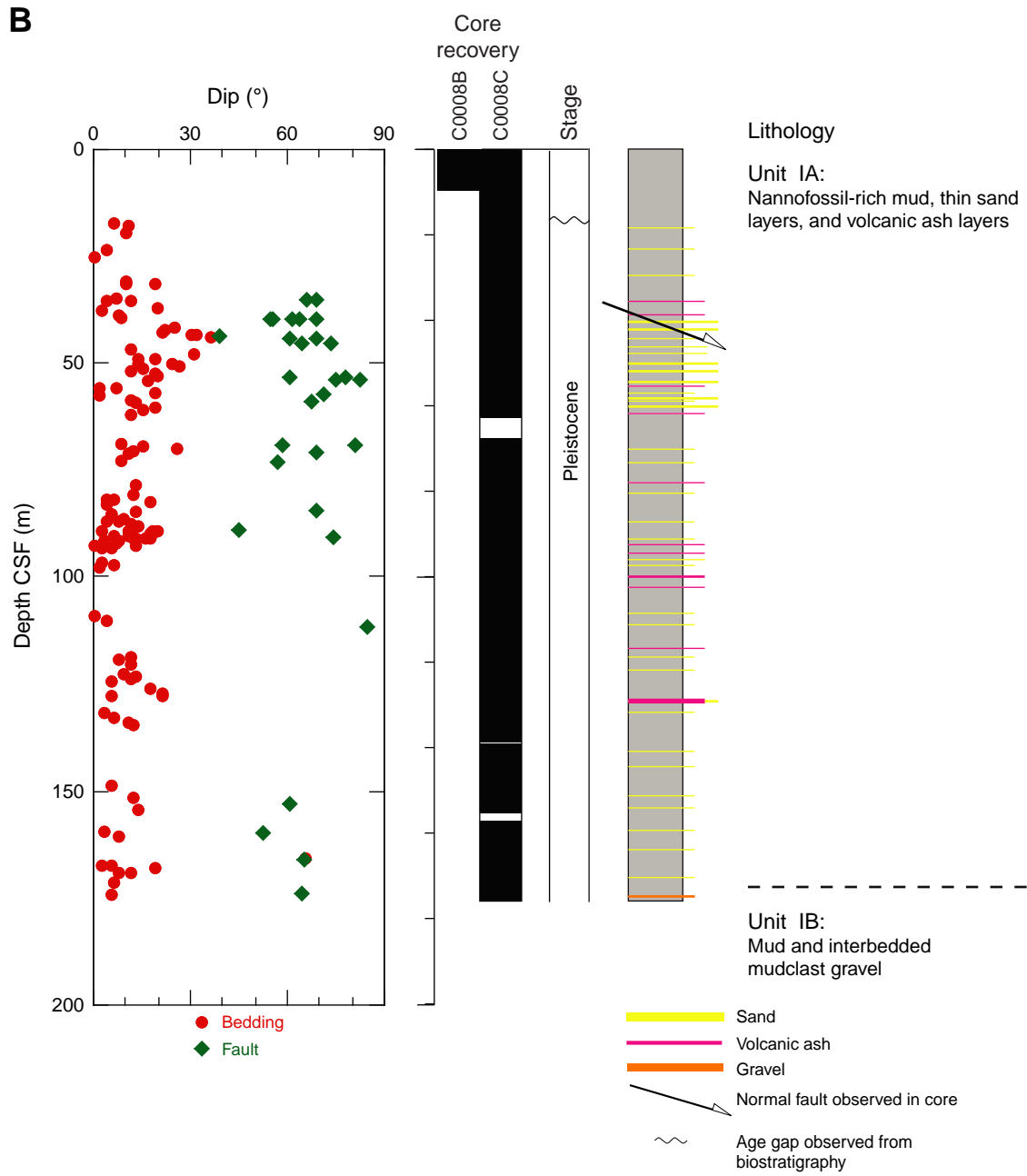


Figure F11. Lower-hemisphere equal-area projections of poles to bedding surfaces, Site C0008. A. Hole C0008A. B. Hole C0008C.

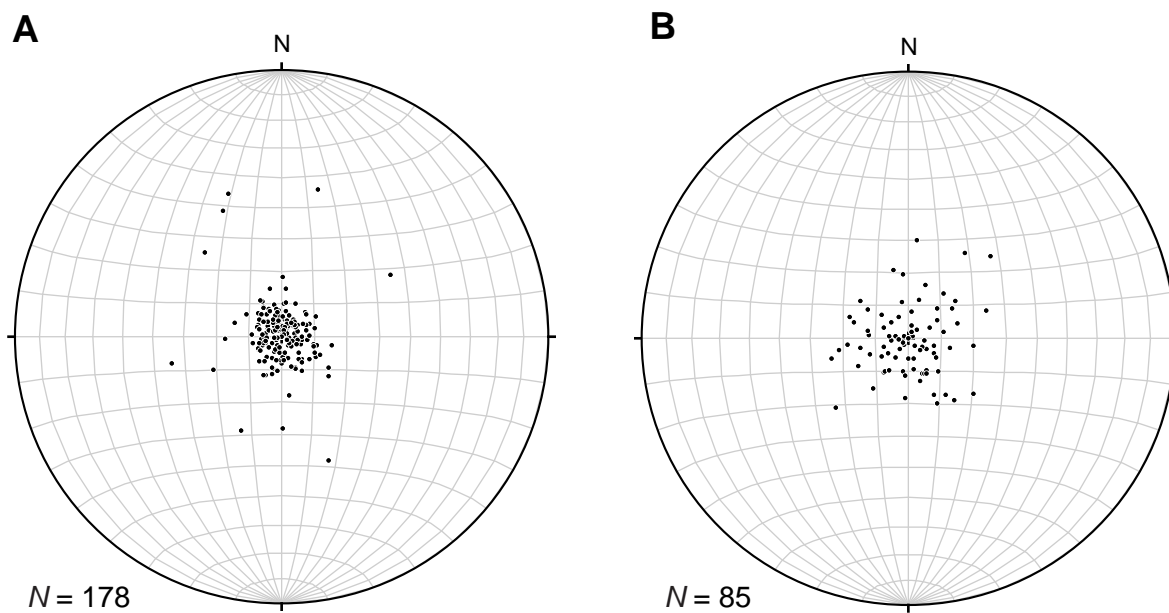


Figure F12. Core photographs showing normal faults, Site C0008. **A.** Interval 316-C0008A-4H-9, 60–77 cm. **B.** Interval 316-C0008C-5H-7, 29–66 cm. **C.** CT image of B. Bright spots possibly correspond to pyrite deposits. Black arrows = sense of shear.

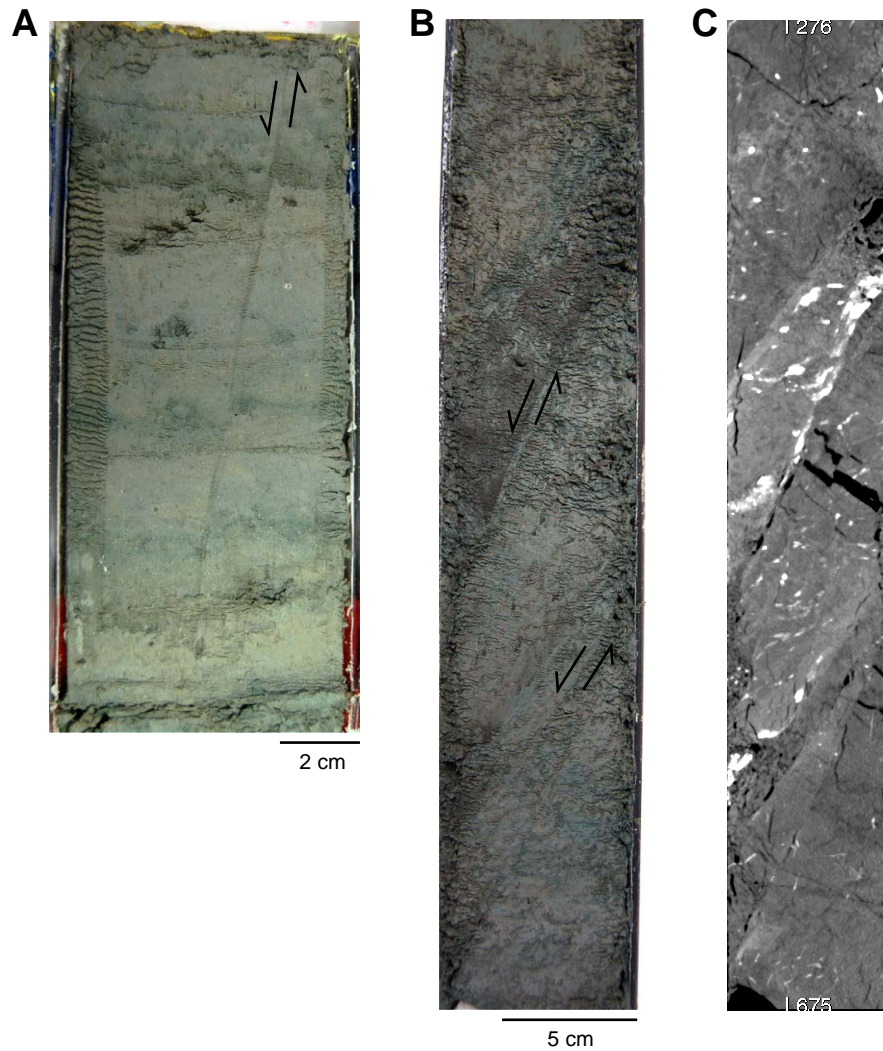


Figure F13. Photographs of healed faults, Hole C0008A. **A.** Layer-perpendicular fault (interval 316-C0008A-31X-4, 62–65 cm). **B.** Layer-parallel fault (interval 316-C0008A-32X-9, 13–16 cm).

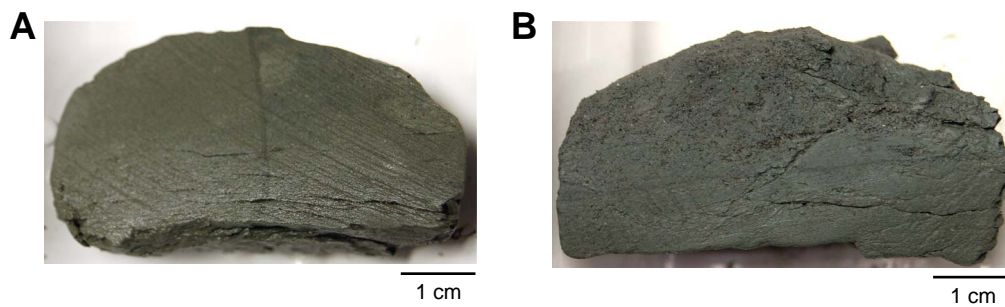


Figure F14. Lower-hemisphere equal-area projections of poles to faults, Site C0008. A. Hole C0008A. B. Hole C0008C.

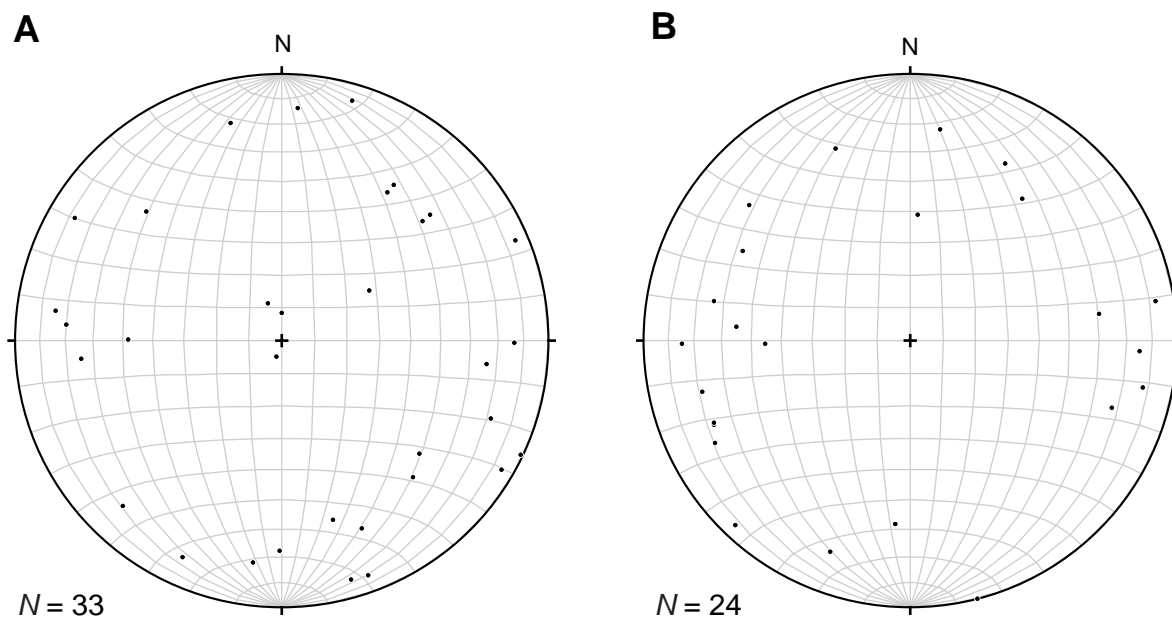


Figure F15. Plots of age and depth in Hole C0008A based on nannofossil events and magnetic data. CSF = core depth below seafloor.

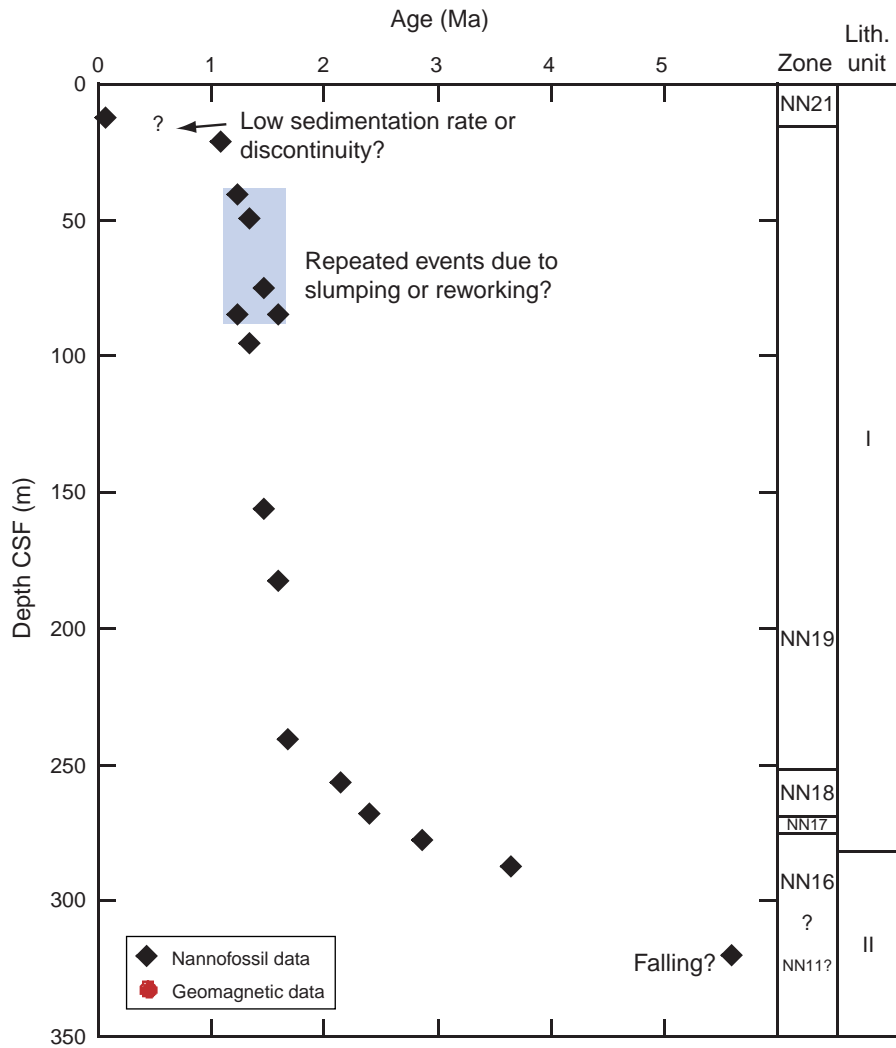


Figure F16. Plots of age and depth in Hole C0008C based on nannofossil events and magnetic data. CSF = core depth below seafloor.

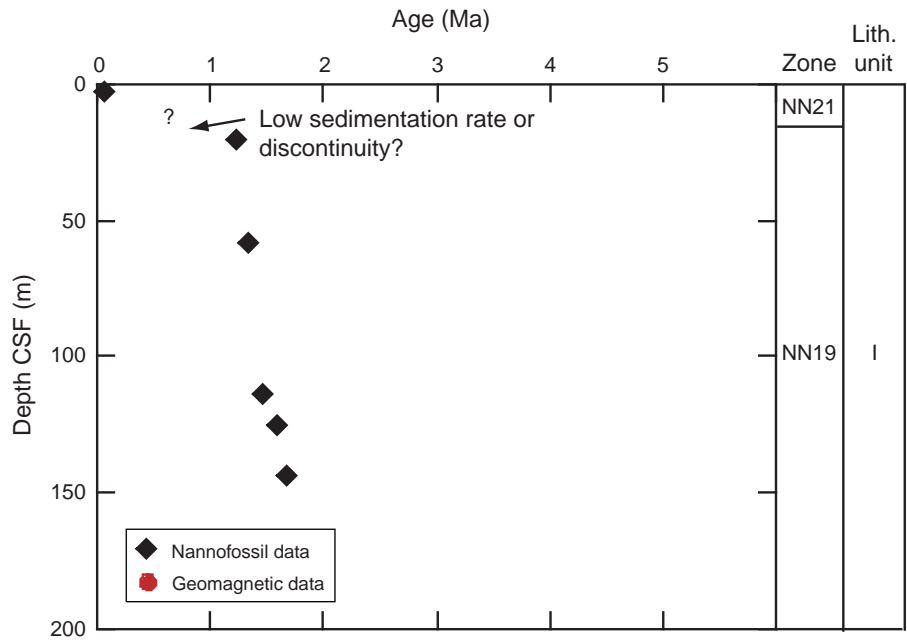


Figure F17. Radiolarian and nannofossil zones and events, Site C0008. CSF = core depth below seafloor.

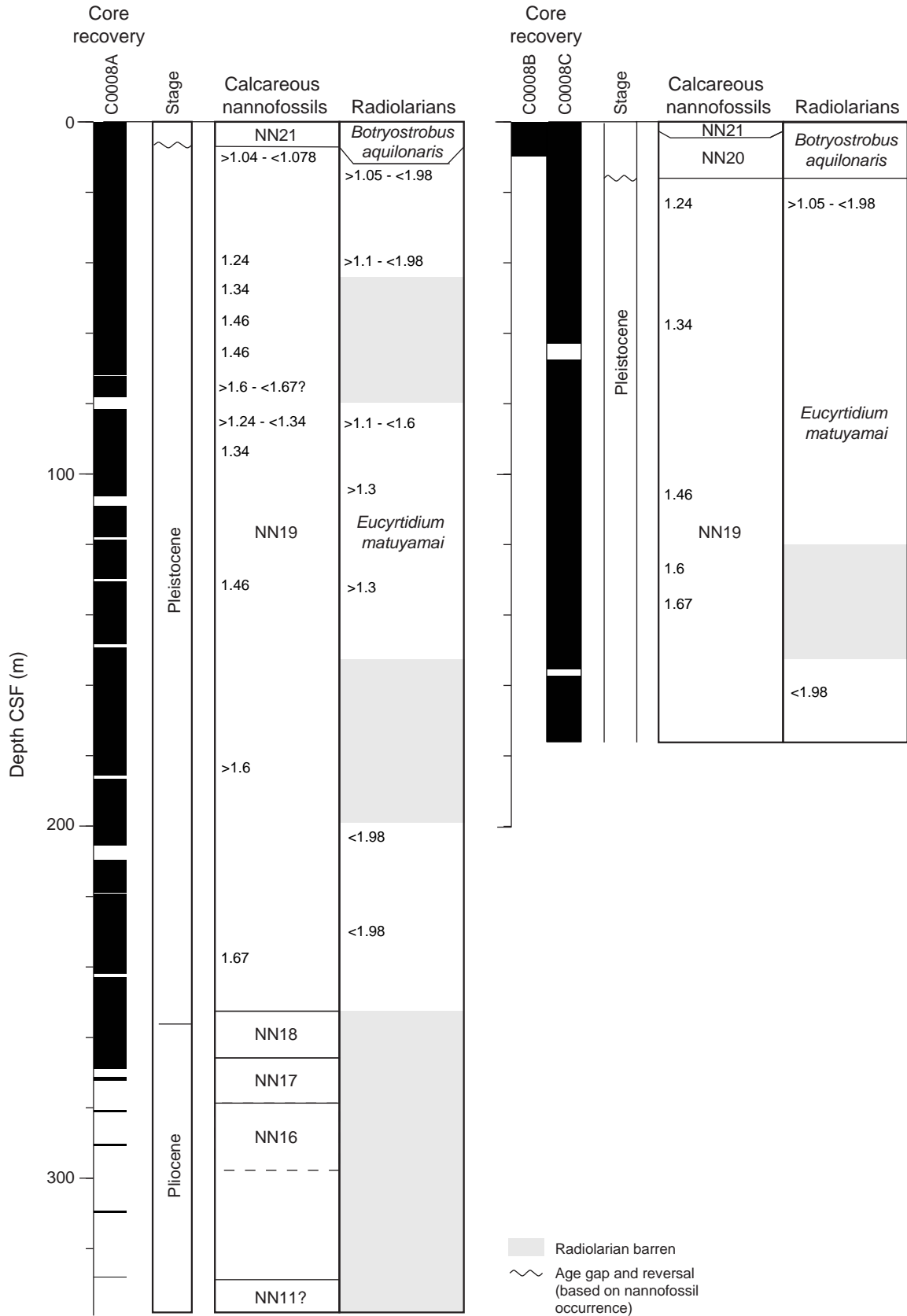


Figure F18. Magnetic susceptibility and remanent magnetization before (green) and after (purple, red, and blue) 40 mT alternating-field (AF) demagnetization. (A) Magnetic susceptibility, (B) intensity, (C) inclination, and (D) declination of archive halves, Hole C0008A. NRM inclinations are biased toward high positive inclinations, suggesting that drilling-induced magnetization is present. AF demagnetization to 40 mT can effectively remove drilling-induced magnetization, as indicated by changes in inclination and intensity. CSF = core depth below seafloor.

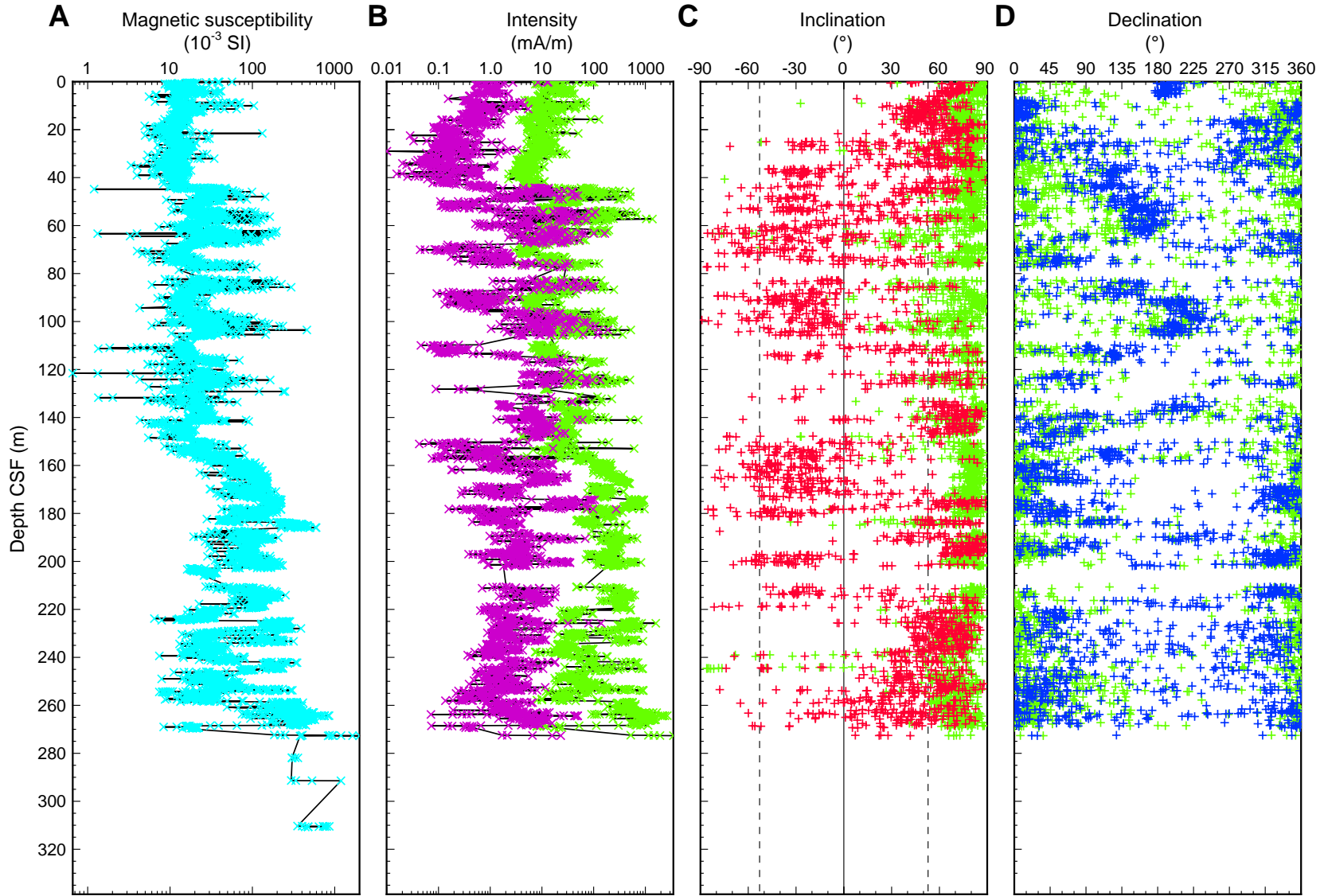


Figure F19. Magnetic susceptibility and remanent magnetization before (green) and after (purple, red, and blue) 40 mT alternating-field (AF) demagnetization. (A) Magnetic susceptibility, (B) intensity, (C) inclination, and (D) declination of archive halves, Hole C0008C. NRM inclinations are biased toward high positive inclinations, suggesting that drilling-induced magnetization is present. AF demagnetization to 40 mT can effectively remove drilling-induced magnetization, as indicated by changes in inclination and intensity. CSF = core depth below seafloor.

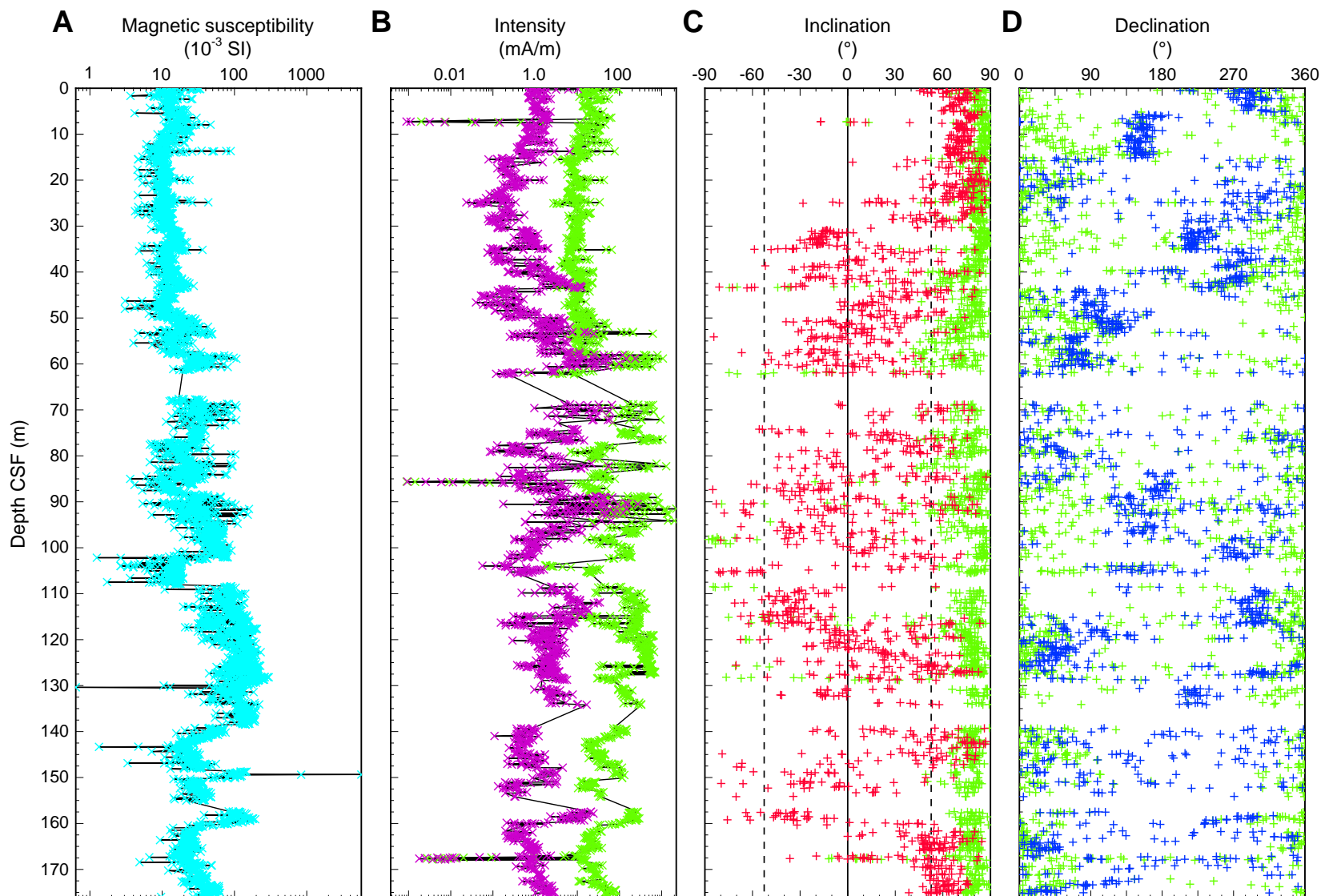


Figure F20. Vector endpoint and stereonet magnetization directions showing the results of AF demagnetization for sediment from (A) Sample 316-C0008A-2H-3, 12–14 cm, (B) Sample 316-C0008A-5H-2, 91–93 cm, (C) and Sample 316-C0008A-12H-2, 73–75 cm. Black dots and white squares = projection of magnetization vector endpoint on the horizontal and vertical planes, respectively. NRM = natural remanent magnetization.

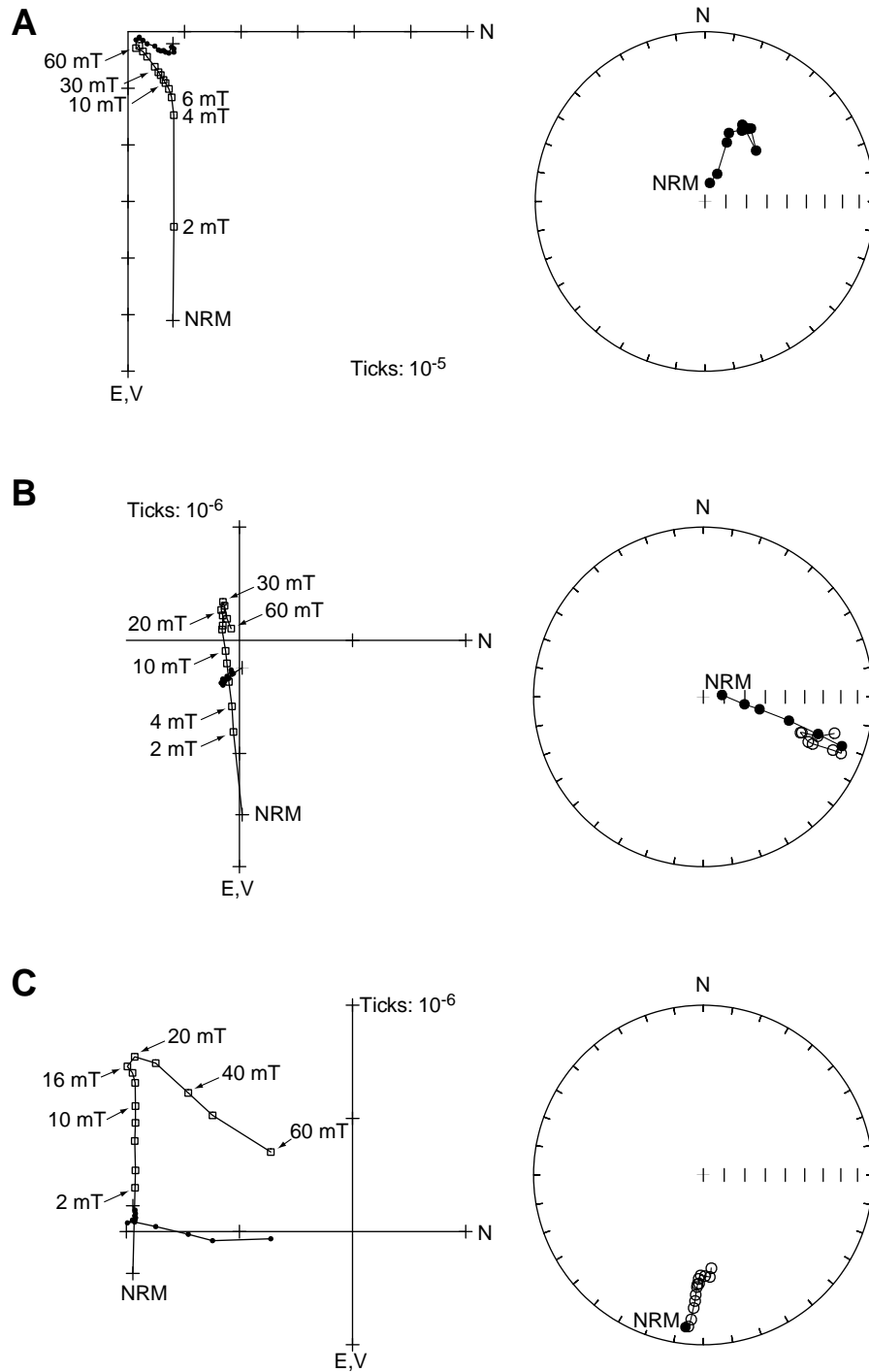


Figure F21. Vector endpoint and stereonet magnetization directions showing the results of thermal demagnetization for sediment from (A) Sample 316-C0008A-30X-5, 26–28 cm, (B) Sample 316-C0008A-34X-1, 49–51 cm, and (C) Sample 316-C0008A-40X-CC, 2–4 cm. Black dots and white squares = projection of magnetization vector endpoint on the horizontal and vertical planes, respectively. NRM = natural remanent magnetization.

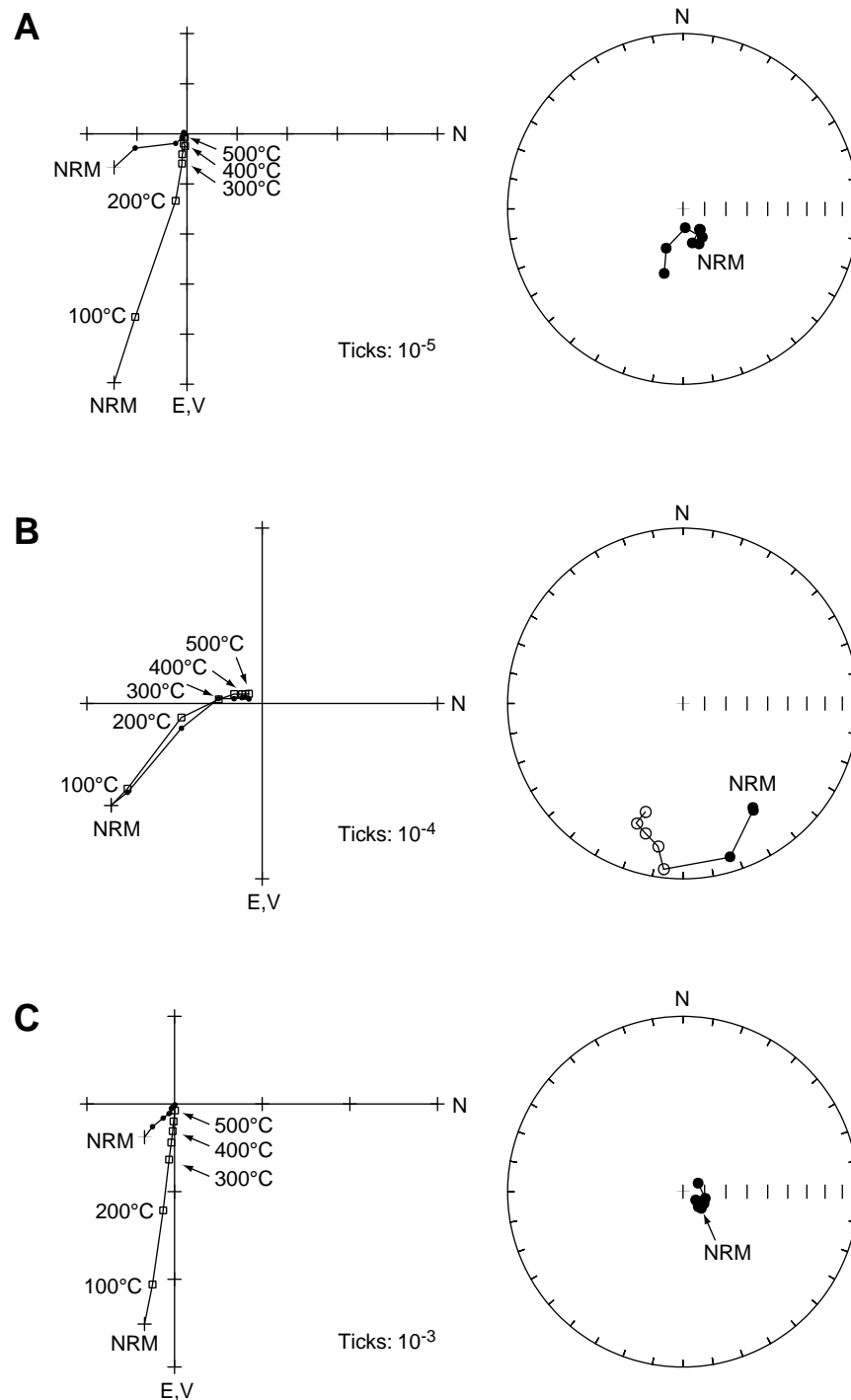


Figure F22. Downhole variation in stable magnetic inclination, inferred polarity, biostratigraphic zones, and lithology for sediments in Hole C0008A. CSF = Core depth below seafloor. Black areas = normal polarity, white areas = reversed polarity, hatched area = mixed or uncertain polarity. Gray text = age from foraminiferal zonation. Black crosses in the inclination plot = alternating field (AF) or thermal demagnetization data of discrete samples.

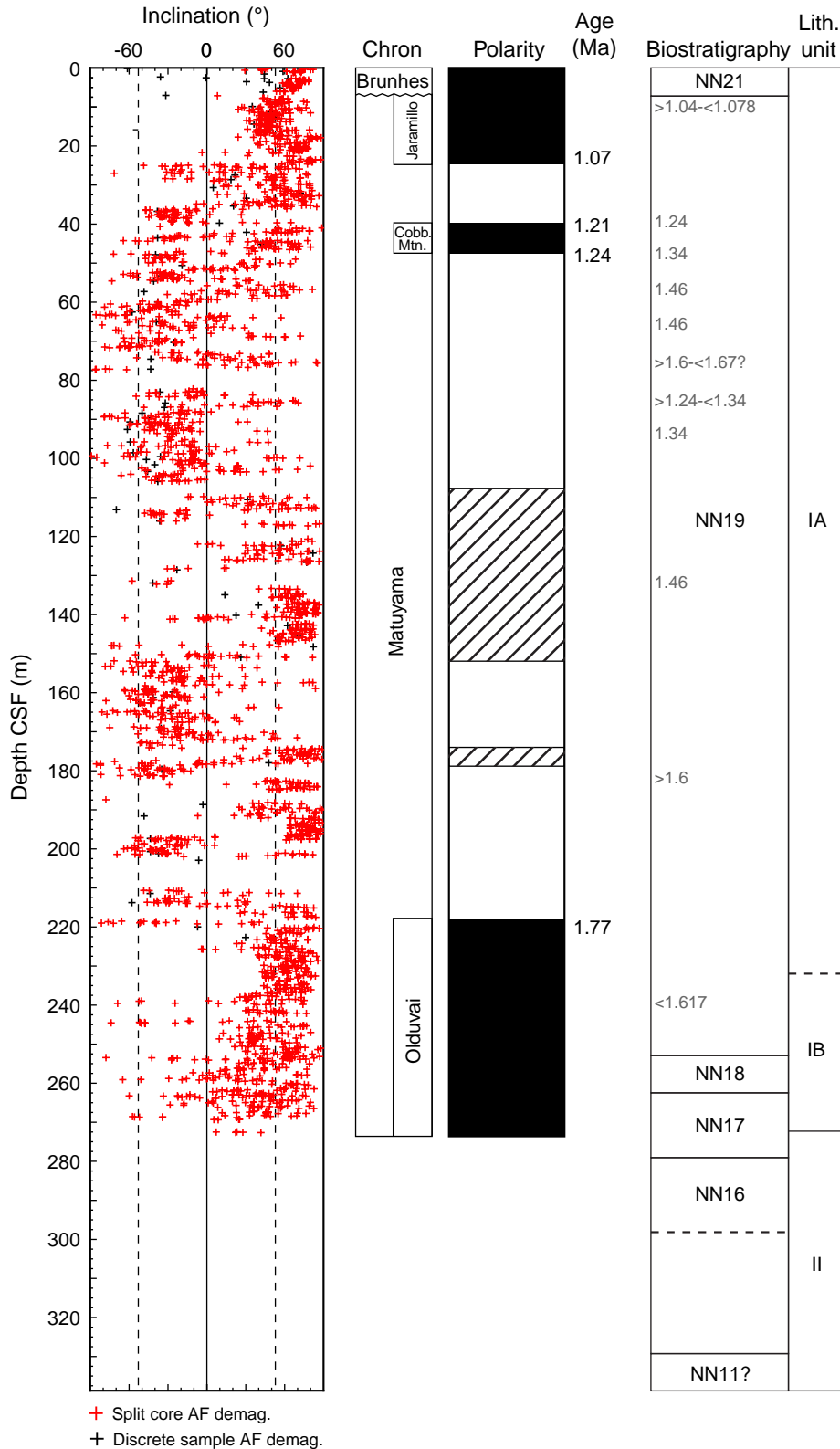


Figure F23. Downhole variation in stable magnetic inclination, inferred polarity, biostratigraphic zones, and lithology for sediments in Hole C0008C. CSF = core depth below seafloor. Black areas = normal polarity, white areas = reversed polarity, hatched area = mixed or uncertain polarity. Gray text = age from foraminiferal zonation.

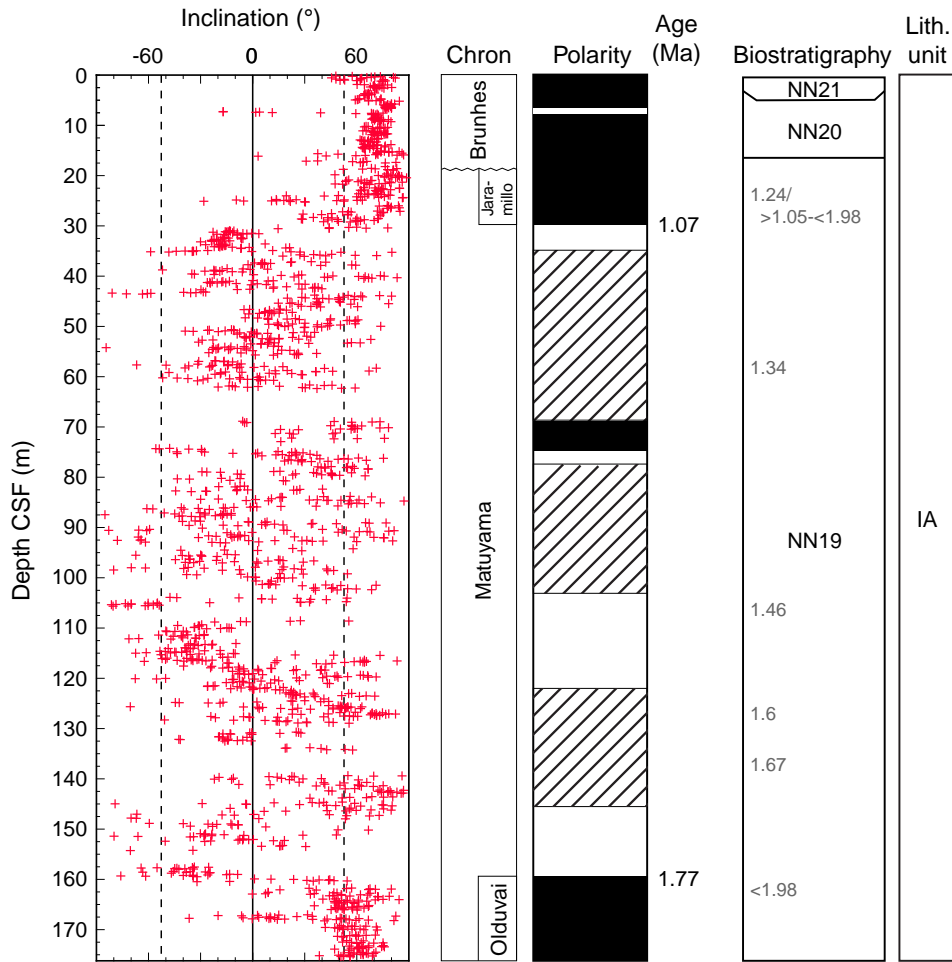


Figure F24. Concentrations of (A) salinity, (B) chloride, (C) sodium, and (D) Na/Cl in interstitial water samples, Hole C0008A; and (E) salinity, (F) chloride, (G) sodium, and (H) Na/Cl in interstitial water samples, Hole C0008C. Salinity is calculated from refractive index, and sodium by charge balance. CSF = core depth below seafloor. SW = seawater values.

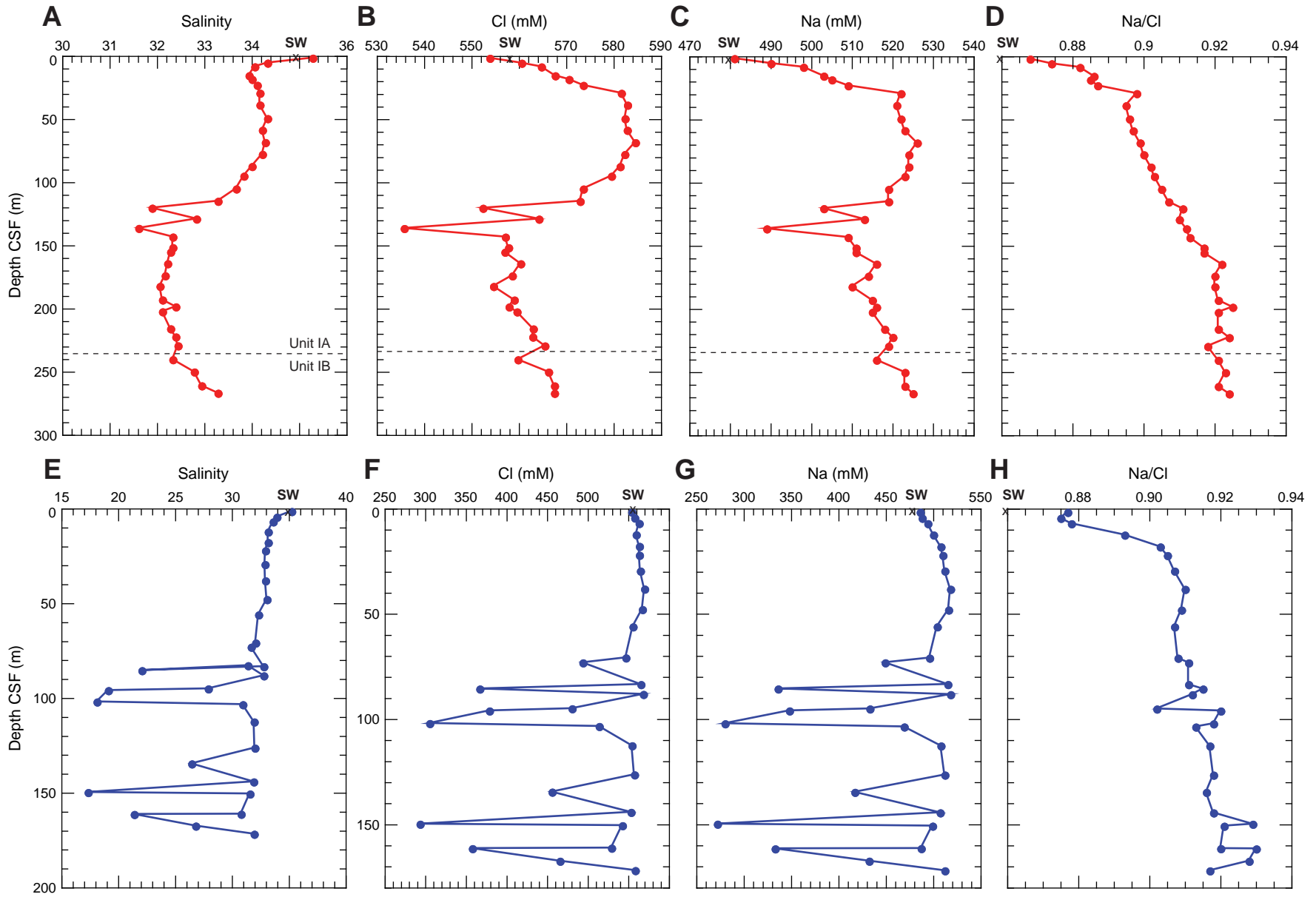




Figure F25. Concentrations of (A) pH, (B) sulfate, (C) alkalinity, and (D) barium, Hole C0008A; and (E) pH, (F) sulfate, (G) alkalinity, and (H) barium, Hole C0008C. CSF = core depth below seafloor. SW = seawater values.

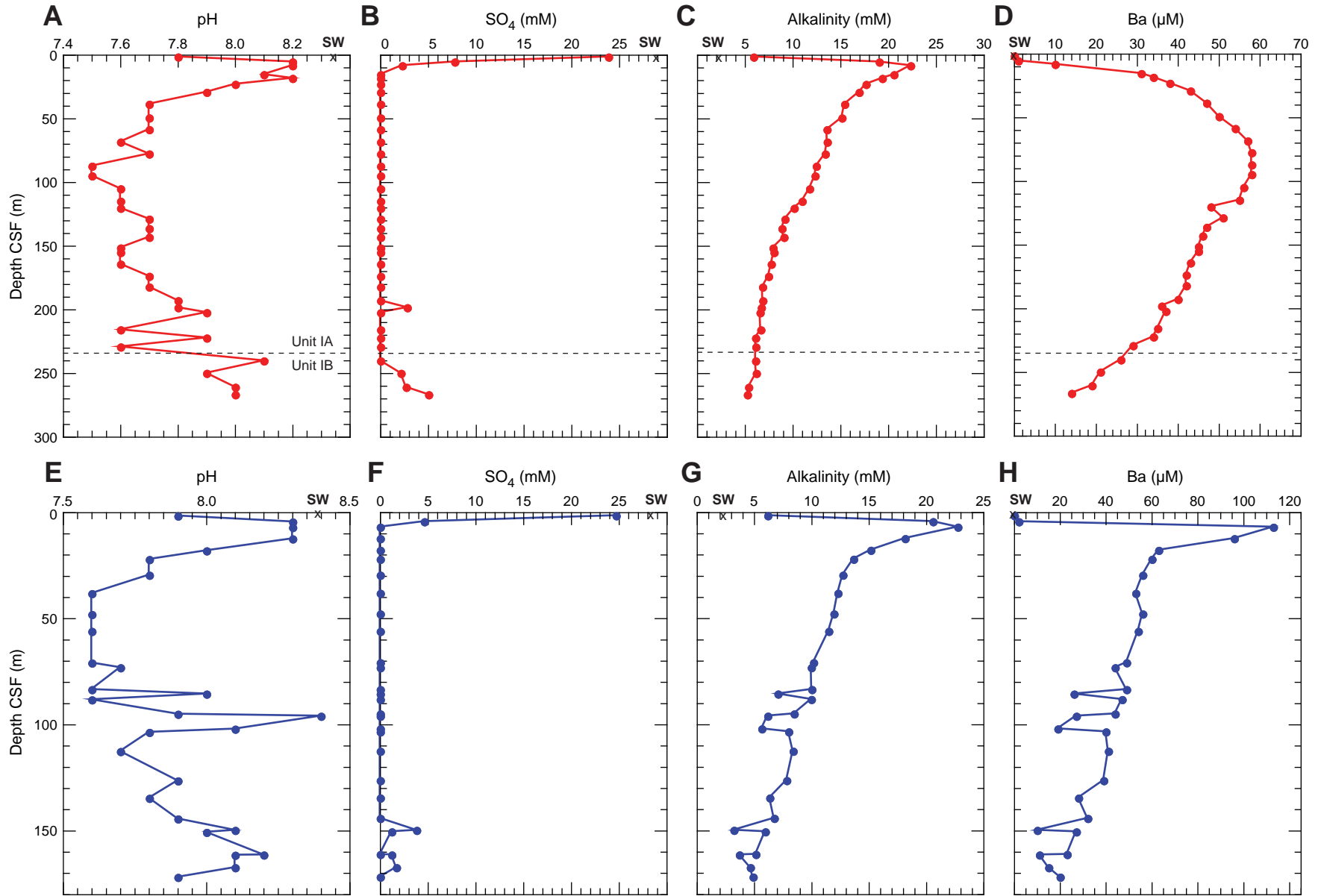


Figure F26. Concentrations of (A) ammonium, (B) phosphate, and (C) bromide from interstitial water samples, Hole C0008A; and (D) ammonium, (E) phosphate, and (F) bromide from interstitial water samples, Hole C0008C. CSF = core depth below seafloor. SW = seawater values.

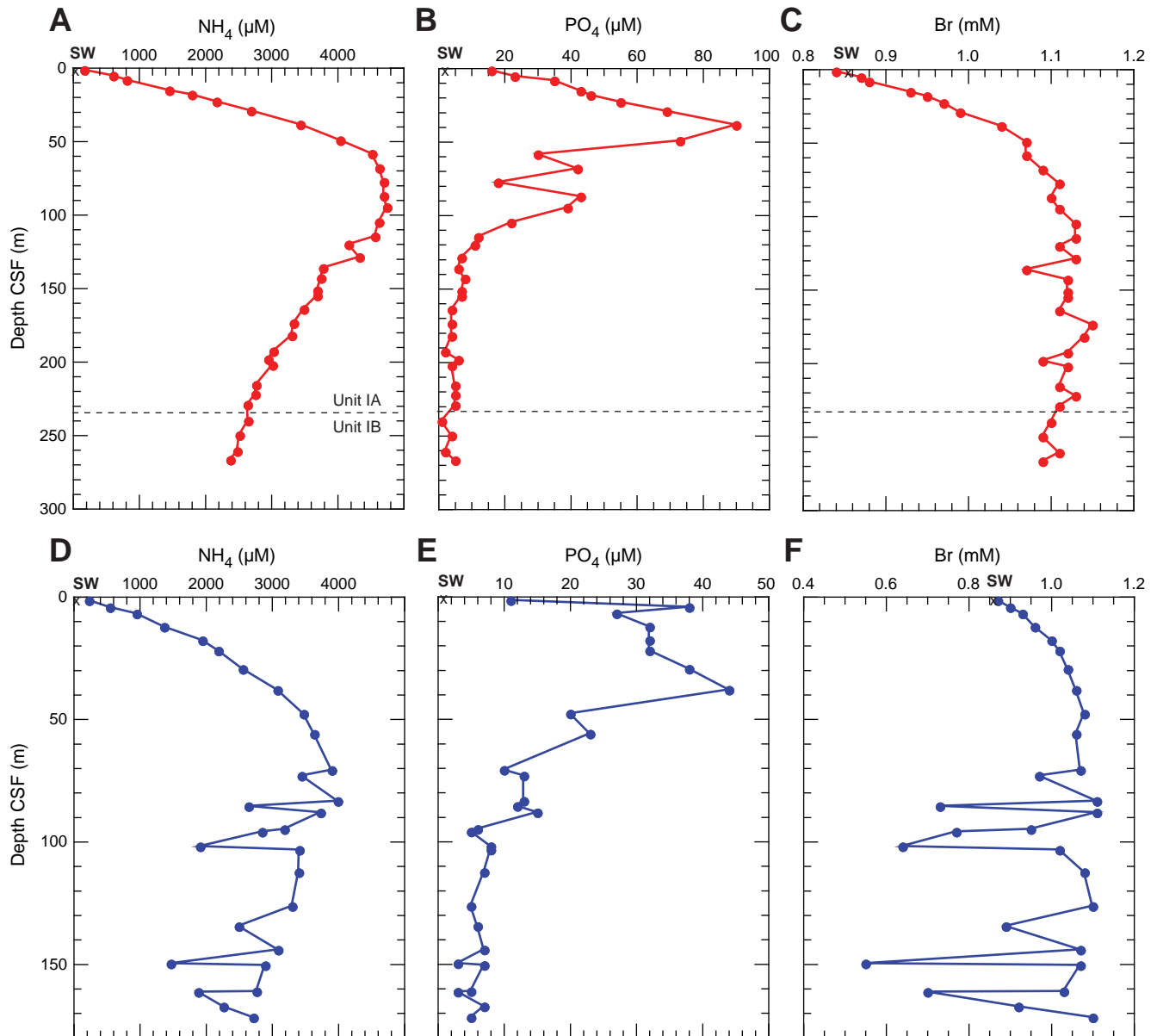


Figure F27. Concentrations of (A) calcium, (B) magnesium, (C) potassium, and (D) silica in interstitial waters, Hole C0008A; and (E) calcium, (F) magnesium, (G) potassium, and (H) silica in interstitial waters, Hole C0008C. CSF = core depth below seafloor. SW = seawater values. (Continued on next page.)

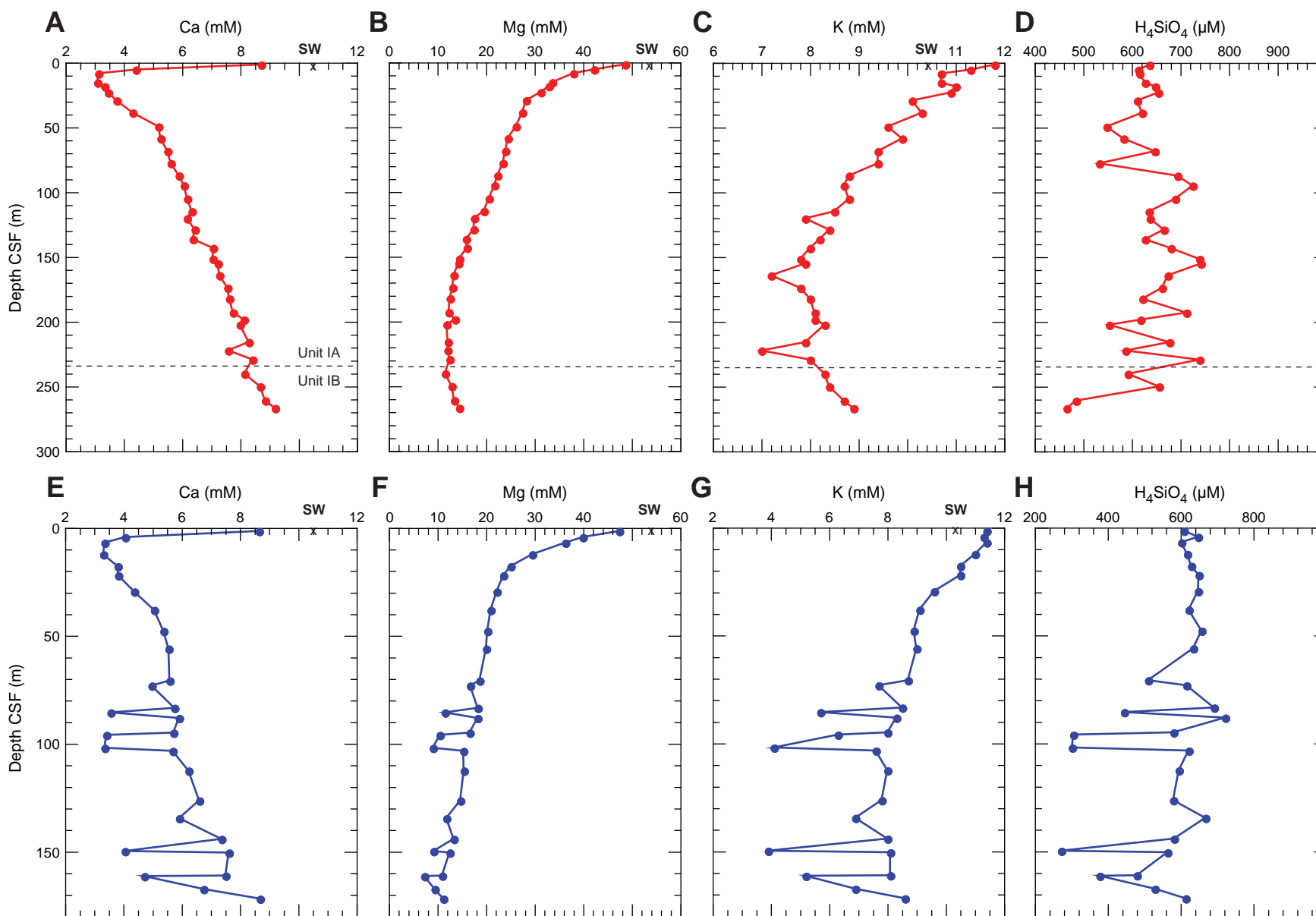




Figure F27 (continued). Concentrations of (I) rubidium, and (J) cesium in interstitial waters, Hole C0008C.

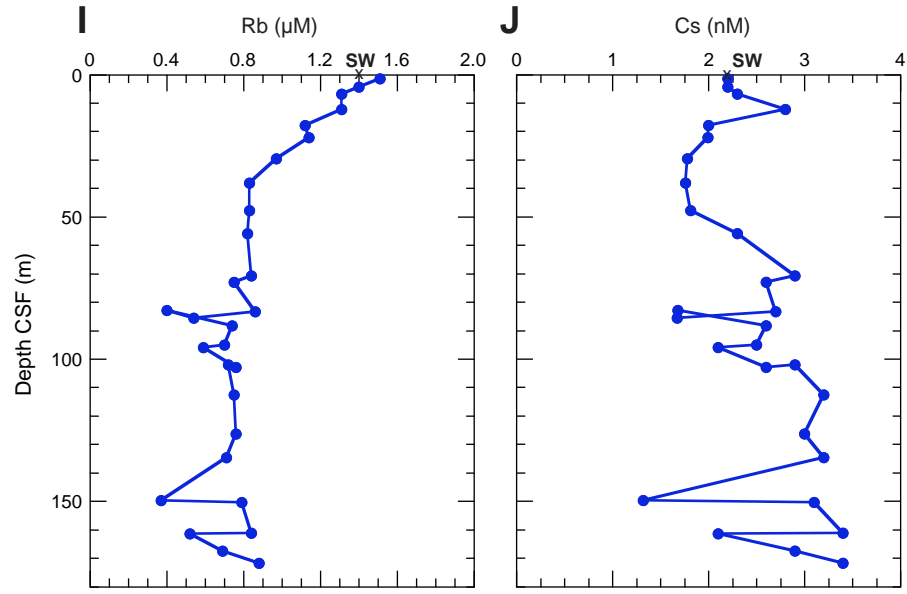


Figure F28. Concentrations of (A) lithium, (B) boron, and (C) strontium in interstitial waters, Hole C0008A; and (D) lithium, (E) boron, and (F) strontium in interstitial waters, Hole C0008C. CSF = core depth below seafloor. SW = seawater values.

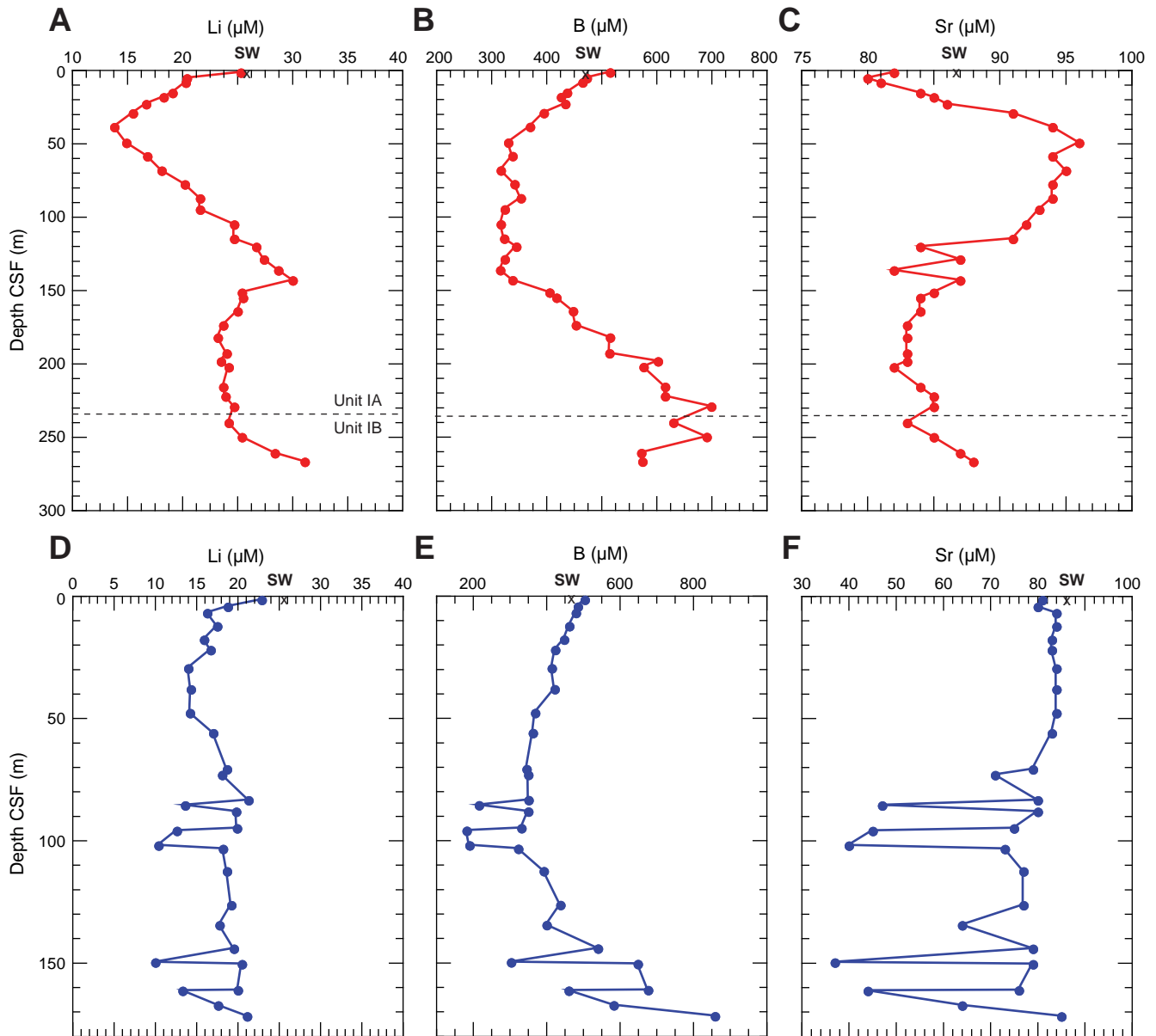




Figure F29. Concentrations of (A) manganese and (B) iron in interstitial waters, Hole C0008A; and (C) molybdenum, (D) lead, (E) manganese, (F) iron, (G) uranium, and (H) yttrium in interstitial waters, Hole C0008C. CSF = core depth below seafloor. SW = seawater values. (Continued on next page.)

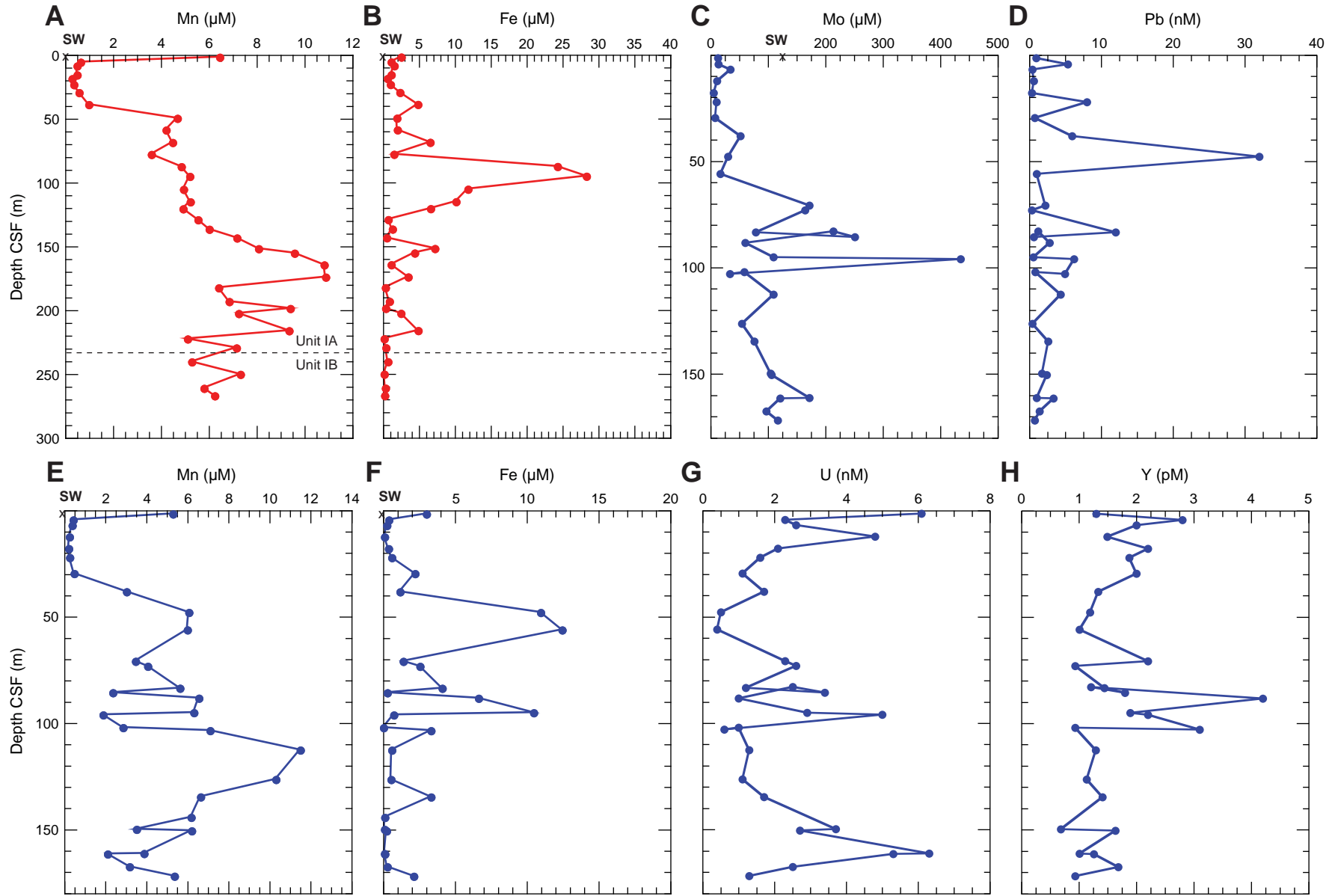




Figure F29 (continued). Concentrations of (I) copper, (J) zinc, and (K) vanadium in interstitial waters, Hole C0008C.

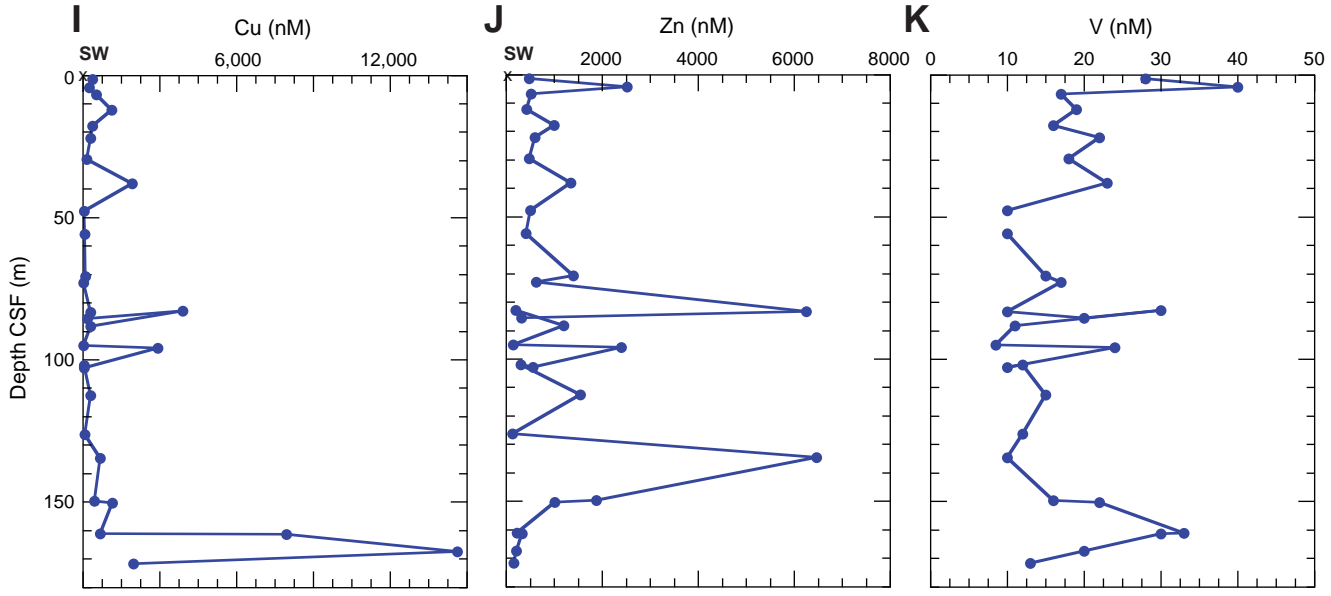


Figure F30. $\delta^{18}\text{O}$ isotopic ratios. **A.** Hole C0008A. **B.** Hole C0008C. CSF = core depth below seafloor. SW = sea-water values.

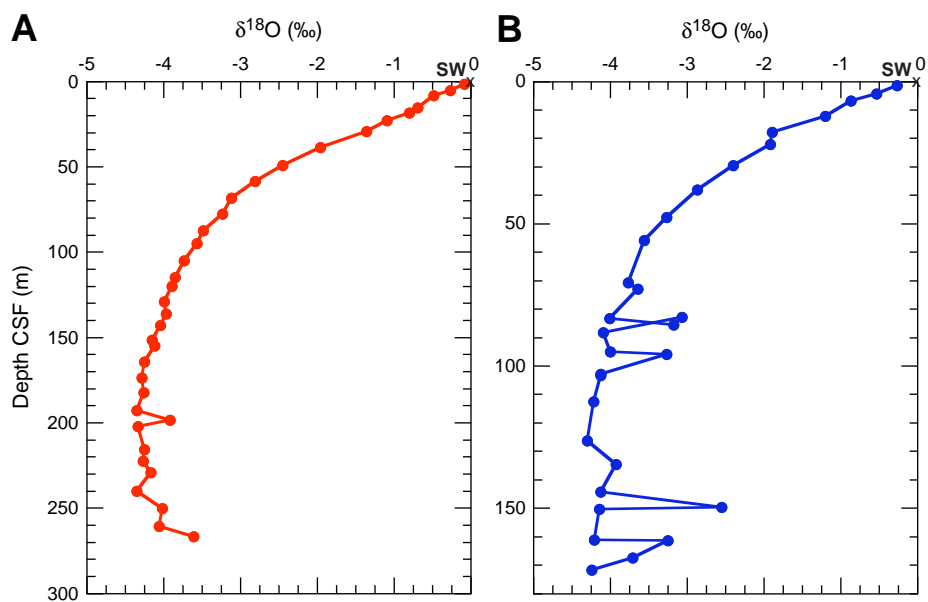


Figure F31. Dissolved methane and ethane concentrations calculated from headspace samples (see Table T15), as well as values of C_1/C_2 in sediments, Site C0008. CSF = core depth below seafloor. Blue = Hole C0008A, red = Hole C0008C.

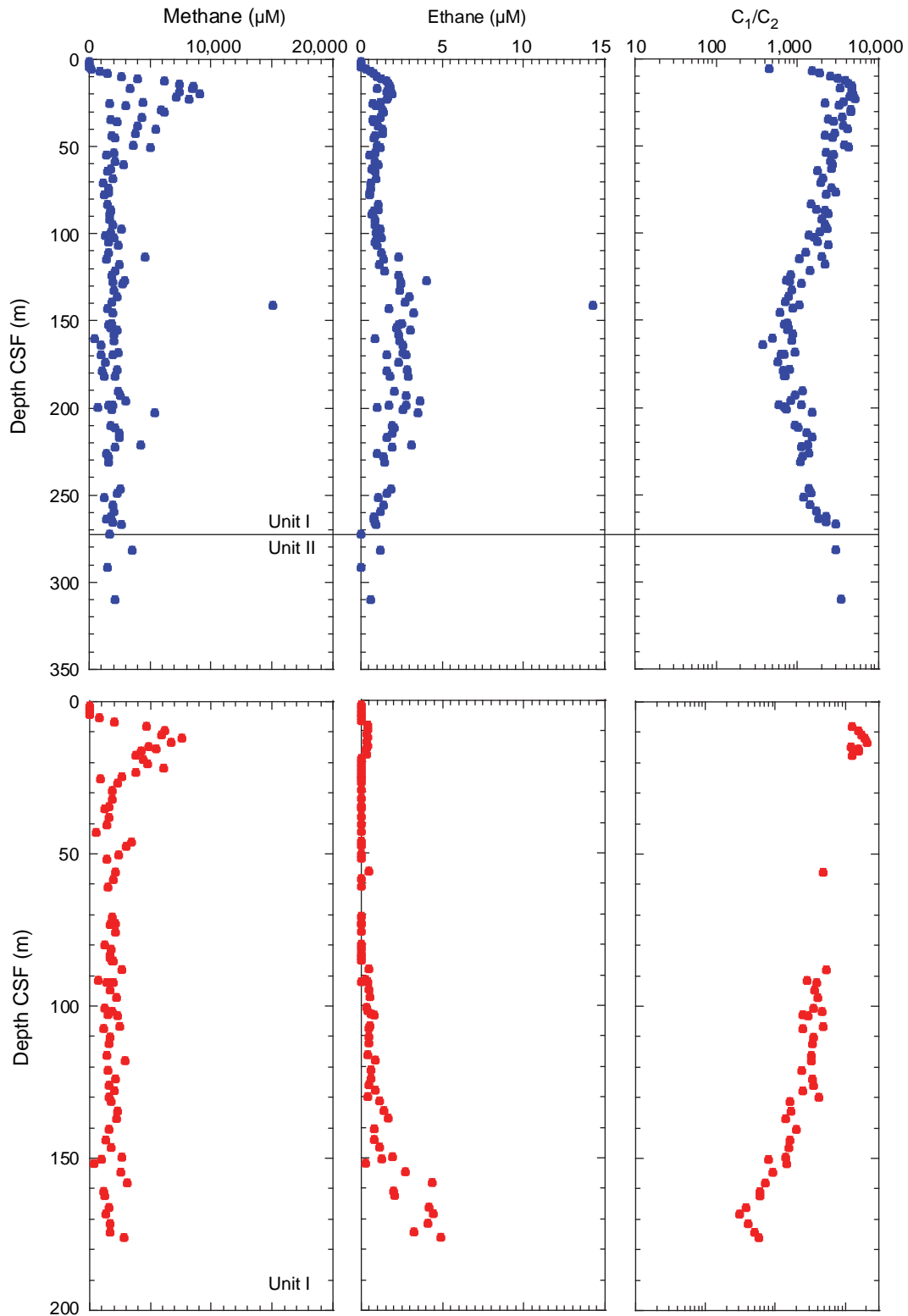


Figure F32. Calcium carbonate (CaCO_3), total organic carbon (TOC), total nitrogen (TN), carbon to nitrogen (C/N) ratio, and total sulfur (TS) in sediments, Site C0008. CSF = core depth below seafloor. Blue = Hole C0008A, red = Hole C0008C.

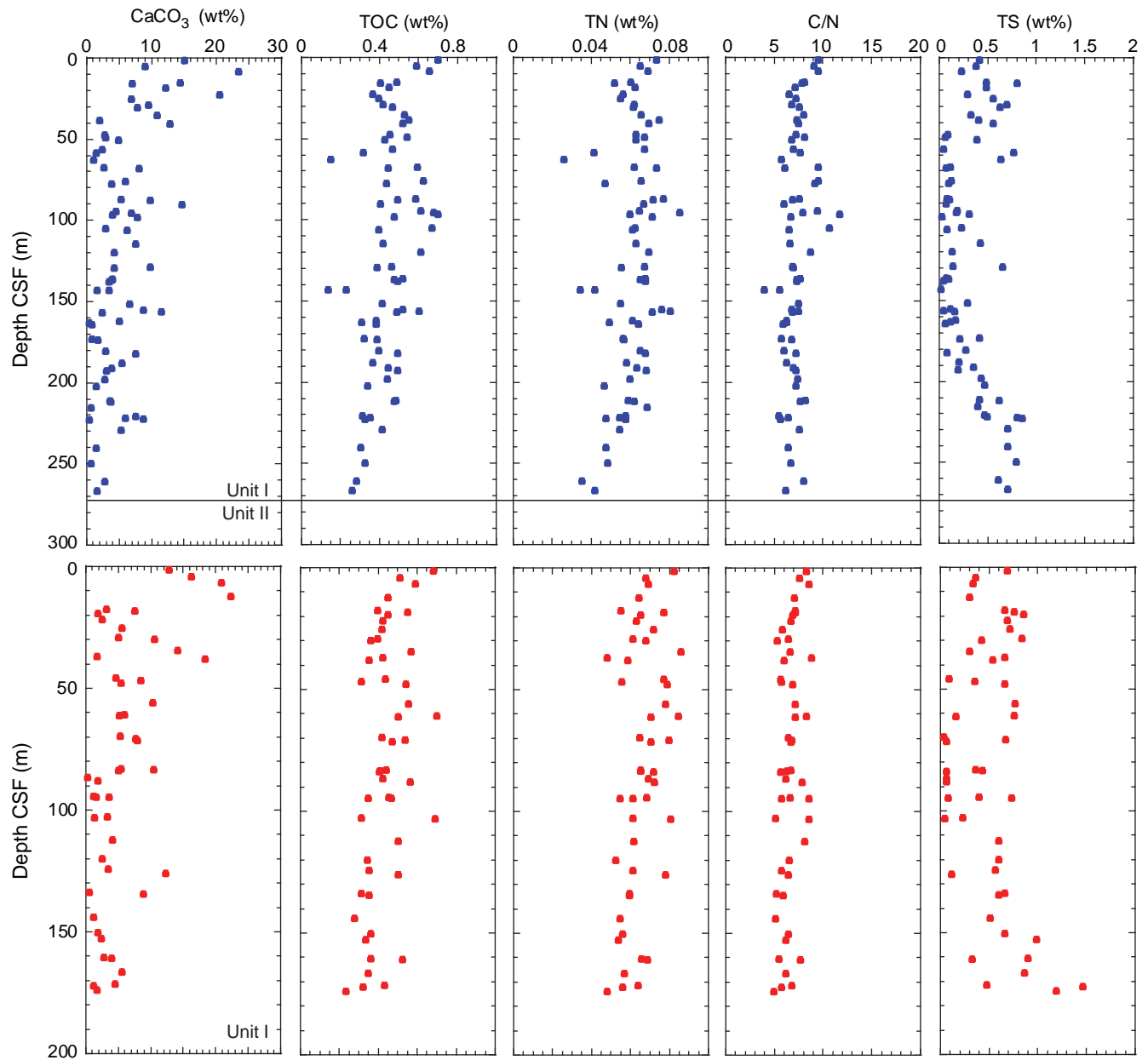


Figure F33. Microbial cell abundance enumerated by microscopic direct count of SYBR Green I-stained cells. Arrows = methane hydrate-bearing sediments. CSF = core depth below seafloor.

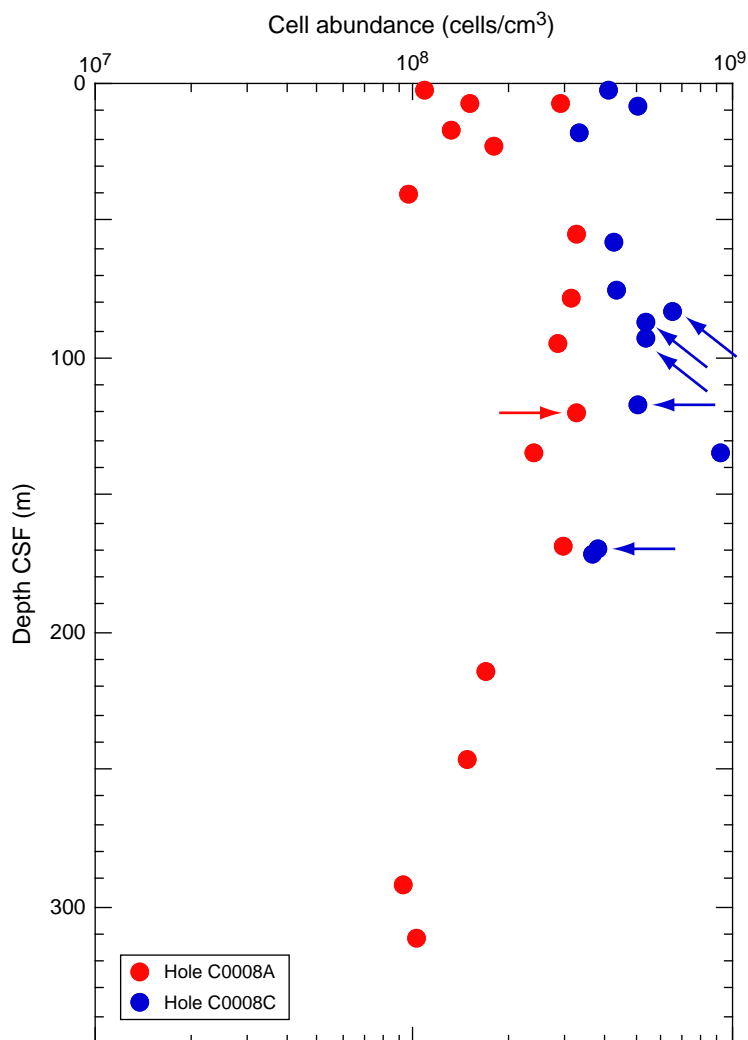




Figure F34. Density and porosity measurement results, Hole C0008A. **A.** Gamma ray attenuation (GRA) density measured using a multisensor core logger (MSCL) system on whole-round core sections (gray dots) and wet bulk density measured on discrete samples using MAD methods (red dots). **B.** Grain density measured on discrete samples using MAD methods. **C.** MSCL-derived porosity (gray dots) and MAD porosity (red dots). CSF = core depth below seafloor.

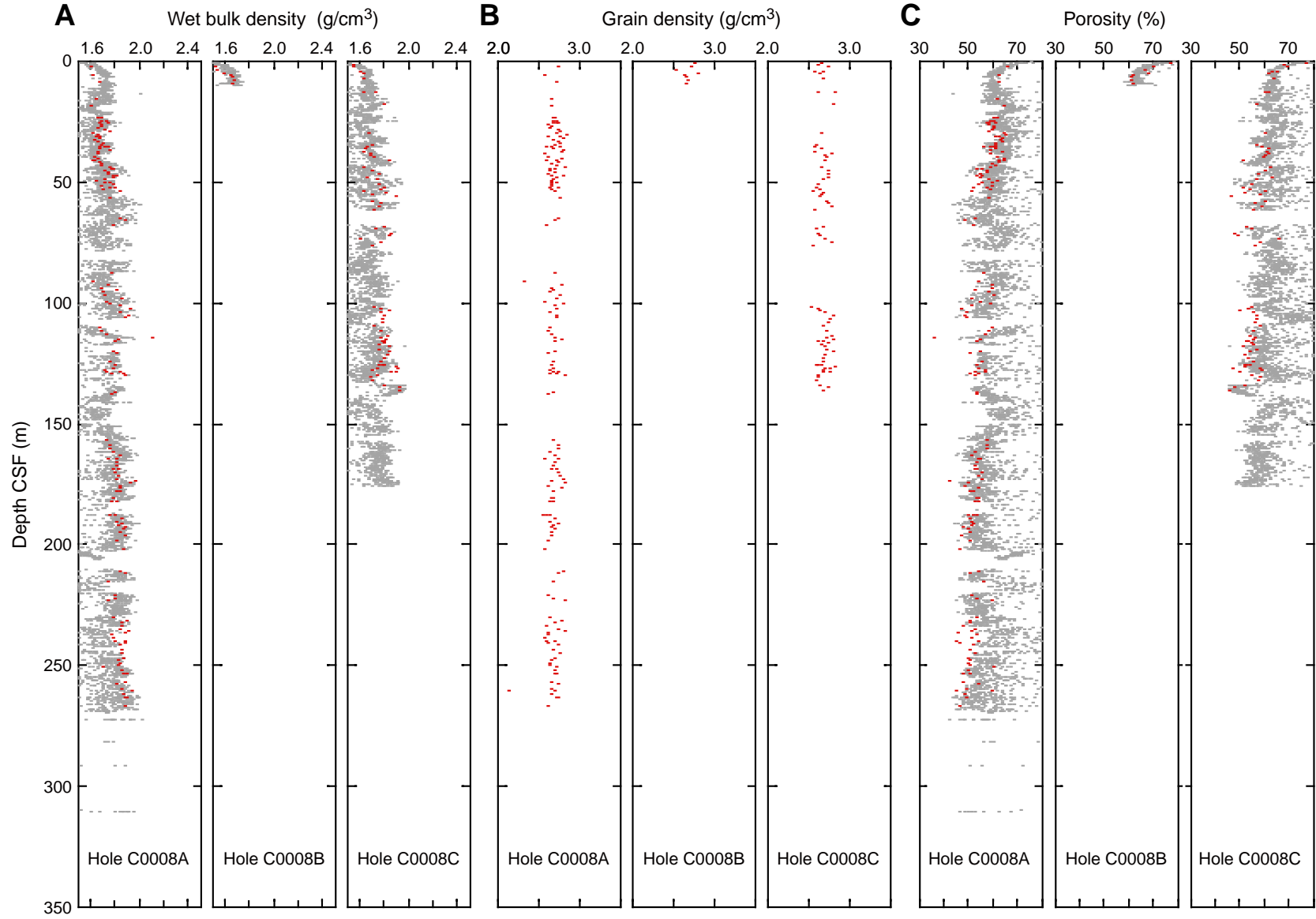




Figure F35. Measurements on discrete samples, Hole C0008A. **A.** *P*-wave velocity. Black crosses = individual measurements, black squares = measurements along core axis, red squares = average velocity per sample. **B.** *P*-wave velocity anisotropy. For transverse anisotropy, positive values equal lower magnitude along the core axis. **C.** Electrical conductivity. **D.** Electrical conductivity anisotropy. CSF = core depth below seafloor.

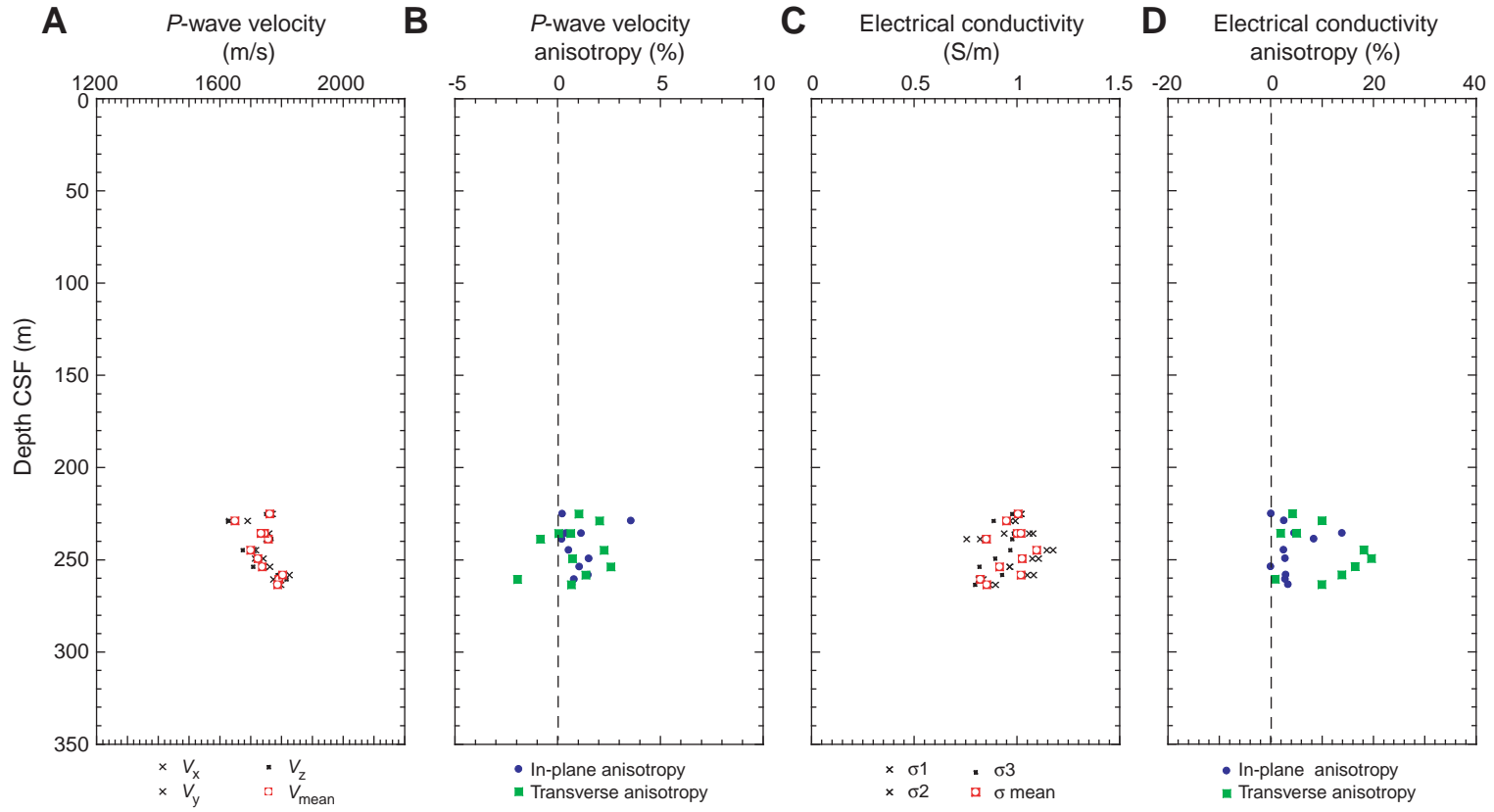


Figure F36. Thermal data, Hole C0008A. **A.** Thermal conductivity. **B.** Equilibrium temperatures (circles) and projected temperatures (line). The best-fit linear gradient to the equilibrium temperatures is 51°C/km. **C.** Temperature as a function of thermal resistance. The best-fit slope gives a heat flow value of 52 mW/m² and a bottom water temperature of 2.0°C. CSF = core depth below seafloor.

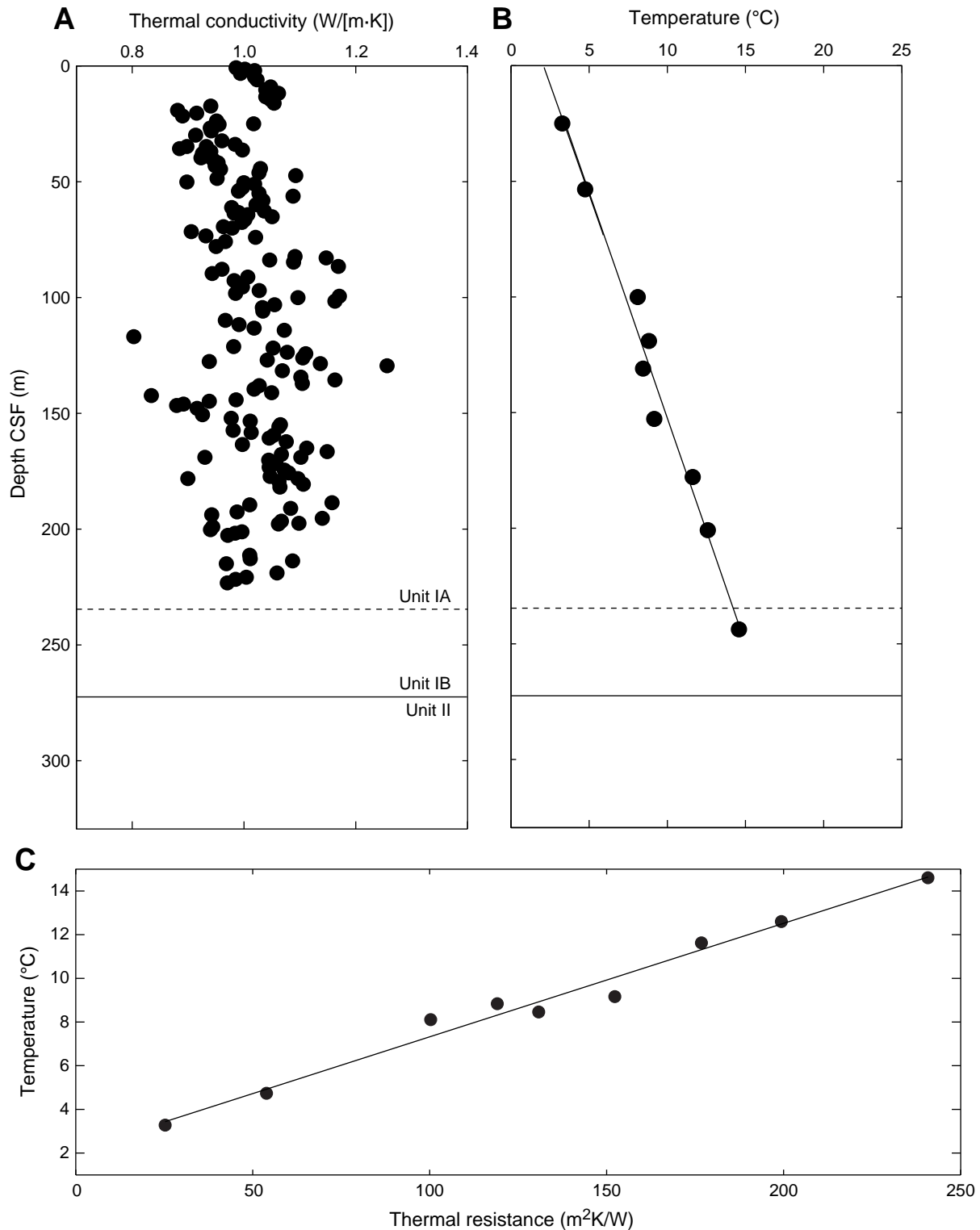


Figure F37. Thermal data, Hole C0008C. **A.** Thermal conductivity. **B.** Equilibrium temperatures (circles) and projected temperatures (line). The best-fit linear gradient to the equilibrium temperatures is 57°C/km. **C.** Temperature as a function of thermal resistance. The best-fit slope gives a heat flow value of 55 mW/m² and a bottom water temperature of 1.8°C. CSF = core depth below seafloor.

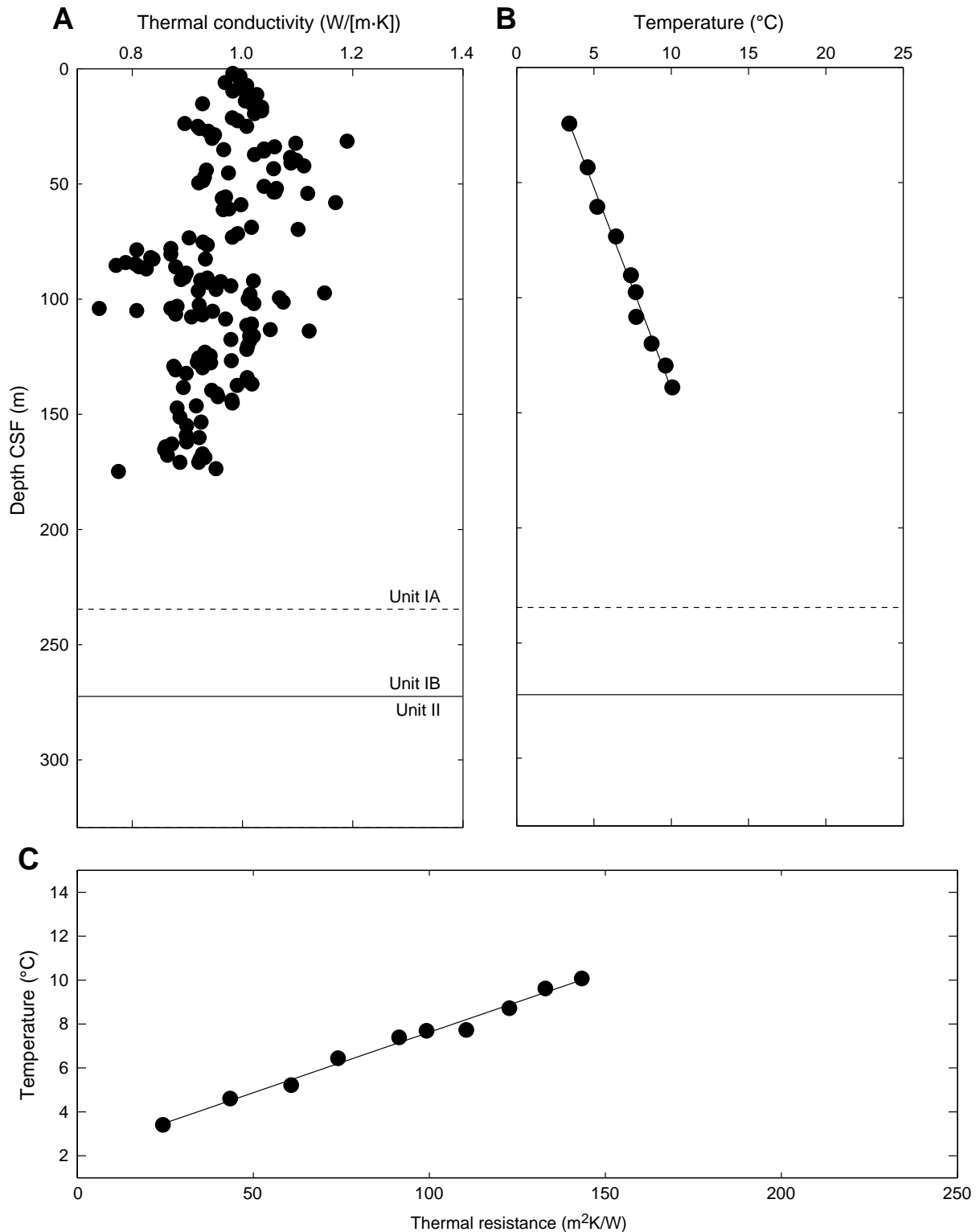


Figure F38. Temperature time series, Hole C0008A (blue line). APCT3 measurements at (A) 25.0 m core depth below seafloor (CSF), (B) 53.5 m CSF, and (C) 100.0 m CSF. Unshaded area = data used for equilibrium temperature fit, red line = theoretical equilibrium curve, triangle = beginning of fit, inverted triangle = end of fit, dashed red line with circles = estimate of equilibrium temperature. Note frictional heating at penetration (dashed vertical line) and at pull out. (**Continued on next two pages.**)

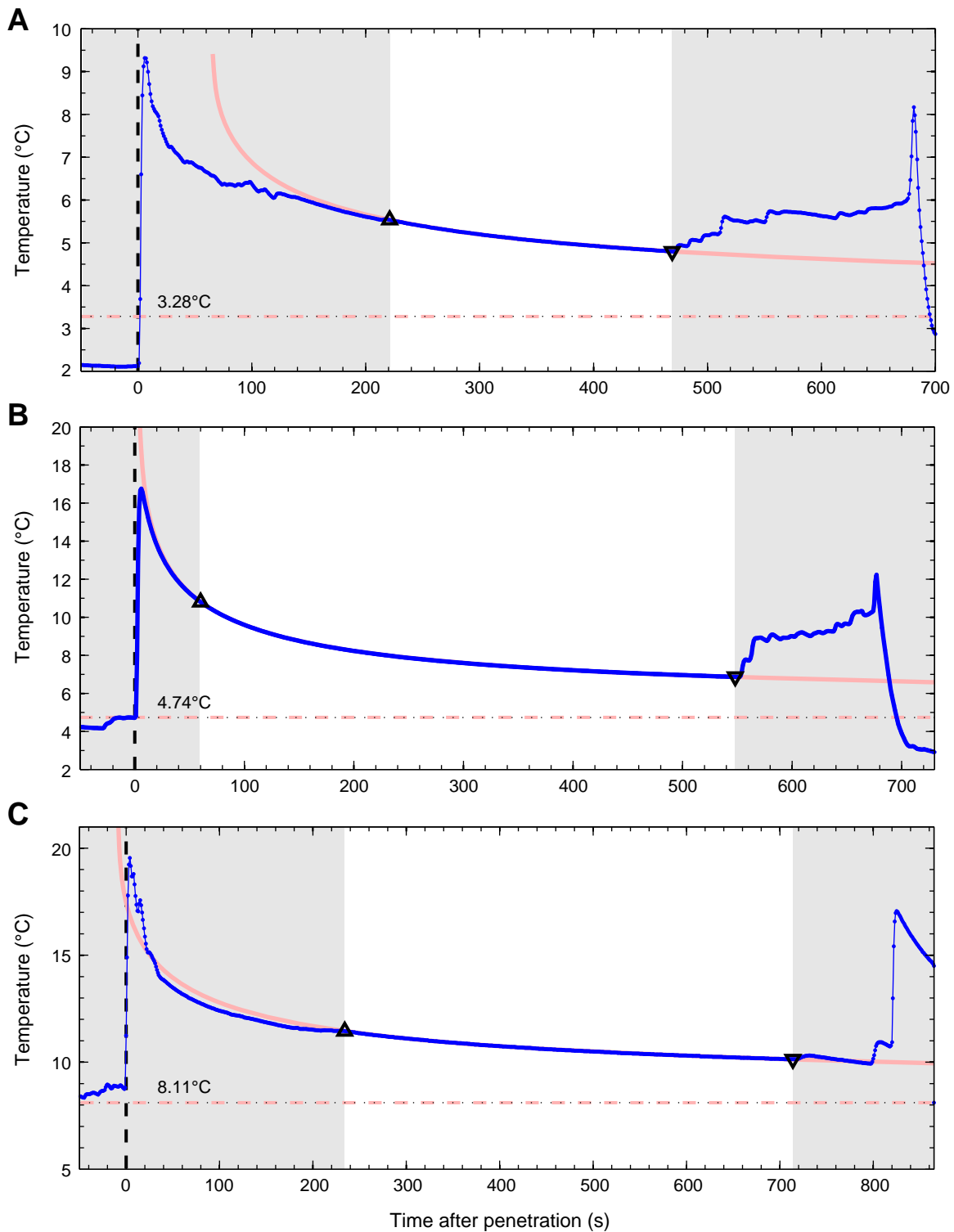


Figure F38 (continued). APCT3 measurements at (D) 119.0 m CSF, (E) 130.9 m CSF, and (F) 152.7 m CSF. (Continued on next page.)

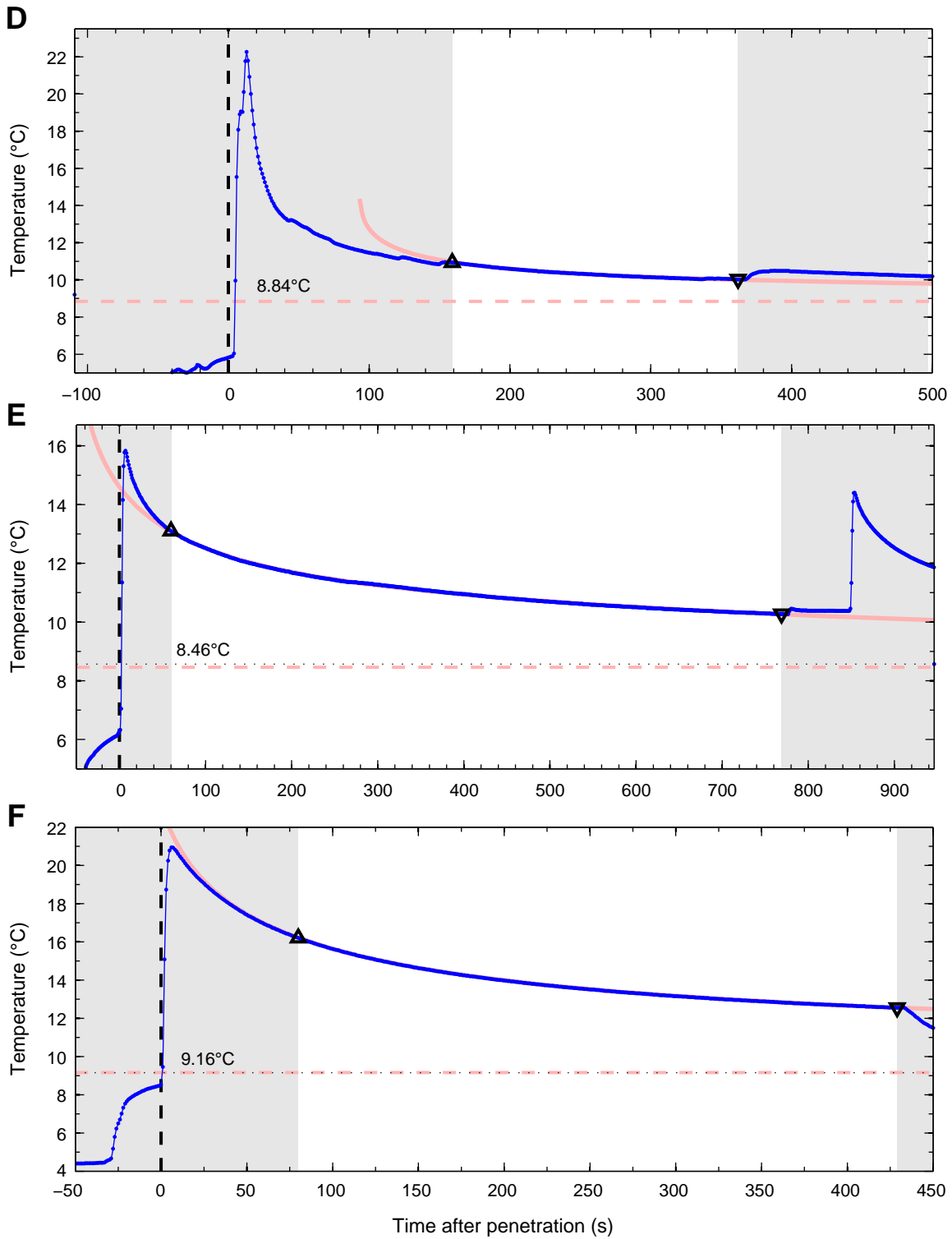


Figure F38 (continued). APCT3 measurements at (G) 177.7 m CSF and (H) 200.9 m CSF. SET tool measurements at (I) 243.8 m CSF.

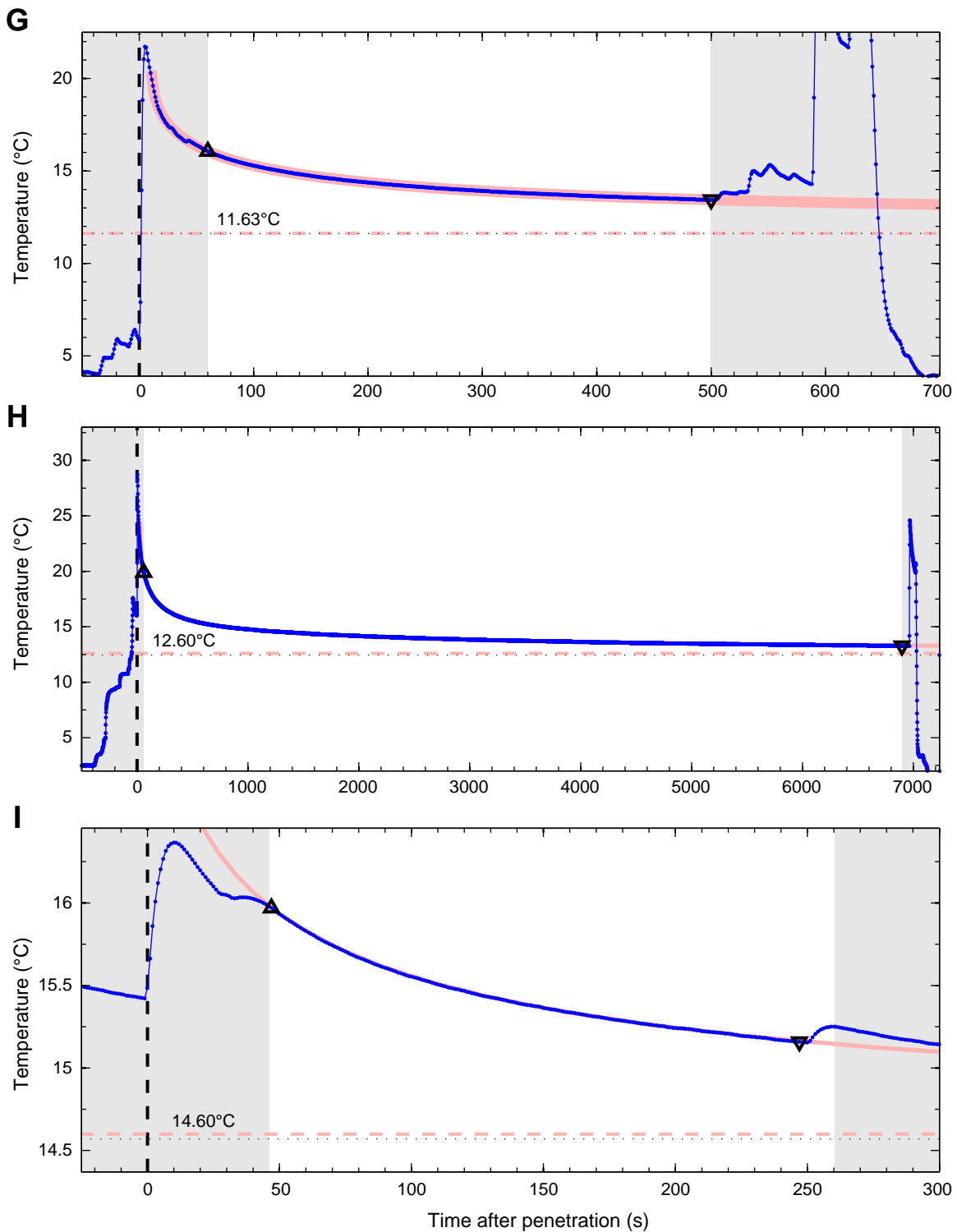


Figure F39. Temperature time series, Hole C0008C (blue line). APCT3 measurements at (A) 24.5 m core depth below seafloor (CSF), (B) 43.5 m CSF, and (C) 60.5 m CSF. Unshaded area = data used for equilibrium temperature fit, red line = theoretical equilibrium curve, triangle = beginning of fit, inverted triangle = end of fit, dashed red line with circles = estimate of equilibrium temperature. Note frictional heating at penetration (dashed vertical line) and at pull out. (**Continued on next three pages.**)

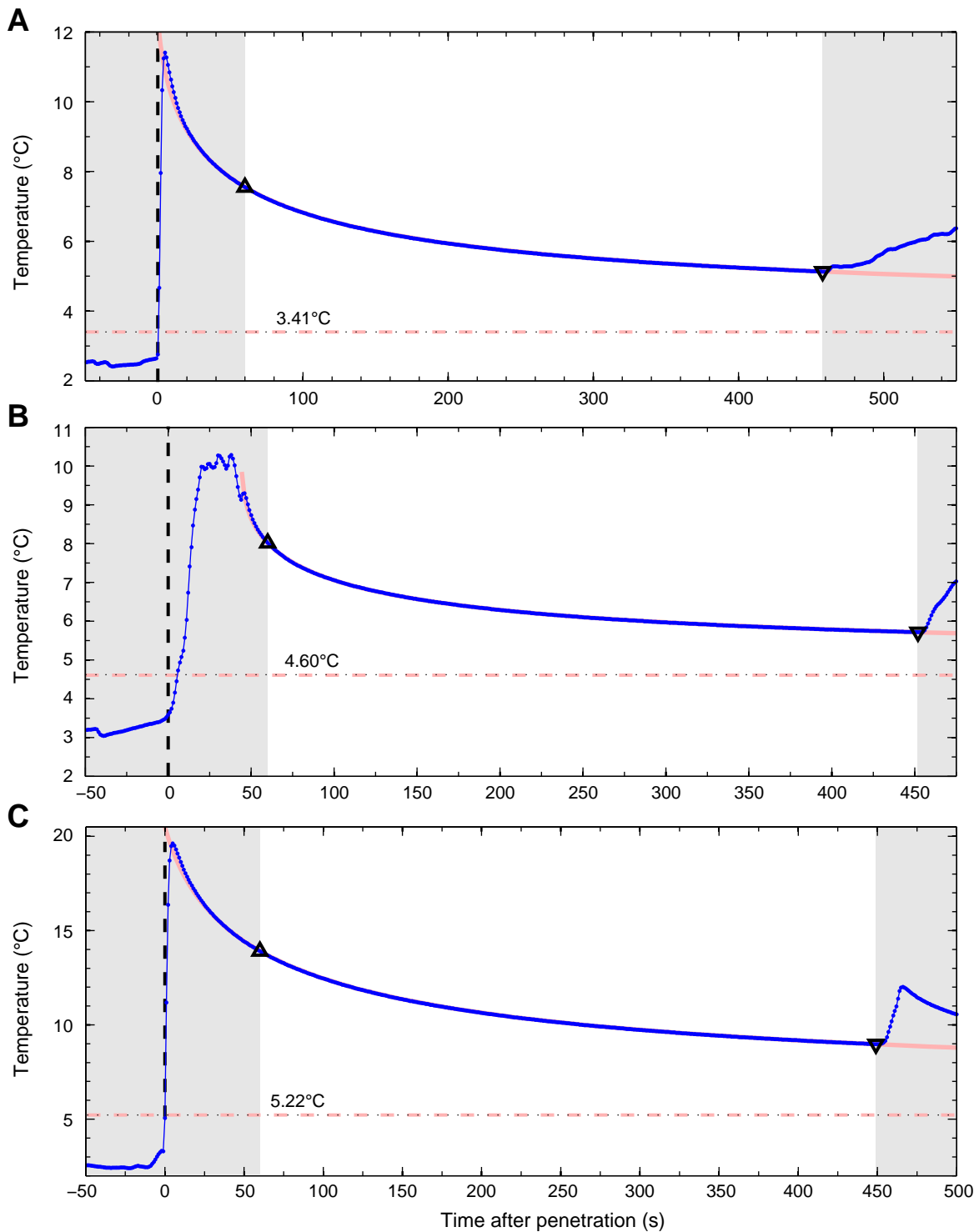


Figure F39 (continued). APCT3 measurements at (D) 73.5 m CSF, (E) 90.1 m CSF, and (F) 97.6 m CSF. (Continued on next page.)

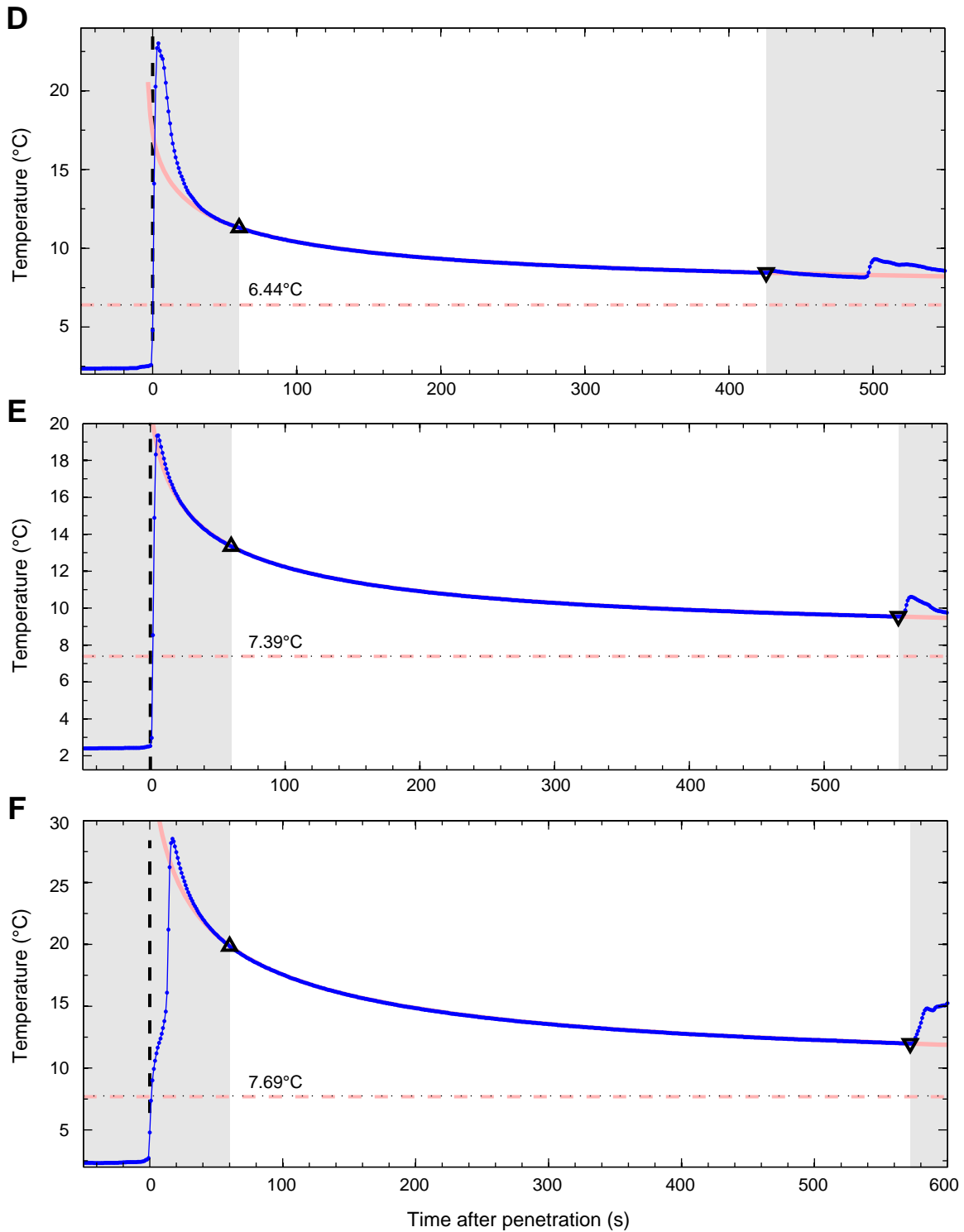


Figure F39 (continued). APCT3 measurements at (G) 108.3 m CSF, (H) 119.9 m CSF, and (I) 129.4 m CSF. (Continued on next page.)

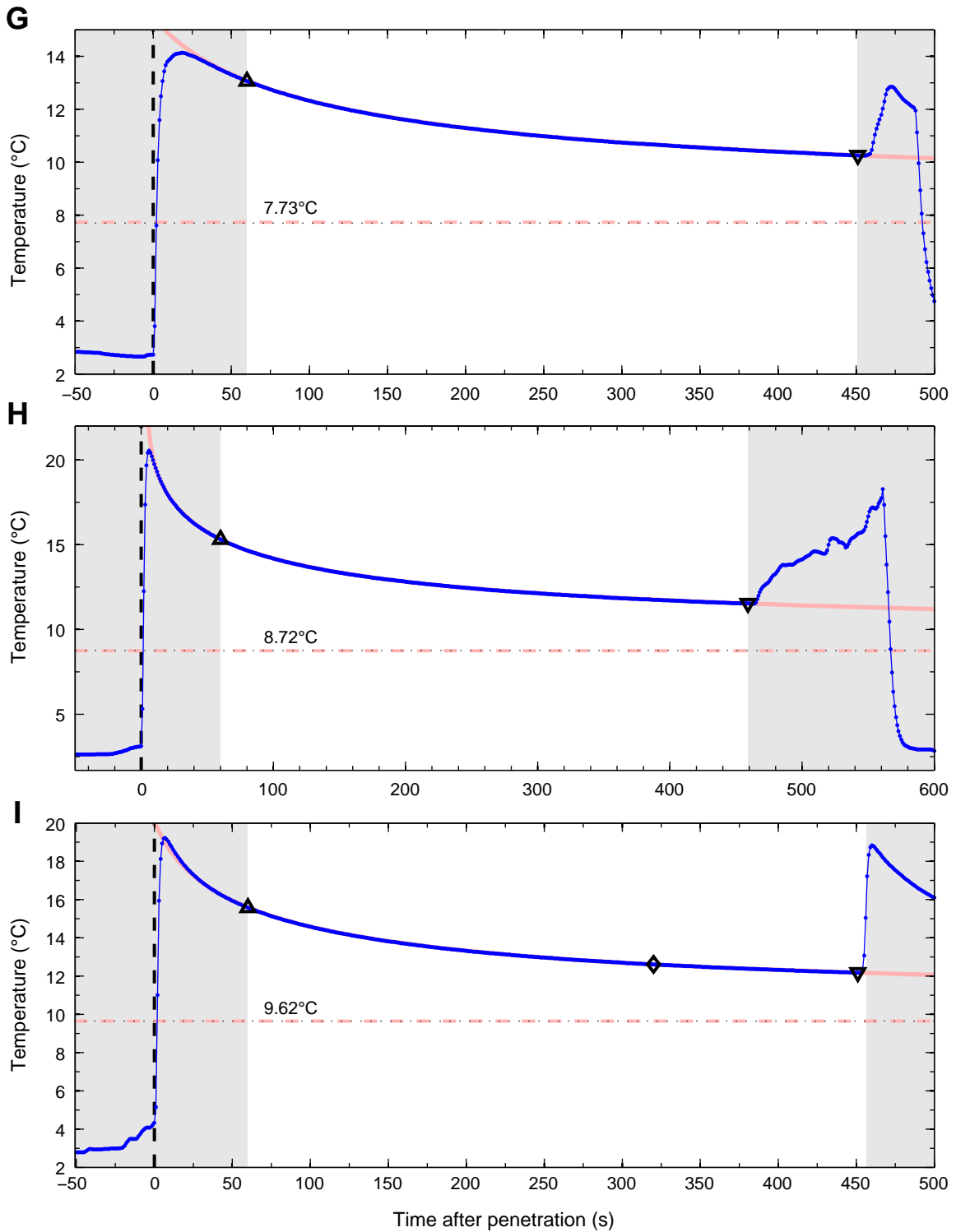


Figure F39 (continued). J. APCT3 measurements at 139.0 m CSF.

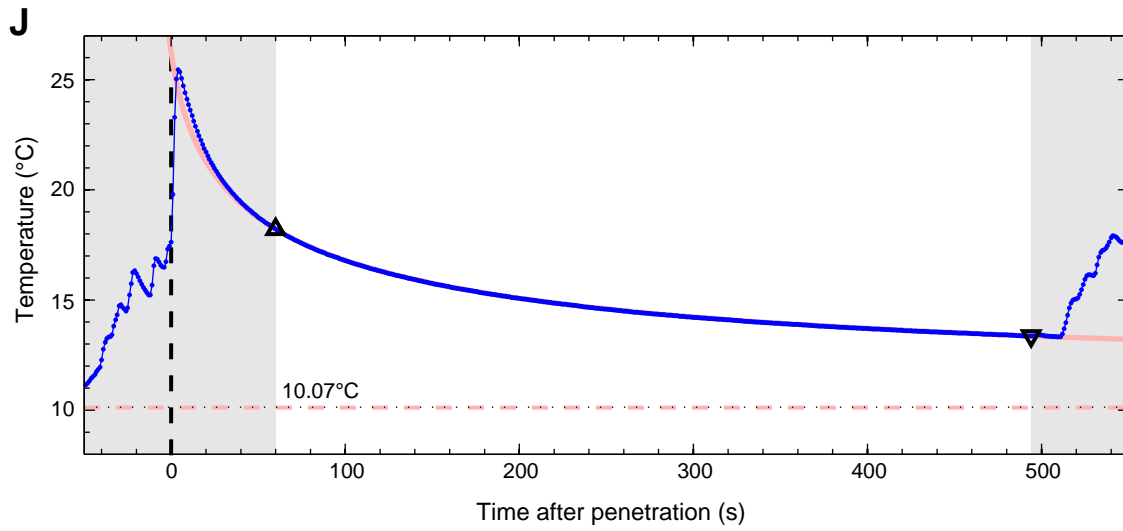


Figure F40. Shear strength at Holes C0008A and C0008C increases linearly along a trend of 0.45 kPa/m. Shear strength at Hole C0008C shows an apparent decrease in strength below a zone of poor core recovery from 60 to 70 m core depth below seafloor (CSF).

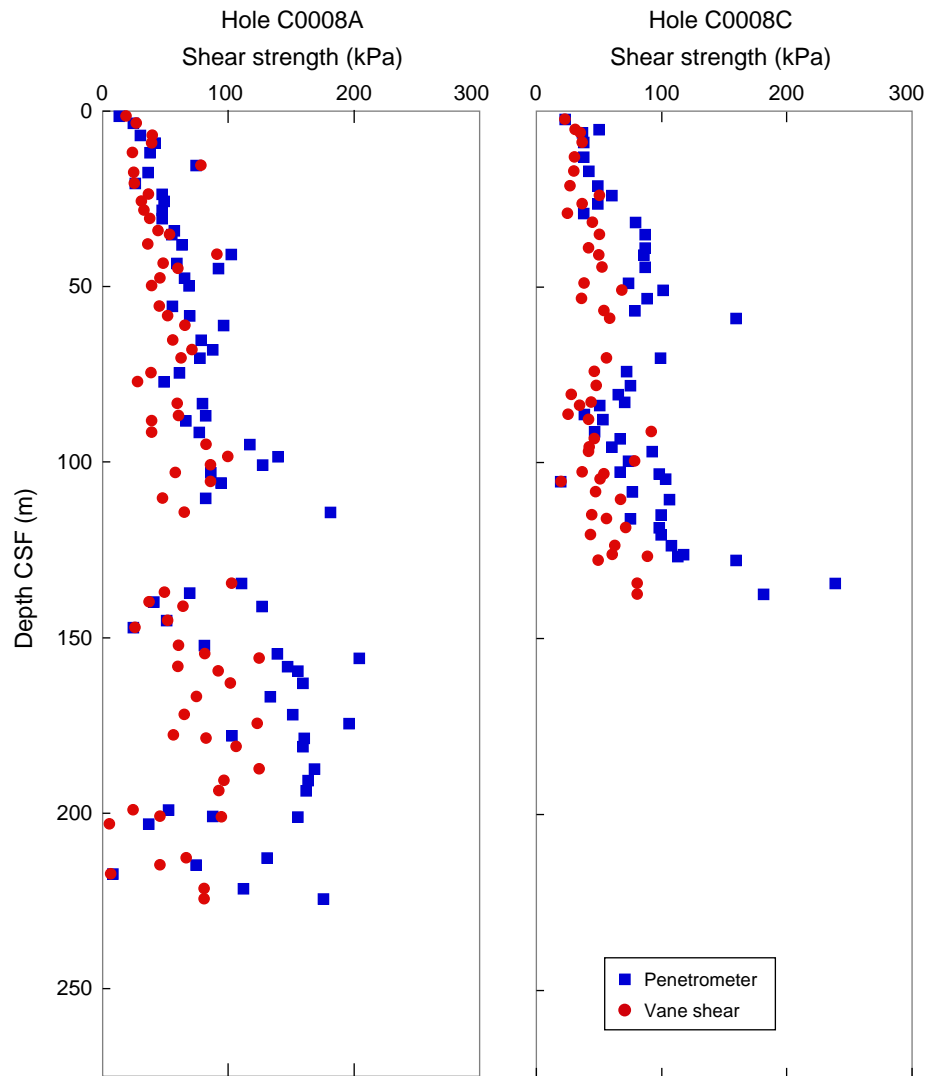


Figure F41. L*, a*, and b* values with depth, Hole C0008A. CSF = core depth below seafloor.

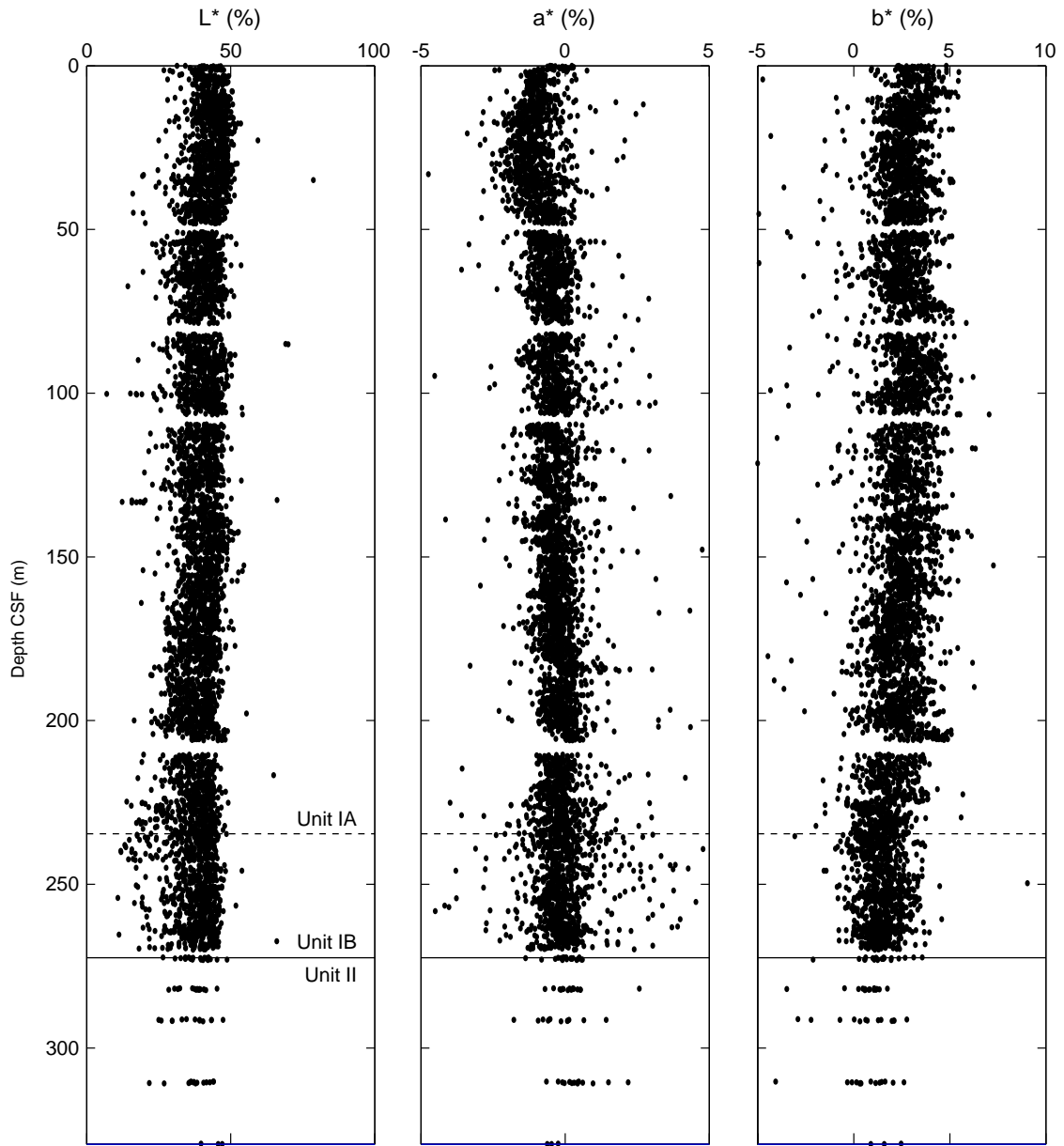


Figure F42. L*, a*, and b* values with depth, Hole C0008C. CSF = core depth below seafloor.

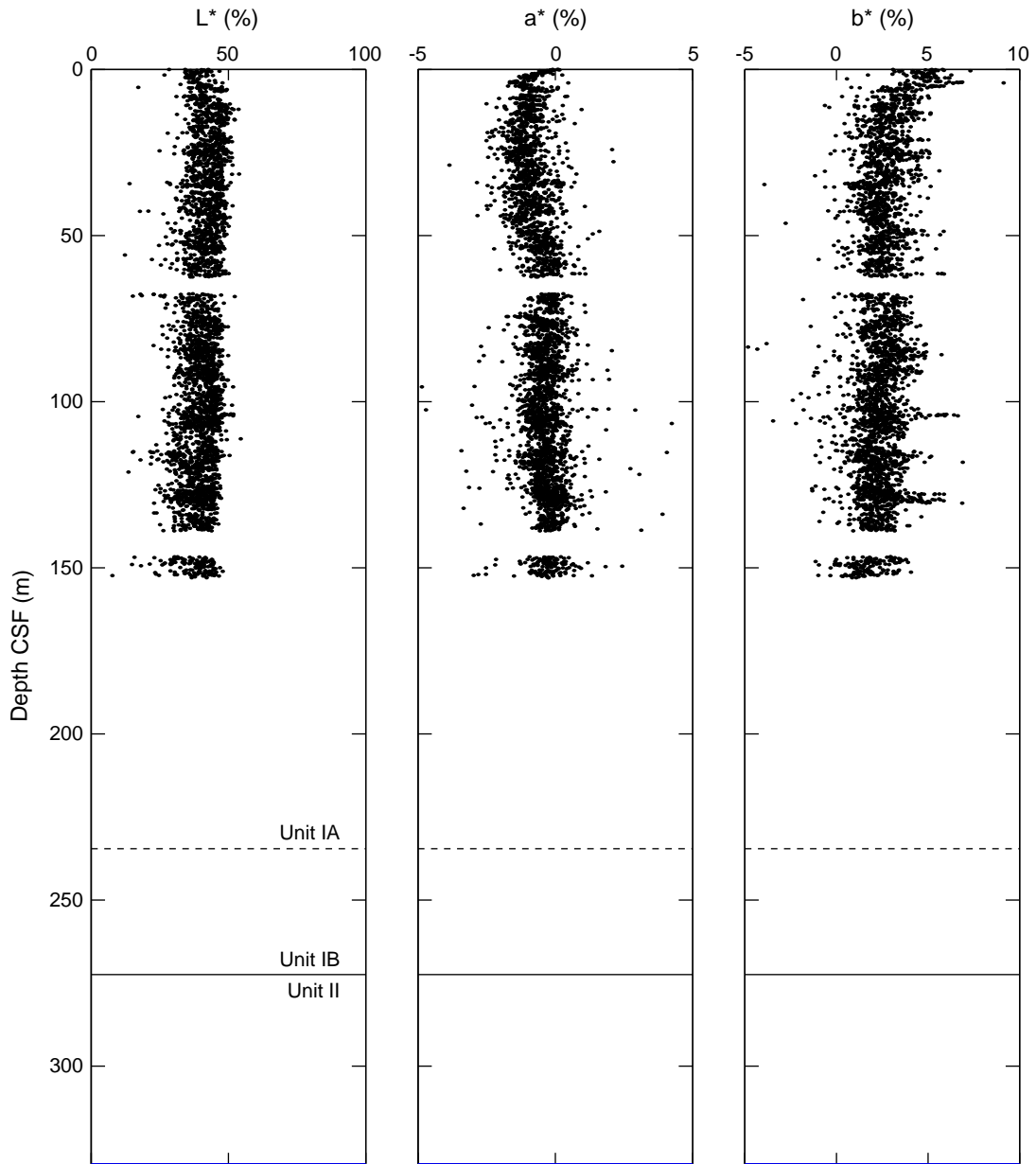


Figure F43. Magnetic susceptibility as a function of depth, Site C0008. A. Hole C0008A. B. Hole C0008C. CSF = core depth below seafloor.

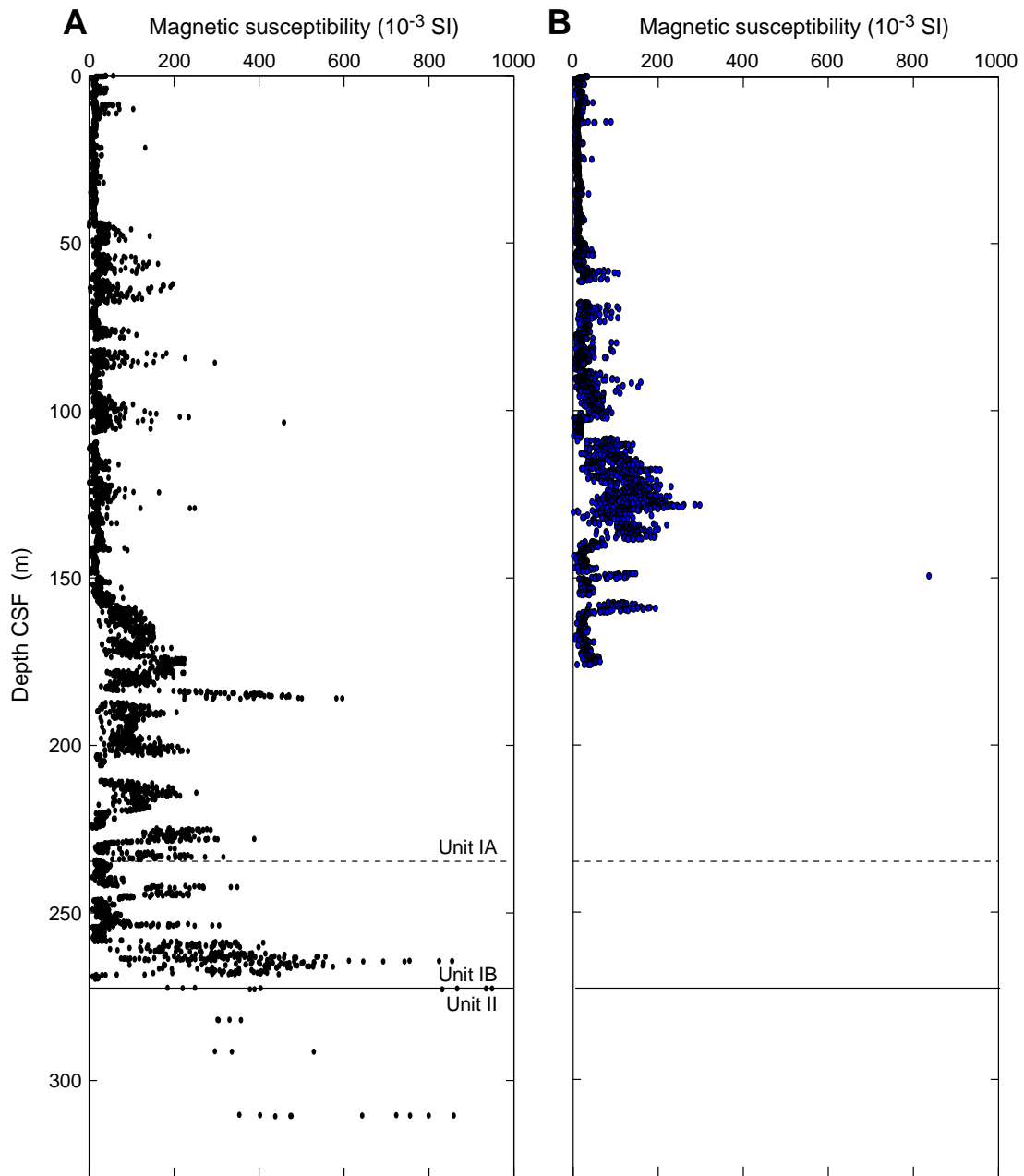


Figure F44. Natural gamma ray (NGR) values with depth, Site C0008. A. Hole C0008A B. Hole C0008C. CSF = core depth below seafloor. cps = counts per second.

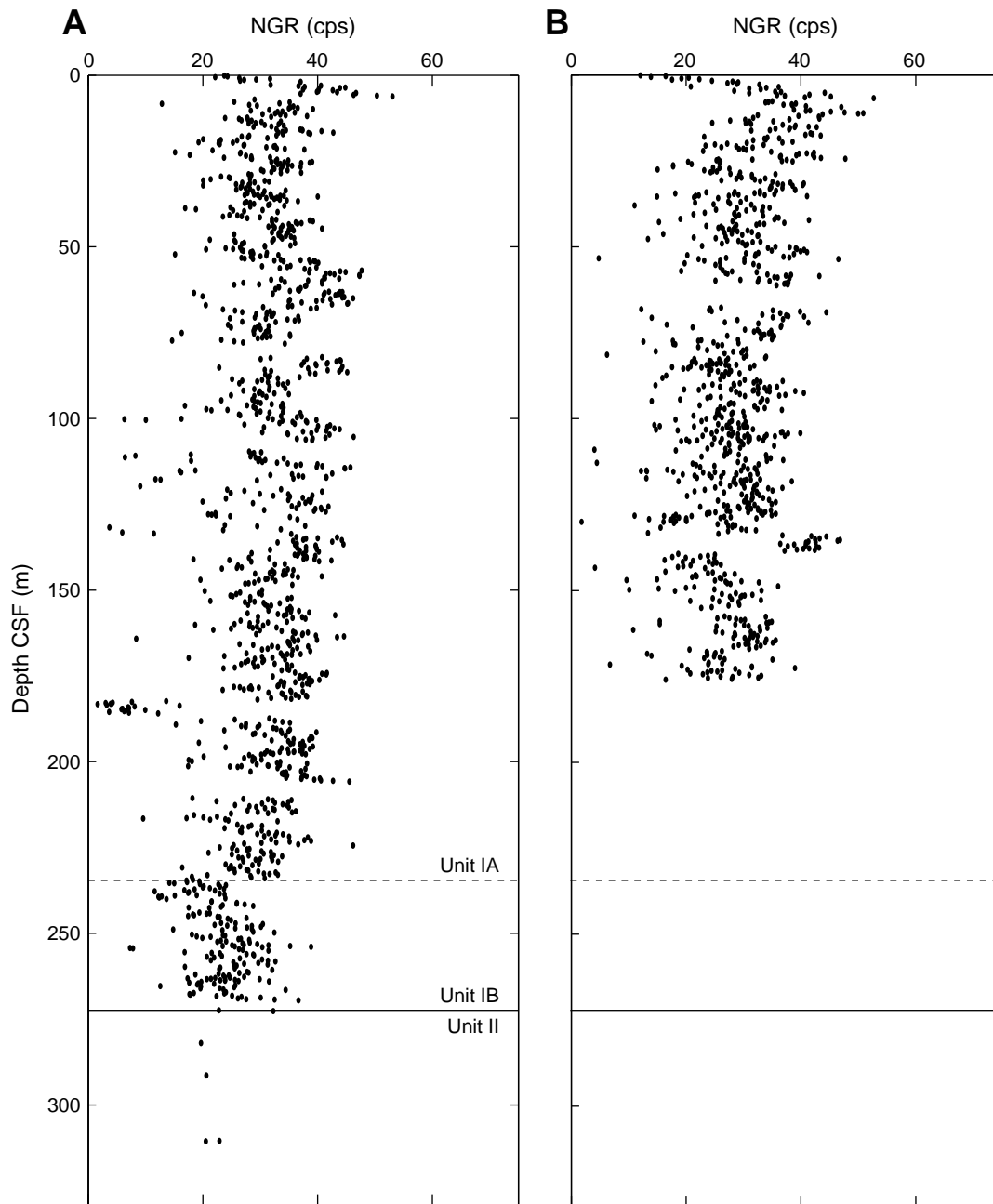




Figure F45. Natural gamma ray (NGR) counts from cores (MSCL-W) at all Site C0008 holes and Holes C0004C and C0004D. Numbers below holes are water depth (meters below mean sea level). For location of Inline 2675 see Figure F1. cps = counts per second. VE = vertical exaggeration.

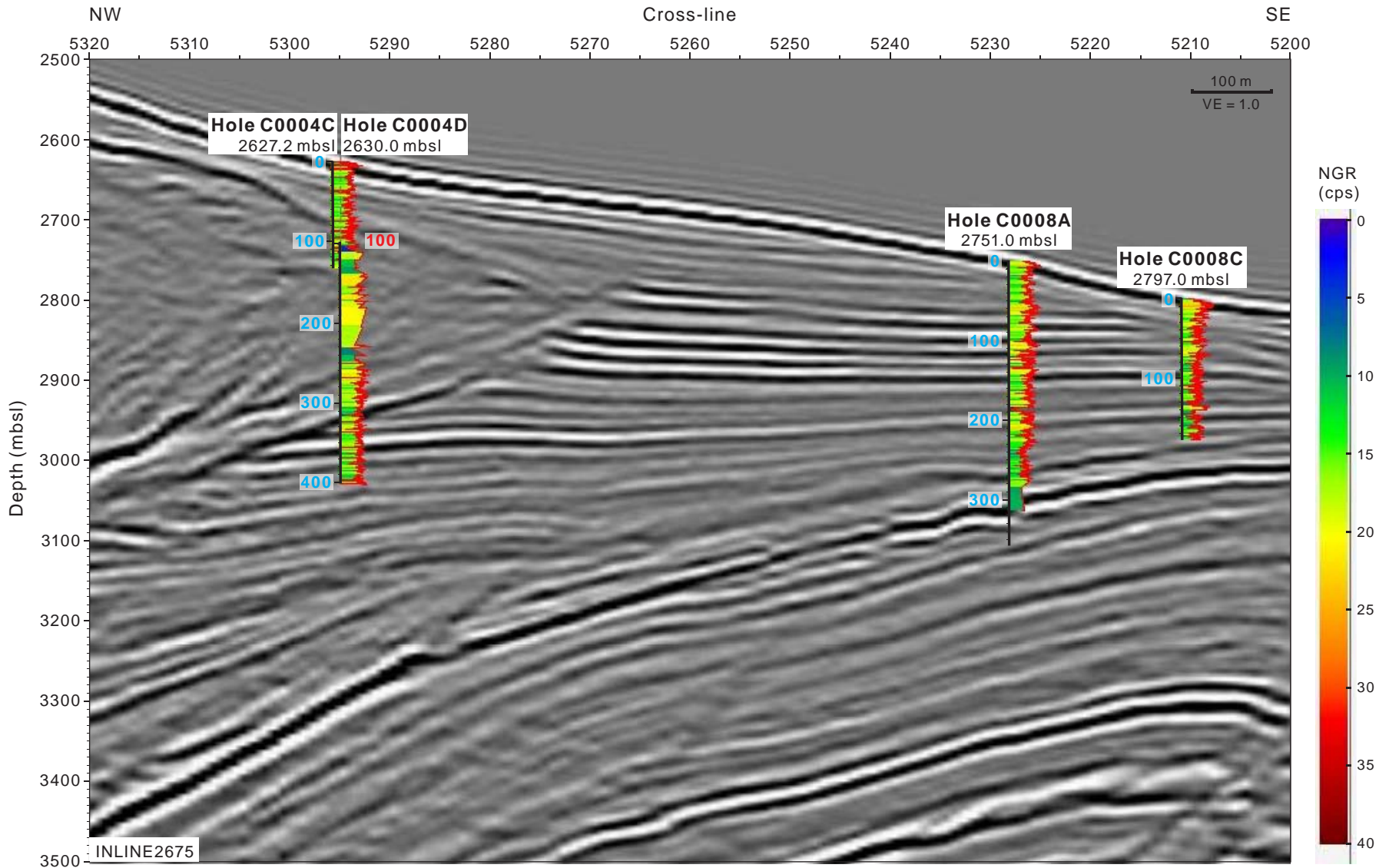


Table T1. Coring summary, Hole C0008A. (See table note.)

Hole C0008A										
Latitude: 33°12.8229'N										
Longitude: 136°43.5997'E										
Seafloor (drillers measurement from rig floor, m): 2779.50										
Distance between rig floor and sea level (m): 28.5										
Water depth (drillers measurement from sea level, m): 2751.0										
Total depth (drillers depth below rig floor, m): 3137.25										
Total penetration (core depth below seafloor, m): 357.75										
Total length of cored section (m): 357.8										
Total core recovered (m): 271.20										
Core recovery (%): 75.81										
Total number of cores: 43										
Core	Date (Jan 2008)	Local time		Depth DRF (m)		Depth CSF (m)		Advanced (m)	Recovered (m)	Recovery (%)
		Shot	On deck	Top	Bottom	Top	Bottom			
316-C0008A-										
1H	27	0315	0342	2779.50	2786.43	0.00	6.93	6.93	6.93	100.0
2H	27	0536	0606	2786.43	2795.00	6.93	15.50	8.57	9.93	115.8
3H	27	0707	0740	2795.00	2804.50	15.50	25.00	9.50	10.00	105.3
4H	27	0847	0918	2804.50	2814.00	25.00	34.50	9.50	10.32	108.6
5H	27	1040	1109	2814.00	2823.50	34.50	44.00	9.50	10.28	108.2
6H	27	1216	1254	2823.50	2833.00	44.00	53.50	9.50	10.45	110.0
7H	27	1334	1401	2833.00	2842.50	53.50	63.00	9.50	10.72	112.8
8H	27	1603	1631	2842.50	2852.00	63.00	72.50	9.50	9.53	100.3
9H	27	1733	1807	2852.00	2861.50	72.50	82.00	9.50	6.03	63.5
10H	27	1907	1935	2861.50	2870.00	82.00	90.50	8.50	8.50	100.0
11H	27	2120	2150	2870.00	2879.50	90.50	100.00	9.50	10.26	108.0
12H	27	2255	2321	2879.50	2889.00	100.00	109.50	9.50	6.32	66.5
13H	28	0108	0314	2889.00	2898.50	109.50	119.00	9.50	8.84	93.1
14H	28	0435	0500	2898.50	2899.06	119.00	119.56	0.56	0.56	100.0
15H	28	0607	0634	2899.06	2906.97	119.56	127.47	7.91	7.91	100.0
16H	28	0840	0925	2906.97	2910.39	127.47	130.89	3.42	2.60	76.0
17H	28	1039	1108	2910.39	2919.89	130.89	140.39	9.50	11.06	116.4
18H	28	1243	1307	2919.89	2929.39	140.39	149.89	9.50	8.62	90.7
19H	28	1423	1452	2929.39	2932.25	149.89	152.75	2.86	2.86	100.0
20H	28	1615	1636	2932.25	2938.23	152.75	158.73	5.98	5.98	100.0
21H	28	1752	1815	2938.23	2947.73	158.73	168.23	9.50	10.04	105.7
22H	28	2027	2100	2947.73	2957.23	168.23	177.73	9.50	10.43	109.8
23H	28	2154	2226	2957.23	2966.73	177.73	187.23	9.50	8.42	88.6
24H	28	2312	2335	2966.73	2976.23	187.23	196.73	9.50	10.55	111.1
25H	29	0242	0503	2976.23	2980.39	196.73	200.89	4.16	4.16	100.0
26H	29	0611	0719	2980.39	2989.89	200.89	210.39	9.50	5.17	54.4
27H	29	0835	0911	2989.89	2999.39	210.39	219.89	9.50	9.33	98.2
28H	29	1020	1135	2999.39	3004.25	219.89	224.75	4.86	4.86	100.0
29X	29	1318	1528	3004.25	3013.75	224.75	234.25	9.50	10.05	105.8
30X	29	1626	1847	3013.75	3023.25	234.25	243.75	9.50	8.56	90.1
31X	29	2344	0105	3023.25	3032.75	243.75	253.25	9.50	10.63	111.9
32X	30	0309	0415	3032.75	3042.25	253.25	262.75	9.50	11.32	119.2
33X	30	0614	0730	3042.25	3051.75	262.75	272.25	9.50	7.12	74.9
34X	30	0941	1055	3051.75	3061.25	272.25	281.75	9.50	0.98	10.3
35X	30	1206	1325	3061.25	3070.75	281.75	291.25	9.50	0.58	6.1
36X	30	1447	1614	3070.75	3080.25	291.25	300.75	9.50	0.56	5.9
37X	30	1723	1836	3080.25	3089.75	300.75	310.25	9.50	0.00	0.0
38X	30	1943	2114	3089.75	3099.25	310.25	319.75	9.50	0.64	6.7
39X	30	2205	2319	3099.25	3108.75	319.75	329.25	9.50	0.00	0.0
40X	31	0004	0134	3108.75	3118.25	329.25	338.75	9.50	0.11	1.2
41X	31	0250	0355	3118.25	3127.75	338.75	348.25	9.50	0.00	0.0
42X	31	0507	0617	3127.75	3137.25	348.25	357.75	9.50	0.00	0.0
43H	31	0840	0903	3137.25	3137.25	357.75	357.75	0.00	0.00	0.0

Note: DRF = drillers depth below rig floor, CSF = core depth below seafloor.

Table T2. Coring summary, Holes C0008B and C0008C. (See table note.)

Hole C0008B

Latitude: 33°12.7313'N
 Longitude: 136°43.6727'E
 Seafloor (drillers measurement from rig floor, m): 2825.5
 Distance between rig floor and sea level (m): 28.5
 Water depth (drillers measurement from sea level, m): 2797.0
 Total depth (drillers depth below rig floor, m): 2835.00
 Total penetration (core depth below seafloor, m): 9.50
 Total length of cored section (m): 9.5
 Total core recovered (m): 9.82
 Core recovery (%): 103.40
 Total number of cores: 1

Hole C0008C

Latitude: 33°12.7313'N
 Longitude: 136°43.6727'E
 Seafloor (drillers measurement from rig floor, m): 2825.5
 Distance between rig floor and sea level (m): 28.5
 Water depth (drillers measurement from sea level, m): 2797.0
 Total depth (drillers depth below rig floor, m): 3001.70
 Total penetration (core depth below seafloor, m): 176.20
 Total length of cored section (m): 176.2
 Total core recovered (m): 189.66
 Core recovery (%): 108.00
 Total number of cores: 25

Core	Date	Local time		Depth DRF (m)		Depth CSF (m)		Advanced (m)	Recovered (m)	Recovery (%)
		Shot	On deck	Top	Bottom	Top	Bottom			
316-C0008B-										
1H	31 Jan 2008	2234	2306	2824.80	2834.30	0.00	9.50	9.50	9.82	103.4
316-C0008C-										
1H	1 Feb 2008	0006	0029	2825.50	2831.01	0.00	5.51	5.50	5.51	100.0
2H	1 Feb 2008	0136	0159	2831.01	2840.51	5.51	15.01	9.50	9.94	104.6
3H	1 Feb 2008	0249	0321	2840.51	2850.01	15.01	24.51	9.50	10.29	108.3
4H	1 Feb 2008	0432	0458	2850.01	2859.51	24.51	34.01	9.50	11.14	117.3
5H	1 Feb 2008	0549	0624	2859.51	2869.01	34.01	43.51	9.50	9.83	103.5
6H	1 Feb 2008	0806	0835	2869.01	2878.51	43.51	53.01	9.50	10.21	107.5
7H	1 Feb 2008	0920	0953	2878.51	2886.01	53.01	60.51	7.50	9.86	131.5
8H	1 Feb 2008	1108	1136	2886.01	2893.01	60.51	67.51	7.00	0.00	0.0
9H	1 Feb 2008	1225	1302	2893.01	2902.51	67.51	77.01	9.50	9.55	100.5
10H	1 Feb 2008	1345	1412	2902.51	2908.01	77.01	82.51	5.50	9.58	174.2
11H	1 Feb 2008	1522	1556	2908.01	2915.61	82.51	90.11	7.60	10.68	140.5
12H	1 Feb 2008	1632	1659	2915.61	2916.76	90.11	91.26	1.20	1.15	100.0
13H	1 Feb 2008	1800	1836	2916.76	2923.09	91.26	97.59	6.30	6.33	100.0
14H	1 Feb 2008	1943	2006	2923.09	2927.19	97.59	101.69	4.10	9.88	241.0
15H	1 Feb 2008	2055	2127	2927.19	2933.79	101.69	108.29	6.60	6.60	100.0
16H	1 Feb 2008	2224	2248	2933.79	2940.09	108.29	114.59	6.30	10.15	161.1
17H	1 Feb 2008	2332	0013	2940.09	2945.39	114.59	119.89	5.30	2.90	54.7
18H	2 Feb 2008	0238	0306	2945.39	2950.89	119.89	125.39	5.50	9.66	175.6
19H	2 Feb 2008	0417	0450	2950.89	2954.89	125.39	129.39	4.00	1.54	38.5
20H	2 Feb 2008	0617	0647	2954.89	2955.60	129.39	130.10	0.70	0.71	100.0
21H	2 Feb 2008	0811	0858	2955.60	2964.60	130.10	139.10	9.00	8.80	97.8
22X	2 Feb 2008	1154	1340	2964.60	2974.10	139.10	148.60	9.50	9.74	102.5
23X*	2 Feb 2008	1444	1559	2974.10	2982.78	148.60	157.28	8.70	6.88	79.3
24X*	2 Feb 2008	1720	1831	2982.78	2992.29	157.28	166.79	9.50	9.48	99.7
25X*	2 Feb 2008	1938	2035	2992.29	3001.70	166.79	176.20	9.40	9.25	98.3

Note: DRF = drillers depth below rig floor, CSF = core depth below seafloor.

Table T3. Summary of lithologic units, Hole C0008A. (See table note.)

Unit	Core, section, interval (cm)		Depth CSF (m)		Thickness (m)	Stratigraphic age	Lithologic description	Processes of formation
	Top	Bottom	Top	Bottom				
IA	316-C0008A-1H-1, 0	316-C0008A-29X-CC, 35	0.00	234.55	234.55	Pleistocene	Nannofossil-rich mud, thin sand layers, and volcanic ash layers	Hemipelagic settling, thin-bedded turbidites, and volcanic ash falls
IB	29X-CC, 35	34X-1, 22	234.55	272.46	37.91	Pleistocene to Pliocene	Mud and interbedded mudclast gravel layers	Mass movement deposition and hemipelagic settling
II	34X-1, 22	40X-CC, 11	272.46	329.36	56.90	Pliocene	Sand layers and minor mud	Thick-bedded sandy turbidites

Note: CSF = core depth below seafloor.

Table T4. Summary of lithologic units, Hole C0008C. (See table note.)

Unit	Core, section, interval (cm)		Depth CSF (m)		Thickness (m)	Stratigraphic age	Lithologic description	Processes of formation
	Top	Bottom	Top	Bottom				
IA	316-C0008C-1H-1, 0	316-C0008C-25X-7, 124	0.00	170.90	170.9	Pleistocene	Nannofossil-rich mud, thin sand layers, and volcanic ash layers	Hemipelagic settling, thin-bedded turbidites, and volcanic ash falls
IB	25X-7, 124	25X-CC, 21	170.90	176.20	5.3	Pleistocene	Mud and interbedded mudclast gravel layers	Mass movement deposition and hemipelagic settling

Note: CSF = core depth below seafloor.



Table T5. XRD data, Holes C0008A and C0008C. (See table notes.) (Continued on next two pages.)

Unit	Core, section, interval (cm)	Core type	Depth CSF (m)	Peak intensity (counts/step)				Integrated peak area (total counts)				Abundance calculated from SVD normalization factor										
				Clay	Quartz	Plagioclase	Calcite	Clay	Quartz	Plagioclase	Calcite	Calculated abundance (wt%)			Normalized abundance (wt%)							
												Clay	Quartz	Plagioclase	Corrected calcite	Absolute total	Clay	Quartz	Plagioclase	Calcite	Relative total	
316-C0008A-																						
IA	1H-3, 0-1.5	WR	1.64	60	893	171	443	2,664	28,578	10,662	16,090	33.5	16.0	12.4	17.8	17.8	79.6	42.0	20.1	15.6	22.3	100
	1H-7, 0-1.5	WR	5.43	73	1,128	262	322	2,106	36,213	15,441	10,769	30.8	20.3	18.8	10.8	10.8	80.8	38.2	25.2	23.3	13.4	100
	2H-2, 0-1.5	WR	8.35	52	842	169	643	1,408	27,488	10,688	23,875	21.4	15.6	12.8	28.9	28.9	78.7	27.2	19.8	16.3	36.7	100
	2H-8, 0-1.5	WR	15.43	44	839	170	481	2,129	28,716	11,820	19,804	29.1	16.1	14.1	23.0	23.0	82.4	35.4	19.5	17.2	27.9	100
	3H-1, 55-56.5	WR	16.05	64	974	205	225	2,935	35,665	14,524	8,794	38.3	19.9	17.3	7.7	7.7	83.2	46.0	23.9	20.8	9.2	100
	3H-3, 0-1.5	WR	18.41	62	880	192	321	2,937	27,956	12,364	12,624	37.3	15.5	14.7	13.0	13.0	80.5	46.3	19.2	18.3	16.2	100
	3H-8, 0-1.5	WR	22.98	61	789	176	464	2,580	26,552	11,489	18,698	33.4	14.8	13.7	21.3	21.3	83.2	40.2	17.8	16.4	25.6	100
	3H-10, 98.5-100	WR	25.40	66	1,162	260	238	2,767	37,411	15,837	8,208	37.5	20.9	19.1	7.0	7.0	84.4	44.4	24.7	22.6	8.2	100
	4H-4, 0-1.5	WR	29.18	69	902	189	264	3,117	30,005	12,475	10,663	39.0	16.6	14.7	10.3	10.3	80.6	48.3	20.7	18.3	12.7	100
	4H-6, 32.5-34	WR	30.89	55	997	203	268	3,208	30,676	13,295	9,276	40.4	17.0	15.8	8.3	8.3	81.5	49.5	20.8	19.4	10.2	100
	4H-9, 59-60.5	WR	35.20	63	1,238	280	342	2,448	39,590	15,859	12,122	34.4	22.2	19.1	12.2	12.2	88.0	39.1	25.3	21.7	13.9	100
	5H-4, 0-1.5	WR	38.72	81	1,135	211	117	3,466	37,630	14,860	2,338	43.4	20.9	17.6	-1.2	0.0	82.0	53.0	25.6	21.4	0.0	100
	5H-6, 72-73.5	WR	40.76	60	608	148	370	2,620	21,714	9,739	12,380	32.5	12.0	11.5	13.2	13.2	69.2	47.0	17.3	16.6	19.1	100
	6H-3, 59-60.5	WR	47.35	62	1,296	268	122	2,867	41,969	16,450	3,906	38.5	23.5	19.7	1.1	1.1	82.9	46.5	28.4	23.8	1.3	100
	6H-5, 0-1.5	WR	49.27	64	1,219	228	109	3,713	37,207	13,721	3,624	45.1	20.7	16.0	0.3	0.3	82.1	54.9	25.2	19.4	0.4	100
	6H-6, 100-101.5	WR	50.50	97	915	214	168	3,297	28,795	11,851	6,376	40.2	15.9	13.9	4.6	4.6	74.6	53.9	21.3	18.6	6.1	100
	7H-3, 28-29.5	WR	56.46	76	1,191	229	102	3,496	39,377	17,026	3,069	45.3	21.9	20.5	-0.4	0.0	87.6	51.7	25.0	23.4	0.0	100
	7H-5, 0-1.5	WR	58.63	78	2,033	427	62	1,407	61,467	28,585	1,836	31.9	34.7	35.9	-1.6	0.0	102.5	31.1	33.9	35.0	0.0	100
	7H-8, 113-114.5	WR	62.75	46	2,324	762	53	1,380	69,290	39,978	1,305	39.5	38.8	51.1	-2.9	0.0	129.5	30.5	30.0	39.5	0.0	100
	8H-4, 72-73.5	WR	67.66	62	977	230	121	2,634	35,230	14,865	2,862	35.3	19.7	17.9	0.2	0.2	73.1	48.3	26.9	24.5	0.2	100
	8H-5, 0-1.5	WR	68.25	62	893	184	255	3,453	31,342	11,685	8,402	41.5	17.4	13.5	7.0	7.0	79.5	52.3	21.9	17.0	8.9	100
	9H-3, 107-108.5	WR	76.19	60	1,263	243	175	2,624	42,759	14,679	5,569	34.9	24.1	17.3	3.5	3.5	79.8	43.7	30.2	21.7	4.4	100
	9H-5, 0-1.5	WR	77.56	43	1,634	368	132	2,189	50,434	23,568	3,490	36.6	28.3	29.3	0.5	0.5	94.7	38.6	29.9	30.9	0.6	100
	10H-6, 0-1.5	WR	87.23	60	1,019	212	191	3,529	35,663	14,844	5,674	44.3	19.8	17.6	3.2	3.2	84.9	52.2	23.3	20.8	3.7	100
	10H-7, 31.5-33	WR	87.83	83	868	220	315	3,017	30,481	13,318	8,852	38.5	16.9	15.9	7.9	7.9	79.2	48.6	21.3	20.1	10.0	100
	10H-8, 125-126.5	WR	90.17	73	814	147	487	3,025	27,658	10,755	14,976	37.1	15.4	12.5	16.1	16.1	81.0	45.8	19.0	15.4	19.9	100
	11H-4, 0-1.5	WR	94.73	63	1,472	269	117	2,400	48,032	16,286	4,552	33.5	27.2	19.3	2.1	2.1	82.1	40.8	33.1	23.5	2.6	100
	11H-5, 49-50.5	WR	95.50	83	927	183	179	4,096	33,806	10,717	6,351	47.0	18.8	11.9	3.8	3.8	81.5	57.7	23.0	14.6	4.7	100
	11H-6, 28-29.5	WR	96.47	59	1,743	360	161	1,954	51,771	21,775	4,931	32.9	29.2	26.8	2.6	2.6	91.6	36.0	31.9	29.3	2.8	100
	11H-7, 31.5-33	WR	98.02	79	939	213	355	2,828	33,451	14,492	11,207	37.4	18.6	17.4	11.0	11.0	84.5	44.3	22.1	20.6	13.0	100
	12H-5, 0-1.5	WR	104.92	70	1,446	301	95	2,697	48,020	20,227	2,662	39.3	26.9	24.7	-0.7	0.0	90.9	43.2	29.7	27.1	0.0	100
	12H-6, 98.5-100	WR	106.18	70	929	232	224	3,284	31,619	14,645	6,569	41.9	17.5	17.6	4.7	4.7	81.7	51.4	21.4	21.6	5.7	100
	13H-5, 0-1.5	WR	114.79	67	1,101	216	222	2,985	35,078	14,317	6,544	38.6	19.6	17.1	4.7	4.7	80.0	48.3	24.5	21.4	5.9	100
	15H-2, 0-1.5	WR	120.14	63	1,043	215	108	3,319	37,371	14,829	3,088	42.0	20.8	17.6	-0.1	0.0	80.4	52.2	25.9	21.9	0.0	100
	16H-4, 0-1.5	WR	128.82	74	1,025	235	312	3,611	33,618	14,716	10,658	45.3	18.6	17.5	9.7	9.7	91.1	49.7	20.4	19.2	10.6	100
	16H-5, 33.5-35	WR	129.44	71	1,295	375	168	1,958	43,525	25,263	5,752	36.0	24.2	32.0	3.8	3.8	96.0	37.5	25.2	33.3	4.0	100
	17H-6, 0-1.5	WR	136.14	62	1,157	259	106	3,517	40,815	14,953	3,766	43.9	22.8	17.5	0.5	0.5	84.8	51.8	26.9	20.7	0.6	100
	17H-7, 21.5-23	WR	136.63	76	1,204	275	100	3,232	38,639	16,506	3,010	42.3	21.5	19.9	-0.2	0.0	83.7	50.6	25.7	23.7	0.0	100
	17H-8, 23.5-25	WR	137.97	86	1,150	255	127	3,172	37,530	14,445	3,350	40.3	20.9	17.1	0.3	0.3	78.7	51.2	26.6	21.7	0.4	100
	18H-3, 0-1.5	WR	143.02	54	341	107	110	2,909	12,554	9,589	3,191	35.3	6.5	11.7	1.3	1.3	54.8	64.4	11.9	21.3	2.3	100
	18H-3, 25.5-27	WR	143.27	63	656	143	137	2,764	23,491	11,409	4,643	34.7	12.9	13.7	2.9	2.9	64.2	54.1	20.1	21.3	4.5	100
	19H-2, 0-1.5	WR	151.38	67	833	218	253	3,410	28,970	15,288	8,584	43.9	15.9	18.6	7.3	7.3	85.5	51.3	18.5	21.7	8.5	100
	20H-3, 0-1.5	WR	155.11	71	901	189	302	3,028	30,026	13,879	10,789	39.1	16.6	16.7	10.4	10.4	82.8	47.2	20.1	20.1	12.6	100
	20H-4, 94.5-96	WR	156.33	60	902	220	292	3,046	29,075	13,383	10,066	38.9	16.1	16.0	9.5	9.5	80.6	48.3	19.9	19.9	11.8	100
	20H-5, 34.5-36	WR	157.05	73	974	172	80	3,841	32,999	13,363	3,247	46.3	18.2	15.6	-0.1	0.0	80.2	57.8	22.7	19.5	0.0	100



Table T5 (continued). (Continued on next page.)

Unit	Core, section, interval (cm)	Core type	Depth CSF (m)	Peak intensity (counts/step)				Integrated peak area (total counts)				Abundance calculated from SVD normalization factor										
				Clay	Quartz	Plagioclase	Calcite	Clay	Quartz	Plagioclase	Calcite	Calculated abundance (wt%)				Normalized abundance (wt%)						
												Clay	Quartz	Plagioclase	Calcite	Corrected calcite	Absolute total	Clay	Quartz	Plagioclase	Calcite	Relative total
	21H-3, 80–81.5	WR	162.34	61	725	202	138	3,985	29,680	15,180	4,714	49.3	16.2	18.2	1.7	1.7	85.4	57.7	18.9	21.3	2.0	100
	21H-4, 48–49.5	WR	163.42	73	950	201	48	3,685	30,340	13,482	1,396	44.9	16.7	16.0	-2.3	0.0	77.6	57.9	21.5	20.6	0.0	100
	21H-5, 26–27.5	WR	164.38	78	1,097	201	60	4,178	34,602	15,508	1,126	51.0	19.0	18.4	-3.2	0.0	88.5	57.7	21.5	20.8	0.0	100
	22H-5, 68.5–70	WR	173.19	59	1,012	238	111	3,373	30,714	15,995	3,956	43.7	16.8	19.5	1.1	1.1	81.2	53.9	20.7	24.0	1.4	100
	22H-6, 0–1.5	WR	173.62	65	1,206	276	107	3,587	38,446	17,949	2,943	46.9	21.3	21.7	-0.6	0.0	89.9	52.1	23.7	24.2	0.0	100
	23H-3, 40–41.5	WR	180.75	63	992	243	107	3,209	35,074	15,294	4,071	41.4	19.5	18.4	1.3	1.3	80.5	51.4	24.2	22.8	1.6	100
	23H-5, 0–1.5	WR	182.04	52	918	204	180	3,322	32,054	14,397	6,927	42.1	17.7	17.2	5.1	5.1	82.2	51.3	21.6	21.0	6.2	100
	24H-2, 23.5–25	WR	187.92	68	930	217	216	3,106	32,064	14,960	6,302	40.4	17.7	18.1	4.4	4.4	80.6	50.1	22.0	22.4	5.5	100
	24H-4, 83–84.5	WR	191.14	64	1,107	239	144	3,227	35,932	16,699	4,257	42.6	19.9	20.2	1.5	1.5	84.2	50.6	23.6	24.0	1.7	100
	24H-6, 0–1.5	WR	192.78	67	1,127	264	109	2,988	37,291	17,715	3,542	40.9	20.7	21.6	0.6	0.6	83.8	48.7	24.7	25.8	0.7	100
	25H-1, 50–52	W	197.23	78	1,178	244	87	3,577	37,146	16,579	3,533	45.9	20.6	19.9	0.2	0.2	86.6	53.0	23.8	23.0	0.3	100
	25H-2, 0–1.5	WR	198.21	61	1,107	287	112	2,878	36,160	18,321	4,177	40.3	20.0	22.6	1.6	1.6	84.4	47.7	23.7	26.7	1.8	100
	26H-1, 24–26	W	201.13	71	840	241	52	2,850	27,999	16,230	1,912	38.8	15.3	20.1	-1.1	0.0	74.2	52.3	20.6	27.1	0.0	100
	26H-3, 33–35	W	201.18	63	1,056	236	205	2,794	33,317	15,495	6,191	37.6	18.5	18.8	4.4	4.4	79.4	47.4	23.3	23.7	5.6	100
	26H-2, 0–1.5	WR	202.21	60	1,228	356	59	2,480	37,291	22,127	2,041	39.0	20.6	27.8	-1.1	0.0	87.4	44.6	23.6	31.9	0.0	100
	27H-1, 68–69.5	WR	211.07	72	1,290	311	164	2,826	40,354	18,516	4,586	39.7	22.5	22.6	2.0	2.0	86.8	45.7	25.9	26.1	2.3	100
	27H-2, 35–36.5	WR	212.05	68	911	244	116	2,740	30,096	17,576	4,078	38.7	16.5	21.9	1.7	1.7	78.8	49.1	21.0	27.8	2.2	100
	27H-5, 0–1.5	WR	215.64	67	1,163	323	50	2,403	36,973	20,176	1,033	36.8	20.5	25.2	-2.3	0.0	82.5	44.6	24.8	30.6	0.0	100
	28H-1, 88.5–90	WR	220.78	71	1,018	225	245	3,062	31,275	16,086	7,779	40.9	17.2	19.7	6.4	6.4	84.1	48.6	20.5	23.4	7.6	100
	28H-2, 83–84.5	WR	222.03	62	1,011	209	216	3,067	30,737	13,919	6,731	39.3	17.0	16.7	5.1	5.1	78.1	50.3	21.8	21.4	6.5	100
	28H-3, 0–1.5	WR	222.22	52	945	195	239	3,071	30,541	13,477	9,626	39.2	16.9	16.1	8.9	8.9	81.1	48.3	20.9	19.9	11.0	100
	28H-4, 51–52.5	WR	223.03	78	962	223	41	4,268	32,189	14,510	1,355	51.3	17.6	17.1	-2.9	0.0	86.1	59.6	20.5	19.9	0.0	100
	29X-5, 0–33	WR	229.25	67	1,196	369	159	2,113	38,586	22,538	6,743	35.8	21.4	28.4	5.2	5.2	90.9	39.4	23.6	31.3	5.8	100
IB	30X-7, 0–36	WR	240.16	56	793	271	89	2,775	26,292	18,901	2,540	40.1	14.2	23.9	-0.2	0.0	78.2	51.3	18.2	30.5	0.0	100
	31X-6, 0–1.5	WR	249.92	62	1,029	265	46	2,658	33,548	19,108	1,152	38.7	18.5	23.8	-2.2	0.0	81.0	47.8	22.8	29.4	0.0	100
	32X-7, 0–1.5	WR	260.72	85	994	308	84	3,160	31,547	18,321	2,152	43.2	17.3	22.7	-1.2	0.0	83.2	51.9	20.8	27.3	0.0	100
	33X-4, 0–1.5	WR	266.70	46	942	443	107	1,721	28,397	31,800	3,731	39.0	15.1	41.8	1.6	1.6	97.4	40.0	15.5	42.9	1.6	100
II	34X-CC, 14–15	W	272.98	49	937	283	84	2,914	27,678	17,856	3,104	40.7	15.1	22.3	0.4	0.4	78.4	51.8	19.2	28.5	0.5	100
	36X-1, 10–11	W	291.35	66	873	234	62	3,624	28,387	16,414	2,006	46.6	15.4	20.1	-1.5	0.0	82.1	56.7	18.8	24.5	0.0	100
	38X-1, 7–8	W	310.32	75	1,044	238	52	3,972	35,258	17,793	1,466	50.7	19.3	21.6	-2.8	0.0	91.6	55.3	21.1	23.6	0.0	100
	316-C0008B-																					
I	1H-5, 0–1.5	WR	5.65	50	755	173	541	1,946	22,810	10,679	19,015	26.8	12.7	12.9	22.3	22.3	74.7	35.8	17.0	17.3	29.9	100
	1H-7, 63–65	W	7.71	59	987	199	494	2,244	32,535	13,894	17,082	31.5	18.2	16.8	19.2	19.2	85.7	36.8	21.3	19.6	22.4	100
	316-C0008C-																					
IA	1H-2, 0–1.5	WR	1.43	54	715	220	198	2,666	23,448	12,860	8,192	35.0	12.8	15.7	7.5	7.5	71.1	49.2	18.1	22.1	10.6	100
	1H-5, 0–1.5	WR	4.27	60	866	225	165	3,245	31,911	14,672	5,603	41.5	17.6	17.6	3.4	3.4	80.2	51.8	22.0	22.0	4.2	100
	2H-2, 0–1.5	WR	6.82	55	1,111	269	149	2,915	38,515	16,292	5,597	39.1	21.5	19.6	3.4	3.4	83.6	46.8	25.7	23.5	4.0	100
	2H-7, 0–1.5	WR	12.19	66	791	221	331	2,458	27,465	13,040	12,664	33.1	15.2	15.8	13.4	13.4	77.5	42.6	19.7	20.4	17.3	100
	3H-3, 0–1.5	WR	17.73	48	1,012	224	177	2,549	37,742	12,314	7,079	32.7	21.3	14.3	5.8	5.8	74.1	44.2	28.7	19.3	7.8	100
	3H-4, 28–29.5	WR	18.26	59	1,060	216	116	2,981	34,182	14,592	3,866	38.7	19.0	17.5	1.3	1.3	76.4	50.6	24.9	22.9	1.7	100
	3H-5, 35–36.5	WR	19.55	67	1,041	171	234	3,342	32,937	12,725	6,335	41.0	18.3	14.9	4.3	4.3	78.6	52.2	23.3	19.0	5.5	100
	3H-7, 0–1.5	WR	21.94	79	876	216	247	2,940	31,692	14,297	7,744	38.3	17.6	17.2	6.5	6.5	79.6	48.2	22.1	21.6	8.1	100
	3H-10, 65–66.5	WR	25.24	72	1,020	189	151	3,195	31,652	15,286	5,482	41.5	17.5	18.5	3.3	3.3	80.7	51.4	21.6	22.9	4.1	100
	4H-5, 0–1.5	WR	29.39	76	826	197	303	3,014	28,442	14,528	10,875	39.5	15.7	17.7	10.6	10.6	83.4	47.4	18.8	21.2	12.7	100
	4H-6, 24–25.5	WR	29.85	75	907	212	201	3,464	32,155	13,768	7,205	43.1	17.8	16.3	5.4	5.4	82.6	52.2	21.5	19.8	6.5	100



Table T5 (continued).

Unit	Core, section, interval (cm)	Core type	Depth CSF (m)	Peak intensity (counts/step)				Integrated peak area (total counts)				Abundance calculated from SVD normalization factor									
				Clay	Quartz	Plagioclase	Calcite	Clay	Quartz	Plagioclase	Calcite	Calculated abundance (wt%)				Normalized abundance (wt%)					
												Clay	Quartz	Plagioclase	Calcite	Corrected calcite	Absolute total	Clay	Quartz	Plagioclase	Calcite
5H-2, 18–19.5	WR	34.58	68	1,009	215	43	3,639	33,194	16,536	1,216	46.5	18.2	20.0	-2.7	0.0	84.8	54.9	21.5	23.6	0.0	100
5H-4, 20–21.5	WR	36.91	70	985	238	85	3,616	35,108	15,790	2,166	45.7	19.4	18.9	-1.5	0.0	84.0	54.4	23.1	22.5	0.0	100
5H-5, 0–1.5	WR	38.02	66	1,088	282	85	2,157	34,026	21,819	2,350	35.7	18.7	27.7	-0.4	0.0	82.1	43.5	22.8	33.7	0.0	100
6H-2, 100–101.5	WR	45.81	61	909	325	62	3,329	29,476	19,479	1,349	45.8	16.0	24.3	-2.3	0.0	86.1	53.2	18.5	28.3	0.0	100
6H-3, 50–51.5	WR	46.80	68	985	294	95	2,951	35,038	19,415	2,798	41.8	19.3	24.1	-0.3	0.0	85.2	49.1	22.7	28.3	0.0	100
6H-4, 0–1.5	WR	47.73	46	764	203	419	2,492	24,561	12,568	13,719	33.2	13.5	15.3	14.9	14.9	76.9	43.2	17.6	19.9	19.3	100
7H-4, 0–1.5	WR	55.87	67	841	197	477	2,291	30,643	14,054	15,929	32.1	17.1	17.1	17.7	17.7	84.0	38.3	20.4	20.3	21.0	100
7H-8, 129.5–131	WR	61.11	69	1,317	305	98	2,674	39,604	21,064	3,294	40.1	22.0	26.2	0.3	0.3	88.6	45.2	24.8	29.6	0.4	100
7H-9, 15–16.5	WR	61.27	94	1,136	289	85	2,828	40,026	22,769	2,797	42.8	22.1	28.5	-0.5	0.0	93.4	45.8	23.7	30.5	0.0	100
9H-3, 58.5–60	WR	69.87	67	1,056	302	150	2,384	32,971	18,632	5,760	35.8	18.2	23.3	4.1	4.1	81.4	44.0	22.4	28.6	5.0	100
9H-4, 0–1.5	WR	70.71	71	1,221	377	74	2,368	38,679	23,520	2,105	38.8	21.4	29.7	-1.0	0.0	89.9	43.2	23.8	33.1	0.0	100
9H-5, 70–71.5	WR	71.64	70	899	231	146	3,417	29,400	15,210	5,480	43.7	16.1	18.5	3.2	3.2	81.5	53.7	19.8	22.7	3.9	100
11H-3, 12.5–14	W	83.08	68	980	211	82	3,099	33,578	14,730	3,075	39.9	18.6	17.7	0.2	0.2	76.4	52.3	24.4	23.2	0.2	100
11H-9, 0–1.5	WR	83.30	55	1,017	289	56	2,856	32,186	20,023	1,695	41.4	17.6	25.1	-1.6	0.0	84.1	49.2	20.9	29.8	0.0	100
10H-10, 45–46.5	WR	83.98	66	701	238	91	2,629	25,739	17,790	3,018	37.9	14.0	22.4	0.6	0.6	74.8	50.6	18.7	30.0	0.8	100
11H-8, 113.5–115	WR	86.58	66	906	276	64	3,310	31,926	20,170	2,152	46.0	17.4	25.2	-1.4	0.0	88.6	52.0	19.6	28.4	0.0	100
11H-10, 0–1.5	W	88.10	77	1,020	499	59	2,783	32,934	26,320	2,042	45.2	17.8	33.7	-1.4	0.0	96.7	46.7	18.4	34.9	0.0	100
12H-1, 50–52	W	90.61	52	758	270	219	2,288	27,014	20,100	7,003	36.3	14.7	25.6	5.9	5.9	82.5	44.0	17.8	31.0	7.2	100
13H-7, 48.5–50	WR	94.25	64	848	181	496	1,954	26,700	10,478	18,666	26.5	15.0	12.5	21.7	21.7	75.7	35.0	19.8	16.5	28.7	100
13H-7, 91–92.5	WR	94.68	58	745	191	603	1,973	25,402	10,895	22,266	27.2	14.2	13.1	26.5	26.5	81.0	33.6	17.6	16.1	32.7	100
13H-8, 0–1.5	WR	94.88	67	924	207	183	3,170	32,747	14,608	5,446	40.7	18.1	17.5	3.2	3.2	79.6	51.1	22.8	22.0	4.1	100
14H-6, 0–1.5	WR	102.71	78	1,339	300	92	3,062	45,056	19,006	2,815	42.1	25.2	23.0	-0.7	0.0	90.3	46.6	27.9	25.5	0.0	100
15H-5, 0–1.5	WR	103.32	83	1,354	267	77	3,712	41,810	16,669	2,461	47.0	23.3	19.8	-1.4	0.0	90.1	52.2	25.8	22.0	0.0	100
16H-5, 0–1.5	WR	112.35	70	1,162	221	204	3,493	39,278	15,108	5,541	43.9	21.9	17.8	2.9	2.9	86.6	50.8	25.3	20.6	3.3	100
18H-1, 35.5–37	WR	120.25	80	821	182	657	2,444	27,852	10,999	20,273	31.7	15.6	13.0	23.4	23.4	83.7	37.9	18.6	15.5	28.0	100
18H-4, 42–43.5	WR	124.27	62	951	195	218	3,185	31,668	13,838	8,326	40.4	17.5	16.5	7.0	7.0	81.6	49.6	21.5	20.3	8.6	100
19H-1, 28–30	W	125.67	61	951	250	256	2,808	33,724	14,077	8,914	36.8	18.8	16.9	8.0	8.0	80.5	45.7	23.4	20.9	10.0	100
18H-6, 0–1.5	WR	126.23	72	951	186	100	2,989	36,997	15,528	2,961	39.3	20.6	18.7	0.0	0.0	78.5	50.0	26.3	23.8	0.0	100
21H-4, 39.5–41	WR	133.95	63	944	191	217	3,740	32,561	14,180	7,168	46.1	18.0	16.8	5.1	5.1	85.9	53.6	20.9	19.5	5.9	100
21H-5, 0–1.5	WR	134.40	79	1,064	213	266	3,253	35,772	13,155	9,015	40.5	20.0	15.4	7.8	7.8	83.6	48.4	23.9	18.4	9.3	100
22X-5, 0–1.5	WR	144.08	82	867	189	329	3,097	31,589	12,584	12,011	38.8	17.6	14.8	12.0	12.0	83.2	46.7	21.1	17.8	14.4	100
23X-4, 0–1.5	WR	150.38	65	1,027	299	314	3,238	34,167	16,362	10,739	42.8	18.9	19.8	10.0	10.0	91.5	46.8	20.7	21.7	10.9	100
23X-6, 107.5–109	WR	152.78	65	827	207	402	3,140	29,222	12,580	14,495	39.5	16.2	14.9	15.3	15.3	85.8	46.0	18.9	17.4	17.8	100
24X-3, 97.5–99	WR	160.63	40	2,020	415	82	1,541	62,055	30,740	2,377	34.8	34.9	38.7	-1.1	0.0	108.5	32.1	32.2	35.7	0.0	100
24X-4, 0–1.5	W	160.96	77	977	188	93	3,100	33,083	13,503	3,116	39.1	18.4	16.0	0.3	0.3	73.8	53.0	24.9	21.7	0.4	100
24X-10, 20–21.5	WR	166.46	66	966	197	137	3,580	31,292	13,138	4,088	43.7	17.3	15.5	1.3	1.3	77.7	56.2	22.2	19.9	1.6	100
IB 25X-9, 0–1.5	WR	171.59	70	1,070	206	83	3,558	38,909	13,396	2,606	43.2	21.7	15.5	-0.9	0.0	80.5	53.7	27.0	19.2	0.0	100
25X-10, 30.5–32	WR	172.23	69	1,132	251	48	3,895	37,120	15,183	1,747	47.9	20.6	17.9	-2.3	0.0	86.4	55.5	23.8	20.7	0.0	100
25X-11, 94.5–96	WR	173.86	65	1,162	330	149	2,679	39,940	22,006	3,832	40.8	22.1	27.5	1.0	1.0	91.4	44.6	24.2	30.1	1.1	100

Notes: CSF = core depth below seafloor. SVD = singular value decomposition. WR = whole-round, W = working half.

Table T6. XRD mineralogy by unit. (See table note.)

Mineral	Maximum	Minimum	Average	Standard deviation
Subunit IA				
Clay	64.4	27.2	47.6	6.6
Quartz	33.9	11.9	22.9	3.6
Plagioclase	39.5	14.6	22.7	4.8
Calcite	36.7	0.0	6.7	8.3
Calcite	36.7	0.2	8.9	8.5
Subunit IB				
Clay	52.0	40.0	47.7	4.5
Quartz	22.8	15.5	19.0	2.3
Plagioclase	42.9	27.3	32.1	5.3
Calcite	7.2	0.0	1.3	2.7
Calcite	7.2	1.6	4.4	4.0
Unit II				
Clay	56.7	51.8	54.6	2.5
Quartz	21.1	18.8	19.7	1.2
Plagioclase	28.5	23.6	25.5	2.6
Calcite	0.5	0.0	0.2	0.3
Calcite	0.5	0.0		

Note: For each subunit, calcite results are first presented for all samples and then for only those samples containing calcite.

Table T8. Calcareous nannofossil range chart of age-diagnostic fossils, Hole C0008C. (See table notes.)

Epoch	Nannofossil zone	Core, section, interval (cm)	Depth CSF (m)			Abundance	Preservation	<i>Amaurolithus tricorniculatus</i>	<i>Braarudosphaera bigelowii</i>	<i>Calcidiscus leptoporus</i>	<i>Calcidiscus macintyreii</i>	<i>Coccolithus pelagicus</i>	<i>Discoaster brauweri</i>	<i>Emiliania huxleyi</i>	<i>Gephyrocapsa</i> spp. large (>5.5 µm)	<i>Gephyrocapsa</i> spp. medium I (>3.5–4 µm)	<i>Gephyrocapsa</i> spp. medium II (>4–5.5 µm)	<i>Gephyrocapsa</i> spp. smaller (<3.5 µm)	<i>Helicosphaera sellii</i>	<i>Pseudoemiliania lacunosa</i>	<i>Reticulofenestra asanoi</i>	<i>Reticulofenestra haqii-minutula</i>	<i>Reticulofenestra pseudoumbilicus</i> (>7 µm)			
			Top	Bottom	Mean																					
Pleistocene	NN21	316-C0008C-1H-CC, 0–5	5.42	5.47	5.45	D	G		C	R																
		2H-CC, 0–5	15.45	15.50	15.48	D	G		C	R				D					D	T	R					
	NN20	3H-CC, 0–5	25.35	25.40	25.37	D	M		C	R					R					D	A		C	R		
		4H-CC, 0–5	36.92	36.97	36.95	D	M		C	R					C		C			D	A		C	R		
		5H-CC, 0–5	43.74	43.79	43.76	C	M			F					C	F	C			C	C		C			
		6H-CC, 0–5	53.65	53.70	53.67	D	M		T	C	R	R			C	F	C	D		C	C		F	T		
		7H-CC, 92–97	62.31	62.36	62.34	D	M			C	R	R			F	F	C	A	F	C	A	F	C	F	T	
		9H-CC, 4–9	77.34	77.39	77.37	D	P			C	R	R			F	F	C	A	C		C		F	T		
		10H-CC, 0–5	86.35	86.40	86.37	D	M			C	R	F			C	F	A	D	F	C	A	F	C	F	T	
		11H-CC, 7–12	90.81	90.86	90.84	C	P			R	F	F		R	R	C	C	R	?	R	C	F	R		F	R
		12H-CC, 0–5	92.92	92.97	92.94	D	P			C	R	F		R	R	C	C	A	F	C	A	F	C	C	R	
		13H-CC, 0–5	97.70	97.75	97.72	D	M			C	R	C		R	T	C	C	A	R	C	A	R	C	C	R	
		14H-CC, 9–14	107.57	107.62	107.59	D	M		R	C	T	C	R		F	F	A	C	F	C	A	R	C	C	R	
		15H-5, 25		103.57	103.57	D	G			C	C				C?	F	C	A	A	R	F					
		15H-CC, 35–40	108.36	108.41	108.38	D	G			C	C				C?	F	C	A	A	R	F					
		16H-CC, 18–23	118.51	118.56	118.53	D	M		T	C	C				C?		C	A	A	C						
		17H-CC, 10–15	120.37	120.42	120.40	C	P			R	T	F				C	C	C	C	C				F	R	
		18H-CC, 33–38	129.52	129.57	129.55	C	P			R	F	F				C	C	C	C	R	C			F	R	
		19H-CC, 8–13	130.01	130.06	130.04	A	P			C	F	C		R		C	C	C	F	C			F	F		
		20H-CC, 0–5	130.41	130.46	130.43	D	M			C	F	C		R		C	C	C	F	C			C	R		
		21H-CC, 19–24	138.72	138.77	138.75	A	P	T		C	F	F		R		C	C	C	F	C			A	R		
		22X-CC, 57–62	148.71	148.76	148.73	R	P				R	R											R			
		23X-CC, 0–5	155.03	155.08	155.06	D	M	T		C	C	C		R		C			A	F	C		A	R		
		24X-CC, 0–5	166.67	166.72	166.70	D	P			C	C	C											C	A		
		25X-CC, 0–5	175.99	176.04	176.02	D	M			C	F	F		T					A	R	C		A	R		

Notes: CSF = core depth below seafloor. Abundance: D = dominant, A = abundant, C = common, F = few, R = rare, T = trace, B = barren. Preservation: M = medium, P = poor. ? = uncertain determination.




Table T9. Recognized nannofossil events, Hole C0008A. (See table notes.)

Epoch	Nannofossil zone	Age (Ma)	Nannofossil event	Top		Bottom		Mean depth CSF (m)		
				Core, section, interval (cm)	Depth CSF (m)	Core, section, interval (cm)	Depth CSF (m)			
Pleistocene	NN21	0.063	<i>Gephyrocapsa</i> spp. (>3.5 μm)– <i>Emiliana huxleyi</i>	316-C0008A-1H-CC, 0–5	6.83	316-C0008A-2H-CC, 4–9	17.01	11.92		
		1.078	FCO <i>Reticulofenestra asanoi</i>	2H-CC, 4–9	17.01	3H-CC, 0–5	25.62	21.31		
	Repeated NN19?	1.24	LO <i>Gephyrocapsa</i> spp. (>5.5 μm)	4H-CC, 6.5–11.5	35.53	5H-CC, 0–5	44.80	40.16		
		1.34	LO <i>Helicosphaera sellii</i>	5H-CC, 0–5	44.80	6H-CC, 56.5–61.5	54.82	49.81		
		1.46	FCO <i>Gephyrocapsa</i> spp. (>5.5 μm)	8H-CC, 0–5	72.13	9H-CC, 0–5	78.50	75.31		
		1.6	LO <i>Calcidiscus macintyreii</i> (≥ 11 μm)	9H-CC, 0–5	78.50	10H-CC, 0–5	90.39	84.44		
		1.24	LO <i>Gephyrocapsa</i> spp. (>5.5 μm)	9H-CC, 0–5	78.50	10H-CC, 0–5	90.39	84.44		
		1.34	LO <i>Helicosphaera sellii</i>	10H-CC, 0–5	90.39	11H-CC, 0–5	100.54	95.46		
		1.46	FCO <i>Gephyrocapsa</i> spp. (>5.5 μm)	19H-CC, 12.5–17.5	152.69	20H-CC, 0–5	158.53	155.61		
		1.6	LO <i>Calcidiscus macintyreii</i> (≥ 11 μm)	22H-CC, 5–10	178.54	23H-CC, 7.5–12.5	186.21	182.37		
		1.67	FO <i>Gephyrocapsa</i> spp. (>3.5 μm)	30X-5, 60	238.91	30X-CC, 0–5	242.71	240.81		
		Pliocene	NN18	2.135	AB <i>Discoaster triradiatus</i>	31X-CC, 0–5	254.10	32X-5, 77	259.22	256.66
			NN17	2.393	LO <i>Discoaster pentaradiatus</i>	33X-3, 25	265.64	33X-CC, 0–5	269.64	267.64
NN16	2.87		LO <i>Discoaster tamalis</i>	34X-CC, 0–5	272.86	35X-1, 2	281.78	277.32		
3.65	LO <i>Sphenolithus</i> spp.		35X-CC, 34–39	282.35	36X-CC, 18–23	291.69	287.02			
Miocene?	NN11? Falling?	5.59	LO <i>Discoaster quinqueramus</i>	38X-CC, 0–5	310.74	40X-CC, 10–11	329.36	320.05		

Notes: CSF = core depth below seafloor. FCO = first consistent occurrence, LO = last occurrence, FO = first occurrence, AB = acme beginning.

Table T10. Recognized nannofossil events, Hole C0008C. (See table notes.)

Epoch	Zone	Age (Ma)	Nannofossil event	Top		Bottom		Mean depth CSF (m)
				Core, section, interval (cm)	Depth (mbsf)	Core, section, interval (cm)	Depth (mbsf)	
Pleistocene	NN21	0.063	<i>Gephyrocapsa</i> spp. (>3.5 μm)– <i>Emiliana huxleyi</i>	316-C0008C-	0.00	316-C0008C-1H-CC, 0–5	5.45	2.72
		NN19	1.24	LO <i>Gephyrocapsa</i> spp. (>5.5 μm)	2H-CC, 0–5	15.48	3H-CC, 0–5	25.37
	1.34		LO <i>Helicosphaera sellii</i>	6H-CC, 0–5	53.67	7H-CC, 92–97	62.34	58.00
	1.46		FCO <i>Gephyrocapsa</i> spp. (>5.5 μm)	15H-CC, 35–40	108.38	16H-CC, 18–23	118.53	113.46
	1.6		LO <i>Calcidiscus macintyreii</i> (≥ 11 μm)	17H-CC, 10–15	120.40	18H-CC, 33–38	129.55	124.97
	1.67		FO <i>Gephyrocapsa</i> spp. (>3.5 μm)	21H-CC, 19–24	138.75	22X-CC, 57–62	148.73	143.74

Note: CSF = core depth below seafloor. LO = last occurrence, FCO = first consistent occurrence, FO = first occurrence.



Table T11. Uncorrected geochemistry results from interstitial waters, Site C0008. (See table notes.) (Continued on next page.)

Core, section	Depth CSF (m)			pH	Alkalinity (mM)	Refractive index	Salinity	Chlorinity (mM)	Cl (mM)	Br (mM)	SO ₄ (mM)	Na (mM)	Na (mM)*	K (mM)	Mg (mM)	Ca (mM)	PO ₄ (μM)	NH ₄ (μM)
	Top	Bottom	Average															
316-C0008A-																		
1H-3	1.64	1.86	1.75	7.8	5.90	1.33934	35.28	555	554	0.84	23.86	451	481	11.8	48.64	8.71	16	169
1H-7	5.43	5.65	5.54	8.2	19.04	1.33917	34.33	561	561	0.87	7.78	446	490	11.3	42.27	4.41	23	608
2H-2	8.35	8.58	8.46	8.2	22.33	1.33912	34.06	566	565	0.88	2.27	441	498	10.7	37.98	3.13	35	812
2H-8	15.43	15.66	15.55	8.1	20.57	1.33910	33.94	569	568	0.93	0	452	503	10.7	33.60	3.10	43	1455
3H-3	18.41	18.64	18.52	8.2	19.36	1.33911	34.00	572	571	0.95	0	475	505	11.0	32.90	3.34	46	1800
3H-8	22.98	23.22	23.10	8.0	17.65	1.33913	34.11	575	574	0.97	0	472	509	10.9	31.26	3.46	55	2169
4H-4	29.18	29.41	29.30	7.9	16.92	1.33914	34.17	583	582	0.99	0	466	522	10.1	28.21	3.75	69	2694
5H-4	38.72	38.94	38.83	7.7	15.43	1.33914	34.17	584	583	1.04	0	501	521	10.3	27.44	4.30	90	3439
6H-5	49.27	49.50	49.38	7.7	15.14	1.33917	34.33	583	582	1.07	0	483	522	9.6	26.17	5.19	73	4043
7H-5	58.63	58.84	58.73	7.7	13.58	1.33915	34.22	584	583	1.07	0	514	523	9.9	24.48	5.27	30	4522
8H-5	68.25	68.48	68.37	7.6	13.61	1.33916	34.28	586	585	1.09	0	494	526	9.4	23.98	5.50	42	4631
9H-5	77.56	77.83	77.70	7.7	13.40	1.33915	34.22	583	582	1.11	0	507	524	9.4	23.42	5.61	18	4702
10H-6	87.23	87.51	87.37	7.5	12.45	1.33911	34.00	582	581	1.10	0	497	524	8.8	22.35	5.89	43	4702
11H-4	94.73	95.01	94.87	7.5	12.32	1.33908	33.83	581	579	1.11	0	506	523	8.7	21.72	6.06	39	4749
12H-5	104.92	105.19	105.05	7.6	11.75	1.33905	33.67	575	574	1.13	0	498	519	8.8	20.57	6.18	22	4627
13H-5	114.79	115.08	114.93	7.6	10.97	1.33898	33.28	574	573	1.13	0	483	519	8.5	19.56	6.33	12	4566
15H-2	120.14	120.48	120.31	7.6	10.13	1.33873	31.89	553	552	1.11	0	469	503	7.9	17.56	6.17	11	4169
16H-4	128.82	129.10	128.96	7.7	9.18	1.33890	32.83	565	564	1.13	0	472	513	8.4	17.44	6.44	7	4330
17H-6	136.14	136.42	136.28	7.7	8.87	1.33868	31.61	537	536	1.07	0	463	489	8.2	15.89	6.37	6	3780
18H-3	143.02	143.29	143.15	7.7	9.07	1.33881	32.33	558	557	1.12	0	473	509	8.0	16.08	7.06	8	3750
19H-2	151.38	151.65	151.52	7.6	7.91	1.33881	32.33	559	558	1.12	0	482	511	7.8	14.52	7.05	7	3696
20H-3	155.11	155.38	155.24	7.6	8.04	1.33880	32.28	558	557	1.12	0	483	511	7.9	14.35	7.23	7	3696
21H-5	164.12	164.41	164.26	7.6	7.73	1.33879	32.22	561	560	1.11	0	460	516	7.2	13.37	7.28	4	3490
22H-6	173.62	173.90	173.76	7.7	7.46	1.33878	32.17	560	559	1.15	0	482	514	7.8	13.10	7.56	4	3338
23H-5	182.04	182.32	182.18	7.7	6.84	1.33876	32.06	556	555	1.14	0	489	510	8.0	12.57	7.62	4	3307
24H-6	192.78	193.09	192.93	7.8	6.85	1.33877	32.11	560	559	1.12	0	492	515	8.1	12.30	7.75	2	3031
25H-2	198.21	198.51	198.36	7.8	6.69	1.33882	32.39	559	558	1.09	2.80	485	516	8.1	13.62	8.12	6	2951
26H-2	202.21	202.54	202.37	7.9	6.56	1.33877	32.11	561	560	1.12	0	496	515	8.3	11.87	7.98	4	3018
27H-5	215.64	215.94	215.79	7.6	6.65	1.33880	32.28	564	563	1.11	0	493	518	7.9	12.16	8.29	5	2771
28H-3	222.22	222.52	222.37	7.9	6.09	1.33882	32.39	564	563	1.13	0	516	520	7.0	12.07	7.58	5	2758
29X-5	229.25	229.58	229.41	7.6	6.12	1.33883	32.44	567	565	1.11	0	589	519	8.0	12.48	8.42	5	2638
30X-7	240.16	240.52	240.34	8.1	6.11	1.33881	32.33	561	560	1.10	0	597	516	8.3	11.56	8.14	1	2651
31X-6	249.92	250.30	250.11	7.9	6.18	1.33889	32.78	567	566	1.09	2.15	592	523	8.4	12.92	8.68	4	2518
32X-7	260.72	261.10	260.91	8.0	5.37	1.33892	32.94	569	567	1.11	2.69	601	523	8.7	13.45	8.85	2	2483
33X-4	266.70	267.03	266.86	8.0	5.24	1.33898	33.28	569	567	1.09	5.04	581	525	8.9	14.47	9.19	5	2379
316-C0008B-																		
1H-5	5.65	5.88	5.77	8.4	23.99	1.33905	33.67	569	568	0.91	0.77	547	497	11.5	38.77	3.54	25	800
316-C0008C-																		
1H-2	1.43	1.67	1.55	7.9	6.17	1.33933	35.22	555	554	0.87	24.70	531	486	11.4	47.41	8.65	11	232
1H-5	4.27	4.49	4.38	8.3	20.57	1.33910	33.94	558	557	0.90	4.62	544	488	11.3	39.92	4.06	38	550
2H-2	6.82	7.05	6.94	8.3	22.75	1.33904	33.61	564	563	0.93	0	548	494	11.4	36.33	3.36	27	952
2H-7	12.19	12.43	12.31	8.3	18.14	1.33896	33.17	560	559	0.96	0	564	500	11.0	29.47	3.31	32	1368
3H-3	17.73	17.98	17.85	8.0	15.15	1.33896	33.17	564	563	1.00	0	571	508	10.5	25.06	3.81	32	1944
3H-7	21.94	22.17	22.05	7.8	13.65	1.33892	32.94	564	563	1.02	0	579	510	10.5	23.58	3.82	32	2186
4H-5	29.39	29.61	29.50	7.8	12.73	1.33891	32.89	565	564	1.04	0	582	512	9.6	22.22	4.37	38	2558
5H-5	38.02	38.25	38.13	7.6	12.29	1.33892	32.94	571	570	1.06	0	573	518	9.1	20.92	5.06	44	3080
6H-4	47.73	48.02	47.88	7.6	11.93	1.33894	33.06	568	567	1.08	0	598	516	8.9	20.27	5.38	20	3478
7H-4	55.87	56.10	55.99	7.6	11.49	1.33881	32.33	557	555	1.06	0	584	504	9.0	20.00	5.55	23	3638
9H-4	70.71	70.94	70.82	7.6	10.16	1.33876	32.06	548	547	1.07	0	566	496	8.7	18.63	5.59	10	3902



Table T11 (continued).

Core, section	Depth CSF (m)			pH	Alkalinity (mM)	Refractive index	Salinity	Chlorinity (mM)	Cl (mM)	Br (mM)	SO ₄ (mM)	Na (mM)	Na (mM)*	K (mM)	Mg (mM)	Ca (mM)	PO ₄ (μM)	NH ₄ (μM)
	Top	Bottom	Average															
9H-7	73.08	73.20	73.14	7.7	9.96	1.33869	31.67	495	494	0.97	0	536	449	7.7	16.72	4.97	13	3446
10H-9	83.30	83.53	83.41	7.6	10.00	1.33889	32.78	566	565	1.11	0	583	515	8.5	18.31	5.75	13	3992
10H-12	85.43	85.59	85.51	8.0	7.05	1.33696	22.06	368	367	0.73	0	384	336	5.7	11.53	3.56	12	2643
11H-2	82.86	82.95	82.91	7.8	9.76	1.33864	31.39	542	541	1.08	0	562	495	8.1	17.38	5.22	15	3651
11H-10	88.10	88.33	88.22	7.6	9.96	1.33889	32.78	569	568	1.11	0	558	518	8.3	18.24	5.91	15	3735
13H-8	94.88	95.11	94.99	7.9	8.46	1.33801	27.89	481	480	0.95	0	552	433	8.0	16.62	5.72	6	3189
13H-10	95.93	96.03	95.98	8.4	6.16	1.33643	19.11	379	379	0.77	0	392	348	6.3	10.48	3.42	5	2848
14H-6	102.71	102.94	102.82	7.7	8.84	1.33879	32.22	560	559	1.12	0	564	512	8.0	16.39	5.98	9	3523
15H-2	101.96	102.13	102.05	8.1	5.64	1.33625	18.11	306	305	0.64	0	326	280	4.1	9.06	3.36	8	1911
15H-5	103.32	103.55	103.44	7.8	7.98	1.33856	30.94	515	514	1.02	0	547	469	7.6	15.35	5.69	8	3414
16H-5	112.35	112.57	112.46	7.7	8.37	1.33874	31.94	555	554	1.08	0	553	508	8.0	15.44	6.24	7	3403
18H-6	126.23	126.50	126.36	7.9	7.82	1.33875	32.00	558	557	1.10	0	568	512	7.8	14.72	6.60	5	3303
21H-5	134.40	134.70	134.55	7.8	6.35	1.33775	26.44	457	456	0.89	0	489	417	6.9	11.84	5.92	6	2496
22X-5	144.08	144.36	144.22	7.9	6.73	1.33873	31.89	554	553	1.07	0	561	507	8.0	13.32	7.37	7	3089
23X-2	149.72	149.79	149.75	8.1	3.22	1.33611	17.33	294	293	0.55	3.801	300	272	3.9	9.15	4.05	3	1468
23X-4	150.38	150.65	150.51	8.0	5.94	1.33867	31.56	543	542	1.07	1.191	552	499	8.1	12.52	7.62	7	2896
24X-4	160.96	161.39	161.17	8.2	5.13	1.33853	30.78	530	529	1.03	0	541	487	8.1	10.92	7.50	5	2767
24X-5	161.39	161.47	161.43	8.1	3.70	1.33684	21.39	358	358	0.70	1.194	376	333	5.2	7.29	4.72	3	1882
25X-2	167.38	167.44	167.41	8.1	4.64	1.33781	26.78	466	466	0.92	1.696	478	432	6.9	9.42	6.75	7	2268
25X-9	171.59	171.92	171.76	7.9	4.89	1.33874	31.94	559	558	1.10	0	562	512	8.6	11.20	8.69	5	2717

Notes: * = calculated by charge balance. CSF = core depth below seafloor.

Table T12. Uncorrected concentrations of minor elements in interstitial waters, Site C0008. (See table notes.)
(Continued on next page.)

Core, section	Depth CSF (m)			Minor elements (μm)							
	Top	Bottom	Average	Li	B	Sr	Ba*	Ba [†]	Si	Fe	Mn
316-C0008A-											
1H-3	1.64	1.86	1.75	25.3	515	82	0	0	636	2.48	6.44
1H-7	5.43	5.65	5.54	20.4	473	80	1	1	613	1.09	0.63
2H-2	8.35	8.58	8.46	20.3	465	81	10	10	616	1.51	0.48
2H-8	15.43	15.66	15.55	19.1	437	84	31	31	627	1.07	0.48
3H-3	18.41	18.64	18.52	18.3	426	85	34	34	648	0.55	0.27
3H-8	22.98	23.22	23.10	16.7	434	86	38	38	654	0.97	0.35
4H-4	29.18	29.41	29.30	15.5	395	91	43	43	611	2.28	0.56
5H-4	38.72	38.94	38.83	13.8	370	94	47	47	621	4.78	0.97
6H-5	49.27	49.50	49.38	14.9	330	96	50	50	548	1.88	4.67
7H-5	58.63	58.84	58.73	16.8	338	94	54	54	583	1.95	4.20
8H-5	68.25	68.48	68.37	18.1	317	95	57	57	647	6.51	4.47
9H-5	77.56	77.83	77.70	20.2	342	94	58	58	533	1.45	3.58
10H-6	87.23	87.51	87.37	21.6	353	94	58	58	694	24.23	4.84
11H-4	94.73	95.01	94.87	21.6	324	93	58	58	725	28.27	5.19
12H-5	104.92	105.19	105.05	24.7	317	92	56	56	689	11.78	4.93
13H-5	114.79	115.08	114.93	24.7	323	91	55	55	635	10.11	5.21
15H-2	120.14	120.48	120.31	26.7	345	84	48	48	637	6.56	4.91
16H-4	128.82	129.10	128.96	27.4	324	87	51	51	666	0.66	5.53
17H-6	136.14	136.42	136.28	28.7	316	82	47	47	627	1.25	6.00
18H-3	143.02	143.29	143.15	30.0	338	87	46	46	680	0.47	7.16
19H-2	151.38	151.65	151.52	25.4	405	85	45	45	739	7.18	8.07
20H-3	155.11	155.38	155.24	25.5	418	84	45	45	742	4.35	9.57
21H-5	164.12	164.41	164.26	25.0	448	84	43	43	674	1.07	10.80
22H-6	173.62	173.90	173.76	23.7	453	83	42	42	662	3.45	10.87
23H-5	182.04	182.32	182.18	23.2	515	83	42	42	622	0.30	6.40
24H-6	192.78	193.09	192.93	24.0	514	83	40	40	712	0.85	6.83
25H-2	198.21	198.51	198.36	23.5	602	83	36	36	618	0.32	9.39
26H-2	202.21	202.54	202.37	24.2	576	82	37	37	553	2.45	7.23
27H-5	215.64	215.94	215.79	23.7	615	84	35	35	677	4.83	9.33
28H-3	222.22	222.52	222.37	23.9	615	85	34	34	587	0.10	5.10
29X-5	229.25	229.58	229.41	24.7	699	85	29	29	739	0.36	7.14
30X-7	240.16	240.52	240.34	24.2	630	83	26	26	592	0.63	5.27
31X-6	249.92	250.30	250.11	25.4	691	85	21	21	656	0.10	7.30
32X-7	260.72	261.10	260.91	28.4	572	87	19	19	485	0.28	5.78
33X-4	266.70	267.03	266.86	31.1	574	88	14	14	466	0.19	6.23
316-C0008B-											
1H-5	5.65	5.88	5.77	16.4	477	81	25	22	603	0.37	0.60
316-C0008C-											
1H-2	1.43	1.67	1.55	22.9	504	81	0	0	609	2.98	5.27
1H-5	4.27	4.49	4.38	18.8	485	80	2	2	648	0.37	0.41
2H-2	6.82	7.05	6.94	16.3	480	84	113	98	602	0.23	0.36
2H-7	12.19	12.43	12.31	17.5	462	84	96	90	618	0.08	0.23
3H-3	17.73	17.98	17.85	15.9	448	83	63	56	629	0.36	0.20
3H-7	21.94	22.17	22.05	16.7	424	83	60	54	650	0.58	0.25
4H-5	29.39	29.61	29.50	14.0	414	84	56	51	648	2.19	0.47
5H-5	38.02	38.25	38.13	14.3	422	84	53	47	622	1.14	3.02
6H-4	47.73	48.02	47.88	14.2	369	84	56	51	658	10.95	6.05
7H-4	55.87	56.10	55.99	17.0	363	83	54	50	635	12.44	5.98
9H-4	70.71	70.94	70.82	18.7	345	79	49	45	511	1.37	3.45
9H-7	73.08	73.20	73.14	18.1	350	71	44	40	616	2.54	4.05
10H-9	83.30	83.53	83.41	21.3	351	80	49	43	692	4.08	5.61
10H-12	85.43	85.59	85.51	13.6	216	47	26	24	445	0.26	2.35
11H-2	82.86	82.95	82.91	19.7	292	74	45	29	625	0.60	4.17
11H-10	88.10	88.33	88.22	19.8	350	80	47	42	722	6.62	6.54
13H-8	94.88	95.11	94.99	19.9	331	75	44	38	581	10.46	6.30
13H-10	95.93	96.03	95.98	12.6	182	45	27	24	306	0.72	1.88
14H-6	102.71	102.94	102.82	19.6	354	78	44	40	677	5.86	6.97
15H-2	101.96	102.13	102.05	10.4	190	40	19	35	302	0.00	2.85
15H-5	103.32	103.55	103.44	18.2	323	73	40	—	622	3.30	7.09
16H-5	112.35	112.57	112.46	18.7	392	77	41	36	595	0.57	11.49
18H-6	126.23	126.50	126.36	19.2	438	77	39	36	580	0.52	10.30
21H-5	134.40	134.70	134.55	17.8	400	64	28	25	668	3.30	6.63
22X-5	144.08	144.36	144.22	19.5	540	79	32	—	582	0.09	6.16
23X-2	149.72	149.79	149.75	10.0	303	37	10	9	272	0.07	3.50
23X-4	150.38	150.65	150.51	20.5	649	79	27	24	564	0.22	6.19

Table T12 (continued).

Core, section	Depth CSF (m)			Minor elements (μm)							
	Top	Bottom	Average	Li	B	Sr	Ba*	Ba [†]	Si	Fe	Mn
24X-4	160.96	161.39	161.17	20.0	677	76	23	20	480	0.08	3.87
24X-5	161.39	161.47	161.43	13.3	460	44	11	10	378	0.09	2.09
25X-2	167.38	167.44	167.41	17.6	583	64	15	14	529	0.26	3.16
25X-9	171.59	171.92	171.76	21.1	859	85	20	18	614	2.11	5.35

Notes: * = shipboard ICP-AES, † = shore-based ICP-MS. CSF = core depth below seafloor. — = not analyzed.

Table T13. Uncorrected concentrations of trace elements and $\delta^{18}\text{O}$ in interstitial waters, Site C0008. (See table notes.) (Continued on next page.)

Core, section	Depth CSF (m)			V (nM)	Cu (nM)	Zn (nM)	Rb (μM)	Mo (μM)	Cs (nM)	Pb (nM)	U (nM)	Y (pM)	$\delta^{18}\text{O}$ (‰)
	Top	Bottom	Depth										
316-C0008A-													
1H-3	1.64	1.86	1.75	—	—	—	—	—	—	—	—	—	-0.08
1H-7	5.43	5.65	5.54	—	—	—	—	—	—	—	—	—	-0.27
2H-2	8.35	8.58	8.46	—	—	—	—	—	—	—	—	—	-0.48
2H-8	15.43	15.66	15.55	—	—	—	—	—	—	—	—	—	-0.69
3H-3	18.41	18.64	18.52	—	—	—	—	—	—	—	—	—	-0.80
3H-8	22.98	23.22	23.10	—	—	—	—	—	—	—	—	—	-1.09
4H-4	29.18	29.41	29.30	—	—	—	—	—	—	—	—	—	-1.36
5H-4	38.72	38.94	38.83	—	—	—	—	—	—	—	—	—	-1.96
6H-5	49.27	49.50	49.38	—	—	—	—	—	—	—	—	—	-2.45
7H-5	58.63	58.84	58.73	—	—	—	—	—	—	—	—	—	-2.81
8H-5	68.25	68.48	68.37	—	—	—	—	—	—	—	—	—	-3.12
9H-5	77.56	77.83	77.70	—	—	—	—	—	—	—	—	—	-3.23
10H-6	87.23	87.51	87.37	—	—	—	—	—	—	—	—	—	-3.48
11H-4	94.73	95.01	94.87	—	—	—	—	—	—	—	—	—	-3.57
12H-5	104.92	105.19	105.05	—	—	—	—	—	—	—	—	—	-3.73
13H-5	114.79	115.08	114.93	—	—	—	—	—	—	—	—	—	-3.85
15H-2	120.14	120.48	120.31	—	—	—	—	—	—	—	—	—	-3.89
16H-4	128.82	129.10	128.96	—	—	—	—	—	—	—	—	—	-3.99
17H-6	136.14	136.42	136.28	—	—	—	—	—	—	—	—	—	-3.97
18H-3	143.02	143.29	143.15	—	—	—	—	—	—	—	—	—	-4.04
19H-2	151.38	151.65	151.52	—	—	—	—	—	—	—	—	—	-4.15
20H-3	155.11	155.38	155.24	—	—	—	—	—	—	—	—	—	-4.12
21H-5	164.12	164.41	164.26	—	—	—	—	—	—	—	—	—	-4.25
22H-6	173.62	173.90	173.76	—	—	—	—	—	—	—	—	—	-4.28
23H-5	182.04	182.32	182.18	—	—	—	—	—	—	—	—	—	-4.26
24H-6	192.78	193.09	192.93	—	—	—	—	—	—	—	—	—	-4.35
25H-2	198.21	198.51	198.36	—	—	—	—	—	—	—	—	—	-3.92
26H-2	202.21	202.54	202.37	—	—	—	—	—	—	—	—	—	-4.33
27H-5	215.64	215.94	215.79	—	—	—	—	—	—	—	—	—	-4.25
28H-3	222.22	222.52	222.37	—	—	—	—	—	—	—	—	—	-4.27
29X-5	229.25	229.58	229.41	—	—	—	—	—	—	—	—	—	-4.17
30X-7	240.16	240.52	240.34	—	—	—	—	—	—	—	—	—	-4.35
31X-6	249.92	250.30	250.11	—	—	—	—	—	—	—	—	—	-4.02
32X-7	260.72	261.10	260.91	—	—	—	—	—	—	—	—	—	-4.06
33X-4	266.70	267.03	266.86	—	—	—	—	—	—	—	—	—	-3.61
316-C0008B-													
1H-5	5.65	5.88	5.77	14	747	690	1.34	10	2.2	0.7	1.5	1.39	-0.59
316-C0008C-													
1H-2	1.43	1.67	1.55	28	368	479	1.51	12	2.2	0.9	6.1	1.30	-0.27
1H-5	4.27	4.49	4.38	40	236	2,524	1.40	13	2.2	5.3	2.3	2.8	-0.53
2H-2	6.82	7.05	6.94	17	533	513	1.31	34	2.3	0.4	2.6	2.0	-0.87
2H-7	12.19	12.43	12.31	19	1,125	432	1.31	11	2.8	0.6	4.8	1.49	-1.20
3H-3	17.73	17.98	17.85	16	368	997	1.12	4.6	2.0	0.3	2.1	2.2	-1.89
3H-7	21.94	22.17	22.05	22	296	596	1.14	10	1.99	8.0	1.6	1.87	-1.92
4H-5	29.39	29.61	29.50	18	156	476	0.97	7.7	1.78	0.7	1.1	2.0	-2.40
5H-5	38.02	38.25	38.13	23	1,934	1,347	0.83	52	1.76	5.9	1.7	1.33	-2.87
6H-4	47.73	48.02	47.88	10	47	501	0.83	30	1.81	32	0.5	1.19	-3.27
7H-4	55.87	56.10	55.99	10	67	407	0.82	17	2.3	1.0	0.4	1.01	-3.56
9H-4	70.71	70.94	70.82	15	92	1,395	0.84	172	2.9	2.2	2.3	2.2	-3.77
9H-7	73.08	73.20	73.14	17	36	630	0.75	164	2.6	0.3	2.6	0.93	-3.64
10H-9	83.30	83.53	83.41	10	299	6,245	0.86	78	2.7	12	1.2	1.44	-4.01
10H-12	85.43	85.59	85.51	20	167	315	0.54	251	1.67	0.6	3.4	1.80	-3.18
11H-2	82.86	82.95	82.91	30	3,894	192	0.40	213	1.68	1.2	2.5	1.21	-3.07
11H-10	88.10	88.33	88.22	11	293	1,194	0.74	60	2.6	2.8	1.0	4.2	-4.09
13H-8	94.88	95.11	94.99	8.5	32	145	0.70	109	2.5	0.5	2.9	1.89	-4.00
13H-10	95.93	96.03	95.98	24	2,937	2,400	0.59	435	2.1	6.2	5.0	2.2	-3.27
14H-6	102.71	102.94	102.82	10	46	556	0.76	33	2.6	4.9	0.6	3.1	-4.13
15H-2	101.96	102.13	102.05	12	47	310	0.72	58	2.9	0.8	1.0	0.93	—
15H-5	103.32	103.55	103.44	—	—	—	—	—	—	—	—	—	-4.13
16H-5	112.35	112.57	112.46	15	307	1,552	0.75	109	3.2	4.3	1.3	1.29	-4.22
18H-6	126.23	126.50	126.36	12	66	136	0.76	54	3.0	0.4	1.1	1.13	-4.30
21H-5	134.40	134.70	134.55	10	685	6,465	0.71	76	3.2	2.6	1.7	1.41	-3.93
22X-5	144.08	144.36	144.22	—	—	—	—	—	—	—	—	—	-4.13
23X-2	149.72	149.79	149.75	16	438	1,885	0.37	104	1.32	1.7	3.7	0.68	-2.55
23X-4	150.38	150.65	150.51	22	1,161	1,011	0.79	106	3.1	2.4	2.7	1.63	-4.14

Table T13 (continued).

Core, section	Depth CSF (m)			V (nM)	Cu (nM)	Zn (nM)	Rb (μ M)	Mo (μ M)	Cs (nM)	Pb (nM)	U (nM)	Y (pM)	$\delta^{18}\text{O}$ (‰)
	Top	Bottom	Depth										
24X-4	160.96	161.39	161.17	33	664	222	0.84	172	3.4	1.0	6.3	1.01	-4.21
24X-5	161.39	161.47	161.43	30	7,942	328	0.52	121	2.1	3.3	5.3	1.26	-3.25
25X-2	167.38	167.44	167.41	20	14,620	213	0.69	97	2.9	1.4	2.5	1.68	-3.71
25X-9	171.59	171.92	171.76	13	1,982	165	0.88	117	3.4	0.7	1.3	0.93	-4.24

Notes: CSF = core depth below seafloor. — = not analyzed.

Table T14. Headspace gas composition from safety monitoring analysis in sediments, Site C0008. (See table notes.)

Core, section, interval (cm)	Depth CSF (m)	Headspace gas (ppmv)		
		Methane	Ethane	C ₁ /C ₂
316-C0008A-				
1H-1, 136.5–140.5	1.39	12.2	0.0	—
2H-1, 137.5–141.5	8.33	8,985.0	2.7	3,374
3H-1, 139.5–143.5	16.92	16,611.1	4.7	3,538
4H-1, 129.5–133.5	26.32	43,903.7	8.1	5,451
5H-1, 128–132	35.80	6,864.6	3.1	2,233
6H-1, 129–133	45.31	6,393.5	2.4	2,615
7H-1, 127.5–131.5	54.80	8,529.3	2.1	4,107
8H-1, 129–133	64.31	4,954.8	2.6	1,920
9H-1, 126.5–130.5	73.79	3,482.3	1.8	1,907
10H-1, 94–98	82.96	5,746.6	4.3	1,324
11H-1, 137–141	91.89	6,817.5	3.2	2,131
12H-1, 86.5–90.5	100.89	5,274.5	3.8	1,399
13H-1, 137.5–141.5	110.90	2,953.0	3.9	759
15H-3, 95–99	121.45	6,701.3	4.9	1,369
16H-1, 38.5–42.5	127.88	4,946.0	8.5	579
17H-2, 126.5–130.5	132.44	6,112.8	9.9	619
18H-1, 128–132	141.69	12,011.4	18.1	665
19H-1, 145–149	151.36	7,764.4	7.8	998
20H-1, 126.5–130.5	154.04	7,730.3	7.5	1,027
21H-1, 136.5–140.5	160.12	1,766.6	4.2	423
22H-2, 127–131	169.79	6,637.6	5.3	1,256
23H-1, 126.5–130.5	179.02	4,730.8	5.0	952
24H-2, 126–130	188.97	3,916.8	10.1	387
25H-1, 143.5–147.5	198.19	5,536.5	8.6	647
26H-1, 128–132	202.19	6,158.3	8.8	702
27H-1, 127–131	211.68	5,389.8	7.8	687
28H-1, 127–131	221.18	10,751.4	5.3	2,018
29X-1, 127–131	226.04	6,935.1	4.0	1,753
30X-6, 80.5–84.5	240.14	1,786.9	2.4	735
31X-2, 124.5–128.5	246.24	26,013.4	6.2	4,192
32X-2, 130–134	255.82	11,800.9	3.9	3,021
33X-1, 127.5–131.5	264.05	6,100.0	5.3	1,148
34X-1, 54.5–58.5	272.82	5,604.5	2.9	1,905
35X-1, 19.5–23.5	281.97	6,952.7	2.5	2,800
36X-1, 19.5–23.5	291.47	7,952.3	0.0	—
38X-1, 42–46	310.69	4,065.8	0.0	—
316-C0008B-				
1H-1, 137.5–141.5	1.40	18.7	0.0	—
316-C0008C-				
1H-1, 139–143	1.41	24.7	0.0	—
2H-1, 127–131	6.80	16,474.5	0.0	—
3H-1, 130–134	16.33	27,087.8	0.0	—
4H-2, 126–130	26.74	10,334.3	0.0	—
5H-2, 96.5–100.5	35.38	7,468.0	0.0	—
6H-1, 126–130	44.79	12,377.5	0.0	—
7H-2, 126–130	54.94	8,383.5	0.0	—
9H-2, 64.5–68.5	69.27	5,188.3	0.0	—
10H-1, 27–31	77.30	3,045.7	0.0	—
11H-4, 63–67	83.51	8,217.3	0.0	—
13H-1, 22.5–26.5	91.51	7,295.1	0.0	—
14H-1, 116–120	98.77	709.6	0.0	—
15H-1, 23–27	101.94	12,289.6	0.0	—
16H-1, 75–79	109.06	953.4	0.0	—
17H-1, 99.5–103.5	115.61	5,515.9	0.0	—
18H-1, 128–132	121.19	2,926.9	0.0	—
20H-1, 58–62	129.99	11,492.7	0.0	—
21H-1, 119.5–123.5	131.32	9,415.7	3.9	2,405
22X-1, 126.5–130.5	140.39	5,997.0	2.7	2,220
23X-1, 107.5–111.5	149.70	11,990.8	6.7	1,782
24X-1, 84–88	158.14	9,147.9	8.7	1,048
25X-1, 54.5–58.5	167.36	3,816.9	11.8	323

Notes: CSF = core depth below seafloor. — = not applicable.

Table T15. Hydrocarbon gas concentration from additional headspace gas analysis, Site C0008. (See table notes.) (Continued on next three pages.)

Core, section, interval (cm)	Depth CSF (m)	Headspace gas (ppmv)			Headspace gas (μ M)	
		Methane	Ethane	C ₁ /C ₂	Methane	Ethane
316-C0008A-						
1H-1, 136.5–140.5	1.39	17.9	0.0	—	3.22	0.00
1H-4, 94–98	2.82	41.0	0.0	—	6.73	0.00
1H-5, 136.5–140.5	4.22	62.1	0.0	—	10.21	0.00
1H-6, 115–119	5.41	871.2	1.9	452	144.3	0.32
1H-8, 111.5–115.5	6.79	5,305.3	3.5	1,518	876.8	0.58
2H-1, 137.5–141.5	8.33	9,163.0	4.9	1,889	1,510.1	0.80
2H-3, 116.5–120.5	9.76	15,866.1	6.1	2,583	2,634.3	1.02
2H-4, 139.5–143.5	11.20	24,091.9	7.5	3,192	4,009.0	1.26
2H-5, 139–143	12.63	36,845.2	9.4	3,901	6,144.8	1.58
2H-6, 139–143	14.06	44,166.8	10.5	4,220	7,382.1	1.75
2H-7, 116.5–120.5	15.26	50,933.0	10.8	4,718	8,517.3	1.81
2H-9, 124–128	16.92	20,081.5	6.1	3,315	3,371.2	1.02
3H-1, 39.5–43.5	16.92	52,954.8	11.2	4,739	8,473.8	1.79
3H-2, 143–147	18.39	48,827.7	10.4	4,709	7,448.1	1.58
3H-4, 124–128	19.90	53,774.9	11.3	4,761	9,068.5	1.90
3H-7, 14–18	22.96	50,289.6	9.8	5,117	8,196.3	1.60
3H-5, 142.5–146.5	21.37	42,086.9	9.6	4,363	7,113.2	1.63
3H-9, 116–120	24.40	25,669.6	7.1	3,622	4,397.8	1.21
3H-10, 114–118	25.58	9,177.0	4.2	2,162	1,642.3	0.76
4H-1, 129.5–133.5	26.32	15,322.5	4.7	3,233	3,029.4	0.94
4H-3, 149.5–153.5	29.16	37,155.8	8.3	4,491	5,898.1	1.31
4H-5, 111–115	30.54	39,015.5	8.7	4,504	6,148.0	1.36
4H-7, 131–135	33.27	19,867.5	5.6	3,555	4,286.8	1.21
4H-8, 127–131	34.58	9,681.1	4.0	2,422	1,798.7	0.74
5H-1, 128–132	35.80	11,658.1	4.2	2,772	2,283.4	0.82
5H-3, 117–121	38.42	16,880.9	4.6	3,698	3,990.2	1.08
5H-5, 106–110	40.02	25,916.9	6.3	4,140	5,468.0	1.32
5H-7, 127–131	42.66	18,262.6	6.3	2,904	3,829.8	1.32
5H-8, 127–131	43.98	7,810.7	3.6	2,189	1,839.5	0.84
6H-1, 129–133	45.31	6,913.2	2.6	2,696	2,113.2	0.78
6H-4, 105–109	49.25	17,070.6	4.5	3,761	3,644.9	0.97
6H-6, 129–133	50.81	30,585.9	7.2	4,232	5,008.9	1.18
6H-8, 126.5–130.5	53.42	8,688.9	3.9	2,237	2,001.8	0.89
7H-1, 127.5–131.5	54.80	7,161.5	2.6	2,803	1,427.1	0.51
7H-4, 110.5–114.5	58.61	10,352.0	4.1	2,528	2,114.4	0.84
7H-6, 139–143	60.25	13,896.8	5.1	2,705	2,869.4	1.06
7H-8, 125–129	62.89	8,663.2	3.3	2,652	1,795.0	0.68
8H-1, 129–133	64.31	6,347.6	3.5	1,795	1,511.5	0.84
8H-4, 127–131	68.23	9,026.4	4.3	2,088	1,956.7	0.94
8H-7, 126–130	70.85	3,422.3	1.8	1,912	1,110.4	0.58
9H-1, 126.5–130.5	73.79	6,557.5	2.5	2,638	1,610.4	0.61
9H-3, 129–133	76.43	6,668.8	2.3	2,962	1,557.6	0.53
9H-4, 107–111	77.54	5,382.0	2.4	2,264	1,258.8	0.56
10H-2, 94–98	83.50	6,565.1	4.5	1,459	1,546.6	1.06
10H-4, 138–142	86.07	6,867.6	4.0	1,708	1,808.6	1.06
10H-5, 110–114	87.21	7,587.3	3.5	2,171	1,779.7	0.82
10H-7, 137–141	88.90	7,726.9	3.2	2,381	1,653.3	0.69
11H-1, 137–141	91.89	6,892.8	3.4	2,027	1,699.5	0.84
11H-3, 137–141	94.71	6,809.2	3.1	2,195	1,901.4	0.87
11H-6, 147–151	97.68	8,781.4	3.8	2,303	2,675.6	1.16
11H-7, 137–141	99.09	5,558.5	3.0	1,868	1,768.3	0.95
12H-1, 86.5–90.5	100.89	6,072.2	4.4	1,376	1,353.1	0.98
12H-2, 136.5–140.5	102.29	6,521.0	4.0	1,622	2,041.1	1.26
12H-4, 115.5–119.5	104.90	7,106.5	4.0	1,779	1,587.8	0.89
12H-6, 119–123	106.40	9,301.4	3.9	2,399	2,352.4	0.98
13H-1, 137.5–141.5	110.90	4,364.3	3.5	1,251	1,555.1	1.24
13H-3, 137.5–141.5	113.72	15,191.1	7.7	1,970	4,581.4	2.33
13H-4, 101–105	114.77	7,016.6	6.6	1,063	1,453.1	1.37
13H-7, 95–99	117.45	10,129.7	4.7	2,159	2,476.6	1.15
15H-3, 95–99	121.45	10,211.6	7.1	1,436	2,083.3	1.45
15H-5, 130–134	124.10	7,502.7	9.1	821	1,875.7	2.28
15H-7, 127–131	126.72	13,113.9	18.2	721	2,898.7	4.02
16H-1, 38.5–42.5	127.88	7,272.7	9.0	809	1,978.7	2.45
16H-4, 0–4	128.84	7,935.3	7.0	1,137	2,753.2	2.42
17H-2, 126.5–130.5	132.44	7,514.6	8.7	864	2,076.5	2.40
17H-5, 100.5–104.5	136.12	8,945.0	11.5	776	2,332.7	3.01

Table T15 (continued). (Continued on next page.)

Core, section, interval (cm)	Depth CSF (m)	Headspace gas (ppmv)			Headspace gas (μM)	
		Methane	Ethane	C_1/C_2	Methane	Ethane
17H-8, 127.5–131.5	139.03	9,749.9	13.9	702	1,897.8	2.70
18H-1, 91.5–95.5	141.33	45,321.0	43.0	1,055	15,049.7	14.27
18H-2, 126.5–130.5	143.00	5,103.2	5.9	870	1,505.9	1.73
18H-5, 110.5–114.5	145.46	6,665.0	11.0	605	1,970.7	3.26
19H-1, 145–149	151.36	7,458.6	10.0	745	1,878.3	2.52
19H-3, 84.5–88.5	152.52	5,356.9	7.8	685	1,592.6	2.32
20H-1, 126.5–130.5	154.04	8,455.8	10.7	789	1,746.3	2.21
20H-2, 101–105	155.09	7,671.4	10.2	751	2,285.1	3.04
20H-5, 96.5–100.5	157.69	10,876.0	12.3	882	2,041.3	2.31
21H-1, 136–140	160.11	1,357.2	2.8	490	413.4	0.84
21H-2, 126–130	161.42	8,163.1	9.7	840	2,029.1	2.42
21H-4, 114–118	164.10	3,380.5	9.1	372	965.1	2.59
21H-8, 127–131	168.49	9,552.5	10.2	933	2,388.3	2.56
22H-1, 127.5–131.5	169.53	4,182.8	6.7	626	995.6	1.59
22H-2, 127–131	169.79	9,992.4	14.4	696	1,933.2	2.78
22H-5, 107.5–111.5	173.60	4,536.5	7.9	578	1,340.1	2.32
22H-9, 127–131	177.82	11,566.2	14.4	803	2,275.8	2.83
23H-1, 126.5–130.5	179.02	3,454.1	5.2	667	1,044.8	1.57
23H-3, 127.5–131.5	181.65	10,955.1	15.3	716	2,087.3	2.92
23H-4, 33–37	182.02	4,466.1	6.4	699	1,252.7	1.79
24H-3, 128–132	190.29	10,287.4	8.9	1,162	2,378.2	2.05
24H-5, 99–103	192.76	12,754.4	13.8	926	2,557.2	2.76
24H-8, 132–136	195.80	8,053.1	9.9	817	2,973.5	3.64
25H-1, 143.5–147.5	198.19	7,738.7	7.0	1,108	1,926.1	1.74
25H-3, 99.5–103.5	198.51	6,487.2	11.1	586	1,614.6	2.75
25H-4, 127–131	199.54	2,855.1	4.2	679	675.5	0.99
26H-1, 128–132	200.89	8,536.6	11.6	733	1,899.9	2.59
26H-3, 34–38	202.54	14,162.1	9.3	1,530	5,381.9	3.52
27H-1, 127–131	210.39	4,894.2	5.2	943	1,801.3	1.91
27H-2, 127.5–131.5	211.70	10,541.7	10.4	1,012	2,093.6	2.07
27H-4, 127–131	214.33	10,039.9	7.8	1,294	2,480.8	1.92
27H-7, 126–130	216.96	10,413.4	6.8	1,537	2,431.4	1.58
28X-2, 98–102	221.20	13,305.5	9.8	1,359	4,267.9	3.14
28X-4, 129–133	222.52	11,257.2	10.0	1,127	2,158.4	1.92
29X-2, 83–87	226.06	4,635.9	3.3	1,404	1,427.2	1.02
29X-4, 97.5–101.5	228.25	4,804.1	4.2	1,151	1,568.9	1.36
29X-7, 128–132	230.89	8,213.0	7.5	1,092	1,577.4	1.44
31X-3, 131–135	246.26	8,261.7	5.9	1,405	2,589.9	1.84
31X-5, 91.5–95.5	248.97	9,996.1	6.9	1,451	2,275.6	1.57
31X-8, 127.5–131.5	251.62	5,380.1	4.6	1,176	1,277.0	1.09
32X-3, 127–131	255.82	9,670.7	6.7	1,435	1,978.1	1.38
32X-6, 91.5–95.5	259.77	9,187.1	5.3	1,729	2,007.3	1.16
32X-9, 128–132	262.40	4,806.3	2.1	2,252	1,726.7	0.77
33X-2, 127.5–131.5	264.07	6,848.4	3.7	1,835	1,440.4	0.78
33X-3, 127.5–131.5	265.38	8,292.6	3.6	2,288	1,955.9	0.86
33X-5, 93.5–97.5	267.03	11,045.6	3.7	2,953	2,688.2	0.91
34X-1, 54.5–58.5	272.25	3,716.8	0.0	—	1,689.0	0.00
35X-1, 19.5–23.5	281.75	10,918.8	3.7	2,926	3,558.2	1.22
36X-1, 19.5–23.5	291.25	5,114.2	0.0	—	1,480.9	0.00
38X-1, 44–48	310.25	10,328.1	3.0	3,468	2,078.9	0.60
316-C0008B-						
1H-1, 137.5–141.5	1.40	33.4	0.0	—	5.6	0.00
1H-2, 137–141	2.81	76.3	0.0	—	20.6	0.00
1H-3, 137–141	4.22	196.6	0.0	—	32.7	0.00
1H-4, 137.5–141.5	5.63	1,353.6	0.0	—	259.5	0.00
1H-6, 116–120	7.06	18,566.1	2.1	8,720	3,135.1	0.36
1H-7, 137.5–141.5	8.48	23,898.2	1.8	13,005	3,993.4	0.31
1H-8, 105–109	9.57	19,115.3	0.0	—	3,777.2	0.00
316-C0008C-						
1H-1, 139–143	1.41	29.1	0.0	—	5.4	0.00
1H-3, 115–119	2.84	78.1	0.0	—	12.0	0.00
1H-4, 137.5–141.5	4.25	203.7	0.0	—	31.8	0.00
1H-6, 89–93	5.40	5,053.2	0.0	—	805.7	0.00
2H-1, 127–131	6.80	12,800.6	0.0	—	2,070.9	0.00
2H-3, 107–111	8.14	28,754.2	2.3	12,356	4,687.2	0.38
2H-4, 128.5–132.5	9.47	39,545.4	2.5	15,607	6,204.9	0.40
2H-5, 130.5–134.5	10.81	37,263.6	2.2	16,921	5,889.8	0.35
2H-6, 132–136	12.17	47,666.8	2.5	19,277	7,548.9	0.39

Table T15 (continued). (Continued on next page.)

Core, section, interval (cm)	Depth CSF (m)	Headspace gas (ppmv)			Headspace gas (μ M)	
		Methane	Ethane	C ₁ /C ₂	Methane	Ethane
2H-8, 109-113	13.54	41,891.7	2.1	20,406	6,704.7	0.33
2H-9, 128-132	14.86	30,077.6	2.5	12,062	4,839.0	0.40
2H-10, 51-55	15.41	32,367.7	2.1	15,341	5,465.9	0.36
3H-1, 130-134	16.33	26,226.4	1.7	15,576	4,241.9	0.27
3H-2, 133.5-137.5	17.71	20,737.3	1.7	12,267	3,762.7	0.31
3H-4, 104.5-108.5	19.04	15,012.6	0.0	—	4,368.7	0.00
3H-5, 138.5-142.5	20.61	26,601.8	0.0	—	4,788.3	0.00
3H-6, 127-131	21.92	30,601.8	0.0	—	6,095.6	0.00
3H-8, 107-111	23.26	17,027.8	0.0	—	3,771.1	0.00
3H-9, 127-131	24.57	13,133.6	0.0	—	2,633.4	0.00
3H-10, 72-76	25.33	5,111.7	0.0	—	931.1	0.00
4H-2, 126-130	26.74	11,211.8	0.0	—	2,259.1	0.00
4H-4, 127.5-131.5	29.37	8,339.1	0.0	—	1,826.4	0.00
4H-7, 127-131	32.00	10,442.9	0.0	—	1,839.2	0.00
4H-9, 127-131	34.63	7,253.4	0.0	—	1,617.7	0.00
5H-2, 96.5-100.5	35.38	7,290.5	0.0	—	1,273.7	0.00
5H-4, 129-133	38.02	7,352.1	0.0	—	1,563.5	0.00
5H-7, 126.5-130.5	40.58	4,871.5	0.0	—	1,392.9	0.00
5H-9, 97-101	42.84	2,353.2	0.0	—	494.1	0.00
6H-2, 144.5-148.5	46.28	16,712.6	0.0	—	3,455.0	0.00
6H-3, 139.5-143.5	47.71	18,615.2	0.0	—	3,020.6	0.00
6H-6, 127.5-131.5	50.35	9,958.7	0.0	—	2,400.9	0.00
6H-7, 126.5-130.5	51.66	6,893.9	0.0	—	1,381.5	0.00
7H-3, 87-91	55.85	9,212.1	1.9	4,857	2,156.9	0.44
7H-6, 127-131	58.49	9,622.9	0.0	—	1,934.2	0.00
7H-8, 127-131	61.10	7,391.0	0.0	—	1,504.9	0.00
9H-3, 138-142	70.69	8,448.3	0.0	—	1,825.4	0.00
9H-6, 108.5-112.5	73.06	6,445.4	0.0	—	2,158.6	0.00
9H-8, 0-4	73.22	6,278.3	0.0	—	1,676.3	0.00
9H-9, 130-134	75.90	11,431.9	0.0	—	2,099.1	0.00
10H-3, 126.5-130.5	79.84	5,408.7	0.0	—	1,224.3	0.00
10H-5, 48-52	81.37	6,334.7	0.0	—	1,783.6	0.00
10H-8, 115-119	83.28	7,423.8	0.0	—	1,684.8	0.00
11H-4, 63-67	84.20	6,500.5	0.0	—	1,640.3	0.00
10H-11, 55-59	85.41	9,123.8	0.0	—	1,971.4	0.00
11H-6, 30-34	85.34	6,549.0	0.0	—	1,849.4	0.00
11H-9, 127-131	88.08	11,092.6	2.1	5,392	2,661.0	0.49
13H-1, 24.5-28.5	91.53	3,011.6	1.1	2,857	724.2	0.25
11H-13, 97-101	92.18	7,587.6	0.0	—	1,925.5	0.00
13H-3, 58.5-62.5	92.21	7,767.2	2.0	3,862	1,458.6	0.38
13H-7, 107-111	94.86	9,096.9	2.5	3,614	1,711.3	0.47
13H-11, 117-121	97.22	10,778.0	2.7	3,968	2,234.6	0.56
14H-3, 126.5-130.5	100.86	4,709.8	1.4	3,487	1,202.0	0.34
15H-1, 23-27	101.94	9,368.2	2.1	4,562	1,841.4	0.40
14H-5, 99-103	102.68	4,344.6	1.7	2,492	1,525.2	0.61
15H-4, 74.5-78.5	103.30	9,108.2	3.1	2,895	2,283.9	0.79
14H-10, 74-78	106.57	8,530.5	1.8	4,765	2,466.9	0.52
15H-8, 122-126	107.51	4,218.6	1.7	2,463	1,173.2	0.48
16H-2, 119-123	110.29	6,228.2	1.8	3,519	1,668.0	0.47
16H-4, 127-131	112.33	7,098.0	2.1	3,383	1,556.0	0.46
17H-2, 47-51	116.12	6,770.2	2.1	3,257	1,393.8	0.43
16H-11, 127-131	118.08	9,963.8	3.0	3,314	2,879.1	0.87
18H-1, 128-132	121.19	5,019.2	2.1	2,373	1,492.3	0.63
18H-3, 127-131	123.83	9,977.4	3.0	3,366	2,102.8	0.62
18H-5, 103-107	126.22	8,330.8	2.4	3,490	1,595.3	0.46
18H-7, 128-132	127.80	10,073.2	4.1	2,443	2,073.6	0.85
20H-1, 58-62	129.99	6,500.4	1.6	4,146	1,559.2	0.38
21H-1, 119.5-123.5	131.32	7,570.2	4.6	1,631	1,801.7	1.10
21H-4, 81-85	134.38	10,660.4	6.3	1,689	2,300.5	1.36
21H-7, 94.5-98.5	136.98	10,023.1	7.3	1,381	2,246.9	1.63
22X-1, 126.5-130.5	140.39	6,314.9	3.2	1,995	1,560.3	0.78
22X-4, 100-104	144.06	6,856.1	4.2	1,625	1,324.5	0.81
22X-7, 106.5-110.5	146.65	7,680.5	4.9	1,559	1,806.7	1.16
23X-1, 107.5-111.5	149.70	8,109.6	5.9	1,384	2,674.2	1.93
23X-3, 55-59	150.36	2,297.1	2.8	808	992.2	1.23
23X-5, 101-105	151.68	1,795.4	1.2	1,457	364.9	0.25
23X-7, 140.5-144.5	154.44	11,374.1	12.2	930	2,551.9	2.75
24X-1, 84-88	158.14	10,543.6	14.8	710	3,096.5	4.36
24X-3, 127-131	160.94	3,978.6	6.7	590	1,169.8	1.98

Table T15 (continued).

Core, section, interval (cm)	Depth CSF (m)	Headspace gas (ppmv)			Headspace gas (μ M)	
		Methane	Ethane	C ₁ /C ₂	Methane	Ethane
24X-6, 80–84	162.29	4,207.6	7.0	602	1,237.8	2.06
24X-9, 128–132	166.24	5,318.6	14.1	377	1,567.0	4.16
25X-3, 94.5–98.5	168.41	3,803.0	12.6	302	1,346.0	4.45
25X-8, 127.5–131.5	171.57	5,595.6	13.9	402	1,652.1	4.11
25X-11, 127–131	174.21	5,922.4	11.6	511	1,653.8	3.24
25X-13, 41–45	175.97	8,595.2	14.8	581	2,864.2	4.93

Notes: CSF = core depth below seafloor. — = not applicable.

Table T16. Carbonate, carbon, nitrogen, and sulfur in sediments, Site C0008. (See table notes.)

Core, section, interval (cm)	Depth CSF (m)	CaCO ₃ (wt%)	TOC (wt%)	TN (wt%)	C/N	TS (wt%)	Core, section, interval (cm)	Depth CSF (m)	CaCO ₃ (wt%)	TOC (wt%)	TN (wt%)	C/N	TS (wt%)
316-C0008A-							28H-3, 0-1.5	222.23	8.77	0.53	0.069	7.65	0.40
1H-3, 0-1.5	1.64	15.03	0.70	0.074	9.53	0.42	28H-4, 51-52.5	223.04	0.35	0.33	0.058	5.67	0.85
1H-7, 0-1.5	5.44	9.03	0.59	0.065	9.04	0.38	29X-5, 0-33	229.41	5.35	0.42	0.055	7.60	0.70
2H-2, 0-1.5	8.35	23.45	0.65	0.069	9.48	0.23	30X-7, 0-36	240.34	1.48	0.31	0.048	6.44	0.70
2H-8, 0-1.5	15.44	14.45	0.49	0.060	8.07	0.48	31X-6, 0-1.5	249.93	0.61	0.33	0.049	6.72	0.79
3H-1, 55-56.5	16.06	7.02	0.41	0.052	7.82	0.80	32X-7, 0-1.5	260.73	2.74	0.28	0.035	8.01	0.61
3H-3, 0-1.5	18.41	12.20	0.45	0.063	7.17	0.49	33X-4, 0-1.5	266.70	1.53	0.26	0.042	6.21	0.71
3H-8, 0-1.5	22.99	20.54	0.37	0.056	6.50	0.29	316-C0008B-						
3H-10, 98.5-100	25.41	6.83	0.40	0.055	7.23	0.55	1H-5, 0-1.5	5.66	19.98	0.45	0.063	7.20	0.47
4H-4, 0-1.5	29.19	9.49	0.42	0.062	6.75	0.69	316-C0008C-						
4H-6, 32.5-34	30.89	7.82	0.47	0.062	7.60	0.63	1H-2, 0-1.5	1.44	12.79	0.68	0.082	8.30	0.69
4H-9, 59-60.5	35.20	10.83	0.53	0.066	8.04	0.33	1H-5, 0-1.5	4.28	16.30	0.51	0.068	7.54	0.36
5H-4, 0-1.5	38.73	2.05	0.55	0.075	7.35	0.41	2H-2, 0-1.5	6.83	20.91	0.59	0.069	8.56	0.33
5H-6, 72-73.5	40.76	12.84	0.52	0.069	7.49	0.55	2H-7, 0-1.5	12.20	22.36	0.45	0.064	7.02	0.30
6H-3, 59-60.5	47.36	2.72	0.45	0.063	7.19	0.09	3H-3, 0-1.5	17.73	3.20	0.40	0.055	7.16	0.66
6H-5, 0-1.5	49.28	2.87	0.54	0.067	8.08	0.06	3H-4, 28-29.5	21.94	2.58	0.42	0.063	6.72	0.69
6H-6, 100-101.5	50.50	4.85	0.43	0.063	6.78	0.39	3H-5, 35-36.5	29.40	4.97	0.40	0.061	6.44	0.84
7H-3, 28-29.5	56.46	2.41	0.47	0.068	6.92	0.04	3H-7, 0-1.5	38.03	18.33	0.35	0.059	5.97	0.54
7H-5, 0-1.5	58.63	1.46	0.32	0.041	7.64	0.77	3H-10, 65-66.5	47.74	5.37	0.54	0.079	6.86	0.66
7H-8, 113-114.5	62.75	1.06	0.15	0.026	5.71	0.64	4H-5, 0-1.5	55.88	10.29	0.56	0.078	7.14	0.77
8H-4, 72-73.5	67.67	2.66	0.60	0.062	9.56	0.11	4H-6, 24-25.5	18.26	7.60	0.55	0.077	7.13	0.76
8H-5, 0-1.5	68.26	8.09	0.45	0.074	6.05	0.07	5H-2, 18-19.5	19.56	1.89	0.45	0.065	6.89	0.86
9H-3, 107-108.5	76.20	5.91	0.63	0.066	9.55	0.12	5H-4, 20-21.5	25.24	5.60	0.42	0.072	5.82	0.71
9H-5, 0-1.5	77.57	3.89	0.44	0.047	9.20	0.10	5H-5, 0-1.5	70.71	7.63	0.54	0.080	6.76	0.67
10H-6, 0-1.5	87.23	5.30	0.58	0.077	7.57	0.08	6H-2, 100-101.5	29.86	10.53	0.36	0.068	5.32	0.42
10H-7, 31.5-33	87.83	9.73	0.50	0.072	6.92	0.11	6H-3, 50-51.5	83.30	10.40	0.41	0.065	6.27	0.43
10H-8, 125-126.5	90.18	14.72	0.40	0.067	6.02	0.07	6H-4, 0-1.5	34.58	14.16	0.57	0.086	6.63	0.30
11H-4, 0-1.5	94.73	4.45	0.61	0.065	9.41	0.19	7H-4, 0-1.5	36.92	1.76	0.42	0.048	8.78	0.66
11H-5, 49-50.5	95.51	6.94	0.68	0.085	7.97	0.17	7H-8, 129.5-131	102.71	3.33	0.31	0.061	5.10	0.23
11H-6, 28-29.5	96.47	4.01	0.70	0.060	11.68	0.31	7H-9, 15-16.5	94.88	3.63	0.35	0.061	5.70	0.08
11H-7, 31.5-33	98.02	7.82	0.48	0.071	6.68	0.03	9H-3, 58.5-60	88.11	1.82	0.57	0.072	7.84	0.07
12H-5, 0-1.5	104.92	2.86	0.67	0.063	10.69	0.23	9H-4, 0-1.5	103.33	1.38	0.69	0.080	8.59	0.05
12H-6, 98.5-100	106.18	6.17	0.40	0.061	6.50	0.08	9H-5, 70-71.5	112.35	4.12	0.50	0.062	8.15	0.60
13H-5, 0-1.5	114.80	7.52	0.42	0.063	6.62	0.42	10H-9, 0-1.5	45.82	4.70	0.44	0.077	5.68	0.09
15H-2, 0-1.5	120.15	4.23	0.61	0.070	8.75	0.14	10H-10, 45-46.5	46.80	8.46	0.31	0.055	5.69	0.35
16H-4, 0-1.5	128.82	9.74	0.46	0.067	6.84	0.14	11H-3, 12.5-14	126.23	12.27	0.50	0.078	6.40	0.12
16H-5, 33.5-35	129.44	4.24	0.39	0.055	6.98	0.65	11H-8, 113.5-115	61.11	5.95	0.70	0.085	8.28	0.76
17H-6, 0-1.5	136.15	3.98	0.52	0.068	7.67	0.07	11H-10, 0-1.5	61.28	5.21	0.50	0.070	7.11	0.16
17H-7, 21.5-23	136.64	3.82	0.48	0.065	7.28	0.10	13H-7, 48.5-50	69.88	5.28	0.42	0.065	6.42	0.04
17H-8, 23.5-25	137.98	3.40	0.49	0.068	7.28	0.04	13H-7, 91-92.5	71.65	7.97	0.47	0.071	6.70	0.07
18H-3, 0-1.5	143.02	1.61	0.14	0.034	3.99	0.01	13H-8, 0-1.5	83.98	5.02	0.40	0.072	5.64	0.06
18H-3, 25.5-27	143.28	3.50	0.23	0.042	5.54	0.02	14H-6, 0-1.5	134.41	8.93	0.35	0.060	5.91	0.60
19H-2, 0-1.5	151.39	6.65	0.41	0.055	7.53	0.29	15H-5, 0-1.5	83.08	5.48	0.44	0.065	6.74	0.36
20H-3, 0-1.5	155.11	8.70	0.52	0.076	6.80	0.11	16H-5, 0-1.5	86.59	0.21	0.43	0.069	6.16	0.07
20H-4, 94.5-96	156.33	11.47	0.61	0.081	7.52	0.05	18H-1, 35.5-37	94.26	1.18	0.45	0.068	6.64	0.40
20H-5, 34.5-36	157.06	2.40	0.49	0.071	6.86	0.16	18H-4, 42-42.5	94.68	1.56	0.47	0.055	8.56	0.73
21H-3, 80-81.5	162.34	4.97	0.38	0.061	6.26	0.17	18H-6, 0-1.5	144.08	1.22	0.28	0.055	5.11	0.51
21H-4, 48-49.5	163.42	0.45	0.31	0.049	6.28	0.11	21H-4, 39.5-41	150.38	1.88	0.36	0.056	6.48	0.66
21H-5, 26-27.5	164.38	0.75	0.38	0.064	5.94	0.06	21H-5, 0-1.5	160.97	4.00	0.53	0.069	7.65	0.33
22H-5, 68.5-70	173.19	0.80	0.32	0.056	5.71	0.42	22X-5, 0-1.5	171.60	4.47	0.43	0.064	6.79	0.47
22H-6, 0-1.5	173.62	1.69	0.39	0.057	6.81	0.21	23X-4, 0-1.5	120.25	2.47	0.34	0.053	6.55	0.60
23H-3, 40-41.5	180.76	2.98	0.39	0.065	6.03	0.27	23X-6, 107.5-109	124.27	3.50	0.35	0.061	5.75	0.57
23H-5, 0-1.5	182.04	7.49	0.49	0.068	7.27	0.08	24X-3, 97.5-99	133.95	0.60	0.31	0.060	5.22	0.67
24H-2, 23.5-25	187.93	5.39	0.37	0.058	6.28	0.20	24X-4, 0-1.5	152.78	2.36	0.33	0.054	6.21	0.99
24H-4, 83-84.5	191.14	3.90	0.44	0.064	6.98	0.35	24X-10, 20-21.5	160.63	2.83	0.36	0.066	5.48	0.90
24H-6, 0-1.5	192.79	3.00	0.49	0.068	7.21	0.19	25X-9, 0-1.5	166.47	5.55	0.35	0.057	6.14	0.87
25H-2, 0-1.5	198.21	2.76	0.44	0.060	7.40	0.43	25X-10, 30.5-32	172.23	1.18	0.32	0.056	5.76	1.46
26H-2, 0-1.5	202.22	1.41	0.34	0.047	7.25	0.47	25X-11, 94.5-96	173.87	1.72	0.24	0.048	4.92	1.19
27H-1, 68-69.5	211.08	3.54	0.48	0.059	8.16	0.42							
27H-2, 35-36.5	212.06	3.67	0.48	0.062	7.71	0.62							
27H-5, 0-1.5	215.64	0.68	0.27	0.048	5.66	0.80							
28H-1, 88.5-90	220.78	7.58	0.31	0.058	5.45	0.47							
28H-2, 83-84.5	222.04	5.96	0.35	0.055	6.43	0.50							

Notes: CSF = core depth below seafloor. TOC = total organic carbon, TN = total nitrogen, TS = total sulfur.

Table T17. Sample depth and processing for microbiological and biogeochemical studies, Hole C0008A. (See table notes.) (Continued on next page.)

Core, section	Depth CSF (m)	Frozen		Anaerobic pack (4°C)	Slurry (-20°C)		Core, section	Depth CSF (m)	Frozen		Anaerobic pack (4°C)	Slurry (-20°C)	
		-80°C	-20°C		FISH	Acetone			-80°C	-20°C		FISH	Acetone
316-C0008A-							8H-6	69.68		X			X
1H-1	0.13	X				X	9H-2	75.22	X				X
1H-1	1.50	X				X	9H-4	77.66	X				X
1H-3	1.95	X				X	9H-6	78.03	X			X	X
1H-4	2.16	X				X	9H-6	78.18			X		
1H-4	2.29			X			9H-6	78.18		X			
1H-4	2.43	X		X		X	9H-6	78.22			X		
1H-4	2.50	X					9H-6	78.28	X				
1H-4	2.56			X			9H-6	78.42	X		X		X
1H-4	2.60		X				10H-3	84.77	X				X
1H-5	4.34	X				X	10H-7	89.03	X				X
1H-8	6.27		X				11H-1	92.02	X				X
1H-8	6.30			X			11H-3	93.81			X		
1H-8	6.36	X					11H-3	93.96	X			X	X
1H-8	6.50	X		X		X	11H-3	94.16	X		X		X
1H-8	6.57			X			11H-3	94.23	X				
1H-8	6.71	X				X	11H-3	94.29			X		
1H-8	6.90	X				X	11H-3	94.33		X			
2H-1	7.26	X				X	11H-7	99.22	X				X
2H-1	7.41			X			12H-5	104.93		X			
2H-1	7.57	X		X		X	12H-4	105.02	X				X
2H-1	7.64	X					12H-6	106.53	X				X
2H-1	7.68		X				13H-3	113.84	X				X
2H-1	8.44	X				X	13H-7	117.58	X				X
2H-3	9.88	X				X	17H-4	119.17	X		X		X
2H-4	11.31	X				X	17H-4	119.81			X		
2H-5	12.74	X				X	15H-1	119.99	X			X	X
2H-6	14.17	X				X	15H-7	126.85	X			X	
2H-7	15.38	X				X	16H-1	128.00	X			X	
2H-9	16.29	X				X	17H-4	133.88	X			X	X
2H-9	16.44			X			17H-4	134.25	X				
2H-9	16.60	X		X		X	17H-4	134.31			X		
2H-9	16.67	X					17H-4	134.35		X			
2H-9	16.73			X			17H-4	134.68			X		
2H-9	16.76		X				21H-8	134.87	X		X		X
2H-9	17.04	X				X	17H-5	136.25	X				X
3H-1	17.04	X				X	17H-8	139.16	X				X
3H-4	20.03	X				X	18H-4	144.44	X				X
3H-6	21.99	X				X	18H-8	148.56	X				X
3H-6	22.14			X			19H-1	151.49	X				X
3H-6	22.29	X		X		X	20H-2	155.21	X				X
3H-6	22.36	X					21H-3	163.04	X				X
3H-6	22.42			X			21H-8	167.95	X			X	X
3H-6	22.46		X				21H-8	168.10			X		
3H-9	24.52	X				X	21H-8	168.32	X				
4H-2	27.75	X				X	21H-8	168.38			X		
4H-6	32.05	X				X	21H-8	168.42		X			
5H-2	37.33	X				X	22H-3	171.20	X				X
5H-6	40.14	X				X	22H-6	173.76		X			
5H-6	40.29			X			22H-8	176.64	X				X
5H-6	40.37	X		X		X	23H-3	181.77	X				X
5H-6	40.51	X					24H-3	190.41	X				X
5H-6	40.57			X			24H-8	195.93	X				X
5H-6	40.61		X				25H-3	199.65	X				X
5H-7	42.79	X				X	26H-1	202.32	X				X
6H-3	48.23	X				X	27H-2	213.12	X				X
6H-4	49.38	X				X	23H-8	213.38	X		X		X
6H-7	52.23	X				X	27H-7	213.80		X			
7H-2	54.92	X				X	27H-7	213.84	X				
7H-2	55.07			X			27H-7	213.98	X		X		X
7H-2	55.15	X		X		X	27H-7	214.07			X		
7H-2	55.29	X					27H-7	214.22	X			X	X
7H-2	55.35			X			28H-2	222.33	X				X
7H-2	55.39		X				29X-4	229.33	X				X
7H-3	57.59	X				X	30X-6	240.27	X				X
7H-8	63.01	X				X	31X-3	246.36	X			X	X
8H-1	64.44	X				X	31X-3	246.51			X		

Table T17 (continued).

Core, section	Depth CSF (m)	Frozen		Anaerobic pack (4°C)	Slurry (-20°C)	
		-80°C	-20°C		FISH	Acetone
31X-3	246.67	X		X	X	
31X-3	246.74	X		X		
31X-3	246.78		X			
31X-5	250.03	X			X	
32X-3	257.24	X			X	
32X-9	263.83	X			X	
33X-2	265.49	X			X	
36X-CC	291.94	X			X	
38X-CC	310.99	X			X	

Notes: CSF = core depth below seafloor. FISH = fluorescence in situ hybridization.

Table T18. Summary of sample depth and processing for microbiological and biogeochemical studies, Holes C0008B and C0008C. (See table notes.) (Continued on next page.)

Core, section	Depth CSF (m)	Frozen		Anaerobic pack (4°C)	Slurry (-20°C)		Core, section	Depth CSF (m)	Frozen		Anaerobic pack (4°C)	Slurry (-20°C)	
		-80°C	-20°C		FISH	Acetone			-80°C	-20°C		FISH	Acetone
316-C0008B-							7H-5	56.35			X		
1H-1	0.01	X			X		9H-3	56.37	X			X	
1H-1	1.41	X			X		7H-5	56.51	X		X	X	
1H-2	2.82	X			X		7H-5	56.58	X				
1H-3	2.93	X			X	X	9H-4	59.93	X			X	
1H-3	3.08			X			7H-8	61.11	X			X	
1H-3	3.23	X		X	X		9H-6	70.40	X			X	
1H-3	3.30	X					9H-7	70.77	X			X	
1H-3	4.23	X			X		9H-4	70.82		X			
1H-4	5.64	X			X		10H-4	72.95	X			X	
1H-5	5.77		X				10H-5	73.59	X			X	
1H-6	7.07	X			X		9H-8	73.60	X			X	
1H-7	7.18	X			X	X	9H-8	73.75			X		
1H-7	7.33			X			9H-8	73.97	X				
1H-7	7.49	X		X	X		9H-8	74.90	X		X	X	
1H-7	7.56	X					10H-6	81.45	X		X	X	X
1H-7	8.49	X			X		7H-4	81.51		X			
1H-8	9.58	X			X		11H-2	82.91			X	X	
316-C0008C-							11H-7	85.40	X			X	
1H-1	1.42	X			X		10H-12	85.49	X			X	X
1H-2	1.55		X				11H-8	85.55	X			X	
1H-3	2.85	X			X		11H-8	85.70			X		
1H-4	2.96	X			X		11H-8	85.85	X		X	X	
1H-4	3.11			X			11H-8	85.92	X				
1H-4	3.26	X		X	X		10H-11	86.14	X			X	
1H-4	3.34	X					11H-10	88.22		X			
1H-4	4.26	X			X		13H-2	91.56	X			X	
1H-5	4.39		X				13H-5	92.40	X			X	
1H-6	5.41	X			X		13H-5	92.55			X		
2H-1	6.81	X			X		13H-5	92.70	X		X	X	
2H-2	6.94		X				13H-5	92.77	X			X	
2H-3	7.17	X		X	X		13H-6	93.74			X	X	
2H-3	7.30	X			X	X	13H-10	95.98		X			
2H-3	7.45			X	X		14H-3	100.87	X			X	
2H-3	8.15	X			X		15H-2	102.01			X	X	
2H-4	9.48	X			X		14H-8	104.46	X			X	
2H-5	9.59	X			X	X	14H-10	106.58	X			X	
2H-5	9.74			X			15H-8	107.52	X			X	
2H-5	9.89	X		X	X		16H-4	112.34	X			X	
2H-5	9.96	X					16H-5	112.46		X			
2H-5	10.82	X			X		16H-9	115.43	X			X	
2H-6	12.18	X			X		16H-11	116.89	X			X	
2H-8	13.55	X			X		16H-11	117.04			X		
2H-9	14.87	X			X		16H-11	117.19	X		X	X	
3H-1	16.34	X			X		16H-11	117.26	X				
3H-2	16.45	X			X	X	18H-3	123.84	X			X	
3H-2	16.60			X			18H-6	126.36		X			
3H-2	16.76	X		X	X		18H-7	127.81	X			X	
3H-2	16.83	X					20H-1	130.00	X			X	
3H-3	17.85		X				21H-3	132.76	X				
3H-5	20.62	X			X		21H-3	132.90	X			X	
3H-7	22.05		X				21H-3	133.05			X		
3H-8	23.27	X			X		21H-3	133.20	X		X	X	
4H-4	29.38	X			X		21H-4	134.39	X			X	
4H-5	29.50		X				21H-5	134.55		X			
4H-8	33.33	X			X		21H-7	137.00	X			X	
5H-2	35.39	X			X		22X-2	141.66	X			X	
5H-3	36.38	X			X		22X-8	147.54	X			X	
5H-3	36.46			X			23X-2	149.75	X			X	
5H-3	36.61	X			X	X	23X-4	150.51		X			
5H-3	36.74	X					23X-7	153.60			X		
5H-5	38.12		X				23X-7	153.75	X			X	
5H-7	40.59	X			X		23X-7	153.96	X		X	X	
6H-2	46.29	X			X		23X-7	154.03	X				
6H-7	51.67	X			X		23X-8	154.54			X	X	
7H-3	55.86	X			X		24X-3	160.95	X			X	
7H-5	56.20	X			X	X	24X-4	161.17		X			

Table T18 (continued).

Core, section	Depth CSF (m)	Frozen		Anaerobic pack (4°C)	Slurry (-20°C)	
		-80°C	-20°C		FISH	Acetone
24X-7	163.61	X			X	
25X-2	167.41	X			X	
25X-4	168.46	X			X	
25X-6	168.92			X		
25X-8	170.38	X			X	
25X-8	170.53			X		
25X-8	170.68	X		X	X	
25X-8	170.75	X				
25X-8	171.58	X			X	
25X-9	171.76		X			
25X-13	175.98	X			X	

Notes: CSF = core depth below seafloor. FISH = fluorescence in situ hybridization.

Table T19. Thermal conductivity measurements, Hole C0008A. (See table notes.) (Continued on next two pages.)

Core, section, interval (cm)	Depth CSF (m)	Method*	Thermal conductivity (W/[m·K])		N	Standard deviation (W/[m·K])	Thermal conductivity (W/[m·K]) [‡]
			Raw average	Calibrated [†]			
316-C0008A-							
1H-1, 85	0.85	V10305	0.93	0.88	1	—	0.91
1H-2, 10	1.51	V10305	0.98	0.93	1	—	0.96
1H-4, 10	1.95	V10305	1.03	0.99	1	—	1.01
1H-5, 50	3.34	V10305	0.95	0.91	1	—	0.93
1H-6, 50	4.74	V10305	1.03	0.99	1	—	1.01
1H-8, 40	6.05	V10305	1.04	1.00	1	—	1.02
2H-3, 50	9.08	V10305	1.08	1.04	1	—	1.06
2H-4, 50	10.28	V10305	1.04	1.00	1	—	1.02
2H-5, 50	11.72	V10305	1.11	1.07	1	—	1.10
2H-6, 62	13.27	V10305	1.05	1.00	1	—	1.03
2H-7, 56	14.64	V10305	1.07	1.03	1	—	1.05
2H-9, 1	15.68	V10305	0.84	0.80	1	—	0.82
3H-1, 50	16.00	V10305	1.09	1.05	1	—	1.07
3H-2, 32	17.26	V10305	0.94	0.90	1	—	0.92
3H-4, 65	19.29	V10305	0.75	0.71	1	—	0.72
3H-5, 65	20.57	V10305	0.85	0.81	1	—	0.83
3H-6, 23	21.62	V10305	0.78	0.73	1	—	0.75
3H-9, 50	23.72	V10305	0.96	0.92	1	—	0.94
3H-10, 50	24.92	V10305	0.98	0.94	1	—	0.96
4H-1, 50	25.50	V10305	0.98	0.93	1	—	0.95
4H-2, 50	26.83	V10305	0.93	0.88	1	—	0.90
4H-3, 50	28.15	V10305	0.93	0.89	1	—	0.91
4H-5, 50	29.91	V10305	0.85	0.80	1	—	0.82
4H-6, 65	31.22	V10305	0.75	0.70	1	—	0.71
4H-7, 58	32.52	V10305	0.99	0.95	1	—	0.97
4H-8, 55	33.84	V10305	1.06	1.02	1	—	1.04
4H-9, 35	34.96	V10305	0.80	0.76	1	—	0.77
5H-1, 48	34.98	V10305	0.91	0.86	1	—	0.88
5H-1, 113	35.63	V10305	0.76	0.71	1	—	0.73
5H-2, 36	36.18	V10305	1.10	1.06	1	—	1.08
5H-2, 120	37.02	V10305	0.93	0.89	1	—	0.91
5H-3, 80	38.03	V10305	0.89	0.84	1	—	0.86
5H-5, 45	39.39	V10305	0.93	0.89	1	—	0.91
5H-5, 81	39.75	V10305	0.88	0.83	1	—	0.85
5H-6, 45	40.49	V10305	0.94	0.90	1	—	0.92
5H-7, 50	41.87	V10305	0.97	0.93	1	—	0.95
5H-7, 70	42.09	V10305	0.99	0.95	1	—	0.97
5H-8, 45	43.14	V10305	0.95	0.91	1	—	0.93
6H-1, 35	44.35	V10305	1.03	0.99	1	—	1.01
5H-9, 65	44.65	V10305	0.98	0.94	1	—	0.96
6H-2, 80	46.13	V10305	1.02	0.98	1	—	1.00
6H-3, 50	47.26	V10305	1.22	1.18	1	—	1.21
6H-4, 63	48.81	V10305	0.80	0.75	1	—	0.77
6H-6, 60	50.10	V10305	0.64	0.59	1	—	0.60
6H-6, 110	50.60	V10305	0.94	0.90	1	—	0.92
6H-7, 43	51.26	V10305	1.00	0.96	1	—	0.98
6H-8, 40	52.53	V10305	0.93	0.89	1	—	0.91
6H-9, 35	53.79	V10305	0.92	0.87	1	—	0.89
7H-1, 50	54.00	V10305	0.92	0.87	1	—	0.89
7H-2, 26	55.08	V10305	1.02	0.98	1	—	1.00
7H-3, 23	56.41	V10305	1.21	1.17	1	—	1.19
7H-4, 60	58.08	V10305	1.05	1.00	1	—	1.03
7H-6, 115	59.99	V10305	1.01	0.97	1	—	0.99
7H-7, 105	61.32	V10305	0.88	0.83	1	—	0.85
7H-8, 94	62.55	V10305	1.05	1.01	1	—	1.03
7H-9, 50	63.41	V10305	0.97	0.93	1	—	0.95
8H-1, 53	63.53	V10305	0.95	0.91	1	—	0.93
8H-1, 118	64.18	V10305	1.03	0.98	1	—	1.01
8H-2, 90	65.23	V10305	1.16	1.12	1	—	1.14
8H-3, 78	66.41	V10305	1.01	0.97	1	—	0.99
8H-4, 77	67.71	V10305	1.00	0.95	1	—	0.98
8H-6, 85	69.33	V10305	0.90	0.85	1	—	0.87
8H-7, 50	70.07	V10305	0.94	0.90	1	—	0.92
8H-8, 60	71.47	V10305	0.84	0.80	1	—	0.82
9H-1, 80	73.30	V10305	0.88	0.84	1	—	0.86

Table T19 (continued). (Continued on next page.)

Core, section, interval (cm)	Depth CSF (m)	Method*	Thermal conductivity (W/[m·K])			Standard deviation (W/[m·K])	Thermal conductivity (W/[m·K]) [‡]
			Raw average	Calibrated [†]	N		
9H-2, 32	74.13	V10305	1.02	0.97	1	—	1.00
9H-3, 60	75.72	V10305	0.94	0.89	1	—	0.91
9H-6, 12	77.95	V10305	0.88	0.83	1	—	0.85
10H-1, 20	82.20	V10305	1.09	1.05	1	—	1.07
10H-2, 50	83.04	V10305	1.24	1.20	1	—	1.23
10H-3, 35	83.87	V10305	0.94	0.89	1	—	0.91
10H-4, 10	84.77	V10305	1.06	1.02	1	—	1.04
10H-5, 60	86.69	V10305	1.21	1.17	1	—	1.19
10H-7, 37	87.88	V10305	0.96	0.92	1	—	0.94
10H-8, 70	89.62	V10305	0.92	0.87	1	—	0.90
11H-1, 80	91.30	V10305	1.11	1.07	1	—	1.09
11H-2, 80	92.71	V10305	1.04	0.99	1	—	1.02
11H-5, 50	95.51	V10305	1.08	1.04	1	—	1.06
11H-6, 74	96.93	V10305	1.17	1.13	1	—	1.16
11H-7, 65	98.35	V10305	1.05	1.00	1	—	1.03
11H-8, 47	99.58	V10305	1.17	1.13	1	—	1.16
12H-1, 17	100.17	V10305	0.97	0.92	1	—	0.95
12H-2, 70	101.61	V10305	1.17	1.13	1	—	1.15
12H-3, 75	103.06	V10305	1.00	0.96	1	—	0.98
12H-4, 77	104.49	V10305	0.95	0.90	1	—	0.93
12H-6, 67	105.86	V10305	1.03	0.99	1	—	1.01
13H-1, 50	110.00	V10305	0.85	0.80	1	—	0.82
13H-2, 75	111.67	V10305	0.92	0.87	1	—	0.90
13H-3, 88	113.21	V10305	1.00	0.96	1	—	0.98
13H-4, 35	114.09	V10305	1.07	1.03	1	—	1.05
13H-7, 60	117.08	V10305	0.80	0.76	1	—	0.77
15H-3, 80	121.28	V10305	0.98	0.94	1	—	0.96
15H-4, 40	121.87	V10305	1.05	1.01	1	—	1.03
15H-5, 85	123.63	V10305	1.08	1.03	1	—	1.06
15H-6, 25	124.37	V10305	1.11	1.07	1	—	1.09
15H-7, 54	125.97	V10305	1.11	1.06	1	—	1.09
15H-8, 30	127.04	V10305	1.04	1.00	1	—	1.02
16H-1, 20	127.67	V10305	0.94	0.89	1	—	0.91
16H-3, 15	128.67	V10305	1.14	1.09	1	—	1.12
16H-5, 33	129.43	V10305	1.26	1.22	1	—	1.24
17H-2, 30	131.46	V10305	0.97	0.92	1	—	0.95
17H-4, 45	134.23	V10305	1.10	1.06	1	—	1.08
17H-5, 40	135.49	V10305	1.20	1.16	1	—	1.18
17H-7, 59	137.01	V10305	1.02	0.97	1	—	1.00
17H-8, 35	138.08	V10305	0.99	0.95	1	—	0.97
17H-9, 45	139.50	V10305	0.95	0.91	1	—	0.93
18H-1, 55	140.94	V10305	1.03	0.98	1	—	1.01
18H-2, 60	142.31	V10305	0.70	0.66	1	—	0.67
18H-4, 80	144.09	V10305	0.93	0.89	1	—	0.91
18H-5, 60	144.93	V10305	0.79	0.74	1	—	0.76
18H-6, 50	145.98	V10305	0.79	0.74	1	—	0.76
18H-7, 42	146.75	V10305	0.75	0.70	1	—	0.72
18H-8, 65	147.93	V10305	0.83	0.78	1	—	0.80
19H-1, 90	150.79	V10305	0.85	0.81	1	—	0.82
19H-3, 60	152.25	V10305	0.92	0.87	1	—	0.89
20H-1, 65	153.40	V10305	0.97	0.92	1	—	0.95
20H-2, 77	154.82	V10305	1.05	1.01	1	—	1.03
20H-4, 50	155.88	V10305	1.02	0.98	1	—	1.00
20H-5, 72	157.43	V10305	0.78	0.73	1	—	0.75
20H-6, 62	158.33	V10305	0.97	0.93	1	—	0.95
21H-1, 65	159.38	V10305	1.09	1.05	1	—	1.07
21H-2, 70	160.84	V10305	1.02	0.98	1	—	1.00
21H-3, 70	162.24	V10305	1.08	1.03	1	—	1.06
21H-4, 50	163.43	V10305	1.00	0.95	1	—	0.98
21H-6, 60	165.01	V10305	1.11	1.07	1	—	1.09
21H-7, 60	166.43	V10305	1.15	1.11	1	—	1.13
21H-8, 41	167.61	V10305	1.02	0.97	1	—	0.99
21H-9, 30	168.80	V10305	1.07	1.02	1	—	1.05
22H-2, 40	168.90	V10305	0.93	0.89	1	—	0.91
22H-3, 50	170.31	V10305	1.10	1.06	1	—	1.08
22H-4, 65	171.77	V10305	1.06	1.01	1	—	1.04
22H-5, 70	173.20	V10305	1.05	1.00	1	—	1.02
22H-7, 70	174.60	V10305	1.13	1.09	1	—	1.11

Table T19 (continued).

Core, section, interval (cm)	Depth CSF (m)	Method*	Thermal conductivity (W/[m·K])		N	Standard deviation (W/[m·K])	Thermal conductivity (W/[m·K]) [‡]
			Raw average	Calibrated [†]			
22H-8, 65	175.86	V10305	1.15	1.11	1	—	1.14
22H-9, 71	177.24	V10305	1.05	1.01	1	—	1.03
22H-10, 24	178.08	V10305	1.06	1.01	1	—	1.03
23H-1, 50	178.23	V10305	0.83	0.78	1	—	0.80
23H-2, 40	179.44	V10305	1.06	1.02	1	—	1.04
23H-3, 32	180.67	V10305	1.13	1.09	1	—	1.11
23H-4, 14	181.81	V10305	1.07	1.02	1	—	1.05
24H-2, 80	188.48	V10305	1.16	1.12	1	—	1.14
24H-3, 42	189.41	V10305	1.01	0.97	1	—	0.99
24H-4, 70	191.01	V10305	1.12	1.07	1	—	1.10
24H-5, 65	192.40	V10305	0.97	0.93	1	—	0.95
24H-7, 70	193.79	V10305	0.94	0.90	1	—	0.92
24H-8, 82	195.28	V10305	1.14	1.10	1	—	1.12
24H-9, 63	196.45	V10305	1.02	0.97	1	—	1.00
25H-1, 68	197.41	V10305	1.07	1.02	1	—	1.05
24H-10, 49	197.63	V10305	1.06	1.02	1	—	1.04
25H-3, 55	199.06	V10305	0.94	0.90	1	—	0.92
25H-4, 65	200.19	V10305	0.94	0.90	1	—	0.92
25H-5, 22	201.07	V10305	1.03	0.98	1	—	1.00
26H-1, 84	201.73	V10305	1.01	0.96	1	—	0.98
26H-3, 20	202.74	V10305	0.95	0.91	1	—	0.93
26H-4, 20	203.11	V10305	0.71	0.66	1	—	0.68
26H-6, 20	203.90	V10305	0.63	0.59	1	—	0.60
27H-1, 80	211.19	V10305	1.01	0.97	1	—	0.99
27H-2, 113	212.83	V10305	1.02	0.98	1	—	1.00
27H-3, 72	213.74	V10305	1.13	1.09	1	—	1.12
27H-4, 65	214.98	V10305	0.96	0.91	1	—	0.93
27H-8, 55	218.81	V10305	1.09	1.05	1	—	1.07
28H-1, 90	220.79	V10305	1.01	0.97	1	—	0.99
28H-2, 54	221.74	V10305	0.99	0.94	1	—	0.96
28H-4, 57	223.09	V10305	0.97	0.92	1	—	0.94
28H-5, 25	224.12	V10305	0.72	0.67	1	—	0.69

Notes: * = V10305 refers to full-space needle probe, H10404 refers to half-space line source, † = thermal conductivities were adjusted based on calibration formulas and constants given in the “Expedition 316 methods” chapter, ‡ = thermal conductivities were corrected for temperature and pressure as described in the “Expedition 316 methods” chapter. CSF = core depth below seafloor. — = not applicable.

Table T20. Thermal conductivity measurements, Hole C0008C. (See table notes.) (Continued on next two pages.)

Core, section, interval (cm)	Depth CSF (m)	Method*	Thermal conductivity (W/[m·K])		N	Standard deviation (W/[m·K])	Thermal conductivity (W/[m·K]) [‡]
			Raw average	Calibrated [†]			
316-C0008C-							
01H-3, 40	2.07	V10305	0.99	0.94	1	—	0.96
01H-4, 40	3.26	V10305	1.03	0.98	1	—	1.01
01H-6, 40	4.89	V10305	1.02	0.97	2	0.00	1.00
02H-1, 40	5.91	V10305	0.99	0.95	2	0.01	0.97
02H-3, 30	7.35	V10305	1.01	0.96	3	0.01	0.99
02H-4, 50	8.66	V10305	0.98	0.93	1	—	0.95
02H-5, 40	9.89	V10305	0.93	0.88	1	—	0.90
02H-6, 32	11.15	V10305	1.03	0.99	2	0.00	1.01
02H-8, 30	12.73	V10305	0.99	0.95	1	—	0.97
02H-9, 43	13.99	V10305	0.97	0.92	1	—	0.95
02H-10, 25	15.13	V10305	0.86	0.82	1	—	0.84
03H-1, 58	15.59	V10305	1.01	0.96	1	—	0.99
03H-2, 40	16.75	V10305	1.06	1.01	1	—	1.04
03H-4, 36	18.34	V10305	1.06	1.01	1	—	1.04
03H-5, 32	19.52	V10305	1.02	0.98	1	—	1.00
03H-6, 81	21.43	V10305	0.98	0.94	3	0.00	0.96
03H-8, 52	22.69	V10305	1.00	0.95	2	0.00	0.98
03H-9, 52	23.80	V10305	0.90	0.85	3	0.00	0.87
04H-1, 59	25.10	V10305	0.96	0.92	1	—	0.94
03H-10, 52	25.11	V10305	0.98	0.93	1	—	0.96
04H-2, 49	25.95	V10305	0.87	0.83	1	—	0.85
04H-3, 43	27.19	V10305	0.94	0.89	3	0.02	0.92
04H-4, 51	28.59	V10305	0.95	0.91	1	—	0.93
04H-6, 50	30.11	V10305	0.94	0.90	2	0.00	0.92
04H-7, 55	31.27	V10305	1.19	1.15	3	0.02	1.18
04H-8, 43	32.45	V10305	1.10	1.05	3	0.01	1.08
04H-9, 54	33.88	V10305	1.04	1.00	2	0.00	1.02
05H-2, 30	34.69	V10305	1.01	0.97	2	0.01	0.99
04H-10, 59	35.24	V10305	1.00	0.95	2	0.00	0.98
05H-3, 50	35.90	V10305	1.04	1.00	3	0.02	1.02
05H-4, 50	37.21	V10305	1.02	0.98	2	0.01	1.00
05H-6, 31	38.56	V10305	1.09	1.04	3	0.00	1.07
05H-7, 31	39.61	V10305	1.12	1.08	1	—	1.10
05H-8, 45	41.05	V10305	1.09	1.04	3	0.00	1.07
05H-9, 35	42.19	V10305	1.16	1.11	1	—	1.14
05H-10, 47	43.32	V10305	1.04	0.99	1	—	1.02
06H-1, 60	44.11	V10305	0.93	0.89	3	0.02	0.91
06H-2, 55	45.37	V10305	1.07	1.03	1	—	1.05
06H-3, 65	46.95	V10305	0.94	0.90	1	—	0.92
06H-5, 65	48.66	V10305	0.93	0.89	1	—	0.91
06H-6, 35	49.41	V10305	0.91	0.86	1	—	0.88
06H-7, 65	51.02	V10305	1.10	1.05	2	0.01	1.08
06H-8, 38	52.05	V10305	1.16	1.11	1	—	1.14
07H-1, 40	53.41	V10305	1.06	1.01	1	—	1.04
06H-9, 65	53.51	V10305	1.06	1.02	3	0.00	1.04
07H-2, 35	54.01	V10305	1.24	1.20	1	—	1.23
07H-3, 58	55.54	V10305	0.80	0.75	1	—	0.77
07H-5, 27	56.37	V10305	0.78	0.73	1	—	0.75
07H-6, 105	58.25	V10305	1.23	1.18	2	0.01	1.21
07H-7, 55	59.06	V10305	0.97	0.92	2	0.03	0.95
07H-8, 95	60.76	V10305	0.94	0.89	2	0.00	0.91
07H-9, 15	61.27	V10305	0.90	0.86	1	—	0.88
09H-2, 40	69.00	V10305	1.00	0.95	2	0.02	0.98
09H-3, 37	69.66	V10305	1.12	1.08	2	0.00	1.11
09H-5, 65	71.59	V10305	0.96	0.91	2	0.00	0.94
09H-6, 103	72.98	V10305	0.95	0.90	2	0.01	0.92
09H-8, 21	73.41	V10305	0.70	0.65	1	—	0.67
09H-9, 51	75.09	V10305	0.78	0.73	1	—	0.75
09H-10, 45	76.37	V10305	0.82	0.77	1	—	0.79
10H-2, 55	77.87	V10305	0.95	0.90	1	—	0.93
10H-3, 22	78.78	V10305	0.83	0.78	1	—	0.80
10H-4, 44	80.30	V10305	0.87	0.82	3	0.00	0.84
10H-7, 48	81.99	V10305	0.76	0.72	1	—	0.73
10H-8, 45	82.56	V10305	0.97	0.92	2	0.02	0.94
11H-1, 20	82.71	V10305	0.84	0.79	3	0.01	0.81

Table T20 (continued). (Continued on next page.)

Core, section, interval (cm)	Depth CSF (m)	Method*	Thermal conductivity (W/[m·K])			Standard deviation (W/[m·K])	Thermal conductivity (W/[m·K]) [‡]
			Raw average	Calibrated [†]	N		
10H-10, 55	84.08	V10305	0.79	0.74	2	0.00	0.76
11H-5, 42	84.64	V10305	0.74	0.69	2	0.01	0.71
10H-11, 35	85.19	V10305	0.75	0.70	1	—	0.72
10H-13, 30	85.89	V10305	0.84	0.79	1	—	0.81
11H-8, 60	86.05	V10305	0.85	0.80	2	0.01	0.82
11H-9, 27	87.06	V10305	0.69	0.65	1	—	0.66
11H-11, 50	88.83	V10305	1.01	0.97	1	—	0.99
12H-1, 58	90.69	V10305	0.87	0.82	2	0.01	0.84
11H-12, 114	91.01	V10305	0.94	0.89	3	0.01	0.91
13H-1, 17	91.43	V10305	0.84	0.80	1	—	0.82
11H-13, 53	91.72	V10305	0.91	0.87	2	0.02	0.89
13H-3, 40	92.00	V10305	0.79	0.74	1	—	0.76
11H-14, 22	92.42	V10305	1.04	1.00	1	—	1.02
13H-5, 45	92.75	V10305	0.84	0.79	2	0.01	0.81
13H-7, 45	94.22	V10305	0.97	0.92	1	—	0.94
13H-9, 68	95.79	V10305	0.95	0.91	3	0.01	0.93
13H-11, 30	96.33	V10305	0.94	0.89	1	—	0.91
13H-12, 16	97.40	V10305	1.15	1.11	3	0.02	1.13
14H-1, 42	98.01	V10305	1.04	1.00	2	0.00	1.02
14H-2, 60	99.40	V10305	1.07	1.02	3	0.01	1.05
14H-3, 43	100.00	V10305	0.90	0.85	1	—	0.87
14H-4, 39	101.26	V10305	1.09	1.04	1	—	1.07
14H-5, 30	101.97	V10305	0.93	0.88	1	—	0.90
15H-3, 30	102.43	V10305	1.12	1.07	1	—	1.10
15H-4, 55	103.08	V10305	1.00	0.95	1	—	0.97
15H-6, 57	104.12	V10305	0.57	0.52	3	0.00	0.53
14H-8, 50	104.14	V10305	0.87	0.82	2	0.01	0.84
14H-9, 55	105.05	V10305	0.77	0.73	1	—	0.74
15H-7, 38	105.39	V10305	0.95	0.90	3	0.00	0.92
14H-10, 55	106.36	V10305	0.63	0.59	1	—	0.60
15H-8, 65	106.92	V10305	0.92	0.87	2	0.00	0.89
15H-9, 17	107.77	V10305	0.85	0.81	1	—	0.83
16H-1, 30	108.59	V10305	1.04	1.00	1	—	1.02
16H-3, 35	110.66	V10305	1.05	1.01	1	—	1.03
16H-4, 37	111.41	V10305	1.03	0.98	1	—	1.01
16H-6, 73	113.30	V10305	1.16	1.11	1	—	1.14
16H-7, 29	113.95	V10305	1.37	1.33	1	—	1.36
17H-2, 25	115.88	V10305	1.04	1.00	1	—	1.02
16H-10, 63	116.11	V10305	1.05	1.01	2	0.01	1.04
16H-11, 65	117.44	V10305	0.94	0.89	1	—	0.92
17H-4, 63	117.93	V10305	1.04	1.00	1	—	1.02
18H-1, 43	120.32	V10305	1.03	0.99	1	—	1.01
18H-2, 53	121.74	V10305	1.03	0.98	1	—	1.00
18H-3, 61	123.15	V10305	0.92	0.88	2	0.01	0.90
18H-4, 85	124.70	V10305	0.94	0.90	1	—	0.92
18H-5, 42	125.59	V10305	0.88	0.83	1	—	0.85
19H-2, 23	126.62	V10305	0.99	0.95	2	0.02	0.97
18H-7, 90	127.40	V10305	0.87	0.83	1	—	0.84
19H-4, 43	127.77	V10305	0.87	0.82	1	—	0.84
18H-10, 21	129.02	V10305	0.63	0.58	1	—	0.59
20H-1, 37	129.76	V10305	0.82	0.77	1	—	0.79
21H-1, 67	130.77	V10305	0.67	0.62	1	—	0.63
21H-2, 75	132.09	V10305	0.73	0.68	1	—	0.69
21H-4, 50	134.05	V10305	1.06	1.01	1	—	1.04
21H-6, 60	135.30	V10305	1.06	1.01	1	—	1.04
21H-7, 65	136.66	V10305	1.09	1.04	1	—	1.07
21H-8, 45	137.45	V10305	1.00	0.96	1	—	0.98
21H-9, 40	138.42	V10305	0.71	0.66	1	—	0.68
22X-1, 50	139.60	V10305	0.86	0.82	1	—	0.84
22X-2, 80	141.21	V10305	0.89	0.85	1	—	0.87
22X-3, 52	142.19	V10305	0.90	0.85	1	—	0.87
22X-4, 75	143.79	V10305	1.00	0.95	2	0.02	0.97
22X-6, 76	145.12	V10305	1.01	0.97	1	—	0.99
22X-7, 86	146.43	V10305	0.92	0.87	3	0.01	0.89
22X-8, 55	147.22	V10305	0.81	0.77	1	—	0.78
23X-5, 60	151.25	V10305	0.87	0.82	2	0.01	0.84
23X-7, 30	153.31	V10305	0.99	0.95	1	—	0.97
23X-9, 25	154.88	V10305	0.89	0.84	2	0.01	0.86

Table T20 (continued).

Core, section, interval (cm)	Depth CSF (m)	Method*	Thermal conductivity (W/[m·K])			Standard deviation (W/[m·K])	Thermal conductivity (W/[m·K]) [‡]
			Raw average	Calibrated [†]	N		
24X-2, 109	159.25	V10305	0.88	0.83	1	—	0.85
24X-3, 58	160.23	V10305	0.94	0.90	1	—	0.92
24X-6, 40	161.87	V10305	0.88	0.83	1	—	0.85
24X-7, 58	162.89	V10305	0.80	0.75	1	—	0.77
24X-8, 50	164.12	V10305	0.83	0.78	2	0.05	0.80
24X-9, 45	165.39	V10305	0.79	0.75	1	—	0.76
25X-1, 25	167.04	V10305	1.00	0.95	1	—	0.98
25X-3, 45	167.89	V10305	0.81	0.76	1	—	0.78
25X-5, 18	168.67	V10305	1.01	0.97	1	—	0.99
25X-7, 38	169.33	V10305	0.99	0.94	1	—	0.96
25X-8, 45	170.73	V10305	0.88	0.83	1	—	0.85
25X-8, 62	170.89	V10305	0.92	0.88	2	0.01	0.90
25X-11, 70	173.60	V10305	1.01	0.96	1	—	0.98
25X-12, 60	174.83	V10305	0.54	0.49	1	—	0.50

Notes: * = V10305 refers to full-space needle probe and H10404 refers to half-space line source, † = thermal conductivities were adjusted based on calibration formulas and constants given in the “Expedition 316 methods” chapter, ‡ = thermal conductivities were corrected for temperature and pressure as described in the “Expedition 316 methods” chapter. CSF = core depth below seafloor. — = not applicable.

Table T21. Temperature measurements, Hole C0008A. (See table notes.)

Core	Tool	Depth CSF (m)	BWT (°C)	Time delay (s)	Fit		Equilibrium temperature (°C)	Remark
					Start (s)	End (s)		
316-C0008A-								
3H	APCT3	25.00	1.75	65.8	221	469	3.28	Marginal
6H	APCT3	53.50	1.81	3.3	60	548	4.74	Good
11H	APCT3	100.00	2.90	-8.5	234	714	8.11	Marginal
13H	APCT3	119.00	1.77	93.3	159	362	8.84	Marginal
16H	APCT3	130.90	1.68	-54.7	60	769	8.46	Fair
19H	APCT3	152.70	2.27	-12.2	80	429	9.16	Good
22H	APCT3	177.70	1.80	10.6	60	500	11.63	Good
25H	APCT3	200.90	—	26.5	60	6,898	12.60	Excellent
30X	SET	243.75	1.63	-2.2	46	247	14.60	Fair

Notes: CSF = core depth below seafloor. BWT = bottom water temperature. APCT3 = advanced piston corer temperature tool, SET = sediment temperature. — = not measured.

Table T22. Temperature measurements, Hole C0008C. (See table notes.)

Core	Tool	Depth CSF (m)	BWT (°C)	Time delay (s)	Fit		Equilibrium temperature (°C)	Remark
					Start (s)	End (s)		
316-C0008C-								
3H	APCT3	24.50	1.78	-1.9	60	458	3.41	Good
5H	APCT3	43.50	1.76	44.4	60	452	4.60	Good
7H	APCT3	60.50	1.89	-11.9	60	449	5.22	Good
9H	APCT3	73.50	—	-3.3	60	426	6.44	Good
11H	APCT3	90.10	1.70	-3.5	60	555	7.39	Good
13H	APCT3	97.60	1.70	-3.0	60	572	7.69	Good
15H	APCT3	108.30	1.78	-33.3	60	451	7.73	Good
17H	APCT3	119.90	1.79	4.6	60	459	8.72	Good
19H	APCT3	129.40	1.79	-13.8	60	451	9.62	Good
21H	APCT3	139.00	—	-4.7	60	494	10.07	Good

Notes: CSF = core depth below seafloor. BWT = bottom water temperature. APCT3 = advanced piston corer temperature tool. — = not measured.